Assessing sandstone reservoir quality: identifying the reality

CHARLAFTIS, DIMITRIOS

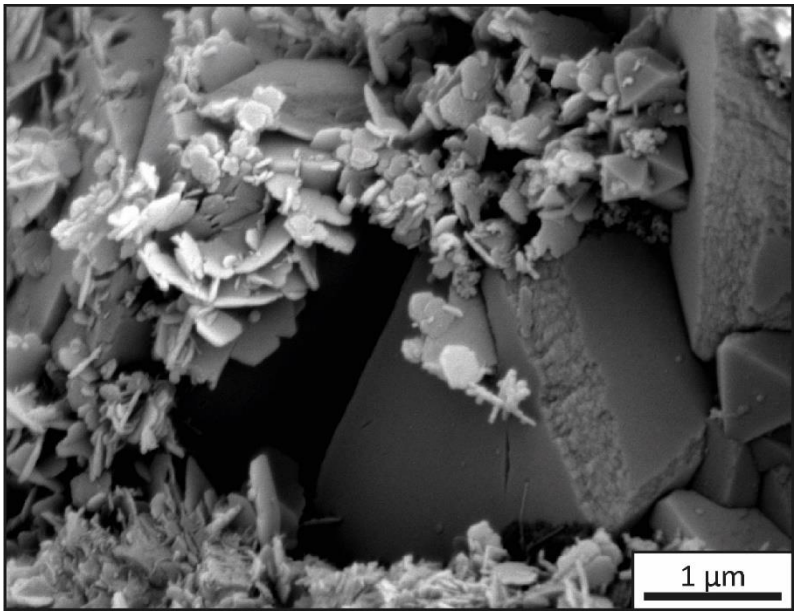

Authigenic grain coating chlorite platelets formed during an experiment

Assessing sandstone reservoir quality: identifying the reality

Dimitrios Charlaftis

This thesis is submitted in partial fulfilment of the requirements for the degree of Doctor of Philosophy at Durham University

Department of Earth Sciences

University of Durham

2021

Abstract

Quartz cementation is one of the most important cements governing reservoir quality in sandstones. The presence of clay coats plays a crucial role in preserving anomalous high porosity in deeply buried sandstones by inhibiting porosity-occluding macroquartz cementation. More robust and greater grain coat coverage is required for higher temperature reservoirs to preserve significant amounts of porosity.

The first and main component of this research entails a series of hydrothermal experiments simulating quartz cementation and grain coat development, particularly authigenic chlorite, at specific temperature steps to mimic the conditions of deeply buried reservoirs and develop predictive models for clay-coat-controlled reservoir quality in such settings. Naturally-occurring sandstone samples from the Lower Jurassic Cook Formation of the Oseberg Field (Norway) were exposed to a silica supersaturated solution for up to 360 hours at temperatures of 0–250 °C. An array of microscopic, analytical and modelling techniques was employed to track the mineralogical alterations, quantify the temperature-dependent volumetric changes of authigenic chlorite, the thickness and coverage of the clay coats, and capture the evolving reservoir quality attributes in the 2D and 3D domain. Results show that grain coating chlorite is formed through a mixture of the solid-state transformation and dissolution-precipitation mechanisms from berthierine transformation, replacement of siderite and neoformation on precursor-free substrate surfaces. Ceasing of porosity loss and permeability maintenance correlate directly to grain coat volume increase at temperatures higher than 175 °C.

The second component presents a series of hydrothermal experiments performed on laboratory synthesised biofilm-rich, pure sand samples to test the influence of microbial extracellular polymeric substances (EPS) on early mineral precipitation at temperatures up to 120 °C. An artificial solution was used to synthesise and preserve the microbial communities and promote mineral genesis during each experimental run. Textural evaluation of the samples shows that EPS-coated surfaces serve as templates for the nucleation of early mineral precipitates. Poorly-ordered, morphologically clay-like material developed at points of contact between quartz grains and where EPS structures pre-existed.

Future energy and climate change mitigation developments require better characterisation of subsurface reservoirs that can act as energy sources or storage media. This research has important implications for diagenesis studies, providing key insights that can be used to improve predictability of reservoir quality modelling applied in a wide range of geoscience applications.

Table of Contents

Declaration

I declare that the present thesis, which I submit for the degree of Doctor of Philosophy at Durham University, is my own work, except where acknowledgement is made in the text, and not substantially the same as any work which has previously been submitted at this or any other institution for any degree, diploma or other qualification.

Note on publications included in this thesis

At the time of submission, two chapters of this thesis had been submitted for publication or published in peer-reviewed journals.

Chapter 3 Charlaftis, D., S. J. Jones, K. J. Dobson, J. Crouch, and S. Acikalin (2021), Experimental study of chlorite authigenesis and influence on porosity maintenance in sandstones, *Journal of Sedimentary Research*, *91*, 1-16, doi:10.2110/jsr.2020.122.

Chapter 4 D. Charlaftis, K. J. Dobson, S. J. Jones, D. Lakshtanov, J. Crouch and J. Cook. Experimental simulation of burial diagenesis and subsequent 2D-3D characterization of sandstone reservoir quality (submitted to a peer-reviewed journal, 2021).

All work presented in this thesis is the author's original contribution.

July 2021

Acknowledgements

First and foremost, I would like to thank my primary supervisor, Dr Stuart Jones, for his invaluable advice and tutelage during my PhD degree. Stuart's treasured support was influential in shaping my experimental methods and critiquing my results. He consistently strived for excellence and created a climate of continuous improvement of both my personal and professional development. I am immensely grateful to Dr Katherine Dobson for her excellent contribution to the XCT component of my research and for numerous stimulating discussions that helped me greatly throughout my PhD. My sincere thanks go to Prof. Phil Dyer for his constant help with the experimental aspect of my research. I would also like to thank Dr Pablo Cubillas, Dr Sanem Acikalin, Dr Mark Osborne, Prof. Andreas Kappler and Prof. Chris Greenwell for their valuable advice and suggestions concerning the study. I must acknowledge Dr Stefan Nielsen and Prof. Andy Aplin for their support and feedback as my internal reviewers. My gratitude extends to Durham University and BP for the generous funding opportunity that allowed me to conduct this thesis.

I would like to thank Ian Chaplin and Sophie Edwards for the preparation of petrographic samples; Leon Bowen and Diana Alvarez-Ruiz for advice and support on scanning electron microscopy; Jackie Kendrick for helium-porosity analysis; Jonathan Crouch for advice and support on quantitative automated mineralogy analysis; Dmitry Lakshtanov and Jennie Cook for assistance with XCT data collection and analysis, and Lars Grimm for assistance with biofilm growth.

A huge thanks to the postgraduate community of the department for facilitating the complex process of balancing studies with social life. Special mention must go to Sean O'Neill, Eloïse Bretagne, Simon Guerin-Marthe, Ilaria Gaiani, Catharina Heerema, Alexandra Tamas, Maximilian Franzel, Joshua Brown, and Craig Withers, who made my PhD years contain a significant amount of fun. Special thanks to the Greek geoscientist group of Durham. Thank you all for your continued friendship and support, Dimitrios Michelioudakis, Georgios-Pavlos Frangitakis, Nikolaos Apeiranthitis, and Christos Vasilopanagos.

Last but not least, I am immensely grateful to my parents for spiritually and practically supporting me throughout my studies and my life in general. I wouldn't be here without them.

Η παρούσα διατριβή είναι αφιερωμένη στον αδελφό μου Ευάγγελο Χαρλαύτη.

Chapter 1: Introduction

1.1 Project context and research rationale

The success of a wide range of geoscience applications, including hydrocarbon extraction, CO_2 storage, hydrogen storage, aquifer development and geothermal exploration, depends mainly on finding sandstone reservoirs with sufficient porosity and permeability. The inclusion of accurate pre-drill reservoir quality assessments becomes more and more critical, especially in poorly explored and more technically challenging areas. Therefore, understanding the parameters that control reservoir quality of sandstones exposed to high pressure and high temperature (HPHT) conditions is of crucial importance to ascertain whether an exploration target is commercially viable.

To predict reservoir quality of deeply buried sandstones, diagenesis, the combined function of mechanical and chemical compaction processes, must be well constrained. Multiple studies of diagenetic clay and microquartz coats suggest that their presence is considered responsible for maintaining porosity in many deep clastic reservoirs, apparently by inhibiting quartz overgrowth cementation and pressure dissolution (Pittman et al. 1992; Ehrenberg 1993; Bloch et al. 2002; Anjos et al. 2003; French et al. 2012; French and Worden 2013).

Quantifying the temperature conditions, mineralogical alterations, and porosity and permeability evolution during progressive burial of a reservoir rock is essential for achieving a holistic understanding and quantitative evaluation of reservoir sandstones. Although reservoir quality preserving factors, such as the presence of clay mineral coats, are generally known to geologists, misconceptions exist in relation to their development and occurrence. This research will provide insights to improve predictability of reservoir quality modelling in high-temperature (> 150 °C), deeply buried reservoir sandstones.

1.1.1 Aims of research

- To undertake a series of hydrothermal experiments to test the fundamental premises that clay coats, particularly chlorite, inhibit quartz cement and evaluate the mechanisms by which this inhibition occurs.
- To quantify in the 2D and 3D domain: (i) the transformation of Fe-rich precursor clays and other Fe-rich minerals to authigenic grain coating chlorite, (ii) other mineral alterations affecting reservoir quality and, (iii) the subsequent porosity and permeability evolution.
- To experimentally identify the role of biofilm communities on the precipitation of early minerals and to assess whether they can act as precursors for authigenic mineral phases.

1.1.2 Thesis outline

The full outlines of chapters 1–6 and appendices are described individually below. Chapters 3–5 have been written as standalone manuscripts that have been published and/or will be submitted for publication in peer-reviewed international journals; these are recast and updated for the thesis where appropriate. As such, each chapter contains a specific introduction, methods, results, discussion, and conclusions. The introduction sections for each chapter represent a content-specific synopsis of the material in chapter 1 and may, therefore, be skipped at the reader's discretion. Co-authors for each manuscript provide scientific advice and discussion and appropriate editorial guidance. The thesis only contains manuscripts for which I am the first author, and I have been responsible for more than 90% of the primary data collection, interpretation, and research manuscript writing.

The following is a description of chapters 1–6 and the appendices:

- Chapter 1 summarises the present state of the literature regarding reservoir quality of siliciclastic reservoirs and discusses the effects of factors such as quartz cementation, grain coats and microbial activity on diagenesis and reservoir properties with increasing burial.
- Chapter 2 outlines the laboratory setup and the analytical techniques used to conduct the hydrothermal experiments and evaluate the experimental results, respectively. Even though parts of this chapter are repeated in the manuscripts (e.g. chapters 3–5), this is all gathered here for clarity.
- Chapter 3 presents a series of temperature-controlled hydrothermal experiments on naturally occurring sandstone samples from the Lower Jurassic Cook formation from the Oseberg field (Norway). Each sample was subjected to specific temperature conditions to investigate the mechanisms and diagenetic processes leading to the development of authigenic chlorite coats and evaluate the impact of these coats on reservoir quality. This chapter has been published in the *Journal of Sedimentary Research (JSR)*, doi: 10.2110/jsr.2020.122
- Chapter 4 extends the methods developed in chapter 3 to quantify the 3D data of the hydrothermally treated samples; applying a multi-scale X-ray computed tomography (XCT) approach allowed the volumetric quantification of the mineralogical and pore-throat alterations, induced by the experimental process, in the 3D domain. A new set of hydrothermal experiments using a single sample from the same Formation has been undertaken to test the findings of the previous chapter in a more geologically realistic

scenario that simulates burial. A methodology capable of quantifying grain coat volume change in the 3D domain and assessing the subsequent influence on reservoir properties via porosity modelling and permeability simulations is presented. This chapter has been submitted for publication to a peer-reviewed journal.

- Chapter 5 presents a novel approach including a series of temperature-controlled hydrothermal experiments on biofilm-rich unconsolidated pure sand grains to demonstrate proof of principle of the role of bacterial EPS (extracellular polymeric substances) on the formation of early grain coats and subsequent development during progressive burial.
- Chapter 6 elaborates on the discussion sections from the preceding chapters while using an integrated approach to summarize and discuss the wider implications of authigenic grain coats on sandstone reservoir quality. Conclusions drawn throughout the body of the thesis are summarised. This chapter also reveals areas of future research that might develop the themes covered in this thesis.
- Appendix A contains supporting information related to the AQM and XCT acquisition characteristics.
- Appendix B lists the titles of scientific papers submitted for publication to peer-reviewed journals, to which I contributed to whilst conducting the research presented in this thesis.

1.2 Reservoir quality of sandstones: a review

1.2.1 Introduction

Rock properties and reservoir quality of sandstones call for a deliberate focus on depositional, shallow diagenetic and deep burial diagenetic processes. Initial rock properties such as grain size, mineral composition and, initial porosity and permeability are dependent on processes associated with the source area and the environment of deposition. Subsequent evolution of these properties is influenced by diagenesis, a continuously active process during which sedimentary mineral assemblages react to equilibrate within an environment of altering temperature, pressure, and chemistry conditions.

Reservoir quality of sandstone reservoirs generally decreases with increasing burial depth, typically due to mechanical compaction and quartz cementation (Worden and Morad 2000). However, a significant number of deeply buried sandstone reservoirs have unusually high porosity and permeability. Numerous studies present a direct link between reservoir quality preservation and early diagenetic clay or microquartz grain coating development (Pittman et al. 1992; Ehrenberg

1993; Aase et al. 1996; Bloch et al. 2002; Ajdukiewicz and Lander 2010; Ajdukiewicz and Larese 2012; French et al. 2012; Worden et al. 2012; French and Worden 2013). The porosity preserving effect of diagenetic clay coats in quartz-rich sandstones is due to their tendency to develop thick and continuous coats on detrital quartz grains, thus limiting the volume of quartz cementation (Ajdukiewicz and Lander 2010; Taylor et al. 2010).

Diagenetic clay coats form via the thermally driven recrystallization of low temperature detrital, precursor, clay-coat material, and in situ precipitation through diagenetic mineral interactions with pore fluids. Potential mechanisms in which detrital clay-coated sands occur include mechanical infiltration (Matlack et al. 1989), bioturbation (McIlroy et al. 2003; Needham et al. 2005), inheritance (Wilson 1992) and sediment ingestion and excretion (Worden et al. 2006). Recent research has also demonstrated the profound influence of biofilm communities and the occurrence of extracellular polymeric substance (EPS) on the formation of early clay grain coats in marginal marine settings (Stal 2003; Stal 2010; Wooldridge et al. 2017a; Virolle et al. 2019a).

1.2.2 Diagenetic regimes

Figure 1.1 presents the depositional environment and three conceptual regimes (e.g., eodiagenesis, mesodiagenesis and telodiagenesis) that relate diagenetic processes with the evolution of sedimentary basins (Worden and Burley 2003).

The primary make-up of the sediment plays a major role in influencing the history and reservoir quality evolution of the subsequent rock (Nguyen et al. 2016; Worden et al. 2018a). Initial reservoir properties are controlled by the initial sand composition, grain size distribution, sorting, sphericity, angularity and packing, which all are a function of the depositional environment. The depositional environment is influenced by the surface interstitial pore water, redox potential (Eh), acidity-alkalinity (pH) conditions, and activities of dissolved species (Ahmed 2008). Provenance and weathering processes are the main controls of the initial clay mineral composition.

The role of shallow burial diagenetic processes (e.g., eodiagenesis) in sandstone reservoir quality is becoming increasingly acknowledged for its influence on the formation of mainly clay coats that potentially inhibit later quartz cement (Dowey et al. 2017). The most common eodiagenetic clay minerals are kaolinite, glauconite, berthierine, verdine, di- and trioctahedral smectite, mixed clay minerals, such as illite-smectite or chlorite-smectite, and magnesium-rich clay minerals such as palygorskite (Worden and Morad 2003). Eodiagenesis may lead to early cementation or dissolution of cements (e.g., carbonates or halite) or the alteration of mineral and detrital components due to reactions with fresh groundwater or highly saline waters. Meteoric water flushing dissolves feldspar and mica and precipitates authigenic clay minerals, most commonly kaolinite (Bjørlykke and Jahren

2010). Finally, vadose zone processes, such as clay infiltration (Matlack et al. 1989), and biologically-related processes, such as bioturbation or microbial driven chemical reactions, are also important contributors of early diagenesis (Worden et al. 2006).

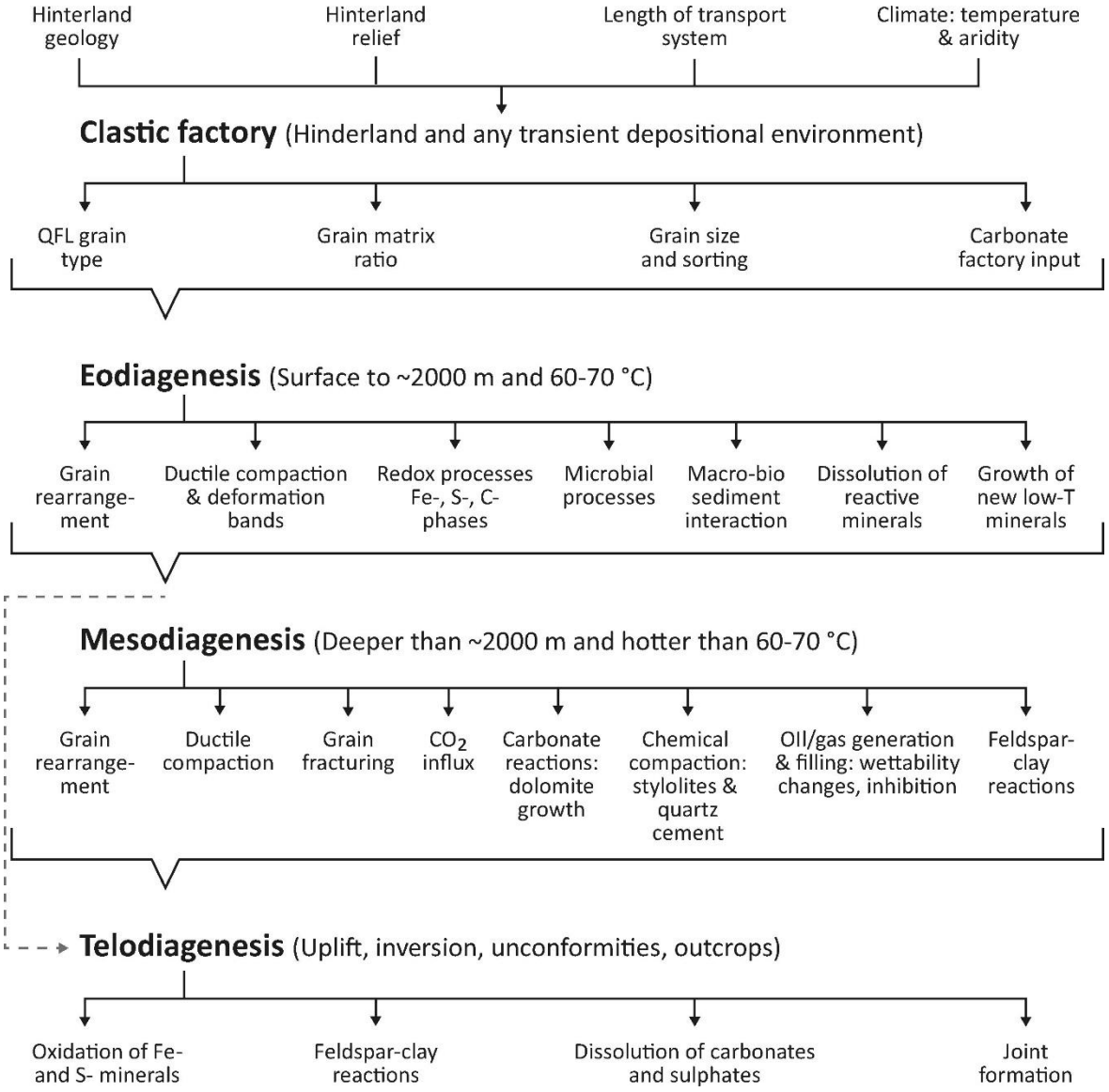

Figure 1.1: Controls on sandstone reservoir quality split between the major controls on clastic grains: the 'clastic factory', eodiagenetic (early/shallow burial diagenetic) controls, mesodiagenetic (burial diagenetic) controls, and even telogenetic (uplift-related) influences (Modified after Worden et al., 2018).

Following eodiagenesis, a series of diagenetic reactions, induced by further changes in temperature, pore-fluid chemistry, pore-fluid circulation through sand bodies, and pressure, take over. In the so-called mesodiagenetic regime, the solubility of the minerals increases, reaction rates also increase and therefore, reactions barriers are more easily overcome. Burial related processes depend on both the primary sediment character and the eodiagenetic processes imposed on the primary sediment (Worden et al. 2018a). Mesodiagenesis can destroy, preserve, or enhance reservoir quality, whatever the depositional characteristics have been. Common mesodiagenetic

alterations and their impact on reservoir quality of sandstones are summarized in Table 1.1 (Morad et al. 2010). Finally, telodiagenesis occurs in inverted basins that have experienced an influx of predominantly meteoric waters, which lead to significant geochemical changes, including feldspar dissolution and alteration to kaolinite (Worden and Morad 2003).

Process	Major Controlling Parameters	Impact on Reservoir Quality
Illite formation	Availability of precursor clay minerals, primarily kaolinite and dioctahedral smectite	Permeability deterioration, increase in water saturation, enhancement of intergranular pressure dissolution
Chlorite formation	Availability of precursor grain-coating berthierine or smectite	Inhibits quartz overgrowth cementation in deep sandstone reservoirs
Dickite formation	Availability of precursor kaolinite; mesogenetic acidic conditions	Prevention of illitization of kaolinite and hence permeability preservation
Albitization of K-feldspars	Abundance of detrital K-feldspar; high Na^+ activities	Enhances illite formation by supplying K^+, hence causing permeability deterioration
Albitization of plagioclase	Abundance of Ca-rich plagioclase; high Na^+ activities	Provides Ca^{2+} and Al^{3+}, which act as sources of small amounts of carbonate and clay mineral cements
Quartz cementation and pressure dissolution of quartz grains	Availability of monocrystalline quartz grains with clean surfaces, or of illite coats and micas, respectively	Substantial deterioration of permeability and porosity
Dissolution of unstable grains and calcite cement	Thermal maturation of organic matter, which generates organic acids and CO_2	Enhancement of reservoir quality through the creation of secondary intragranular and intergranular porosity
Cementation by ankerite, Mg-siderite, barite, and anhydrite	Flux of basinal fluids, primarily along faults	Deterioration of reservoir quality

Table 1.1: Typical mesodiagenetic processes in sandstones, their controlling parameters, and potential impact on reservoir quality (from Morad et al., 2010).

1.2.2.1 Open or closed system diagenesis

The topic of closed versus open chemical systems during diagenesis in sedimentary basins is a matter of considerable debate. Some authors have suggested that diagenesis within sandstones of the North Sea sedimentary basin is best described by a closed geochemical system (Ehrenberg 1993). In a closed-system model, diagenetic reactions can be written as geochemically balanced mineral reactions so that the precipitated cement equals dissolution in a local scale (Bjørlykke 2014). Therefore, the variation in the primary sediment composition is important for the prediction of rock properties. Contrarily, an open-system model is characterised by large-scale mass transfer

in the subsurface, allowing very significant changes in the rock composition and, hence predictions of rock properties are difficult (Gluyas and Cade 1997). An open chemical system is used to explain diagenetic trends within Tertiary Gulf Coast sediments (Milliken et al. 1994; Lynch 1996; Land 1997).

1.2.3 Compaction in sandstones

Compaction in sandstones is the reduction in the bulk volume of a given mass of sediment or rock, increasing its density (Figure 1.2). It occurs in response to the following mechanisms: (1) grain rearrangement and grain bending, (2) plastic deformation, (3) brittle deformation, and (4) pressure solution (Wilson and Stanton 1994).

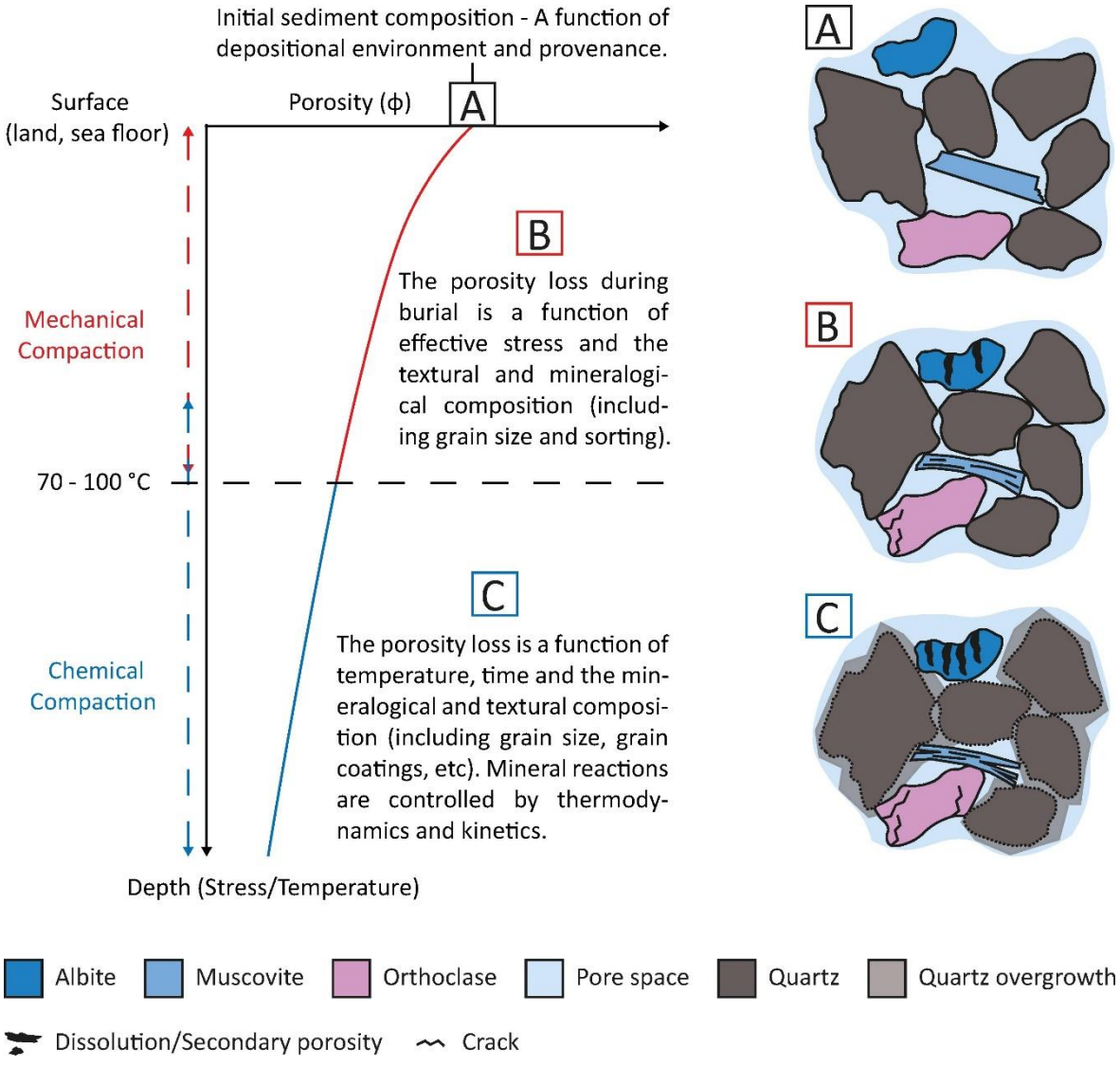

Figure 1.2: Schematic illustration of the principal aspects of siliceous sediment compaction during burial in sedimentary basins (Modified after Bjorlykke, 2014). A) Sediment at time of deposition. B) Mechanical compaction due to overburden. C) Chemical compaction with quartz cement development.

Upon burial, a process that includes the first three of the aforementioned compactive mechanisms, referred to as mechanical compaction, is the major factor reducing sand porosity from surface

depositional values of 40–50% to typical values of 25–32% before lithification (Paxton et al. 2002). Mechanical compaction is responsive to effective stress and increases with ongoing burial to a physical lower limit of compaction at around 2 to 3 km burial depth and temperature between 70 and 100 °C (Bjørlykke 2014). Sandstone composition and texture govern the rate of mechanical compaction. Namely, rocks containing labile grains (e.g., clay clasts, altered rock fragments, or delicate fossils) are more prone to undergo significant porosity loss through mechanical compaction than rocks made of rigid grains, such as quartz. Poorly sorted sands compact more rapidly than sands with high grain angularity (Fawad et al. 2011). Uniaxial compression tests on loose sands up to effective stress of 50 MPa showed that the degree of grain crushing and porosity loss is greater in coarse-grained sands than fine-grained sands (Chuhan et al. 2002).

Mechanical compaction determines the intergranular volume (IGV), i.e., sum of porosity, cement and matrix, before chemical compaction and quartz cementation. In clean sandstones, porosity and IGV typically coincide, whereas, in argillaceous sandstones, porosity will be lower than IGV due to matrix content. North Sea sandstones have IGV values varying from about 38 to 28% (Walderhaug 1996).

At burial depths greater than 2 km, quartz precipitation, marking the transition from the mechanical compaction to the chemical compaction regime, will gradually produce a rigid framework of quartz overgrowths, adequate to prevent further mechanical compaction, and infill the primary pore space (Paxton et al. 2002; Bjørlykke 2014). The precipitation of as little as 2-3% quartz cement is probably sufficient to stabilize the grain framework and cause no further depletion of the IGV (Bjørlykke et al. 2015). The chemical compaction process also referred to as pressure solution, is the enhanced dissolution of minerals or amorphous material and subsequent precipitation of mineral cement. Chemical compaction is mainly driven by temperature, vertical effective stress and the pore fluid and mineral composition (Sheldon et al. 2003).

The concentration of effective stress at points of grain-to-grain contact, either at a level of individual grains termed suturing or along a continuous surface termed stylolite, leads to an increase of the solubility of the material along that surface. Subsequently, the dissolved silica precipitates on adjacent grain surfaces, which experience a lower degree of stress (Wilson and Stanton 1994). Effective stress provides the driving force for diffusion from grain boundaries to the unconstrained grain surfaces adjacent to pores (Sheldon et al. 2003). Recent studies have suggested that the supply of silica controls the rate and extent of quartz cementation due to intergranular pressure solution and, therefore, the history of vertical effective stress rather than the history of temperature (Oye et al. 2018; Oye et al. 2020). In contrast, there have been claims that chemical

compaction in sandstones is nearly independent of effective stress and primarily influenced by elevated solubility due to increased temperature or specific mineral-chemical conditions (Walderhaug 1994; Oelkers et al. 1996; Bjørkum and Nadeau 1998; Kristiansen et al. 2011).

The occurrence of clay minerals at grain contacts is ambiguous as dissolution may be enhanced or reduced based on their morphology. For example, early precipitation of chlorite grain coats can preserve porosity by inhibiting extensive quartz cementation (Worden and Morad 2000; Bloch et al. 2002; Ajdukiewicz and Lander 2010). Additionally, small amounts of mineral cements can also preserve porosity by strengthening the grain framework and hence, inhibit late-stage compaction. In contrast, extensive pore filling authigenic mineral cements, controlled by fluid flow, pore fluid chemistry and temperature, usually diminish reservoir quality destabilising the grain framework (Bloch et al. 2002).

1.2.4 Quartz overgrowth cement

Quartz cement is responsible for most of the porosity and permeability reduction in well-sorted quartz-rich sandstones buried deeper than 3 km (Bjørlykke and Egeberg 1993). Quartz cement is favoured in basins with a slow subsidence rate and high geothermal gradients (Bjørlykke and Jahren 2010). The precipitation of as little as 2-3% quartz cement is adequate to stabilize the grain framework and cease further depletion of the IGV. Porosity continues to decline proportionally to the amount of quartz cement precipitated.

The most common form of quartz cement, an overgrowth, is a syntaxial rim with the same crystallographic orientation and optical continuity as that of the detrital host grain (McBride 1989). Overgrowths start as numerous tiny crystals merging into a single large crystal with well-formed crystal faces. Subsequently, overgrowths develop either by overlapping and merging similarly oriented subunits or by the envelopment of smaller subunits by one overgrowth that becomes dominant (Pittman 1972). The neoformed large crystal faces may take the form of hexagonal dipyramids (Waugn 1970).

Quartz cement typically occurs during burial diagenesis at temperatures above 70 °C (i.e., more commonly between 80–90 °C), marking the transition from mechanical to chemical compaction. Two models have been proposed for the derivation of the silica precipitating as quartz cement. It can be derived either from local sources and transported by diffusion over short distances (e.g., centimetres up to meters) or from distant sources (>10-100 m from the site of precipitation) and transported by pore-water flow (Bjørlykke and Egeberg 1993). However, mass balance and fluid-flow calculations support the view that most quartz cement is derived from local sources (Bjørlykke

and Egeberg 1993; Giles et al. 2000). The flow flux of pore water is many orders of magnitude too low to be significant in terms of mass transport during burial (Bjørlykke 1994).

A variety of interpretations have been made concerning the origin and significance of quartz cement. McBride (1989) provided an extensive list of sources proposed for silica in quartz cement in sandstones. Those favoured by most workers are pressure solution, illitization of smectite, dissolution of siliceous microfossils and spicules, and dissolution of volcanic glass (Wilson and Stanton 1994). According to Bjorlykke and Egeberg (1993), amorphous silica (biogenic and volcanic) and opal CT may be important sources of quartz cement at depths of 2.5-3 km. Important sources of silica that precipitates below several thousand meters causing porosity reduction in sandstones are combinations of the following: (1) dissolution, due to pressure solution, of quartz grains at contact points, (2) silica dissolved in circulating pore fluids by flow over quartz grains in sandstones, (3) silica (including amorphous phases) from shales, and (4) liberation of silica during mineral reactions (Leder and Park 1986).

As discussed previously, pressure solution is considered by many workers as one of the major mechanisms of porosity loss in many sandstones, particularly those having a high content of quartzose components. However, large amounts of data indicate that silica is sourced by quartz grains that are preferentially dissolved along stylolites and clay laminae due to increased quartz solubility at these interfaces and not by grain-to-grain dissolution. This mechanism is referred to as Clay-Induced Dissolution (CID) (Oelkers et al. 1996; Bjørkum et al. 1998; Oelkers et al. 2000). Cementation sourced by dissolution along stylolites results in passive infilling of the pore space preserving IGV. If silica were sourced from grain-to-grain dissolution, the continuous compaction of the grain framework would cause the IGV to decrease further. According to Paxton et al. (2002) even deeply buried sandstones rarely have IGV values below 26%, suggesting that grain to grain pressure solution is not significant in most sandstones.

Some authors suggest that the rate of quartz cementation in most sandstones is controlled by the rate of crystal growth and not by the rate of production or transport of dissolved silica. This assumption requires that dissolved silica is supplied at a rate that equals or exceeds the rate of crystal precipitation, without taking into account whether the silica is derived from local diffusion or larger scale fluid advection (Walderhaug 1994; Walderhaug 1996; Walderhaug et al. 2000). Walderhaug (1996) has modelled the quartz cementation process as a precipitation rate-controlled reaction where quartz precipitation rate per unit time and surface area can be expressed as a function of temperature. He estimated that the rate of quartz cementation may increase by a factor of 1.7 for every 10 °C temperature increase. Other parameters such as grain size, detrital quartz

content, mineralogy, and grain coats are also included in this model. However, other authors dispute this interpretation, claiming that quartz precipitation is flux- and not rate-controlled. This is based on cathodoluminescence studies of zoned quartz overgrowths in North Sea Jurassic sandstones, indicating that cementation occurred in pulses interrupted by periods of non-deposition, therefore generating heterogeneous zoning and dissolution boundary development which promotes the idea of flux-controlled precipitation (Hogg et al. 1992).

Numerous studies have proposed that grain size is a significant control on quartz growth kinetics (Heald and Renton 1966; Walderhaug 2000; Makowitz and Sibley 2001). Makowitz and Sibley (2001) showed that the thicknesses of quartz overgrowths increase systematically with grain size in the Cambrian Galesville Sandstone (Wisconsin, U.S.A). Similarly, quartz cementation is more extensive in the finer-grained quartz-rich Triassic sandstones of the Ivishak Formation (Prudhoe Bay Field, Alaska) than in the coarser, chert-rich lithofacies (Melvin and Knight 1984). Laboratory studies by Heald and Renton (1966) showed that in medium- to coarse-grained sand, cementation is ~ 67% faster than in very coarse sands and 16 times faster in fine sands. As the rate of quartz cementation is proportional to the surface area available for quartz overgrowth, well-sorted, fine-grained sand is less prone to mechanical compaction than coarser sand. Therefore, its greater surface will host larger amounts of quartz cement compared to coarse-grained sands (Bjørlykke 2014).

Finally, the internal structure of detrital quartz grains (e.g., undulosity, polycrystallinity) influences the volume of cement sequestered by individual grains. Finer-grained beds, which have fewer polycrystalline and undulose grains than coarser-grained beds, possess larger amounts of quartz overgrowths (McBride 1989). Studies on the Nugget Sandstone of the Washakie Basin-Rock Springs Uplift area (Wyoming, USA) have shown that overgrowths are three times more likely to form on monocrystalline than polycrystalline quartz and more likely to form on nonundulose compared to undulose grains (James et al. 1986).

1.2.5 Grain coats as a control on reservoir quality of sandstones

1.2.5.1 Clay mineral grain coats

Clay minerals are hydrous aluminosilicates that belong to the phyllosilicate group of minerals and are characterized by crystal sizes less than 2 μm in diameter (Deer et al. 2013). The phyllosilicate structure is based upon SiO_4 tetrahedral and AlO_4 octahedral sheets. In the tetrahedral sheet, each tetrahedron comprises a cation coordinated with four oxygen atoms and linked to adjacent tetrahedra by sharing three corners. Common tetrahedral cations are Si^{4+}, Al^{3+} and Fe^{3+}. In the octahedral sheet, connections between each octahedron to neighbouring octahedral is made by sharing edges. Common octahedral cations are Al^{3+}, Fe^{3+}, Mg^{2+} and Fe^{2+}. The tetrahedral and

octahedral sheets have a two-dimensional hexagonal mesh pattern and a hexagonal or pseudo-hexagonal symmetry, respectively (Brigatti et al. 2006). A clay with 1:1 structure consists of one tetrahedral and one octahedral sheet, and examples are kaolinite and serpentine. A 2:1 clay consists of an octahedral sheet sandwiched between two tetrahedral sheets, and examples are illite and chlorite.

There are five dominant groups of clay minerals in sandstones: kaolin, illite, chlorite, smectite and mixed-layer varieties. Clay minerals can be of detrital/allogenic or diagenetic/authigenic origin. Allogenic clays are originated before deposition and are mixed with the sand fraction during or immediately following deposition. Authigenic clays develop subsequent to burial either as a direct precipitate from formation waters (neoformation) or through reactions between precursor materials and the contained waters (regeneration) (Wilson and Pittman 1977). All the major varieties of clay minerals in sandstones are known to form authigenically.

The term clay coat encompasses both detrital and diagenetic origins (Ajdukiewicz and Larese 2012). Detrital clay coats occur most commonly within embayed surfaces of sand particles and consist of clay particles oriented tangentially to grain surfaces. They are typically originated on sand grains as precursor phases, which, with increasing burial, can be recrystallized to authigenic clay coats (Matlack et al. 1989; Pittman et al. 1992; Bloch et al. 2002; Worden and Morad 2003). Furthermore, authigenic clay coats grow in situ due to the alteration of detrital or early diagenetic minerals interacting with the pore fluids during burial (Worden and Morad 2003; Ajdukiewicz and Larese 2012; Dowey et al. 2012; Dowey et al. 2017). The clay particles of authigenic coats commonly exhibit a preferred orientation normal to or parallel to the sand grain surfaces (Pittman et al. 1992).

The importance of clay mineral coats in sandstones is widely known and accepted. The amount, distribution pattern and morphology of clay mineral coats have significant effects on the reservoir quality of sandstones. Clay mineral coats are known for their beneficial effect in preserving reservoir quality to greater burial depths than is normally predicted, thus extending the potential of a sandstone body to serve as a hydrocarbon reservoir (Heald and Larese 1974; Thomson 1979; Dewers and Ortoleva 1991; Pittman et al. 1992; Ehrenberg 1993; Bloch et al. 2002; Anjos et al. 2003; Billault et al. 2003; Taylor et al. 2004; Berger et al. 2009; Taylor et al. 2010; Ajdukiewicz and Larese 2012; Bahlis and De Ros 2013; Nguyen et al. 2013; Haile et al. 2015; Taylor et al. 2015). The most reported types of clay mineral coats associated with deeply buried sandstones are diagenetic chlorite, diagenetic illite and diagenetic mixed-layer smectite-illite, smectite-chlorite and or illite-chlorite coats (Ajdukiewicz and Larese 2012).

The completeness and thickness of clay coats are key for porosity maintenance in deeply buried sandstones, as higher coat coverage leads to less quartz cementation (Figure 1.3) (Pittman et al. 1992; Bloch et al. 2002; Ajdukiewicz and Lander 2010; Ajdukiewicz and Larese 2012). When coats on quartz grains are incomplete, quartz overgrowths developing on uncoated surfaces may extend out and onlap the edges of the coats (Wilson and Stanton 1994; Oye et al. 2018). Reservoir-quality predictive models assume that all grain coats decrease net cement growth rate in proportion to the fraction of grain surface covered, with no differences in inhibitory mechanisms among coats of equal coverage but different composition. However, other authors argue that inhibitory effectiveness varies with coat composition (Heald and Larese 1974).

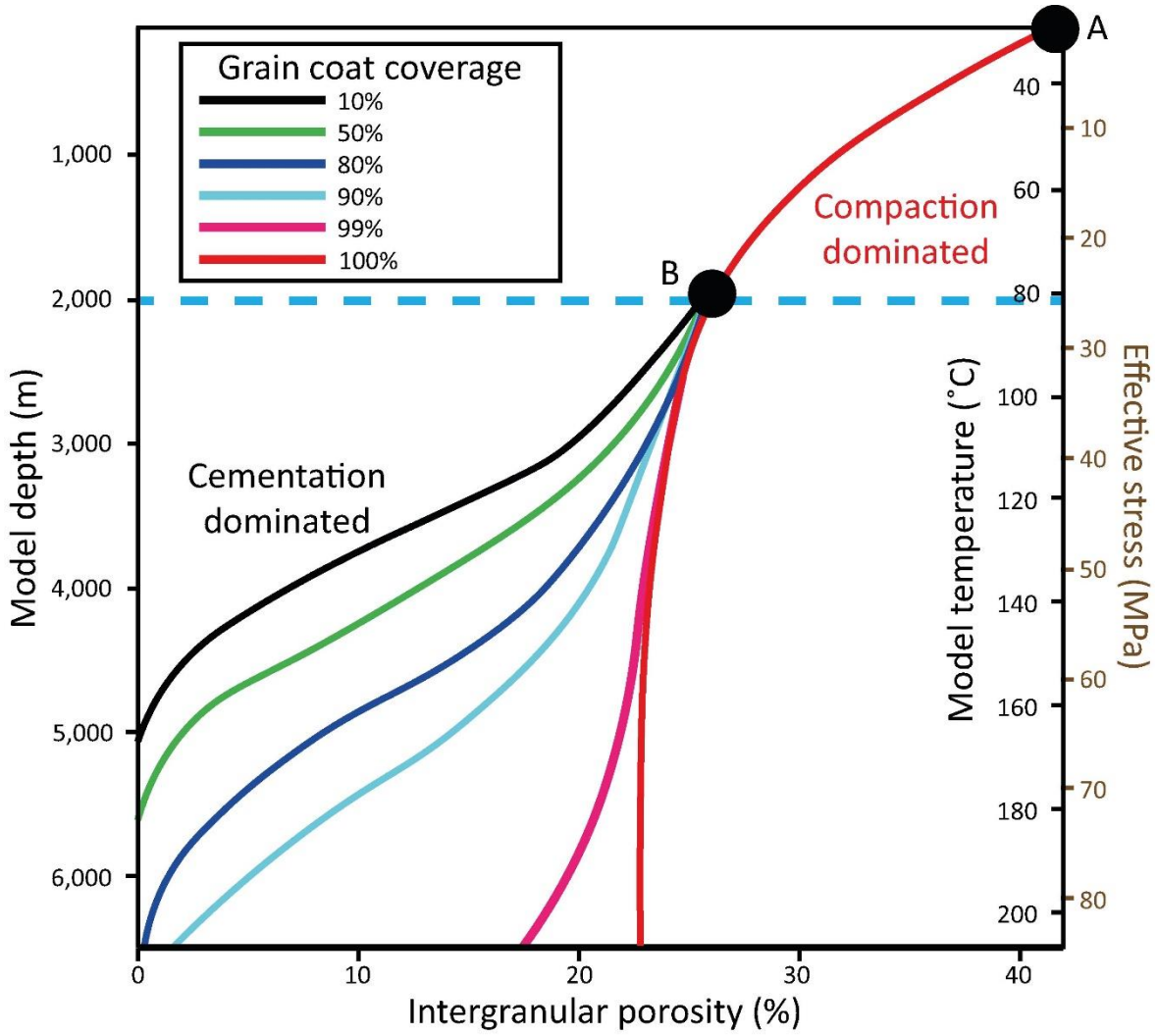

Figure 1.3: Modelled porosity evolution with burial for a well-sorted, fine-grained, quartzo-feldspathic aeolian sandstone with variable clay coats near the surface. The higher the coat coverage, the less the cement formation. A: Recently deposited sand, B: Initiation point of cement precipitation (80°C and 2 km depth). In this hypothetical example, the highest porosities are preserved at depth where compaction and cement are minimised, in this case, by rigid grains and well-developed grain coats (Modified after Ajdukiewicz and Lander, 2010).

The absence of quartz cement is not exclusively related to clay mineral coats. Other factors such as limited availability of silica due to early hydrocarbon saturation and abnormally high pore fluid

pressures and temperature may have been more important (Heald and Larese 1974; Bahlis and De Ros 2013). Contrarily, their presence within a reservoir may also have a negative effect on reservoir quality. Porosity can be reduced, and fluid flow restricted due to the tendency of the clay mineral coats to encroach into pore space and the fact that water can become trapped within the clay structure creating high irreducible water saturations within the rock (Dewers and Ortoleva 1991; Worden and Morad 2003; Morad et al. 2010; Taylor et al. 2010; Sun et al. 2014; Wilson et al. 2014; Dowey et al. 2017).

1.2.5.2 Non-clay grain coats

Except for clay mineral coats, microquartz and siderite coats on detrital grains are documented as an effective mechanism for inhibiting the formation of pore-filling quartz overgrowths (McBride 1989; Aase et al. 1996; Dutton et al. 1996; Jahren and Ramm 2000; Karim et al. 2010; Weibel et al. 2010; French et al. 2012; French and Worden 2013).

Microquartz in sandstones is typically derived from biologically derived silica through the in-situ dissolution of sponge spicules or volcanic rock fragments or by the passage of groundwater with elevated silica concentrations due, for example, to organic complexing (Vagle et al. 1994; Hendry and Trewin 1995; Lima and De Ros 2002; French and Worden 2013).

Siderite is a common cement in sandstones. It grows at all the diagenetic stages of siliciclastic sedimentary units showing variable chemical compositions and crystal habits. This variability is related to lithofacies (Gould et al. 2012), microbial activity occurring within shallow buried sediments (Dutton et al. 1996), initial fluid composition and evolution of basinal fluids and, the paragenetic sequence of diagenesis (Pe-Piper and Piper 2020).

1.2.6 Chlorite

1.2.6.1 Chlorite chemistry and structure

Chlorite is a layered hydrous aluminosilicate comprised of a negatively charged 2:1 (tetrahedral–octahedral–tetrahedral) layered structure (i.e., talc-like layers) interlayered with an additional octahedral layer composed of cations and hydroxyls (e.g., brucite-like sheets with composition $M_6(OH)_{12}$) that is positively charged (Worden and Morad 2003). The 2:1 type structure of chlorite mineral is made up of a 14Å basic structural unit that is stable at high temperatures due to the interlayer filling of the positively charged octahedral sheet (Figure 1.4).

Chlorite is chemically complex due to isomorphous substitution of the octahedral and tetrahedral cations (Peng et al. 2009) and can be represented by the following generalised chemical formula:

$(R^{+2}, R^{+3})_{4\text{-}6}[(Si,Al)_4O_{10}](OH,O)_8$

R^{+2} = Mg, Fe, Mn, Ni, Zn

R^{+3} = Al, Fe, Cr

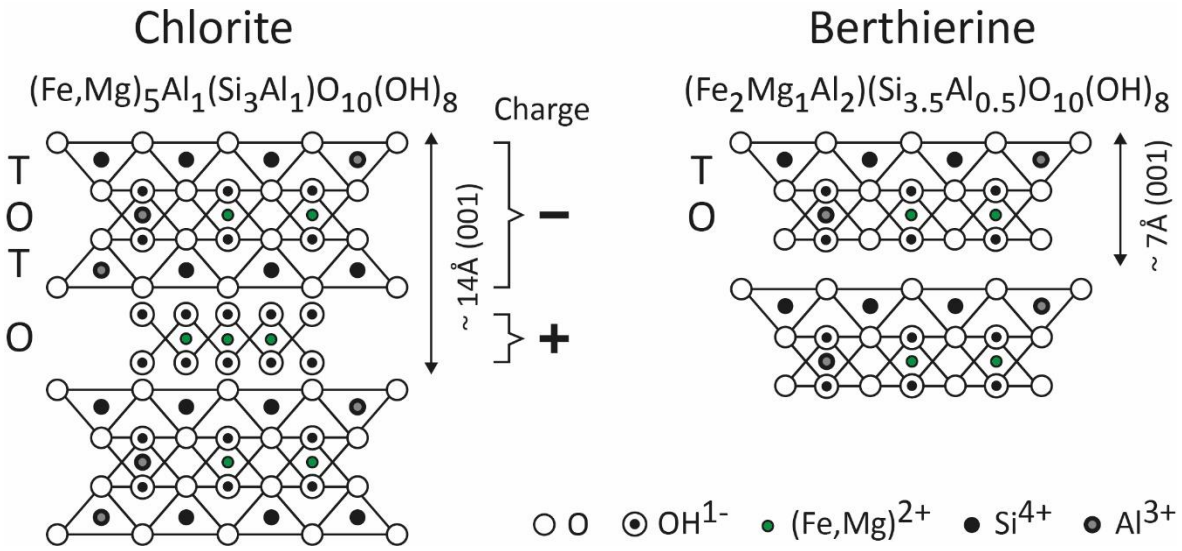

Figure 1.4: Crystal structure of chlorite and berthierine. Berthierine is considered a precursor for authigenic chlorite. Berthierine and chamositic chlorite have similar chemical structures and stoichiometry. Berthierine has a smaller repeating unit cell in the c axis (its d(001) is about 7 Å) compared to chamosite (its d(001) is about 14 Å) (Modified from Worden et al. 2020).

Chlorite can be subdivided into the following groups (Bayliss 1975; Hillier 1994; Deer et al. 2013):

1. Fe-rich, known as chamosite
2. Mg-rich, known as clinochlore
3. Mn-rich, known as pennantite,
4. Ni-rich, known as nimite
5. Zn-rich, known as baileychlore

Based on the literature, Fe-rich and Mg-rich types appear to be the most common pore-lining chlorites in siliciclastic sandstones. Mn-rich, Ni-rich, and Zn-rich chlorites are less important in terms of porosity preservation due to grain coating and can be neglected. According to different superposition modes of octahedron and layered hydrous aluminosilicate, chlorite is divided into four polytypes Ia, Ib, IIa and IIb. Each polytype gives information regarding the diagenetic stage and crystalline maturity of chlorites (Spotl et al. 1994). Chemical analysis performed by Hillier (1994) suggests that Fe-rich types occur as individual euhedral crystals, are invariably interstratified with 7 Å layers (probably berthierine or odinite), and form as the Ib (β=90°) polytype due to diagenetic crystallisation at low temperatures. The Ib type is mainly formed in diagenetic environments. Berger et al. (2009) observed that chlorites that have an Ib structure polytype are morphologically characterised by thin pseudohexagonal plates. With increasing temperature and pressure, chemistry changes, 7 Å layers are lost, crystal size increases, and eventually, the Ib chlorites

transform to the high-temperature IIb (β=97°) polytype. The IIb polytype, formed near the metamorphic zone (150 °C–200 °C), is more stable at higher temperatures than the Ib polytype (Hillier 1994; Peng et al. 2009). The Ib to IIb transformation is reported to occur via recrystallization and replacement through polytype-mixtures. Contrarily, the Mg-rich types occur without interstratification with 7 Å layers and belong to the IIb polytype (Hillier 1994). The main differences between Fe-rich and Mg-rich pore-lining chlorites in siliciclastic sandstones are summarized in Table 1.2 (Hillier 1994).

	Fe-rich	**Mg-rich**
Morphology	Pseudo-hexagonal	Cornflake-like
Arrangement	Individual plates and rosettes, edge to face contacts	Boxwork, face to face contacts
XRD	Interstratified with 7 Å layers at <200 °C	Often associated and/or interstratified with corrensite
Polytype	Ib (β = 90°) transforming to IIb (β = 97°) above 200 °C	Exclusively IIb (β=97°)
Occurrence	Near-shore marine sandstones in tropical climates, frequently deltaic	Coastal aeolian dunes and sandy sabkhas plus any facies in close contact with evaporite brines
Facies associations	Oolitic ironstones	Evaporites
Common diagenetic minerals/events	Siderite, quartz, calcite, kaolinite, feldspar dissolution	FeO rims, anhydrite, K-feldspar, calcite, quartz, dolomite, fibrous illite
Origin	From 7 Å mineral probably berthierine possibly odinite	From Mg-smectite to corrensite sequence

Table 1.2: Differences between Fe-rich and Mg-rich pore-lining chlorites (After Hillier, 1994).

1.2.6.2 Chlorite origin and formation

Chlorite is the most common authigenic clay mineral in sediments. It is present in deltaic, fluvial and shallow marine reservoir sandstones. Fe-rich chlorite implies a coastal environment, whereas mixed Mg- and Fe-rich chlorite are found in marine and terrestrial environments (Dowey et al. 2012). Fe-chlorite can develop where there was insufficient supply of dissolved sulphate and, typically biogenic, carbonate during eodiagenesis that would otherwise lock the iron up by creating pyrite and siderite, respectively (Worden et al. 2018a; Worden et al. 2020). The source of iron required for chlorite precipitation can be derived from a fluvio-deltaic setting. As the river water is discharged into the sea, increased salinity causes Fe to flocculate and become highly reactive. Ehrenberg (1993) proposed that grain-coating chlorite is a consequence of syn-sedimentary concentration of precursor Fe-rich detrital clay rims in shallow marine settings influenced by fresh water discharge. The presence of chlorite ooids in Lower to Middle Jurassic sandstone reservoirs from the Norwegian Continental Shelf implies that chlorite coats are, in fact, a primary depositional feature. These concentrically layered structures were interpreted to be formed by mechanical

accretion as the grains were rolled by water currents suggesting concentration of a Fe-rich precursor clay at the time of deposition. The geometry of chlorite distribution is determined by the sedimentary facies architecture and the paleo-river discharge pattern in the architecture (Ehrenberg 1993).

The origin of authigenic chlorite in siliciclastic reservoirs is predominantly diagenetic and controlled by the clay mineral precursors, mineralogical composition of the reservoir, pore fluid chemistry and temperature (Chen et al., 2011). The diagenetic stage of chlorite differs in response to different diagenetic conditions. Authigenic chlorite continuously reequilibrates with its diagenetic environment throughout burial history (Grigsby 2001). Chlorite growth is a gradual and continuous process led by the instability of low-temperature compositions with increasing burial depth. During diagenesis, chlorite forms preferentially in fluids with high pH values and high Fe and Mg ion contents (Berger et al. 2009).

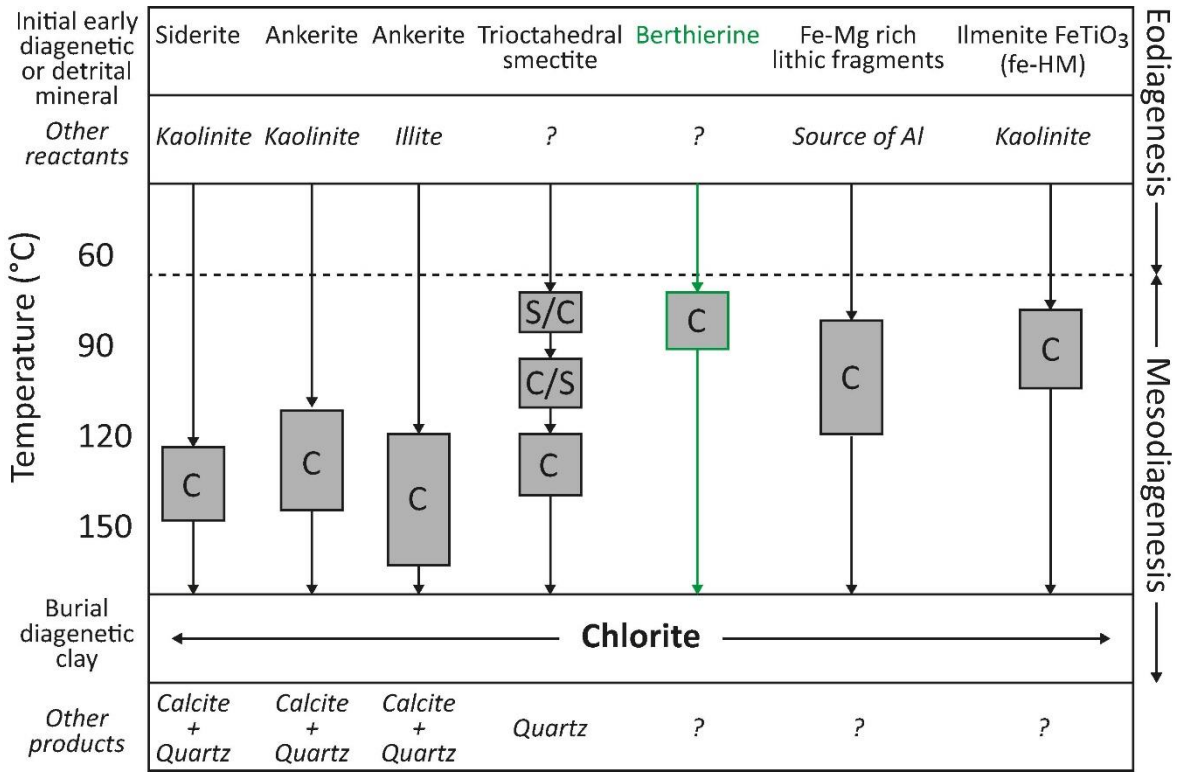

Figure 1.5: Schematic illustration of the common mesodiagenetic pathways for minerals related to chlorite formation in sandstones, where S is smectite, and C is chlorite. Highlighted in green is the pathway investigated in this study (After Worden et al., 2020).

The process of chlorite formation in reservoir sandstones has previously been reviewed (Pittman et al. 1992; Ehrenberg 1993; Hillier 1994; Bloch et al. 2002; Anjos et al. 2003; Worden and Burley 2003; Peng et al. 2009; Dowey et al. 2012; Bahlis and De Ros 2013). Chlorite authigenesis can be achieved by: (1) Replacement of non-clay material, (2) Precursor clay minerals and, (3) Neoformation (e.g.,

direct precipitation from pore fluids). Common pathways for chlorite precipitation during mesodiagenesis are presented in Figure 1.5.

1.2.6.2.1 Replacement of non-clay material

Authigenic chlorite may develop during diagenesis as a result of:

1. The dissolution and replacement of basic volcanic rock fragments and glasses, and Fe- and Mg-rich lithic fragments, such as garnet, biotite or amphibole (Galloway 1979; Surdam and Boles 1979; Thomson 1979; De Ros et al. 1994; Remy 1994; Worden and Morad 2003; Taylor et al. 2010).
2. The alteration of feldspars, such as microcline and albite (Morad and Aldahan 1987).
3. The replacement of mud intraclasts by microcrystalline chlorite aggregates (Worden and Morad 2003; Bahlis and De Ros 2013).
4. The alteration of glauconite (Drits et al. 2001; Boyd et al. 2004).

1.2.6.2.2 Diagenetic chlorite from precursor minerals

The early chlorite coats described in the literature are the product of chloritisation processes of chlorite precursor materials. Several potential precursors that can be transformed to chlorite have been proposed. The processes involving these precursors are:

1. The replacement of Fe-rich, green 7 Å clays, such as berthierine, or clays belonging to the Verdine group, such as odinite, by 14Å ferroan chlorite (e.g., chamosite) upon deep burial, (Ehrenberg 1993; Hillier 1994; Aagaard et al. 2000; Morad et al. 2010; Beaufort et al. 2015). The only requirements for the development of the Verdine facies are a source of Fe, compositionally susceptible grains, shallow water depths between 5m and 60 m, and warm water (> 20 °C) temperatures (Grigsby 2001). Both berthierine and odinite form in similar settings and are chemically similar to Fe-rich chlorite (Ryan and Reynolds 1996).
2. The chloritisation of kaolinite (Bjørlykke and Aagaard 1992; Moraes and De Ros 1992; Worden and Morad 2003) favoured by the simultaneous destabilisation of eodiagenetic ferroan carbonates, such as siderite and Fe-dolomite, or of organometallic iron compounds (Surdam et al. 1989).
3. The chloritisation of detrital or eogenetic trioctahedral smectites, such as saponite (Hillier 1994; Humphreys et al. 1994; McKinley et al. 2003; Deer et al. 2013).
4. The transformation of a swelling chlorite (e.g., irregularly interstratified chlorite/smectite or well-ordered corrensite) (Curtis et al. 1985; Humphreys et al. 1989).

1.2.6.2.3 Neoformation

During mesodiagenesis, direct precipitation of chlorite cements from Fe- and Mg-rich pore waters in siliciclastic sediments occur alongside chloritisation of different mineral substrates (Anjos et al. 2003). The source of Mg and Fe ions for chlorite authigenesis can be supplied from eodiagenetic hematite in red beds (Dixon et al. 1989), from the destruction of organometallic complexes (Surdam et al. 1989), or from clay transformation reactions occurring in associated mudrocks (Moncure et al. 1984). Remy (1994) showed a two-stage growth of clay cementation in volcaniclastic sandstones. The Middle Park Formation illustrates a first generation of clay coats covered by a later stage generation of rims formed by precipitation from pore waters.

1.2.6.3 Berthierine

The most important chlorite precursor clay mineral associated with the present research is berthierine. It is a common clay mineral that is present in modern sediments and Fe-rich sedimentary rocks (Rohrlich et al. 1969; Bhattacharyya 1983; Van Houten and Purucker 1984; Hornibrook and Longstaffe 1996). Some sandstone examples containing berthierine-coated quartz grains include the Norwegian Continental Shelf (Ehrenberg 1993), the Clearwater Formation, Alberta, Canada (Hornibrook and Longstaffe 1996), the Logan Canyon Formation, Scotian Basin, Canada (Pe-Piper and Weir-Murphy 2008) and, the Siri Field in the Danish North Sea (Stokkendal et al. 2009).

Berthierine is an aluminous Fe^{2+}-rich 1:1 clay belonging to the kaolinite–serpentine series of minerals. The average composition of berthierine is $Fe^{2+}_{1.5}\ Al\ Fe^{3+}_{0.2}\ Mg_{0.2}\ Si_{1.1}\ Al_{0.9}\ 0_5\ (OH)_2$. The predominance of ferrous iron in berthierine suggests that it is formed under strongly reducing conditions (e.g., pore waters relatively depleted in dissolved oxygen). Berthierine forms primarily in transgressive systems tract and early highstand systems tract deltaic and estuarine deposits (Morad et al., 2010). Authigenesis of berthierine is favoured in volcanogenic sediments deposited in estuarine-coastal-plain environments (Jeans et al. 2000). Huggett et al. (2018) have shown that berthierine crystallization is due to the replacement of fecal pellets or resulting from oxy-hydroxide ooids and kaolinite. Recent studies on shallowly buried (400–1000 m) coastal sandstones from within the Wealden Group of the Paris Basin have shown that berthierine formed from a source material consisting of aluminous and ferric detrital clays (mainly kaolinite, hydroxy-interlayered clay minerals) and ferruginous-aluminous ooids. With progressive burial the crystallization of authigenic berthierine proceeded as authigenic clay coats around detrital grains and early eodiagenetic minerals and by replacement of ooid grains (Virolle et al. 2021).

It generally occurs as small (< 5 μm), lath-shaped grain coats and crystals, as coats (fringes or tangentially arranged), pellets, ooids and void-fillings, or form by the replacement of silicate and carbonate bioclasts (Worden and Morad 2003). Eodiagenesis promotes the accumulation of Fe-rich clay coats, such as berthierine, on detrital grain surfaces. Abundant supply of iron is a prerequisite for the precipitation of these early phases. Microbial activities at intermediate depths and low temperatures can lead to large quantities of chemically reduced species of iron (McMahon et al. 1992) which then contribute to the growth of the eodiagenetic Fe-rich clay coats.

Berthierine and chlorite have similar chemical structures and stoichiometry. Specifically, berthierine's chemical composition overlaps with that of the ferrous chlorite endmember chamosite (Xu and Veblen 1996), with which also shares a significant number of X-ray powder diffraction (XRD) lines. The main difference between berthierine and chamosite is the arrangement of their tetrahedral and octahedral sheets resulting in periodicities along the c axis of ~ 7 Å and ~ 14 Å, respectively. Berthierine is also chemically and structurally similar to odinite, a poorly crystallized di-trioctahedral Fe^{3+} rich phyllosilicate with a serpentine-like structure (Bailey 1988; Odin 1990), but exhibits several key differences, including the valence state of iron (Hornibrook and Longstaffe 1996). The conversion of berthierine to chamosite may occur through a polymorphic mineral reaction. In shallow-marine environments in tropical regions at temperatures as low as 25 °C, odinite is transformed into berthierine (Porrenga 1967), which is altered to chamosite at temperatures above 90 °C (Ryan and Hillier 2002). The transformation is reported to be complete above 160 °C (Iijima and Matsumoto 1982). Temperatures lower than 70 °C and, early in the diagenetic history, hydrocarbon emplacement have the ability to preserve berthierine and attenuate chloritization processes, respectively (Hornibrook and Longstaffe 1996).

1.2.6.4 Reaction mechanisms of chloritisation

The reaction mechanisms for the conversion of potential clay precursors to chlorite can be classified into two broad categories: 1) Solid-State Transformation (SST) and 2) Dissolution-Crystallisation (DC).

SST mechanisms involve the gradual replacement of the parent mineral (e.g., precursor clay mineral) with a daughter mineral (e.g., Mg, Fe-chlorite) in close topotactic contact. During SST the crystal habit of the parent mineral is conserved. Moreover, the polytype, chemistry and defects of the parental mineral are inherited by the daughter mineral. SST mechanisms proceed in the presence of fluids that can act as catalysts and transport media (Veblen 1992) and influence the structure and composition of the daughter minerals (Baronnet 1992).

During DC the precursor mineral is completely dissolved. The neoformed daughter mineral nucleates and grows as a separate or epitaxial grain. In such a chloritization mechanism, the reaction is marked by major changes in the parental mineral's chemical and structural properties and textural properties. A particular type of DC mechanism, driven by a decrease in surface energy and proposed for chloritisation processes, is Ostwald Ripening (OR) (Jahren 1991; Grigsby 2001). OR is a recrystallization process that occurs after the initial nucleation of different-size crystals and is common in chemically closed systems. The dissolution of smaller crystals release elements that contribute to the growth of larger pre-existing crystals. At the end of the process, large crystals are found in the authigenic core of a grain surrounded by progressively younger epitaxial overgrowths (Baronnet 1982).

1.2.6.4.1 Mechanism of the conversion of berthierine to chlorite

The determination of the transformation mechanism of clay minerals is typically complex, but the issue is important for understanding the evolution of diagenetic systems. The main mechanisms proposed for phyllosilicate reactions, whether they take place via mixed-layer phases or not, are dissolution-precipitation and solid-state transformation (Cuadros 2012).

Solid-state transformation has been proposed as a mechanism regarding the mineral reactions taking place during the progressive replacement of berthierine by chlorite (Banfield and Bailey 1996; Ryan and Reynolds 1996; Xu and Veblen 1996). HRTEM analysis by Xu and Veblen (1996) indicates a cell preserved phase transition operating simultaneously in different domains of berthierine. Since the primary difference between berthierine and chlorite structures lies on the arrangement of their tetrahedral and octahedral sheets, chlorite structure can be generated by inverting the orientation of half of the tetrahedral sheets in the berthierine structure (Beaufort et al. 2015). The reversing of a tetrahedral sheet can be obtained by cross shifting the Si and O atoms between two adjacent berthierine layers. With increasing temperature, all the original 7 Å layers are progressively transformed to chlorite layers. The 7 Å layers disappear completely at temperatures between 150 and 220 °C (Hillier 1994). The resulting low-temperature Fe-chlorites inherit berthierine's Ib (β=90°) polytype (Brindley 1951) and structural defects and preserve its chemistry and crystal texture.

An increase in temperature is one of the factors that has been considered to raise the possibility of DC (Altaner and Ylagan 1997). DC requires large morphological changes between the initial and final clay mineral (Cuadros 2012). In natural systems, the recrystallization of low-temperature, berthierine-derived chlorites to the higher-temperature chlorites is efficient at temperatures near 200°C (Walker 1993). However, because this temperature usually represents the beginning of

metamorphism, more comparative data regarding the microstructure of Fe-rich chlorites from diagenetic environments are required to test the aforementioned findings in lower-temperature geological systems.

1.2.6.5 Authigenic chlorite

Authigenic chlorite displays a variety of morphologies such as cardhouse, honeycomb, rosette or fan, and cabbagehead (Wilson and Stanton 1994). Authigenic chlorite can mainly be found in the following forms: (1) Grain coating, (2) Pore filling, (3) Grain replacive, (4) Isolated crystals.

1.2.6.5.1 Chlorite grain coats

Authigenic chlorite is one of the most important and effective grain coating minerals in terms of limiting extensive quartz cementation and maintaining reservoir quality in deeply buried sandstones (Humphreys et al. 1989; Ehrenberg 1993; Grigsby 2001; Anjos et al. 2003; Berger et al. 2009; Ajdukiewicz et al. 2010; Chen et al. 2011; Bahlis and De Ros 2013).

Chlorite coats are commonly 5-10 µm thick and partly or wholly cover detrital grains. Well-developed chlorite coats show a two-layered structure with an inner layer or root zone and an outer layer. The root zone is in direct contact with the detrital grain and consists of amorphous to poorly developed chlorite crystals. The outer layer usually consists of well-developed crystals covering the root zone (Pittman et al. 1992).

Recent studies on Middle to late Triassic sedimentary strata in Svalbard, Norway, have shown that the inner layer consists of chlorite precursor clay coats, while the outer layer comprises authigenic chlorite coats. Although both the precursor material and authigenic chlorite have similar bulk composition, SEM-EDS analysis indicates different textures and orientations. The precursor appears to be flaky with ragged outlines, oriented parallel to the grain surface with an anhedral texture. Conversely, authigenic chlorite is oriented perpendicular to the surface of the framework grains and has a pseudohexagonal plate texture (Haile et al. 2018). Berger et al. (2009) have also identified two rim types based on the time of the formation and the degree of crystallisation of each. The younger, better developed, coarse-crystalline rims comprise subhedral to euhedral, pseudohexagonal crystals. The underlying older, poorly developed, fine-crystalline chlorite rims are only observable in areas where the younger ones have broken away. In general, Fe-rich chlorite coats are euhedral, random to each other and oriented sub-perpendicular to perpendicular to the host grain surfaces. In contrast, Mg-rich coats are typically more anhedral and are characterized by organized crystals in the form of a honeycomb or boxwork (Hillier 1994).

SEM observations by Billault et al. (2003) suggest that both the arrangement and microtexture of chlorite coat particles change with respect to the site of chlorite precipitation (Figure 1.6D). Namely, chlorite coats formed at the contact between two adjacent detrital grains are arranged parallel to the surface of the host grains and appear as xenomorph flakes with an average diameter of <1μm. Contrarily, chlorite coats on the wall of pore spaces are oriented perpendicular to the framework grain surface showing a fibrous pattern. Moreover, regardless of the nucleation site, chlorite particles at contact with the clastic substratum are very fine-grained, composed of xenomorph flakes, while near the pore centre are coarse-grained and composed of euhedral subhexagonal plates with face-to-edge or face-to-face morphology.

Experimental chlorite synthesis by Cho and Fawcett (1986) can be used to interpret that grain coating chlorite growth can be divided into three phases; i) Initial 3D nucleation of 7Å chlorite on all detrital grain surfaces, irrespective of mineralogy or orientation (Figure 1.6A), ii) Subsequent 2D nucleation or layer growth during which the plates grow, perpendicularly to the grain surfaces, as very thin sheets to a maximum length and width of about 10 μm (Figure 1.6B), and iii) Appearance of 14Å chlorite with a plate thickening process occurring in accordance to Frank's spiral mechanism (Frank 1949) without any length or width alterations (Figure 1.6C).

The effectiveness of chlorite coats usually increases with increasing surface coverage and thickness (Ajdukiewicz and Lander 2010; Taylor et al. 2010). Some authors suggest that chlorite coats tend to isolate quartz surfaces, by lining the interface between detrital grains and the pore space, from interstitial pore water so that later crystallization of authigenic quartz is retarded or prevented (Pittman and Lumsden 1968; Hillier 1994; Aagaard et al. 2000). However, TEM observations by Billault et al. (2003) indicated that detrital quartz surfaces were not physically isolated from contact with pore fluids by chlorite crystals. The inhibition of quartz cementation was essentially due to the drastic limitation of the epitaxial growth of quartz into the interparticle space at the base of the chlorite coat and not to a lack of nucleation sites.

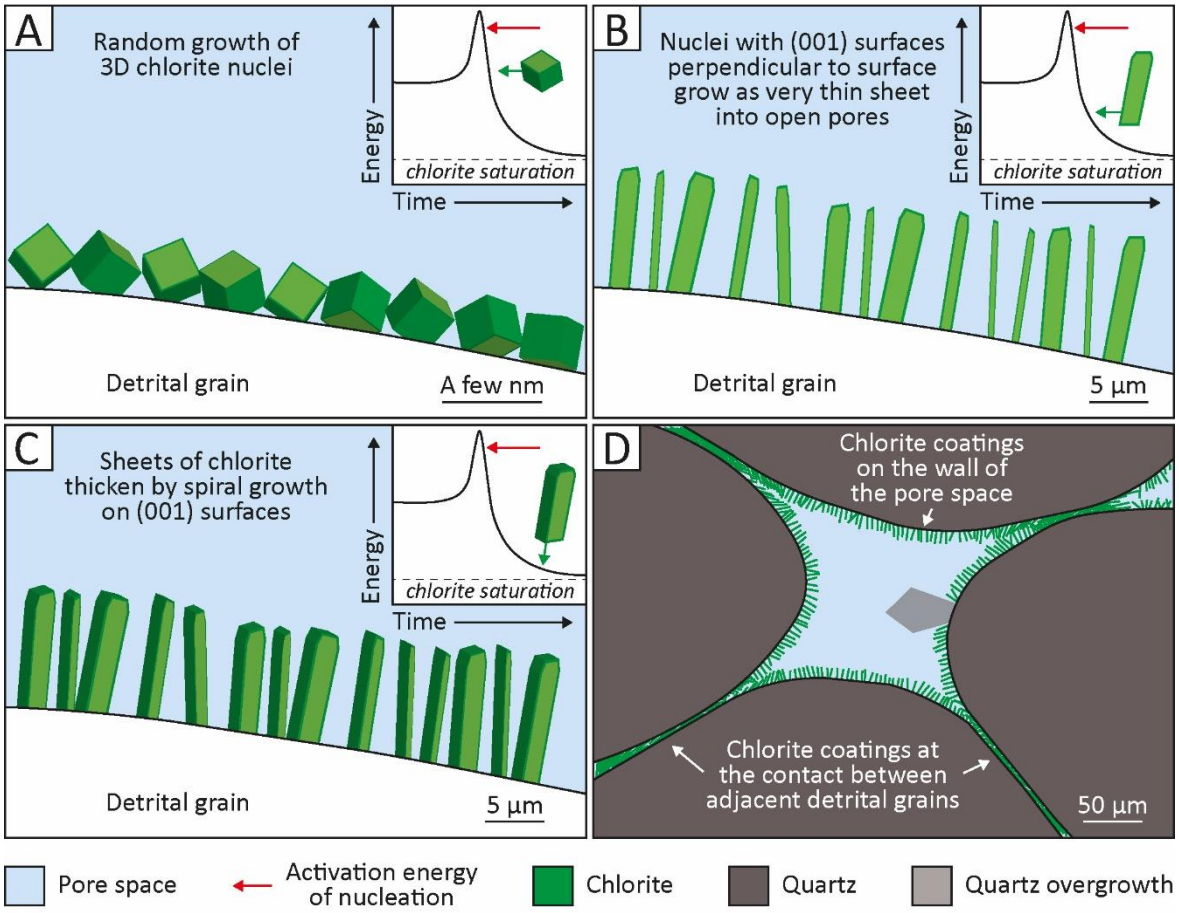

Figure 1.6: Illustration of authigenic grain-coating chlorite growth phases and the influence of the site of precipitation on arrangement and microtexture of the platelets (Modified after Worden et. al. 2020 and after Billault et al. 2003). A schematic diagram representing the energy of the system versus time involving nucleation and then growth is depicted at each phase. Before chlorite growth, the water-rock geochemical system must have been extremely supersaturated with respect to chlorite. A) Phase 1 includes the formation of randomly oriented 3D nuclei of chlorite indiscriminately on all available surfaces creating an extremely thin coat. B) In phase 2, as supersaturation decreases following the initial chlorite nucleation, very thin chlorite sheets extend into the intergranular pore space. C) In phase 3 the plates become thicker but maintain their length and width. D) Chlorite coat morphology at the contact between adjacent grains and on the wall of the pore space. Breaks on the coat coverage promote quartz overgrowth precipitation.

Studies by Bahlis and De Ros (2013) on the impact of authigenic chlorite in the Upper Cretaceous sandstone reservoirs of the Santos Basin (Eastern Brazil) indicate that pore-lining chlorites significantly reduce permeability. Permeability of chlorite-rich sandstones ranges between 0.01 and 30 mD. Permeability of the majority of the examined samples was below 5 mD, suggesting that the chlorite obstructed pore throats and connectivity.

1.2.6.5.2 Pore filling, grain replacive, and chlorite isolated crystals

Pore-filling chlorite is detrimental to reservoir quality (Armitage et al. 2010; Cao et al. 2018). The extensive growth of grain coats can ultimately lead to pore filling chlorite that blocks the pore throats and fills the pore space. Other types of pore-filling chlorite probably originated as chlorite-rich grains, such as Fe-ooids, or possibly allogenic lithic grains (Anjos et al. 2003), or metamorphic rock fragments that underwent ductile compaction during burial (Worden et al. 2000).

Grain replacive chlorite develops when detrital Fe-Mg-Al- Si-bearing minerals, or rock fragments, undergo authigenic replacement by chlorite. For this to happen, pore fluids should not contain H_2S and CO_2 to avoid the preferential development of pyrite and siderite or ferroan dolomite instead of chlorite, respectively (Worden et al. 2020). Grain replacive chlorite is incapable of inhibiting quartz cementation and therefore does not help reservoir quality in sandstones.

Chlorite crystals are typically volumetrically limited, scattered and isolated, and occur either as chlorite plates that co-existed with small quartz, kaolinite and illite crystals (Chen et al. 2011) or as chlorite rosettes composed of euhedral blades (Grigsby 2001). Bahlis and De Ros (2013) observed the presence of chlorite rosettes formed by platelets in divergent arrangements, partially filling intragranular and intergranular spaces. In some cases, the rosettes are engulfed by quartz and albite overgrowths or nucleated upon pyrite framboids, diagenetic TiO_2 crystals or faecal pellets.

1.2.7 Kaolinite

Kaolinite is a 1:1 layered silicate mineral with the following composition: $Al_2Si_2O_5(OH)_4$. Kaolinite is typically an eodiagenetic or detrital precursor clay mineral with a book-like or worm-like vermicular habit. Kaolinite formation is promoted, under humid conditions in continental sediments, by the interaction between low-pH groundwaters and detrital aluminosilicate minerals such as feldspars, mica, rock fragments, mud intraclasts and heavy minerals (Emery et al. 1990). Early precipitation of kaolinite is in general related to flushing by meteoric waters whose availability is increased due to humid conditions (Lanson et al. 2002; Worden and Morad 2003).

In the course of progressive burial and temperatures between 70°C and 130°C, kaolinite increases its degree of stacking order and eventually transforms into its high-temperature polytype, dickite. Dickite shows a uniform chemical composition with kaolinite and presents a euhedral blocky pseudohexagonal habit (Figure 1.7) (Beaufort et al. 1998; Worden and Morad 2003). Considering the substantial depths at which dickite forms, kaolinite to dickite transformation is controlled by the geochemical environment and probably results from invasion by acidic fluids of organic origin and not from meteoric water incursion (Morad et al. 1994). Some authors suggest that the transformation proceeds through a dissolution reprecipitation mechanism due to the pervasive dissolution of eodiagenetic kaolinite (Ehrenberg et al. 1993). Others suggest a kinetic control as the transformation is more pervasive in high permeability sandstones than in low permeability sandstones (Cassagnabere 1998).

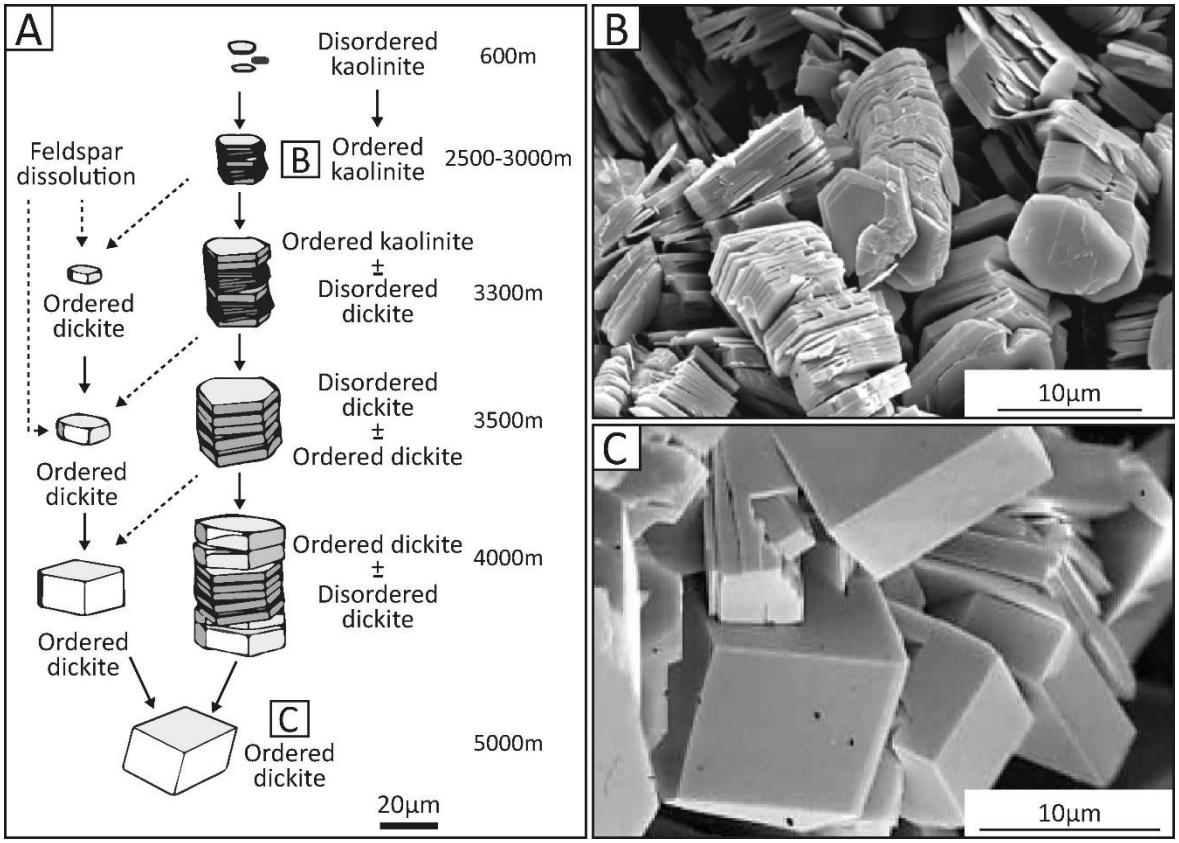

Figure 1.7: Kaolinite to dickite transformation. A) Schematic model of the kaolinite to dickite reaction showing both morphological and structural changes resulting from water-rock interaction with increasing burial depths of sandstone reservoirs. Arrows indicate the transfer of matter due to material redistribution involved in the dissolution-crystallization processes (Beaufort et al. 1998). B) SEM image of well-crystallized kaolinite from sandstone. Note hexagonal morphology and smooth basal surfaces (Wilson et al. 2014). C) SEM photomicrograph of blocky dickite buried at 5000 m (Beaufort et al. 1998).

The two polytypes coexist over a depth interval until the onset of illitization (Lanson et al. 2002). At temperatures of ~120-140 °C, kaolinite reacts with K-feldspars leading to illite precipitation (Ehrenberg and Nadeau 1989; Bjørlykke and Aagaard 1992; Storvoll et al. 2002). Dickite is less susceptible to illitization due to its better-ordered structure (Morad et al. 1994). Illitization of kaolinite is detrimental for reservoir quality due to the tendency of illite to retain the pseudohexagonal form and pore filling character of kaolinite.

1.2.8 Illite

Illite is a mainly dioctahedral, rarely trioctahedral layered sheet silicate. The general formula is $K_{1.5\text{-}1.0}Al_4[Si_{6.5\text{-}7.0}Al_{1.5\text{-}1.0}O_{20}](OH)_4$ (Deer et al. 2013) presenting a 2:1 layered structure. Illite is one of the most common diagenetic clay minerals in sandstone reservoirs and typically occurs as grain coat with a flaky or fibrous structure (Figure 1.8) (Heald and Larese 1974; Pittman et al. 1992; Gaupp et al. 1993; Storvoll et al. 2002; Tang et al. 2018). Common pathways for the development of Illite include the following transformations: kaolinite to illite, dickite to illite, muscovite to illite, k-

feldspar to illite and dioctahedral smectite to illite (Abercrombie et al. 1994; Storvoll et al. 2002; McKinley et al. 2003; Worden and Morad 2003).

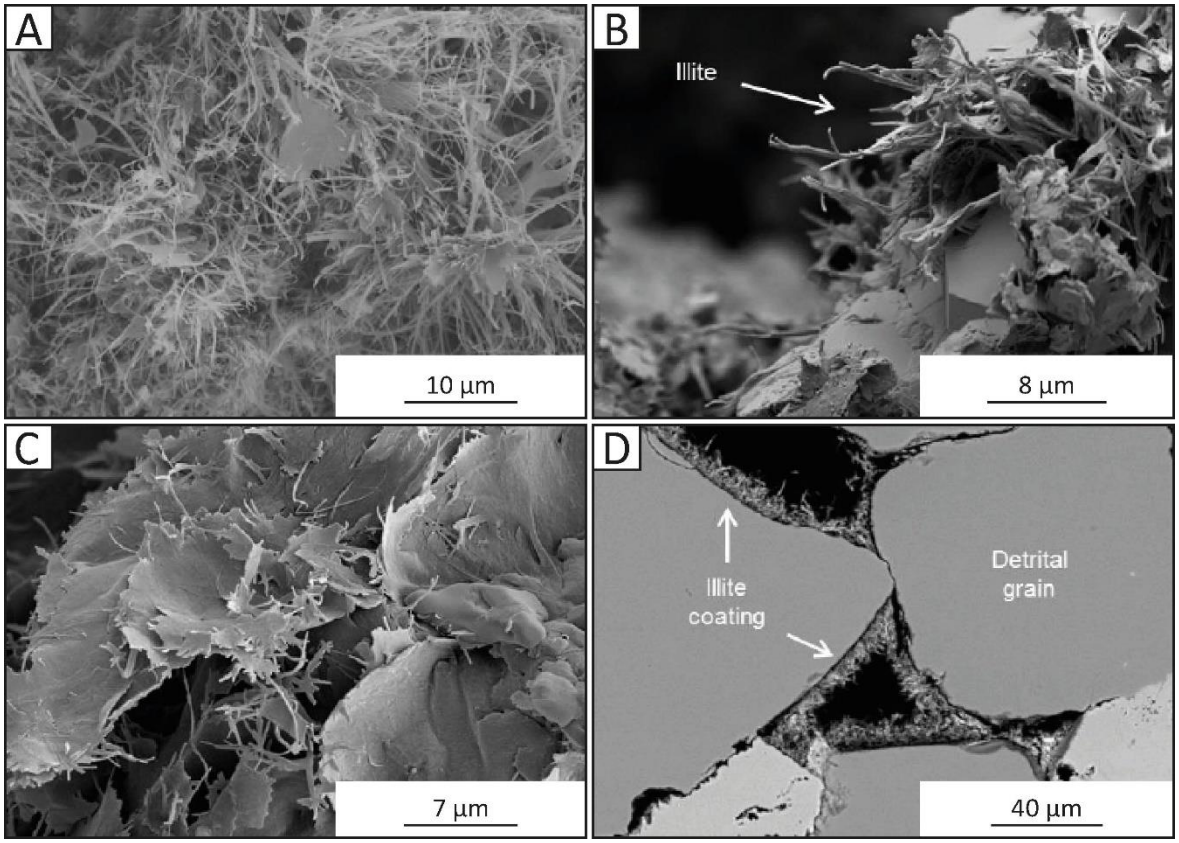

Figure 1.8: Illite grain coats. A) Fibrous illite. B) Long illite fibres filling pore space. C) Flaky illite in a flower-like or rosette-like structure. D) Cross section of illite-coated quartz grains (Stricker 2016).

Illite coats grow from a root zone of flatly attached crystals, which is in direct contact with the surface of the substrate grain and, therefore, preserves porosity by inhibiting extensive quartz cementation. However, illite's fibrous structure has a detrimental effect on permeability and also allows the development of illite and quartz cement intergrowths (Kantorowicz 1990; Ajdukiewicz and Larese 2012; Weibel et al. 2017). The less common flower-like structure has the tendency to encroach into the pore space and bridge between grain surfaces diminishing reservoir quality (Gaupp et al. 1993).

1.2.9 Smectite

Smectite is a 2:1 layered silicate with the following general formula: $(0.5Ca,Na)_{0.7}(Al,Mg,Fe)_4(Si,Al)_8O_{20}(OH)_4 \times nH_2O$. The cation exchange ability of smectites allows them to structurally expand by binding water or organic molecules between their layers (McKinley et al. 2003; Worden and Morad 2003; Deer et al. 2013).

Smectites can be subdivided into dioctahedral and trioctahedral smectites, of which the most common ones are montmorillonite and saponite, respectively (Deer et al. 2013). Smectite formation is promoted by weathering of igneous material (McKinley et al. 2003).

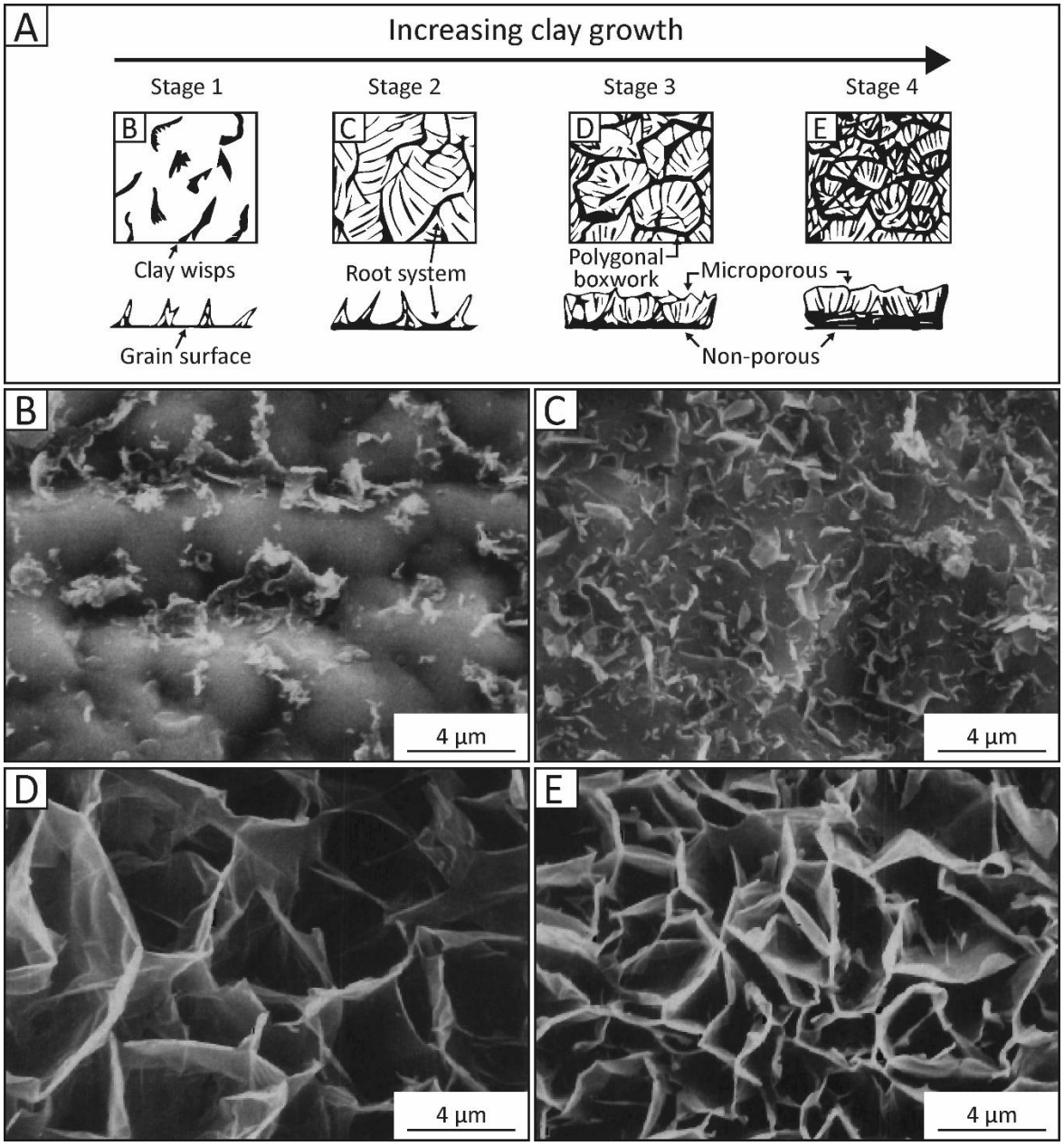

Figure 1.9: Growth stages of smectite coats (Modified after Pittman et al. 1992). A) Schematic illustration of the four growth stages of smectite coating development resulted from hydrothermal reactor experiments. B) Discrete clay platelets/wisps exhibiting random orientation. C) Initial coalescing of discrete clay platelets forming "root system" tangential to grain surface. D) Polygonal boxwork with clay growth mainly normal to grain surface. E) Dense clay growth resulting in infilling of polygonal boxwork. Clay coat appears to be one layer thick.

In sandstone reservoirs, smectites are predominantly linked to shallow burial and low temperatures due to their detrital or eodiagenetic grain coating nature. Smectites represent a common precursor for authigenic, high-temperature illite or chlorite minerals. These coats are generally formed as clay particles oriented parallel to the grain surfaces, with curled edges (Matlack et al. 1989; McKinley et

al. 2003; Worden and Morad 2003). Authigenic smectite coats are less common and develop a dense, flat root zone attached on the substrate surface covered by an outer zone of well-developed smectite crystals. Hydrothermal experiments by Pittman et al. (1992) revealed the four stages of diagenetic smectite coat growth (Figure 1.9).

1.2.10 Microquartz

1.2.10.1 Microquartz origin and morphology

The presence of grain-coating microquartz cement appears to inhibit the development of pore filling macroquartz overgrowths, resulting in anomalously high porosity in deeply buried sandstones (Aase et al. 1996). Microquartz precipitates at lower temperatures (60-65 °C) than quartz cementation (80-100 °C) (Bjørlykke and Jahren 2010). These coats have been identified in many regions such as Brazil (Lima and De Ros 2002), Colombia (Warren and Pulham 2001), the United States (Haimson and Lee 2004), the North Sea basins (Vagle et al. 1994; Hendry and Trewin 1995; Aase et al. 1996; Ramm et al. 1997; Weibel et al. 2010), North Africa (Goldstein and Rossi 2002), Saudi Arabia (Çağatay et al. 1996) and Japan (Hattori et al. 1996). In these examples, sand intervals with robust microquartz coats have higher intergranular porosities than associated sandstones lacking well-developed microquartz coats.

Microquartz is mainly associated with sandstone beds rich in biogenic silica, derived through the in-situ dissolution of sponge spicules or volcanic fragments. Microquartz forms from highly silica supersaturated pore waters as opal A and opal CT dissolve. The transformation is a sequential dissolution-reprecipitation process of opal A to opal CT and opal CT to quartz (Williams et al. 1985). In several of the Upper Jurassic reservoir rocks from the North Sea, *Rhaxella* sponges are the main silica providers (Bjørlykke and Jahren 2010). According to Vagle et al. (1994) and Hendry and Trewin (1995), microquartz seems to develop at the expense of bioclasts at relatively shallow burial depths corresponding to temperatures in the range of 35 to 70 °C. Additionally, the circulation of silica-rich groundwater, due, for example, to the destabilization of organo-silica complexes, through sandstone bodies is regarded as being another source of microcrystalline quartz (Vagle et al. 1994; Hendry and Trewin 1995; Lima and De Ros 2002; French and Worden 2013).

The crystal size of microcrystalline quartz ranges between 0.5 and 10 µm in length (Vagle et al. 1994), and microquartz coats consist of a single layer or multiple layers of prismatic quartz crystals. SEM observations on sandstones that exhibit anomalously high porosities from the Ula and Gyda fields (Norwegian continental shelf) indicate that normal macroquartz overgrowths are commonly 100 µm in diameter and that most of the microquartz crystals have a radius of 0.1–0.4 µm (Aase et al. 1996). Additionally, microcrystalline quartz is parallel to, but randomly oriented on, host grain

surfaces (Aase et al. 1996; Haddad et al. 2006). In contrast, normal quartz cement grows in optical and crystallographic continuity with the quartz substrate (McBride 1989). The random c-axis orientations of microquartz crystals may prevent their merging into larger, syntaxial, quartz overgrowths. Experimental and numerical modelling studies suggest that quartz nucleation and growth on microquartz substrates are slower than on monocrystalline quartz hosts (Bonnell et al. 2006a; Bonnell et al. 2006b; Lander et al. 2006). Micro-quartz can also resist pressure solution by solidifying contacts between quartz grains (Bloch et al. 2002).

TEM examination of numerous samples from the Oligocene Fontainebleau Formation (Paris Basin, France) and the Cretaceous Heidelberg Formation (Germany) identified the presence of an amorphous, non-crystalline silica layer and a layer of chalcedony, nucleated within the amorphous silica, covering the detrital quartz grains and the early syntaxial quartz overgrowths (French et al. 2012; French and Worden 2013). Both the amorphous silica and the subsequent chalcedony layer act as precursors to microquartz growth.

1.2.10.2 Porosity preservation due to microquartz coating

The particular geometry of microcrystalline quartz crystals formed on top of the amorphous silica and inferred chalcedony nanofilm plane ensures porosity preservation in sandstones. The first mechanistic explanation on how microquartz grows and why it is beneficial for the reservoir quality of sandstones was provided by Worden et al. (2012) (Figure 1.10).

The amorphous silica insulates the detrital quartz grains preventing further syntaxial macroquartz development. Microquartz is precipitated on the chalcedony-coated layer inheriting its crystal structure and orientation as a template (Worden et al. 2012). Therefore, the fastest growth axis (e.g., c-axis) of each individual microquartz crystal is randomly oriented but parallel to the host grain surface. This misorientation provokes the impingement of each crystal on each other as they grow, hence limiting their growth length and size. The slower-growing axis (e.g., a-axis) of the microcrystalline quartz is not parallel to the grain surface but directed into the pore space, and so pore-filling cement development is significantly slower.

Hendry and Trewin (1995) suggested that elevated silica saturation, resulting from microquartz precipitation, inhibits quartz dissolution with increasing depth and prevents quartz cementation. Since microquartz tends to precipitate at lower temperatures than macroquartz, it provides an early method of porosity preservation during burial. Similar to chlorite, the quality of microquartz coats is of major importance to porosity preservation. The more robust and continuous the coat is, the better macroquartz cementation is prevented. Nguyen et al. (2013) showed that anomalously high porosities in the fluvial channel sandstone facies of the Triassic Skagerrak Formation (North Sea)

were maintained by a combination of overpressure generation, early microquartz cementation and subsequent precipitation of chlorite grain coats. Microquartz coats stiffened the Skagerrak sands during early burial, enabling them to maintain a high porosity.

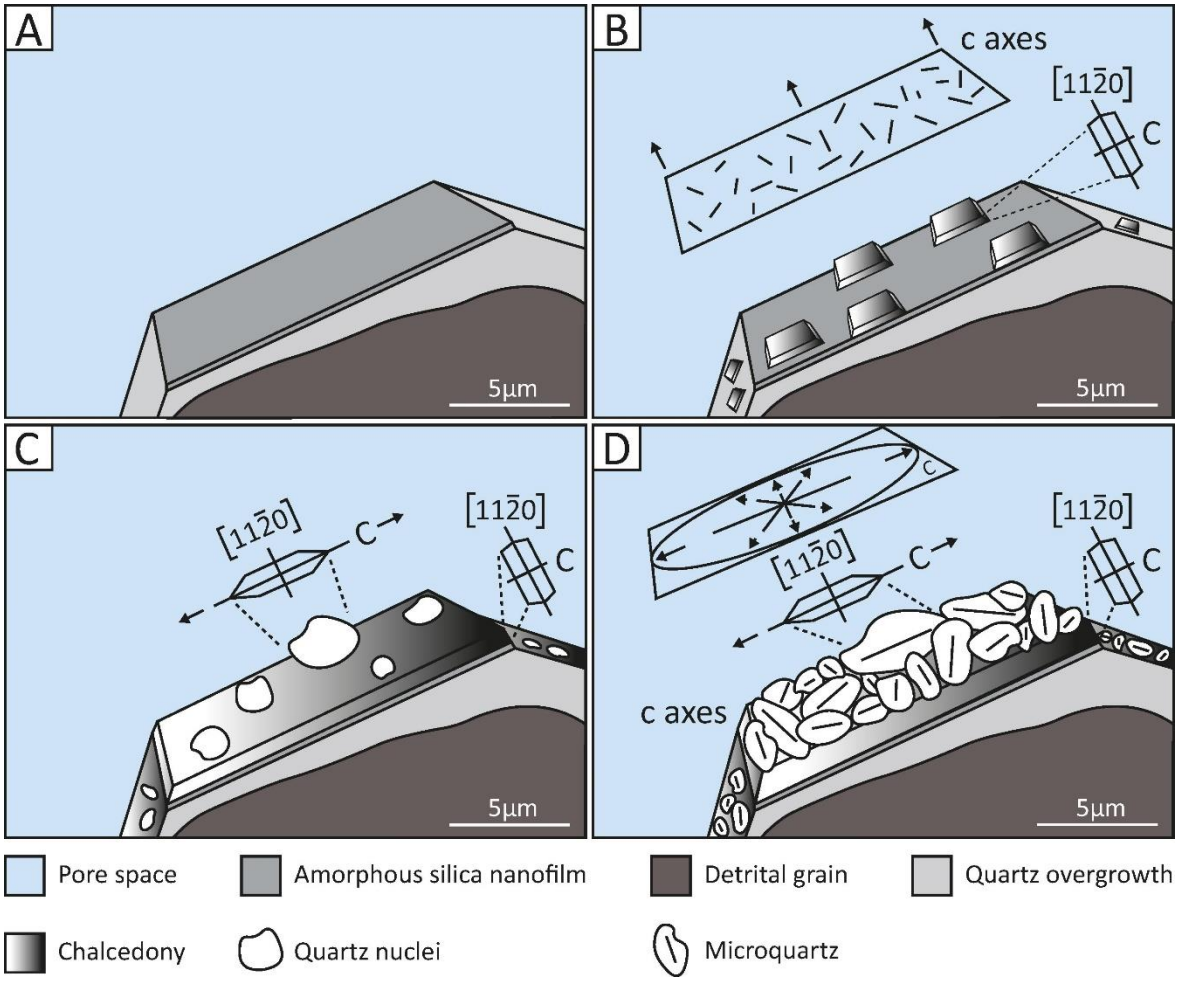

Figure 1.10: Model showing microcrystalline quartz growing on amorphous silica nanofilms, with chalcedony. A) During early diagenesis, pore-filling quartz overgrowths form, with the same crystallographic orientation as detrital grains, around detrital quartz sand grains. Both the detrital grains and the early-formed overgrowths are covered by an amorphous silica nanofilm layer. B) Fibrous chalcedony crystals crystallize in the amorphous silica and grow into the pore space with their [1120] directions perpendicular to the substrate surface. The c-axes of the chalcedony crystals are always perpendicular to [1120] and are thus parallel to the detrital grain surface and randomly oriented within the nanofilm plane. C) Microcrystalline quartz nucleates on chalcedony-coated substrate and uses chalcedony crystal structure and orientation (c-axis parallel to grain surface) as a template. D) Microcrystalline quartz grows along the chalcedony crystal c-axis and parallel to the detrital grain surface, preventing quartz cement growth into the pore space (From Worden et al., 2012).

1.2.11 Siderite

Siderite, $FeCO_3$, is a trigonal carbonate mineral found in several geological environments and a common cement in siliciclastic sequences. It precipitates under various conditions and processes, during sea floor diagenesis and at all stages of burial diagenesis (Morad et al. 1994; Milliken 1998; Rossi et al. 2001; Stel 2009). It forms under reducing conditions providing sufficient iron in the 2+ oxidation state to build the mineral. Siderite has a variable composition as Mg, Ca, and Mn

frequently substitute for the Fe in its crystal structure (Lippmann 1973). Such substitutions are strongly dependent on the composition of the pore fluids, whether it is fresh, brackish, or marine waters, or hot saline brines. Changes in pore water chemistry, induced by fluid flow within an aquifer system, have been interpreted to promote chemical zonation within siderite crystals (Haszeldine et al. 1992). In addition, bacterial activity within shallow depths influences both the isotopic and the chemical composition of the precipitating siderite (Dutton et al. 1996; Mortimer et al. 1997).

Freshwater siderite is relatively pure $FeCO_3$ with a high Ca/Mg ratio (Mozley 1989). In meteoric or brackish water environments, the precipitation of iron sulphides is prevented due to low sulphate activity; thus, Fe^{2+} remains available for siderite authigenesis during microbial Fe-reduction and methanogenesis. Marine waters have high activity of Ca^{2+} and Mg^{2+}, resulting in extensive substitution of Mg and Ca for Fe. Mg siderite is reported to precipitate at higher temperatures compared to Ca- and Fe-rich varieties (Morad 1998). Analysis of siderite cements in sandstones from the Scotian Basin, offshore eastern Canada, identified five chemical types of siderite based on the amount of substitution of Ca, Mg and Mn for Fe (Table 1.3) (Pe-Piper and Piper 2020).

Type	**Composition** (mole percentage)
Fe Sd	>75% $FeCO_3$ and mostly >10% $CaCO_3$
Ca Sd	>10% $CaCO_3$ and <25% $MgCO_3$;
Mg Sd	>25% $MgCO_3$ and 10 to 25% $CaCO_3$
Fe-Mg Sd	15 to 25% $MgCO_3$ and <10% $CaCO_3$
Mn Sd	>3% $MnCO_3$ and generally >20% $MgCO_3$

Table 1.3: Chemical types of siderite (After Pe-Piper and Piper 2020).

Early eodiagenetic siderite is related to lithofacies, which are influenced by the sequence stratigraphic evolution of a basin (Morad et al. 2012). It usually occurs as intergranular pervasive cement (Milliken 1998), nodules and, concretions (Curtis and Coleman 1986). It is also commonly enriched in Mn due to the strong association between the Fe and Mn reduction zones (Tasse and Hesse 1984). Contrarily, late diagenetic authigenic siderite occurs as isolated crystals rimming framework grains, or within cleavage, fractures and secondary pores. Typical crystal habits include rhombic shaped blocky (Mozley and Carothers 1992), wheat-seed (McBride et al. 1988), bladed (Floran and Papike 1975) and lozenge (Machemer and Hutcheon 1988) types.

Carbonate cements can either deteriorate or benefit the reservoir properties of sandstones. When sandstones are highly cemented, the reservoir properties are diminished. However, a small amount of carbonate cement that is evenly distributed within the reservoir can support the overburden and prevent primary porosity loss (Souza et al. 1995). In addition, the dissolution of carbonate cements

contributes to the enhancement of reservoir properties by creating secondary porosity (Morad 1998).

Siderite cementation is the principal porosity-destroying agent in certain reservoirs (Mozley and Carothers 1992), whereas, in others, it led to porosity preservation by inhibiting compaction and quartz cementation (Dutton et al. 1996; Rossi et al. 2001). Siderite dissolution is considered less significant in terms of secondary porosity generation (Rezaee and Schulz-Rojahn 1998). It is less soluble than other carbonates and is generally not regarded as susceptible to sedimentary recrystallization during diagenetic conditions (Mortimer and Coleman 1997; Morad 1998; Odigi and Amajor 2010). However, studies of siderite in fluvial successions from the Jurassic Khatatba Formation (Egypt's Western Desert), have shown: (i) significant siderite dissolution and subsequent generation of secondary porosity and (ii) recrystallization or replacement that changed the content of Ca, Mg and $\delta^{13}C$ in siderite, with lesser changes in $\delta^{18}O$.

1.2.12 Overpressure and vertical effective stress

Recent research focused on deeply buried HPHT sandstone reservoirs has demonstrated the role played by overpressure and its effect on the vertical effective stress history that is key to determining reservoir quality (Stricker and Jones 2018). It has been observed that overpressure reduces the effective stress acting on the grain framework (Gluyas and Cade, 1997; Grant et al., 2014; Nguyen et al., 2013) and limits or prevents quartz cementation by forestalling and eliminating intergranular pressure dissolution at grain contacts (Osborne and Swarbrick 1999; Sheldon et al. 2003; Walgenwitz 2003). Hence, porosity that would be lost to mechanical compaction and quartz cementation is held open, resulting in anomalously porous sandstones at significant burial depths.

Vertical effective stress (VES) acting on intergranular and cement-grain contacts is the primary driver of mechanical compaction and porosity decrease during shallow burial. Therefore, the shallower the depth of onset, the greater the potential for preserving high primary porosity (Stricker and Jones 2018). Grant et al. (2014) and Nguyen et al. (2013) have demonstrated that even diagenetically and structurally complex sandstone reservoirs can retain anomalous porosities due to the early onset of overpressure. Experimental studies on the rate of chemical compaction of quartz-rich sandstones at depths greater than 2.5 km showed that compaction is mainly controlled by stress-induced pressure dissolution (De Boer et al. 1977; Niemeijer et al. 2002; van Noort et al. 2008).

Vertical effective stress is an effective driver of intergranular pressure dissolution, and its magnitude depends on the pore pressure regime. The development of pore fluid overpressure always lessens the vertical effective stress and reduces the load borne by intergranular contacts

within buried sand (Gluyas and Cade 1997). Therefore, low vertical effective stress limits the source of silica, reduces the rate of macroquartz cementation and preserves porosity regardless of the temperature regime (Osborne and Swarbrick 1999; Sheldon et al. 2003; Stricker et al. 2016a; Oye et al. 2018). However, there have been claims that overpressure has no effect on reservoir quality maintenance (Bjørkum 1996) or has been considered less significant (Audet and McConnell 1992; Taylor et al. 2010) attributing the enhanced porosity solely to temperature or chlorite grain coats. A growing body of literature focused upon increased overpressure and corresponding reduction of vertical effective stress has identified the importance for reservoir quality studies. However, it is critical to ensure an early onset of overpressure and maintenance for extended geological periods of time (Stricker et al. 2016a; Oye et al. 2018; Oye et al. 2020).

1.2.13 Oil emplacement

The effect of oil emplacement on quartz cementation in reservoir sandstones is controversial; some studies have concluded that early oil emplacement can inhibit quartz cementation preserving porosity (Gluyas and Cade 1997; Worden et al. 1998; Wilkinson et al. 2004; Wilkinson and Haszeldine 2011; Worden et al. 2018b), while other studies have concluded that quartz cementation can continue unhindered even after oil emplacement (Ramm and Bjorlykke 1994; Bjørkum and Nadeau 1998; Aase and Walderhaug 2005; Molenaar et al. 2008; Taylor et al. 2010).

The effect of oil emplacement on diagenesis has been investigated using different approaches and datasets, such as cement volume trends in oil and water legs (Marchand et al. 2002), oil inclusions in quartz cements (Walderhaug 1990; Gluyas et al. 1993), wettability and oil-water saturation (Barclay and Worden 2000), supply and precipitation of solutes (Murphy et al. 1989), transport of solutes in solution. Comprehensive reviews of the controversial topic of oil emplacement inhibiting (slowing down) quartz cementation concluded that quartz cement should be inhibited if (i) the system is mixed- or oil-wet, (ii) silica is supplied by external sources, (iii) the rate of diffusion is rate-controlling, or (iv) advection is an important part of the transport process. In internally sourced silica systems with diffusion as the transport control, the added tortuosity reduces the net rate of diffusion; hence quartz cementation is inhibited (Worden et al. 1998; Worden and Morad 2000).

1.2.14 Biofilm communities and clay mineral authigenesis

The formation of authigenic minerals is a key aspect of the interaction between ambient environment and microbial life (Ferris et al. 1986; Ferris et al. 1987; Ferris et al. 1991; Chafetz and Buczynski 1992; Konhauser et al. 1993; Konhauser and Urrutia 1999). The interrelation between microbes and clay authigenesis has been demonstrated in laboratory experiments (Fomina and Gadd 2002; Fomina and Gadd 2003), natural sedimentary environments, lacustrine sediments

(Konhauser et al. 1994; Konhauser 1998), hydrothermal areas (Konhauser and Ferris 1996), terrestrial rock habitats (Wierzchos et al. 2003) and within the subsurface in igneous biosphere of both continents and oceans (Bengtson et al. 2014; Drake et al. 2017).

Microorganisms preferentially adhere to solid surfaces, where nutrients tend to concentrate, and through active growth and cell division, they expand in surface coverage, forming complex microbial communities (Konhauser and Urrutia 1999). Namely, these communities are known as biofilms and represent 3-D structures of extracellular polymeric substances (EPS) containing a matrix of microcolonies of multiple species of bacteria, archaea, fungi, cyanobacteria, algae and other microbial eukaryotes, each with a specific metabolic function. This matrix is usually highly hydrated, and the main constituents of EPS are organic molecules such as polysaccharides (50-90%), proteins, lipids and nucleic acids (P. Stoodley et al. 2002; Flemming and Wingender 2010). Biofilm formation can be subdivided into three stages (Figure 1.11); 1) attachment which is mainly affected by the surface properties and the rate of microbial transport to the surface, 2) colonization, and 3) growth which are mainly affected by the mass transport of nutrients (Lewandowski and Beyenal 2013).

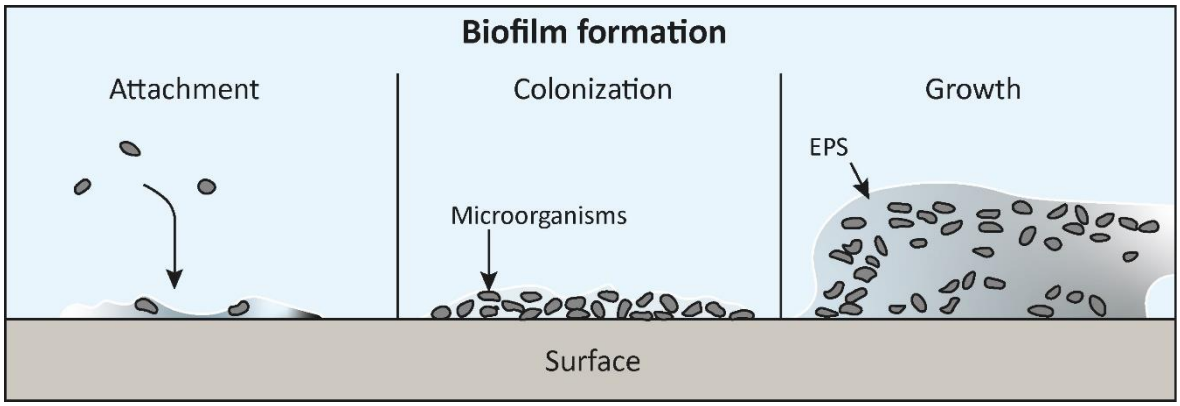

Figure 1.11: Stages of biofilm formation (Lewandowski and Beyenal 2013). The surface could represent sediment grains where the biofilm can restrict the movement of grains in marine and non-marine settings.

Microbial secreted EPS play a crucial role in maintaining the structural integrity of biofilms by affecting the cohesive interactions in the biofilm matrix (Chen and Stewart 2002). Moreover, in modern-day soft sediments, such as in estuary and shallow lagoonal settings, EPS affects sediment dynamics. This, by enhancing the cohesive forces between sediments, binding them together hence affecting their stability, and by coating sediment particles hence changing the micromorphology of individual grains (Van Colen et al. 2014). In general, biofilm accumulation is observed in several substrates such as surfaces submerged in water, in soils and subaerial rock surfaces, and in endolithic environments (Los Ríos et al. 2003).

Numerous studies document microbe-clay mineral interactions and their importance in geological processes (Folk and Lynch 1997; Douglas and Beveridge 1998; Konhauser and Urrutia 1999; Dong 2012; Cuadros 2017). Both clay minerals and microbes are abundant in soils, sediments, and sedimentary rocks, presenting similarities in terms of their dimensions, surface area, and surface electric charge. Minerals affect the physical environment where microorganisms live and support microbial growth by providing essential nutrients, while biofilms support mineral genesis and or transformation by providing the chemical conditions and nucleation sites necessary. Clay mineral formation mediated by microbial communities is not limited to the surface but also deep underground (up to 5 km) in both the continental and oceanic crust.

Microorganisms precipitate clay minerals: i) from solution, ii) through weathering or dissolution of silicate minerals, and iii) through the transformation of pre-existing clay minerals or large-grained phyllosilicate species (Cuadros 2017). Biofilms also have the ability to encapsulate mineral particles. Encapsulation is an effective way of modifying the environmental conditions (e.g., water regime, temperature, salinity, etc.) at the surface of mineral grains for microbial activity to be active (Cuadros et al. 2013).

Cellular surfaces and their EPS are highly reactive and have the potential to adsorb, retain and exchange chemical species, including elements essential for microbial metabolism (Sutherland 2001; Flemming and Wingender 2010). These characteristics can invoke nucleation of secondary minerals in association with microbial walls or sheaths by lowering the activation energy (Costerton et al. 1995; Dupraz et al. 2009)

Mineralisation associated with bacteria cells depends on the chemical composition of the waters in which bacteria are growing (Konhauser et al. 1998). Extracellular polymeric substances surrounding the bacteria cells are exposed to metal ions in the bulk aqueous phase, with some polysaccharides exhibiting a preference toward specific metal ions. Microorganisms can control the concentration of solutes reaching the cell surface through interactions with reactive amphoteric groups present within their cell wall polymers and external sheaths and capsules (Beveridge 1989). The presence of charged chemical groups on their surface allows mineral nucleation on the cells. The metal ions stoichiometrically interact with the charged groups in the surface structures; hence an electrostatic charge between the metal ions and the cellular polymers is created. Subsequently, due to the presence of bound metal ions in the wall fabric, the total free energy of the system is lowered, and further metal deposition is initiated. The size of the neoformed metal aggregates is dependent upon the physical presence of the polymer meshwork (Douglas and Beveridge 1998).

1.2.14.1 Microbial reduction of ferric iron

Mineral solubility and oxidation state of certain constituent elements are altered by microbial activity. Iron is an omnipresent component of most clays due to its great abundance in Earths' crust. Several studies have confirmed that a wide variety of mesophilic, thermophilic, and hyperthermophilic microorganisms have the ability to reduce Fe^{3+} in clay minerals (Kostka et al. 1999a; Kostka et al. 1999b; Stucki and Kostka 2006), resulting in the formation of several new or altered minerals. The main bacteria related to these studies include *Geobacter metallireducens* (Kostka et al. 1999b), *Pseudomonas* (Ernstsen et al. 1998; Gates et al. 1998), *Bacillus* (Kostka et al. 2002), *Shewanella oneidensis* (Dong et al. 2003), and *Shewanella putrefaciens* (Zhang et al. 2007).

Multiple clay minerals, such as smectite, illite, mixed-layer illite–smectite, chlorite, vermiculite, palygorskite, and their various mixtures, have been used for microbial-reduction studies (Dong et al. 2009). The extent and rate of the reduction vary depending on: i) the bacterial system, ii) the amount and the crystal-chemical environment of structural Fe^{+3} and, iii) the layer charge of clay mineral structures which is related to layer expandability which in turn affects the electron transfer process (Jaisi et al. 2007).

Although several bioexperimental studies have been carried out, the mechanisms of microbial reduction of ferric iron in clay minerals are not well constrained. Some experiments indicated that partial dissolution of clay structure was induced by the reduction of ferric iron (Dong et al. 2003; Furukawa and O'Reilly 2007; Zhang et al. 2007), while other introduced evidence for a solid-state reduction mechanism (Stucki and Kostka 2006; Kashefi et al. 2008). The reasons for this inconsistency lie in the fact that the mechanism of ferric reduction may: i) be mineral specific, ii) be dictated by the extent of the reduction, iii) depends on the type of medium, the presence or absence of organic matter, and differences in the solution pH used for bioreduction experiments and, iv) depends on the concentration and type of microorganisms (Dong et al. 2009).

1.2.14.2 Microbially mediated clay mineral authigenesis from solution

The role of bacteria in forming iron-rich minerals, in particular authigenic clays, involves a complex interaction between metals in solution with the reactive components of bacteria cells (Ferris et al. 1991; Fortin et al. 1998). In many diverse environments, including river systems, mine tailings and hot springs, silicate minerals with a Si-Al-Fe composition and clay-like morphology are closely associated with microbes (Konhauser et al. 1993; Konhauser and Ferris 1996; Fortin and Beveridge 1997). Clay minerals of microbial origin are compositionally variable and have lower crystal order than clay minerals formed by inorganic processes in the same environment (Douglas and Beveridge 1998).

Studies on natural samples from the Rio Solimoes river system (Brazil) pointed out the central role of Fe in the nucleation of very fine clay particles on bacteria cells. The precipitation of these particles has likely started with the accumulation of Fe on the cells, followed by the trapping of Al and Si (Konhauser et al. 1993). Konhauser and Urrutia (1999) proposed that clay mineral crystallization in the presence of bacteria begins with the formation of iron-rich aggregates on the membrane of microbial cell walls, followed by progressive mineralisation, which in turn leads to partial and/or complete encrustation of some bacterial cells. The authigenic origin of these inorganic particles is supported by the following: i) the majority of the grains are amorphous to poorly ordered structures with differing chemical compositions in relation to the detrital material carried in suspension, ii) the grain types on each individual bacterium have similar Fe, Si and Al ratios, iii) most grains exhibit a similar, tangential orientation around the bacterial cells and, iv) the generally small size of the particles indicates that the grains formed via a chemical reaction with the organic ligands (Konhauser and Urrutia 1999).

Apart from bacteria cell walls, EPS of biofilms can also serve as a template for layer-silicate synthesis. Nontronite (e.g., iron-rich smectite) layers were found embedded in EPS from metalliferous sediments of the Iheya Basin, Japan, suggesting that EPS catalyses the precipitation of the mineral. Nontronite formation was induced by the accumulation of Si and Fe ions from the ambient sea water (Ueshima and Tazaki 2001). Similarly, studies on Upper Jurassic phosphate stromatolites from a pelagic environment indicated that the crystallization of Fe-rich smectite occurred from Fe-Si-Al gels during early diagenesis. These amorphous precursor phases were of synsedimentary origin. They were produced within the biofilms of stromatolite-forming bacteria, with EPS presumably acting as a catalyst for the attraction of cations and other chemical species. Subsequently, they were partially recrystallized, leading to the precipitation of smectitic clays (Sánchez-Navas et al. 1998).

1.2.14.3 Importance of biofilm communities for diagenesis

In estuary and shallow lagoonal settings, most sediment is composed of noncohesive, unconsolidated sand grains. Biofilms provide important ecosystem functions, including sediment stabilization (Vignaga et al. 2013; Paterson et al. 2018), sediment transportation and bedform stabilization (Malarkey et al. 2015). Furthermore, biofilms in tidal and intertidal sediments have been documented to form an adhesive coat on sand grains that acts as a binding agent capable of forming clay minerals (Kessarkar et al. 2010; Virolle et al. 2019a). Wooldridge et al. (2017a) identified a positive statistical correction between sediment biofilm abundance (chlorophyll-a) and clay-coat coverage in the intertidal siliciclastic sediments of the Ravenglass Estuary (UK). Duteil et al. (2020) performed laboratory experiments producing clay-coated quartz sands, texturally akin to

those observed in modern and ancient estuarine sands, by mixing EPS derived from intertidal diatom biofilms with clay minerals and quartz reference materials.

Biofilm-mediated clay mineral precipitates could represent precursor phases to authigenic clays that, with progressive burial, can act as effecting barriers blocking potential nucleation sites for quartz overgrowths and thus preserving reservoir quality.

1.2.15 Clay coats and hydrothermal reactor experiments

The presence of clay minerals can significantly affect the reservoir quality in siliciclastic reservoirs. Numerous laboratory experiments have been performed to investigate clay mineral coating growth and quartz cement nucleation (Pittman et al. 1992; Hillier 1994; Aagaard et al. 2000; Ajdukiewicz and Larese 2012; Haile et al. 2015).

The first experiment of Pittman et al. (1992) showed that physical blockage of quartz nucleation sites by clay minerals, in this occasion illite, is an effective mechanism for inhibiting quartz overgrowth development. In the second experiment, a chlorite-coated sandstone sample was artificially compacted, causing the quartz grains to fracture. Subsequently, the sample was transferred to an autoclave where quartz overgrowths were experimentally precipitated, suggesting that quartz overgrowths are formed where the chlorite coat is breached by fractures. In the final experiment, a hydrothermal reactor was used to grow smectite, illite and chlorite coats on serpentinite and quartz, sand-sized rounded fragments. This experiment showed the importance of root zones (e.g. link between the authigenic coat and the detrital grain) for authigenic clay coat growth. Root zones are formed by clay platelets tangentially oriented to the detrital grain surface. They are generally hidden by superseding crystal structures (e.g., honeycomb), typically associated with authigenic clay coats. Pittman et al. (1992) compared the synthesised smectite coats with the naturally grown coats and concluded that, if well developed, root zones can effectively cover the detrital grain and serve as a barrier to nucleation of syntaxial quartz overgrowths.

Small et al. (1992) hydrothermally simulated clay mineral precipitation using naturally occurring quartz sand substrates and various aqueous solutions together with solid minerals or amorphous gels. In this closed-system experiment, a temperature gradient enabled the dissolution of a starting material at one end of the vessel and precipitation of a range of clay minerals on sand grains at the other end. Although attempts to produce 14 Å chlorite were unsuccessful, the authors were able to generate a magnesium-rich 7Å-phase (e.g., berthierine) coat with platy boxwork morphology. The fact that 14 Å authigenic chlorites have different morphologies than the berthierine generated in this study suggests that authigenic chlorites are direct precipitates and do not require pre-existing precursors (Small et al. 1992).

Hydrothermal experiments were performed on naturally occurring, berthierine-coated sandstones from the Oseberg and Veslefrikk Fields offshore Norway (Aagaard et al. 2000). The main goals of these experiments were to explore if chlorite coats could indeed be synthesised in the laboratory and to decipher how chlorite coats form during diagenesis. The samples were heated to 200 and 250 °C (at water vapour pressure) in a hydrothermal bomb for 2–4 weeks. The outcome of this research indicated that grains with thin, discontinuous coats of berthierine precursor, when subjected to conditions corresponding to shallow burial temperatures and pressures, will recrystallize at about 100 °C to form thick, continuous coats of authigenic Fe-rich chlorite (e.g., chamosite) that is similar to naturally formed Fe-rich chlorite. However, the mechanism by which berthierine was converted into chlorite was not investigated by this research and remains elusive. The study by Hillier (1994) on naturally occurring sandstone samples containing Fe-rich pore-lining chlorites showed that individual chlorite crystals grow with increasing temperature. An increase in crystal size and thickness (c-axis), which tightens the coating structure of Fe-rich chlorites, was observed at temperatures ranging from 90 to 220 °C.

Ajdukiewicz and Larese (2012) conducted high-temperature reactor experiments (>120˚C) with chlorite-coated quartz sands and observed abundant microquartz beneath the chlorite grain coats. They suggested that the effectiveness of clay coats depends on temperature. Clay coats permit quartz nucleation at temperatures above 115˚C, and from that onwards, clay coats permit quartz cement nucleation in the microporosity between the clay crystals. However, they concluded that the clay particles of coats preserve porosity by forming barriers to initial cement coalescence and growth. Hence, quartz cement overgrowth at higher temperatures is dependent on the clay coat structure, which differs with clay mineral composition and origin of the clay mineral coat. Quartz cement intrudes into the main pore system only at breaks or gaps in the coat (Ajdukiewicz and Larese 2012).

Haile et al. (2015) conducted an experiment where clay mineral coats were synthesized using a multi-batch reactor system by varying the pH, temperature, and supersaturation. This study demonstrated that grain coating smectites and chlorites could form on clean quartz and feldspar surfaces at 100 and 150 °C, given sufficient supersaturation and time. The lab-formed clay coats were morphologically similar to naturally occurring clay coats (Haile et al. 2015).

Murphy (2016) conducted hydrothermal experiments, using synthetic brines and sandstone core material from the Vesselfrikk field (Norwegian North Sea), to examine and quantify any changes in the mineralogy of illite or other clays. Several converging lines of evidence from chemical, computer modelling, and petrographic analyses indicate that illite crystallinity changed over a short period of

time (several weeks) under the pressures (450 bars), temperatures (140 and 150 °C) and geochemical conditions utilized in the hydrothermal experiments. Namely, a significant change in the clay mineral fraction, with dissolution of both K-feldspar and illite and formation of muscovite, was observed.

Similarly, Birkle et al. (2019) conducted hydrothermal laboratory experiments (T = 100 - 150 °C; P= 300 - 450 bars) to trace brine-sediment interaction relevant to understanding illite diagenesis in the Late Carboniferous-Early Permian Unayzah sandstone reservoir, Saudi Arabia. The results suggested incipient illite precipitation on kaolinite grains exclusively under deep reservoir conditions of 150 °C and 450 bars. Excluding temperature, which is the major controlling factor, other parameters, such as local grain mineralogy, grain surface substrate and large-scale potassium mobility, affect the heterogeneous illite distribution in the Unayzah formation.

1.2.16 Conclusions

Assessing the reservoir quality of sandstones, located in complex geological systems, subjected to extensive diagenetic alterations is paramount when analysing how best to explore and effectively develop energy resources. Sandstone reservoir quality is influenced by many factors such as depositional environment, relative sea-level change, initial rock properties (e.g., grain size, sorting, composition), biogenic input, depositional rate, palaeoclimate, fluid composition (early and deep water), rate of burial and heating, timing of oil emplacement, timing and magnitude of fluid overpressure development, fracturing, redox conditions, and mass transfer associated with diffusion and fluid advection.

Several combinations of the factors mentioned above can act together to minimize the effects of mechanical and chemical compaction (e.g., cementation) and preserve porosity and permeability at greater burial depths than is normally predicted. Of particular importance is the presence of clay mineral coats, the most reported of which is chlorite, which can inhibit quartz cementation that typically occurs at temperatures > 80 to 100 °C. Chlorite coats of detrital or authigenic origin physically isolate the surface of quartz grains from the pore water required to allow quartz to grow. The continuity of these coats dictates the effectiveness of porosity preservation as gaps or breaks in the coating structure allow quartz cement to grow, albeit at a slower rate than if no chlorite coats were present.

The most important origins of chlorite in sandstones are chlorite precursor clays such as berthierine (e.g., a low temperature 7 Å Fe-clay), smectite, kaolinite reacting with a source of Fe, Fe-rich lithic grains, and Fe-bearing heavy minerals. Marginal marine settings of estuaries and deltas are associated with the accumulation of sedimentary iron, hence the development of early grain coats.

Additionally, in such environments, microorganisms are known to be key for creating detrital grain coats. With increasing burial and temperature, the early grain coats (i.e., clay precursor phases) convert to authigenic chlorite that contains abundant Mg and Fe as well as Al and Si. The most important chlorite-producing reactions in sandstones (i.e., such as the berthierine to chlorite transformation), through which authigenic coats develop, start to occur at about 60 °C.

Integrating experimental data with high-quality quantitative 2D and 3D petrographic data and modelling techniques is crucial to enhance our understanding of the mechanisms for diagenetic processes and obtain meaningful predictive data. In the following chapters, a novel methodology is presented aiming to unravel the paths of chlorite authigenesis, subsequent reservoir quality influence, and the precipitation of early biomediated grain coats.

Chapter 2: Methods and materials

2.1 Introduction

A novel multidisciplinary approach comprising hydrothermal experiments, detailed microscopy and analytical techniques were undertaken as part of this research. The hydrothermal experiments were developed to simulate early- and deep-burial diagenetic processes leading to mineral formation. The microscopy and analytical techniques were used to evaluate, qualitatively and quantitatively, the mineralogical and petrophysical alterations in both the 2D and 3D domain, and to model the reservoir quality evolution of the experimentally treated samples. The starting materials and key methods used are presented below.

2.2 Sampling: Cook Formation (Lower Jurassic), Oseberg Field, Norway

Core material, thin sections, and polished blocks for the experimental procedure described in chapters 3 and 4 are taken from the Lower Jurassic Cook Formation, Well 30/6-17R, from the Oseberg Field, Norway (Figure 2.1A). The Oseberg field is located on the eastern flank of the Viking Graben, at the rim of the Horda Platform. Cook Formation was deposited during a phase of overall tectonic inactivity and subsidence that followed the Permo-Triassic rift phase of the North Sea (Folkestad et al. 2012).

Lower Jurassic rocks in the Norwegian North Sea include the Statfjord Group and the Dunlin Group, which is underlain by the Middle Jurassic Brent Group (Vollset and Doré 1984). The Cook Formation stratigraphically lies within the Dunlin Group (Pliensbachian – Toarcian) and is bound by the Burton Formation below and the Drake Formation above (Figure 2.1B).

Cook Formation is extensively distributed in the northern North Sea and has been reported in the literature with different depositional environments at different locations. In Oseberg Field, it is subdivided into three units (i.e., Cook A, Cook B and Cook C). Cook A was characterised as prograding subtidal sand body. Cook B is comprised of mud and siltstones with thin lenses of sandstones. Cook C was deposited as an offshore sand ridge (Livbjerg and Mjøs 1989). The rock samples (e.g., polished blocks, rock chips, and core plugs of 4 mm diameter and length varying between 5 mm and 9 mm) used for the present research were obtained from core material from unit A (depth: 7988.18 ft. / 2434.8m) and have been selected for the high berthierine, a chlorite precursor, and siderite content.

The Cook Formation of the Oseberg Field consists of medium to fine-grained sandstones in the upper part, becoming fine to very fine with depth. The sandstones were oil-bearing down to 2419.5 m, with an average porosity and water saturation of 26.4% and 40.1%, respectively. More information about the studied well, including stratigraphy, co-ordinates, and maps, is available on the Norwegian Petroleum Directorate's web pages at http://factpages.npd.no/factpages/.

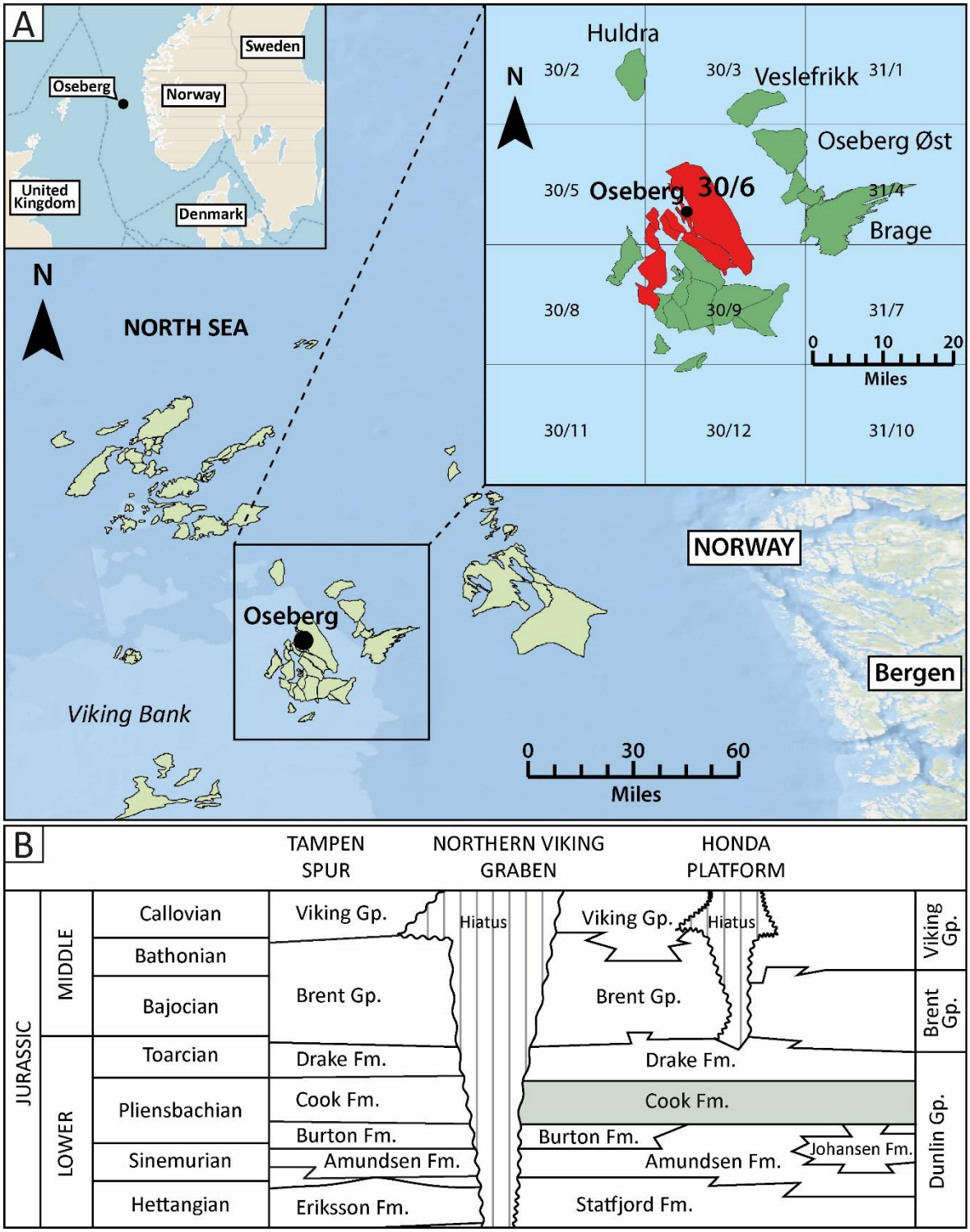

Figure 2.1: Location and stratigraphy of the Oseberg Field and Cook Formation, respectively. A) Location of the Oseberg Field. B) Chronostratigraphic setting of the Late Pliensbachian (Early Jurassic) Cook Fm. in the offshore of the northern North Sea. From Vollset and Doré 1984 and Marjanac and Steel (1997). Highlighted is the stratigraphic setting of Cook Fm associated with the Oseberg Field.

2.3 Sampling: Unconsolidated quartz grains and bacterial communities

2.3.1 Microorganism cultivation and mixing with sand grains

The experiments presented in chapter 5 were conducted on biofilm-rich pure sand grains. Biofilm growth within the unconsolidated sand grains (ACROS Organics™**,** particle size: 40-100 mesh) was laboratory synthesized using *Geobacter sulfurreducens* cultures, selected for their wide distribution in freshwater and or marine environments (Coates et al. 1996; Lonergan et al. 1996; Venkateswaran et al. 1999; Lovley et al. 2004), and the fact that are well characterized and easy to cultivate. The *Geobacter* cultures were obtained from laboratory stocks from the University of Tuebingen (Germany).

The strains were cultivated in the dark under anoxic conditions (N_2:CO_2; 90:10 headspace) at 35 °C in a modified mineral medium (pH 6.8) containing trace elements, vitamins, electron acceptor fumarate, electron donor acetate, and cysteine. Full details of the composition of the mineral medium are included in chapter 5. Growth and cell concentration were monitored by optical density measurements at 600 nm (OD600). Stationary phase cultures of *G. sulfurreducens* were harvested by centrifugation at 5000 rpm at 10 °C three times for 20 minutes and washed with bicarbonate buffer (30 mM, pH 6.8) to prepare a cell suspension with a final cell density of 10^9 cells/mL.

Subsequently, 10 mL of the cell suspension was dispensed in a newly prepared mineral medium (pH 6.8). 50 g of pure sand grains were placed in 250ml serum bottles. 50 mL of the new medium was then added in the bottles under anoxic conditions and let in the dark at 35 °C for incubation. The bottles were manually rotated daily to ensure biofilm development in between the sand particles.

2.4 Hydrothermal experiments

A valuable way to develop a new understanding of sandstone reservoir quality and diagenesis is to perform hydrothermal laboratory experiments. Even though no experiment can fully reproduce naturally occurring conditions, this type of experiment is an essential contributor to our knowledge of burial diagenetic processes. The applied hydrothermal experiments simulate water-rock/sediment interaction processes with well-defined temperature, pressure, and water chemistry conditions and specifically model the effects of temperature on quartz cementation and grain coating precipitation.

The hydrothermal synthesis experiments are conducted in the following vessels, hosted at the Integrated Chemical Reaction Facility (Durham University, Department of Chemistry):

1. the Parker Autoclave Engineer AE Closure Vessel (Figure 2.2A) and;

2. the Parr© Series 4560 Mini Reactor (Figure 2.2B)

During the experiments, temperature was controlled within ± 0.5 °C through a Eurotherm© PID temperature controller. More information regarding the adopted experimental procedure and associated limitations are provided in the relevant chapters (e.g., chapters 3–5).

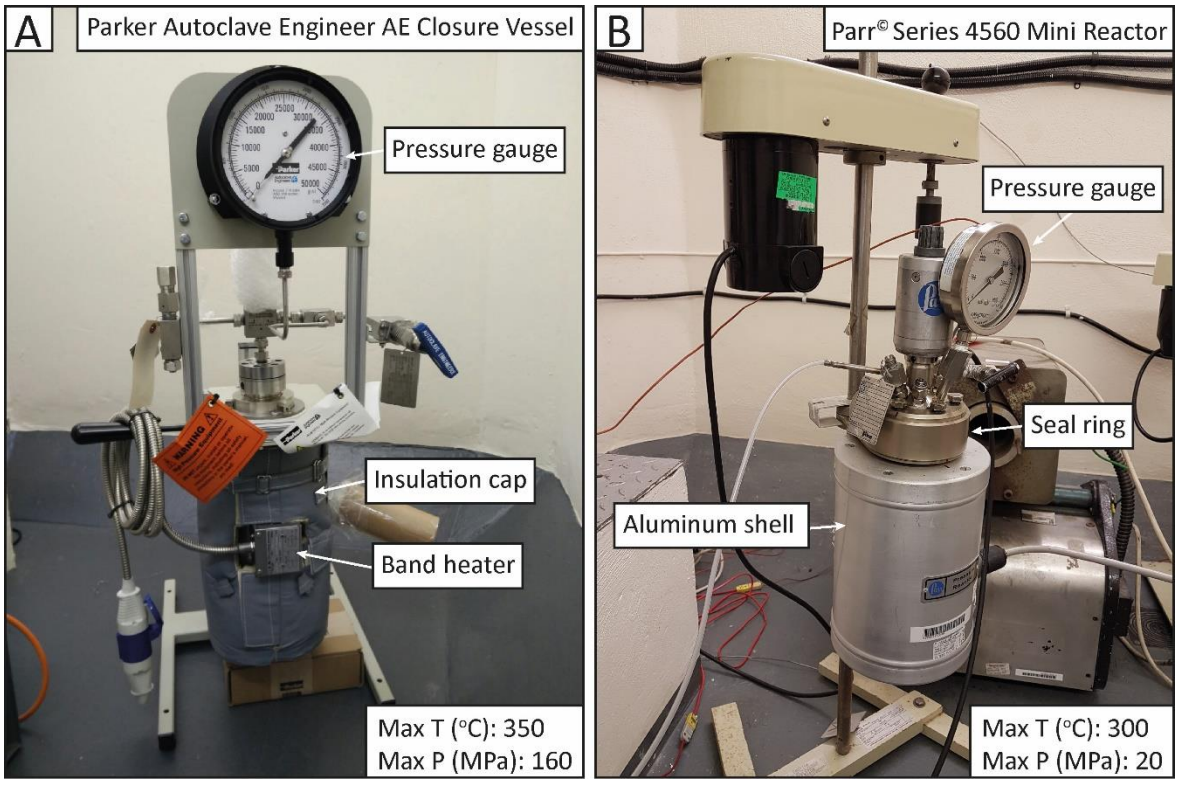

Figure 2.2: Hydrothermal vessels used as part of this research. A) Parker Autoclave Engineer AE Closure Vessel. Front view showing the pressure gauge and the vessel assembly with the ceramic band heater surrounded by an insulation cap. B) Parr© Series 4560 Mini Reactor assembly. The vessel is heated by a quartz fabric mantle housed in an aluminium shell.

2.5 X-ray diffraction (XRD) Analysis

X-ray diffraction (XRD) analysis, both bulk rock and clay fraction, of the untreated Cook Formation samples and the unconsolidated sand samples was conducted by X-Ray Mineral Services Ltd.

2.5.1 Whole (bulk) rock analysis

The bulk rock samples of the Cook Formation were de-oiled, disaggregated and powdered to a mean particle diameter of between 5 and 10 µm. Samples were analysed using a Philips PW1730 Generator coupled with a Philips PW1050 Goniometer with graphite monochromator and a PW1170 automatic sample changer. The analysis was performed at 2θ (theta) angles between 4.5˚ and 75˚, with a step size of 0.06˚/s using X-ray radiation from a copper anode at 40 kV, 40 mA.

The unconsolidated sand samples were disaggregated and powdered to a mean particle diameter of between 5 and 10 µm. The sample as a slurry was dried overnight at 80 °C, re-crushed to a fine

powder and back-packed into an aluminium cavity mount, producing a randomly orientated sample for presentation to the X-ray beam. Samples were analysed using a PANalytical X'Pert3 Diffractometer coupled with an MPD Goniometer with graphite monochromator and a 45 position automatic sample changer. The analysis was performed at 2θ angles between 4.5˚ and 75˚, with a step size of 0.013˚/s and nominal time per step of 0.2 s using X-ray radiation from a copper anode at 40 kV, 40 mA.

Mineral identification of both the Cook Formation and unconsolidated sand samples was achieved by comparing the X-ray diffraction pattern of the sample, obtained through the X-ray Mineral Services Ltd in-house 'Traces' and 'Search-Match' software, with the International Centre for Diffraction Data PDF-4 Minerals database. The maximum intensity of each mineral was measured and compared to the standard intensity of the pure mineral. Any amorphous content was not taken into account, and the results were normalised to 100% based on the assumption that the whole mineral content is accounted for in the diffractogram.

2.5.2 Clay mineral analysis

Extraction of the clay fraction of both the Cook Formation and unconsolidated sand samples was performed to allow the quantification of the clay mineral components of the samples. Initially, separation of the clay fraction (<2 μm fraction) was achieved by ultrasound and centrifugation. After removing a 25ml aliquot of the final clay suspension and evaporating to dryness at 80°C, the total weight of the extracted clay was determined. The samples were analysed as untreated clay, after saturation with ethylene glycol vapour overnight and following heating at 380˚C for 2 hours, with further heating to 550˚C. The same machine was used for the initial scan of these four treatments. The 2θ angles were between 3˚ and 35˚ with a step size of 0.05˚ per second using X-ray radiation from a copper anode at 40 kV, 40 mA. The untreated samples were also analysed between 24˚ and 27˚ 2θ at a step size of 0.2˚ per 2 seconds to further define kaolinite and chlorite peaks. In the Cook Formation samples, where discrimination between specific minerals (e.g., chlorite and berthierine) was required, reflections at higher diffraction angles (e.g., d_{060}) were measured.

Identification of the clay mineral assemblages and assessment of the effect of the treatment on the clay minerals were performed by overlaying the diffractograms from the four clay treatments. Peak intensities were measured and analysed to indicate the relative amounts of clay minerals present, which then were referenced to the total amount of clay minerals present in the whole rock analysis.

2.6 Petrographic analysis

2.6.1 Scanning electron microscope (SEM) and Energy-dispersive X-ray spectroscopy (SEM-EDS)

The Cook Formation samples were studied electron optically using a Hitachi SU-70 field emission gun scanning electron microscope (SEM) equipped with an energy-dispersive detector (EDS). Prior to analysis, selected thin sections and blocks were diamond polished and carbon-coated to avoid charging, reduce thermal damage and improve the secondary electron signal. Backscatter scanning electron microscopy was conducted at acceleration voltages of 15 kV with a beam current of 0.6 nA. SEM-EDS was used for rapid identification of chemical species and their orientation in the sample. Scanning electron microscopy was undertaken on selected samples, providing additional information on the pore-system geometry, habits and textural relationships and authigenic mineralogy. The analysis was undertaken on gold-coated (35 nm), freshly broken samples glued onto aluminium stubs with silver paint at acceleration voltages of 5 kV with a beam current of 1.0 nA.

The biofilm-rich quartz samples were carbon-coated (20nm). Secondary and backscatter electron imaging was conducted at acceleration voltages of 15 kV with a beam current of 0.6 nA. SEM-EDS was used for rapid elemental identification of the new, due to the experimental treatment, mineral precipitates.

2.6.2 Automated quantitative mineralogy

Automated mineralogy analysis of the Cook Formation samples was performed to quantitatively define the mineralogical content and characterise the petrographic relations at the micrometric scale at each temperature step. A Zeiss Gemini SUPRA 40VP field emission scanning electron microscope coupled with an XFlash® 6 Bruker energy-dispersive spectrometer (EDS) and Mineralogic Reservoir software suite was used for the EDS spectra acquisition and digital analysis, respectively. A step size of 3.5 microns at a 255x magnification was employed, ensuring the analysis of the fine fraction of each sample. An electron beam of 20 kV acceleration voltage was directed at the sample. Dwell time was adjusted to capture approximately 20,000 counts per pixel. Based on the grey scale of the backscatter image, a threshold value was chosen to differentiate the sandstone components from the epoxy resin before the EDS analysis. A mineral classification library, tailored to the needs of this research, was developed using the initial XRD data, and the performed SEM imaging and SEM-EDS elemental analysis. The EDS spectra of each analysed point were compared to that library assigning a specific mineral to each point. Consequently, a high-resolution SEM

backscatter image of the whole circular disk surface of each core coupled with a fully quantitative mineralogy map was produced.

2.6.3 Coat thickness and grain coat coverage quantification

The clay coat thickness of the Cook Formation samples was estimated based on the scale bar on the SEM backscatter photomicrographs using ImageJ image processing software. Fifty measurements, with an average ± 0.05 µm error for each measurement, per sample, were performed. Subsequently, clay coats were categorized into four classes: 1) 1-3 µm; 2) 3-5 µm; 3) 5-7 µm and 4) 5-9 µm, to evaluate the distribution of their thickness, within these classes, per experimental step.

Gain coat coverage was quantified using Petrog (Conwy Valley Systems Limited) cross-sectional perimeter length method (Wooldridge et al. 2019). Namely, the percentage perimeter of a grain covered by clay coats was calculated by measuring its total perimeter and the length that is covered by attached clay. Measurements of 50 grains per sample were performed to track the progress of the coverage with increasing temperature. The standard error of the analysis of each sample was ± 2%.

2.7 Aqueous chemistry of the sand-biofilm experiments

The mineral medium used for the biofilm-sand experiments presented in chapter 5 was analysed at each experimental stage by triple quadrupole inductively coupled plasma mass spectrometry (TQ ICP-MS) to determine the concentration of selected elements. The analysis was conducted by X-Ray Mineral Services Ltd. The aqueous bulk solutions were analysed using a Thermo Elemental TQ ICP-MS using a combination of single quad kinetic energy discrimination (KED) and triple quad (using O_2 as the reaction cell gas) modes to remove potential interferences and hence enhance accuracy.

2.8 X-ray computed tomography (XCT)

2.8.1 Data acquisition

X-ray micro-computed tomography is a non-destructive 3D imaging process capable of imaging and analysing internal structures within solid samples at the micrometre scale. A simple sketch of an XCT machine setup is shown in Figure 2.3.

The X-ray source (e.g., typically an X-ray tube) comprises a focused electron beam directed at a target which, when hit, decelerates the electrons, and generates X-rays. Subsequently, the X-ray beam is shaped into a cone as it passes through a circular aperture upon exiting the tube. As the X-rays travel through a sample, the signal is attenuated through scattering and absorption. In

geological samples, the attenuation rate is a function of the mineralogical properties (e.g., mainly elemental composition and density) and X-ray energy. After exiting the sample, the attenuated beam hits a scintillator where the X-rays are converted into photons and captured as a grey-scale radiographic image on a CCD detector. A series of radiographic images or 2D projections are captured by rotating the sample in small known increments. These are used to perform a mathematical reconstruction to generate a 3D volume of the sample described by a series of voxels. Each voxel contains a grey-scale value representing the mean X-ray attenuation of the sample at the voxel's location.

In this research, XCT was used to investigate the evolution of the petrophysical properties and mineralogy qualitatively and quantitatively in a same sample before and after being subjected to different temperatures. Regarding mineralogy, the produced radiographic images are based on differences in X-ray attenuation dependent on the density and atomic mass of each mineral phase. This means that within sandstone samples, the silicate phases (e.g., mainly quartz grains) can be readily distinguished from the Fe-rich phases (e.g., primarily siderite cement).

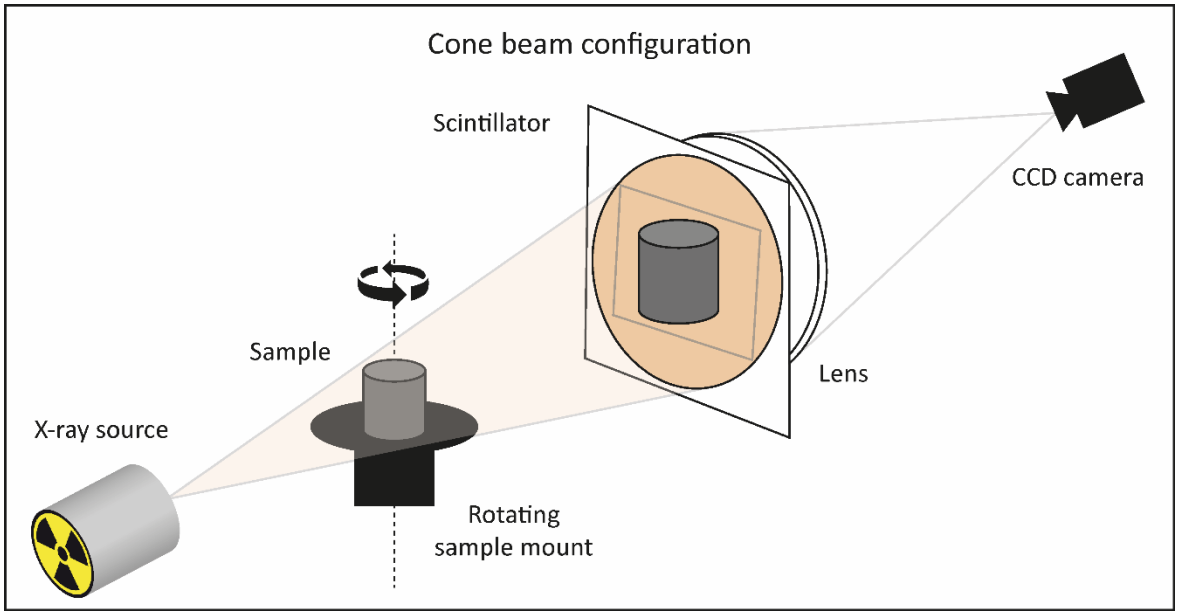

Figure 2.3: Schematic diagram of a typical XCT machine setup.

The two XCT scanners used in this research are:

1. An XRadia/Zeiss VersaXRM 410 microscope operating 150kV transmission micro-focus X-ray source and a detector assembly with a turret of four objectives (0.4X, 4X, 10X and 20X) and a 2k x 2k 16bit CCD X-ray camera (Durham X-ray Centre, Engineering Department, UK).

2. A BP proprietary XCT system operating 160kV transmission nano-focus X-ray source and an amorphous-silicon flat panel detector with 194 µm pixels and 600 µm thick columnar CsI scintillator (Sunbury-on-Thames, UK).

2.8.2 Image processing

Depending on the CT scanner used, the acquired 2D projections (e.g., TIFF slices) were reconstructed, via the means of a back filtered projection, producing a 3D render of the structure of each sample (e.g., pre- and post-reaction) or by using an algorithm that corrects for geometric motion errors via passive auto-focus (Kingston et al. 2011) and iterative reprojection alignment (Latham et al. 2018). Before reconstruction with the back filter projection, the centre of rotation about which the sample has moved, and therefore the reconstruction should be performed, was located by inspecting a series of images of a single 2D slice through the sample, each with a slightly different rotation centre, to identify the clearest image.

For computational efficiency, the collected 3D data were first cropped to remove unwanted regions from the processed volumes. The *Register Images* and *Resample Transformed Image* modules were then used to register and align the initial to the hydrothermally treated cores. The former module provides automatic optimised registration of two 3D renders. An affine transformation to match a reference image (e.g., pre-reaction) to a transformed model image (e.g., post-reaction) is computed using an iterative optimization algorithm that allows the progressive resampling of the data set from coarser to finer quality. *Normalized Mutual Information* was the metric chosen to specify the similarity measure between the two data sets. The latter module allows the registered images to share the same coordination system. *Lanczos* was the interpolation method chosen for the resampling as it is the most accurate method trying to approximate a low-pass filter that is in accordance with the sampling theorem (e.g., a signal can be exactly reproduced if it is sampled at a frequency F, where F is greater than twice the maximum frequency in the signal).

Subsequently, image filtration was applied to reduce image noise and remove potential acquisition artefacts. *Anisotropic Diffusion* is a widely applied image enhancing algorithm filter commonly used for denoising scalar volume data (Wildenschild and Sheppard 2013), which effectively preserves strong edges and enhances their contrast and was used when necessary. Image filtration was not required for the highest resolution data collected.

The image processing workflow was performed in Thermo Scientific Avizo® (v 2019.2). Cylindrical, cubic and cuboid subvolumes were extracted, using the *Volume Edit* module, from the reconstructed CT volumes to perform the segmentation and quantification analysis. Segmentation is the process of labelling voxels based on their grey scale intensity values, belonging to a particular

class or having a particular attribute. In this research, the tomograms were digitally segmented into porosity, grain coating and microporous material volumes. The *Volume Fraction* module was then used to yield the volume percentages of each segmented phase and therefore allowed the quantification of the volumetric alterations induced by the hydrothermal treatment.

High resolution scanning electron microscopy imaging and automated mineralogy mapping were used to support the XCT results and provide a true evaluation of how representative a 2D view of a 3D object is. Detailed information on the segmentation and quantification steps and the 2D to 3D registration are presented in chapter 4 and Appendix A.

2.9 Helium pycnometry and imageJ analysis

A Micromeritics AccuPyc II 1340 pycnometer was used to measure the skeletal volume of the Cook Formation core samples, which was then employed to assess the density and the connected porosity. Quality control of the measured volume was performed using the XCT derived volume of each sample. The gas chosen for the analyses was helium as it allows gas penetration into most of the smallest pores of the samples; it is chemically inert and with a smaller kinetic radius (260 ppm) compared to other gases. Porosity was calculated using the following equation:

$$\Phi = \left(1 - \frac{\rho_b}{\rho_{gr}}\right) * 100\% \quad (1)$$

Where ρ_b is the bulk density measured of a calculated volume and mass, and ρ_{gr} is the measured grain density for each sample.

Additionally, 2D porosity was measured using selected backscatter SEM images and the digital image analysis technique, jPOR (Grove and Jerram 2011).

2.10 Porosity modelling and permeability simulations

The XCT-captured 3D geometry of the pore phase of the hydrothermally treated samples was further used to construct pore network models and computationally simulate fluid flow to determine permeability. Namely, a topologically equivalent network of the pores and throats from the 3D XCT images was extracted based on the maximum ball concept (Silin et al. 2003; Silin and Patzek 2006; Dong et al. 2007), providing quantitative information regarding the coordination number (e.g., number of throats connected to a given pore), radius, area, and volume of each pore as well as the radius and length of each throat. Single-phase flow simulations of the interconnected porosity phase were computed via the implementation of the finite volume method (Harlow and Welch 1965) and Stokes equations. The Stokes equations are given by:

$\nabla \cdot u = 0$ (2)

$\mu \nabla^2 u - \nabla p = 0$ (3)

$u = 0$ on grains (4)

Where p is the pressure (Pa), $\mu = 1x10^{-3}$ Pa.s is the viscosity of water, u is the fluid velocity vector ($m.s^{-1}$), and ∇ indicates the gradient differential operator.

Permeability (k) is obtained by the application of Darcy's Law:

$$k = -Q \frac{\mu}{\Delta P} \frac{L}{A} \quad (4)$$

Where ΔP is the gradient of pressure applied to the boundary (input pressure - output pressure), A is the cross-sectional area (m^2), and L is the length of the computational domain. More information on the porosity network and permeability models are presented in chapter 4 and Appendix A.

Chapter 3: Experimental study of chlorite authigenesis and influence on porosity maintenance in sandstones

This chapter has been published in the Journal of Sedimentary Research (JSR):

Charlaftis, D., S. J. Jones, K. J. Dobson, J. Crouch, and S. Acikalin (2021), Experimental study of chlorite authigenesis and influence on porosity maintenance in sandstones, *Journal of Sedimentary Research*, *91*, 1-16, doi:10.2110/jsr.2020.122.

3.1 Summary

Chlorite is recognised as a key mineral for preserving reservoir quality in deeply buried sandstones, as chlorite coats inhibit the nucleation of quartz overgrowths. A limited understanding of the mechanisms and conditions under which these authigenic chlorite coats form prevents the accurate forward modelling of diagenesis and limits reservoir quality models critical to a wide range of geoscience applications. We present experimental data that show how authigenic chlorite grain coats preserve porosity in deeply buried sandstone reservoirs, using a series of hydrothermal reactor experiments to simulate quartz cementation and capture the evolving porosity. To simulate reservoir evolution, berthierine-bearing sandstone samples (Lower Jurassic Cook Formation, Oseberg Field, 30/6-17R, Norway) were exposed to a silica-supersaturated Na_2CO_3 (0.1 M) solution for 72 hours at temperatures of between 100 and 250 °C. Quantification of the temperature-dependent changes in the volume of authigenic chlorite, the thickness and coverage of the clay coats, and the sample porosity shows increases in chlorite volume (from ~ 2% to ~ 14%). This occurs by the transformation, of patchy amorphous berthierine into grain-coating Fe-chlorite cements through a mixture of the solid-state transformation and dissolution-precipitation mechanisms, siderite replacement, and direct precipitation on clay-free surfaces. With increasing temperature, the chlorite coats increase from ~ 3.8 µm to ~ 5.4 µm thick and expand their grain surface coverage from ~ 28% to ~ 50%. The face-to-edge and face-to-face foliaceous structure of the clay coats produced are morphologically similar to those observed in deeply buried sandstones. Only above the experimental temperatures of 175 °C is porosity preserved as a consequence of inhibition of quartz overgrowths and the generation of secondary porosity.

Our quantitative approach enhances our knowledge regarding the temperature and mineral precursor influence on chlorite-coat authigenesis and therefore provides key insight for chlorite grain coats for reservoir potential in sedimentary sequences greater than 2.5 km.

3.2 Introduction

Quartz cementation is a major cause of porosity reduction in deeply buried sandstone reservoirs, typically initiating at temperatures of 80-100 °C and reducing both porosity and permeability during progressive burial (McBride 1989; Bjørlykke and Egeberg 1993; Worden and Morad 2000). However, quartz precipitation can be inhibited by the prior growth of grain coats forming a barrier that prevents widespread nucleation of quartz. Grain coats, such as chlorite, illite–chlorite, smectite, illite, and microcrystalline quartz (Bloch et al. 2002; Worden and Morad 2003; Worden et al. 2018a) are the most effective at limiting extensive quartz cementation in sandstones. Authigenic grain-coating chlorite has the tendency to form continuous layers that line the interface between

detrital grains and intergranular pore space. The completeness of coverage of chlorite grain coats is considered the principal factor dictating the effectiveness of quartz cement inhibition (Ajdukiewicz and Lander 2010; Ajdukiewicz and Larese 2012; Dowey et al. 2012). Chlorite has been the subject of many diagenetic studies where the importance of clay coats in limiting porosity loss due to quartz cementation has been recognized (Ehrenberg 1993; Ehrenberg et al. 1998; Jahren et al. 1998; Anjos et al. 2003; Berger et al. 2009; Dutton et al. 2018; Stricker and Jones 2018).

The development of authigenic chlorite coats during burial is dependent on chlorite precursor clay minerals, such as 7 Å clays (Ehrenberg 1993), trioctahedral smectites (McKinley et al. 2003), swelling chlorites (Humphreys et al. 1989), and kaolinite-series minerals (Moraes and De Ros 1992). Berthierine, the precursor mineral present in the samples used here, is an aluminous, Fe^{2+}-rich, 1:1 clay belonging to the kaolinite-serpentine series, often present in marginal marine sediments such as deltaic and estuarine deposits and Fe-rich sedimentary rocks (Bhattacharyya 1983; Hornibrook and Longstaffe 1996; Morad et al. 2010). Berthierine occurs as small lath-shaped grain coats (fringes or tangentially arranged), crystals, as pellets, ooids, and void fillings (Worden and Morad 2003). Apart from clay precursors, the destabilization of eodiagenetic ferroan carbonates, such as siderite, can also produce authigenic chlorite at temperatures > 120 °C (Curtis et al. 1985).

The role of high temperatures (> 100 °C) in controlling authigenic chlorite coats on detrital quartz grains has been determined experimentally, with increases in individual chlorite crystal size and thickness (c-axis) observed from 90 to 220 °C (Hillier 1994), and more efficient prevention of quartz growth at temperatures above 115°C (Ajdukiewicz and Larese 2012). Hydrothermal experiments replicating burial diagenesis qualitatively showed that thin, discontinuous, poorly crystalline berthierine coats will start to recrystallize to chamosite at about 70 °C (Aagaard et al. 2000). An interstratification phase occurring between 70 and 160 °C (Jahren and Aagaard 1989), and the conversion is thought to be complete above 160 °C (Iijima and Matsumoto 1982). Ajdukiewicz and Larese (2012) have shown that the effectiveness of clay coats at preserving porosity depends on temperature and the continuity of the coat based on experimental evidence. Grain-coating clay minerals can form on clean quartz and feldspar surfaces at 100 and 150 °C, given sufficient supersaturation and time (Haile et al. 2015).

In this study, a multi-method approach comprising a series of temperature-controlled hydrothermal reactor experiments on sandstone samples from the Lower Jurassic Cook Formation of the Oseberg Field, Norway (30/6-17R), was carried out. An artificial solution and silica granules were used to maintain silica-saturated conditions during each experimental run. Mineralogical evaluation, using X-ray diffraction (XRD), scanning electron microscopy (SEM) and energy-dispersive X-ray

spectroscopy (SEM-EDS), and automated quantitative mineralogy (AQM), has been undertaken to simulate and quantitatively assess berthierine-to-chlorite transformation, grain-coating chlorite authigenesis, cementation, and diagenesis of the sandstone samples. The experimental results complement previous studies on chlorite synthesis (Aagaard et al. 2000) and provide important insights into the role played by precursor clays, temperature, and Fe-rich minerals, such as siderite, upon chloritization processes, decline of quartz precipitation, and subsequent preservation of reservoir quality.

3.3 Materials and Methods

3.3.1 Sampling

Naturally occurring sandstone samples were obtained from core material from the Lower Jurassic Cook Formation of the Oseberg Field (Norway, Well 30/6-17R). The Cook Formation lies stratigraphically in the Dunlin Group (Pliensbachian–Toarcian) and is extensively distributed in northern North Sea. Polished blocks, rock chips, and core plugs (4 mm diameter and length varying between 5 mm and 9 mm) were taken from a prograding subtidal sand body (Livbjerg and Mjøs 1989) at a depth of 7988.18 ft. (2434.8 m), selected for the high content of berthierine and siderite.

3.3.2 Hydrothermal reactor experiments

Hydrothermal reactor experiments were carried out in a Parker Autoclave Engineers 500 ml cylindrical 316 stainless steel pressure vessel with an all-metal seal configuration operating at temperatures up to 350 °C. The vessel was heated by a ceramic band heater and, during the experiments, temperature was controlled within ± 0.5 °C through a Eurotherm© PID temperature controller. Six core plugs were subjected to hydrothermal treatment at specific temperature steps under strictly closed conditions (Table 3.1).

Experiment	Sample	Solution (M)	Temperature (°C)	Duration (h)
1	Sst + silica gel	0.1 Na_2CO_3	100	72
2	Sst + silica gel	0.1 Na_2CO_3	150	72
3	Sst + silica gel	0.1 Na_2CO_3	175	72
4	Sst + silica gel	0.1 Na_2CO_3	200	72
5	Sst + silica gel	0.1 Na_2CO_3	225	72
6	Sst + silica gel	0.1 Na_2CO_3	250	72

Table 3.1: Experimental conditions for the hyrothermal reactions. The sandstone (Sst) samples are from the the Lower Jurassic Cook Formation of the Oseberg Field (Norway, Well 30/6-17R).

For all the experimental runs, silica gel granules and an aqueous solution of 0.1 M Na_2CO_3 (reagent grade) dissolved in high-purity water (Milli-Q) were used as a source of silica and pore fluid, respectively. The experimental setup is depicted in Figure 3.1A. In each experiment, five grams of silica gel and one core sample were enclosed in two different 50 µm stainless steel meshes. The meshes were then attached to the bottom of the sample holder (Figure 3.1B), using stainless-steel wire, and the sample assembly was lowered into the pressure vessel. The vessel was gradually filled with 300 ml of 0.1 M Na_2CO_3 solution (giving 200 ml headspace at room temperature), sealed and heated to the experimental temperature at 2.5 °C per minute. All samples were held at the desired experimental temperature for 72 hours before the heater was switched off. Once cooled to room temperature, the vessel was removed from the reactor, and the sample was removed and air-dried.

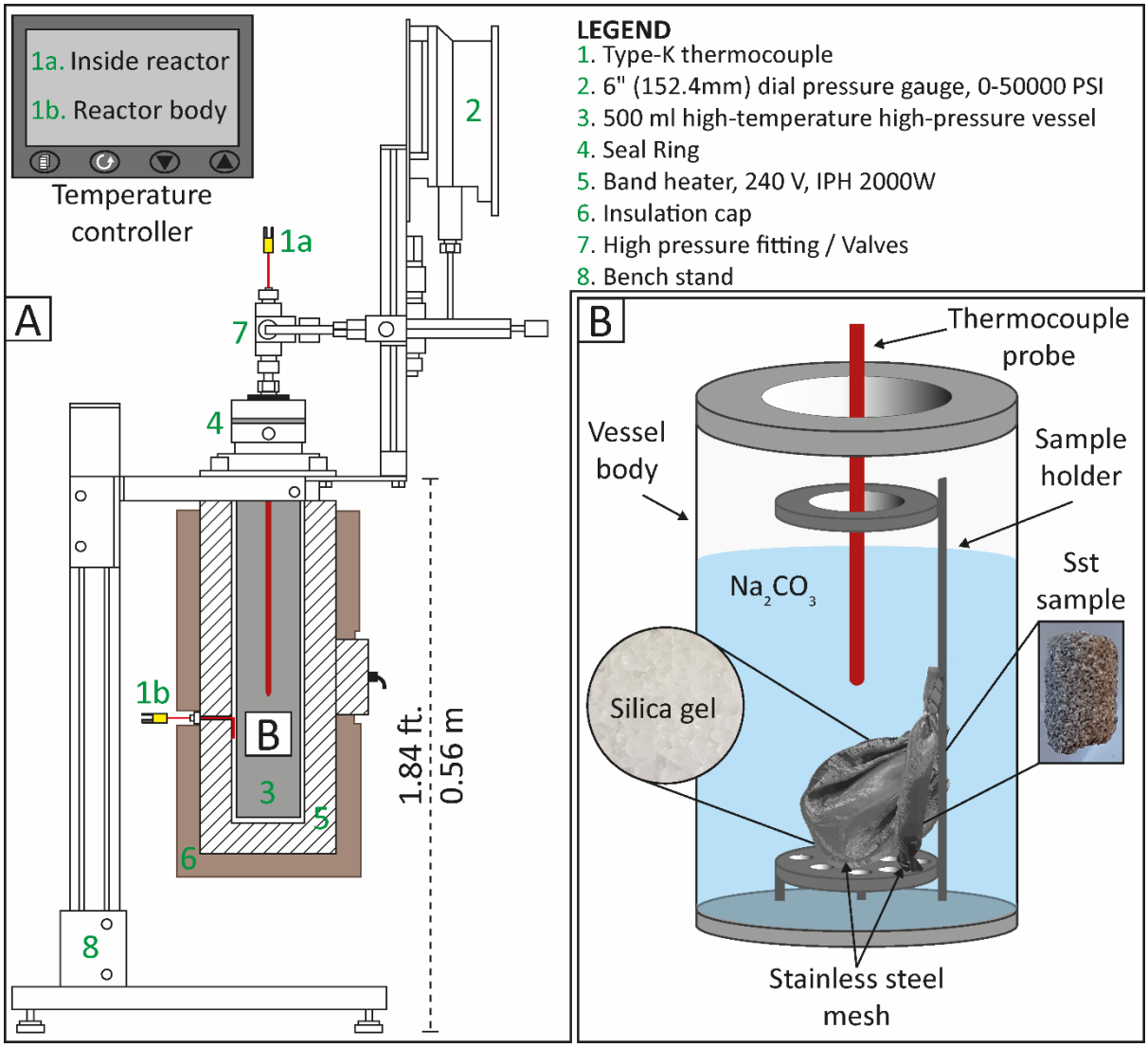

Figure 3.1: Illustration of the experimental setup. A) Schematic representation of the hydrothermal vessel and its main parts utilized for the diagenesis experiments. The system comprises solely stainless-steel components and a Eurotherm temperature control. B) The interior of the hydrothermal vessel. Approximately 2/3 of the vessel is filled with Na_2CO_3. The meshes including the silica gel and the sandstone sample are attached to the bottom of the sample holder.

Natural diagenetic conditions cannot be fully reproduced in the laboratory due to the short experimental time compared to a geological timeframe and the simplification and uncertainties associated with the chosen aqueous chemistry. The experimental conditions used are chosen based on the following assumptions:

1. The experiments were conducted under zero-flow conditions mimicking a closed-system geological model. Grain-coating chlorites are likely to develop from closed-system diagenesis at the bed scale (Worden et al. 2020).

2. The artificial solution was selected so as to be nonreactive (e.g., Fe-free chemical composition) with the Fe-rich minerals and to provide CO_2 pressures of 0.2–1 bar, typical for sedimentary systems in the North Sea (Aagaard and Egeberg 1998). Additionally, chlorite is preferentially stable under alkaline solutions (White et al. 1942).

3. Quartz dissolution is evident in many alkaline diagenetic environments (Pichat et al. 2016; Li et al. 2020). Experimental studies on quartz dissolution indicate that dissolution rates increase as the pH increases into the alkaline region (Knauss and Wolery 1988; Crundwell 2017). Additionally, the use of a 0.1 M Na_2CO_3 solution coupled with a source of silica can generate strong quartz-cementing conditions as shown by previous hydrothermal experiments investigating cement growth-limitation mechanisms (Ajdukiewicz and Larese 2012). The silica-saturated solution promotes the precipitation of quartz cement; simulating the mechanical compaction that would drive quartz cementation even when compaction cannot be performed during the experiments.

4. Prior research has shown that the applied experimental duration and temperatures are adequate to stimulate growth of clay coats and quartz cement (Small et al. 1992; Aagaard et al. 2000; Ajdukiewicz and Larese 2012). The initial temperature of 100 °C was selected to exceed the commonly accepted threshold of 80 °C for quartz cementation (Walderhaug et al. 2000; Lander et al. 2008) and the threshold of 60 °C proposed for berthierine-to-chlorite transformation (Ehrenberg 1993; Worden and Morad 2003).

3.3.3 Analytical Techniques

3.3.3.1 Sample mineralogy

The clay mineralogy of the initial natural sample was determined by X-ray powder diffraction (XRD). Bulk rock samples were de-oiled, disaggregated, and powdered to a mean particle diameter of 5–10 μm, and the mineralogy was analysed using a Philips PW1730 Generator (copper anode at 40

kV, 40 mA), a PW1050 Goniometer with graphite monochromator, and a PW1170 automatic sample changer. The bulk mineralogy analysis was performed at 2θ (theta) angles = 4.5˚–75˚ (step size of 0.06˚/s). The clay fraction (< 2 µm fraction) was separated from the bulk rock using ultrasound and centrifugation. Analysis of the clay fraction analysis allowed the quantification of the clay mineral components. A 25 ml aliquot of the clay suspension was evaporated to dryness at 80 °C, and the total weight was determined. The samples were analysed as an untreated clay, after saturation with ethylene glycol vapour overnight and heated at 380 ˚C for 2 hours and 550 ˚C for 1 hour. The samples were then analysed at 2θ = 3˚–35˚ (step size of 0.05˚ per second). The untreated clays were also analysed at 2θ = 24˚–27˚ (step size of 0.2˚/2 s) to further define kaolinite and chlorite peaks. Identification of the clay-mineral assemblages was performed by overlaying the diffractograms from the four clay treatments. Moreover, as chlorite and berthierine are not readily discriminated, reflections at higher diffraction angles (e.g., d_{060}) were also measured.

An untreated and six hydrothermally treated cores were encapsulated in resin and a circular cross section exposed using diamond polish for SEM examination. The polished blocks were carbon-coated and backscatter (BSE) SEM imaging was carried out on a Hitachi SU-70 FEG SEM scanning electron microscope with an energy-dispersive detector (EDS) (GJ Russell Microscopy Facility, Durham University), at acceleration voltages of 20 kV and measured beam current of 0.6 nA. SEM-EDS was used for rapid elemental identification on randomly selected areas in each polished block sample. In addition, secondary electron (SE) SEM imaging was conducted on an untreated rock chip and a small fraction of rock that was carefully detached from the core plug was subjected to hydrothermal treatment at 250 °C before encapsulation. The gold-coated samples were analysed at an acceleration voltage of 5 kV with a beam current of 1 nA.

AQM was also performed on the polished blocks to quantify the mineralogy and characterize the petrographic relations at each temperature step. A Zeiss Gemini SUPRA 40VP field emission scanning electron microscope coupled with a Bruker XFlash® 60 EDS detector and Mineralogic software suite were used for the EDS spectra acquisition and digital analysis, respectively. Images were collected using a high-resolution raster, with step size of 3.5 µm at a 255x magnification and a 20 kV acceleration voltage. Dwell time was adjusted to capture approximately 20,000 counts per pixel. After differentiating the mineral phases from the epoxy resin by thresholding the grey BSE image before EDS analysis, a mineral-classification library tailored to this research was developed using the initial XRD, SEM-BSE and SEM-EDS analyses. AQM compared the EDS spectra of each point to the library, assigning a specific mineral to each point and producing a mineralogical map.

3.3.3.2 Coat thickness, grain-coat coverage and porosity quantification

ImageJ was used to measure coat thickness from the BSE images at 50 points per sample (± 0.05 µm). The measured thicknesses were binned into four classes: 1) 1–3 µm; 2) 3–5 µm; 3) 5–7 µm, and 4) 5–9 µm, to evaluate any changes in distribution between the different hydrothermal treatments. Grain-coating coverage was quantified using Petrog (Wooldridge et al. 2019), with the percentage perimeter of a grain-coated with clay calculated by measuring its total perimeter and the length covered by attached clay for 50 grains for each of the different hydrothermal treatments. The standard error of the analysis of each sample was ± 2%.

Before the preparation of the polished blocks, each core was imaged using X-ray microtomography to accurately derive the volume of each. Scanning was performed on a Zeiss Xradia VersaXRM 410 scanner (Durham University) operating at 80 kV (no beam filtration). All samples were imaged with a spatial resolution of 3.8 µm/voxel (3D equivalent of a pixel). Subsequently, each core was subjected to helium pycnometry analysis on a Micromeritics AccuPyc II 1340 pycnometer and, by using the micro-CT-derived volume, numerical porosity data were generated. In addition, 2D porosity was extracted by the SEM-BSE image of each polished block using the digital image-analysis technique, jPOR (Grove and Jerram 2011).

3.4 Results

3.4.1 Mineralogical evaluation of the Cook Fm prior to the hydrothermal experiments

The composition of the Cook Formation comprises medium- to fine-grained, moderately sorted, angular to subangular grains. EDS elemental mapping illustrates the increased iron content in the sample (Figure 3.2). Bulk X-ray diffraction analysis suggests the dominance of quartz as a primary mineral, with kaolinite and berthierine being the clay minerals, and siderite the main carbonate mineral identified. The clay-fraction analysis proves that berthierine is the main Fe-rich clay in the sample. Chlorite occurs in traces only (Table 3.2).

Minerals	Ill–Sme	Kln	Chl	Be	Qtz	Mca	Kfs	Plg	Cal	Dol	Sd
Bulk	TR	8.9	0.0	11	48	6.9	4.8	3.1	1.2	0.9	15.6
< 2µm	TR	70/W	TR/P	29/P	1	-	-	-	-	-	-

Table 3.2: Bulk rock and clay fraction (< 2 µm) XRD results for the Cook formation sandstone samples (Well 30/6-17R, 2434.8 m) with the crystallinity of the clay minerals (TR = trace; W = well crystallized; P = poorly crystallized). Data are reported in weight %. Where Be = berthierine; Cal = calcite; Chl = chlorite; Dol = siderite; Ill = illite; Kfs = k-feldspar; Kln = kaolinite; Mca = mica; Plg = plagioclase; Qtz = quartz; Sme = smectite; Sd = siderite.

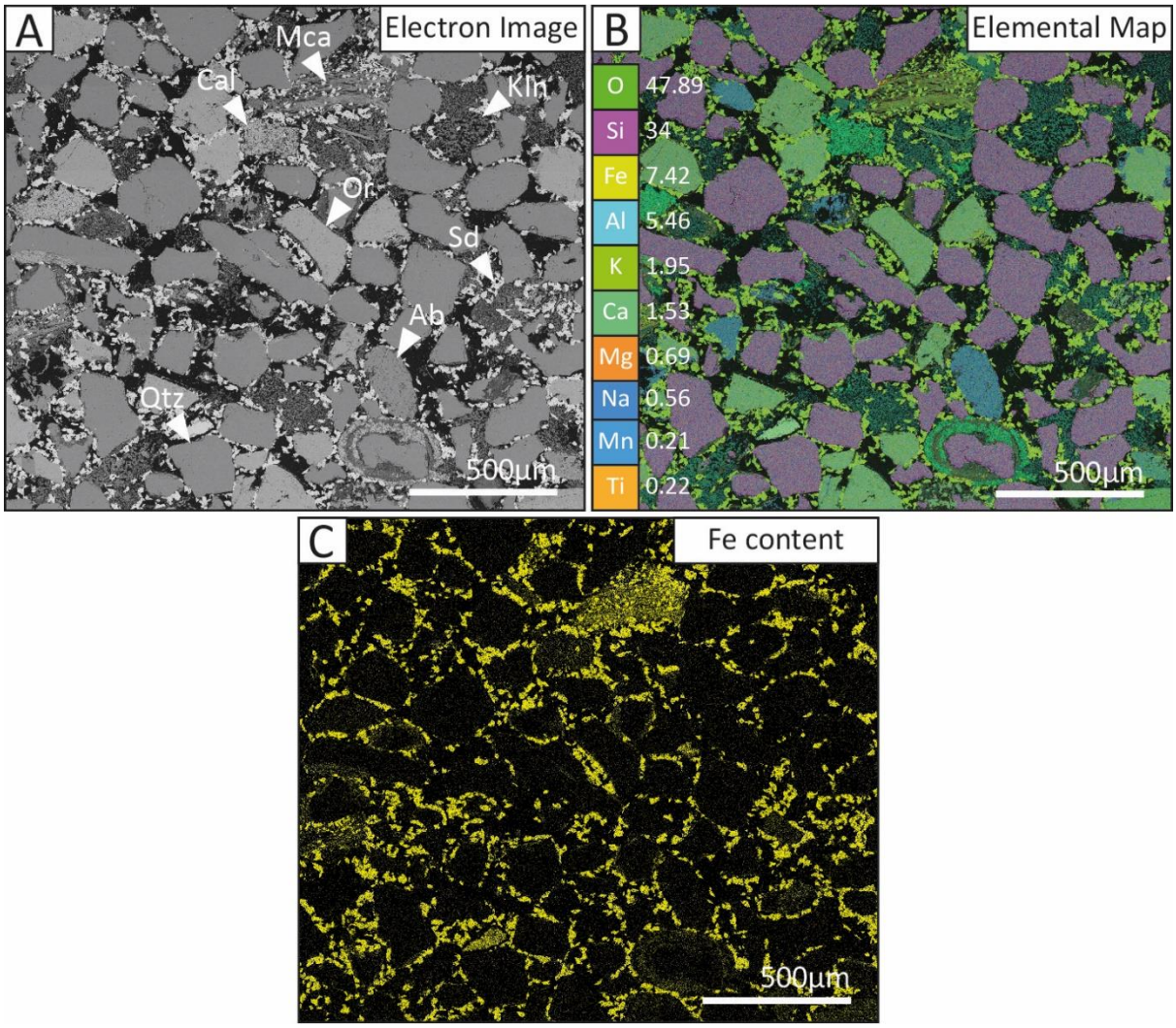

Figure 3.2: EDS elemental analysis of the Cook Formation (Well 30/6-17R, 2434.8 m). A) Montaged electron image of the analysed sample. Where Ab=albite; Cal = calcite; Kln = kaolinite; Mca = mica; Or = orthoclase; Qtz = quartz; Sd = siderite. B) Elemental distribution. Data reported in weight per cent. C) Increased iron content, important for chlorite precipitation.

Figure 3.3A shows the overlaid diffractograms after the various chemical and heat treatments. Kaolinite has its 001 peak at 12.39° 2θ, chlorite has its 002 peak at 12.29–12.55° 2θ, and berthierine has the 001 peak at 12.52° 2θ. The 002 peak of kaolinite is at 24.9 °2θ, the 004 peak of chlorite is at 25.1–25.2° 2θ, and the 002 peak of berthierine is at 25.2° 2θ. The presence of a peak at 12.40° 2θ after the heat treatment at 550 °C for one hour is proof of the presence of kaolinite. The presence of trace of chlorite is shown by the peak at 6.3° 2θ after the heat treatment at 550 °C. The presence of berthierine is indicated by the reduction of intensity of the peak at 25.2° 2θ after the heat treatment at 380 °C for two hours. Additionally, the d_{060} reflection value for kaolinite is about 1.490 Å (62.31° 2θ), for chlorites is about 1.538-1.549 Å (60.15-59.69° 2θ) and for berthierine is about 1.555 Å (59.44° 2θ) (Figure 3.3B). No other clay mineral has its d_{060} peak in this position (Bailey 1980).

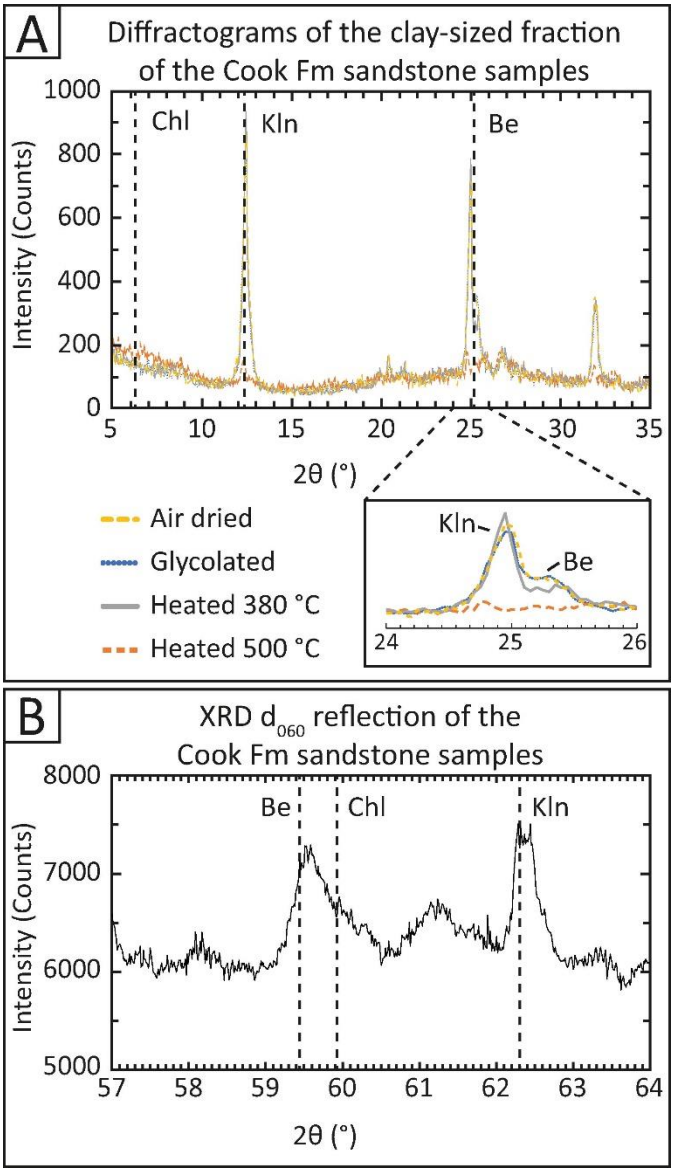

Figure 3.3: Representative XRD patterns of the Cook Formation (Well 30/6-17R, 2434.8 m) verifying the presence of berthierine. Where Be = berthierine; Chl = chlorite; Kln = kaolinite. A) Overlaid diffractograms of the < 2 mm fraction after the various chemical and heat treatments. The presence of berthierine is indicated by the reduction of intensity of the peak at 25.2° 2ϑ after the heat treatment at 380° C for 2 h. B) XRD d060 reflection allowed the discrimination between chlorite and berthierine. The d060 value for berthierine is about 1.555 Å (59.44° 2ϑ).

Three forms of berthierine were distinguished based on their morphological characteristics. 1) Thick concentrically laminated ooidal coats with thickness ranging from 10 to 50 µm (Figures 3.4A). 2) Thin, patchy and discontinuous grain coats covering detrital grains with an average thickness of 3.6 µm (Figures 3.4B). The thickest expressions have been preferentially observed in grain indentions. 3) Pore-filling material (Figures 3.4D).

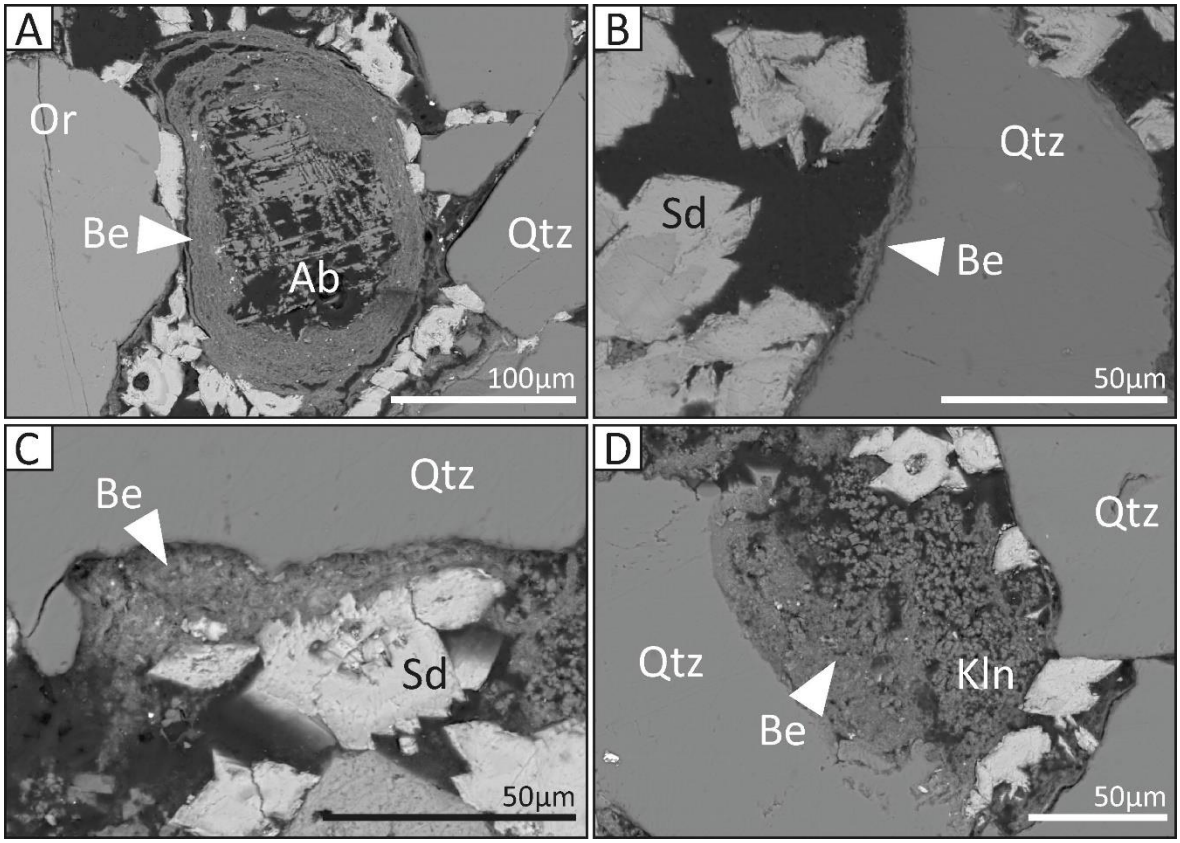

Figures 3.4: Backscattered electron images (BEIs) showing the different types of berthierine in the sandstone reservoir interval of the Cook Fm (Well 30/6-17R, 2434.8 m). Where Ab = albite; Be = berthierine; Kln = kaolinite; Qtz = quartz; Sd = siderite. A) Ooids made up of concentrically laminated berthierine accreted on a dissolving albite grain. B) Berthierine grain coat. C) Berthierine predates siderite grain coat precipitates. D) Pore filling berthierine and kaolinite booklets.

Quartz, orthoclase, albite, and Ti-rich grains have been observed at the centre of the ooidal structures acting as nucleus grains. In this case, berthierine identified at the outer cortex of the ooid shows a fibrous texture. In contrast, the patchy berthierine coats comprise a network of poorly developed, flake-shaped crystals (Figure 3.5B) lying subparallel to the surface of the host grains. Edged surfaces and cavities appear to favour the presence of berthierine. Quartz-overgrowth development and siderite cement are associated with these coats (Figure 3.5A). Finely crystalline (< 50 µm) siderite occurs on the rims of framework grains postdating berthierine precipitates (Figures 3.4C). Crystals lying directly on host grain surfaces are also common. Crystal habit includes lozenge-shaped isolated crystals (Figure 3.5D), and aggregates of those. Berthierine is associated with kaolinite (Figure 3.5C), the main pore-filling material identified. Kaolins present face-to-face stacks of thin, irregular, pseudohexagonal plates with ragged edges. Microporosity is visible in the pore filling.

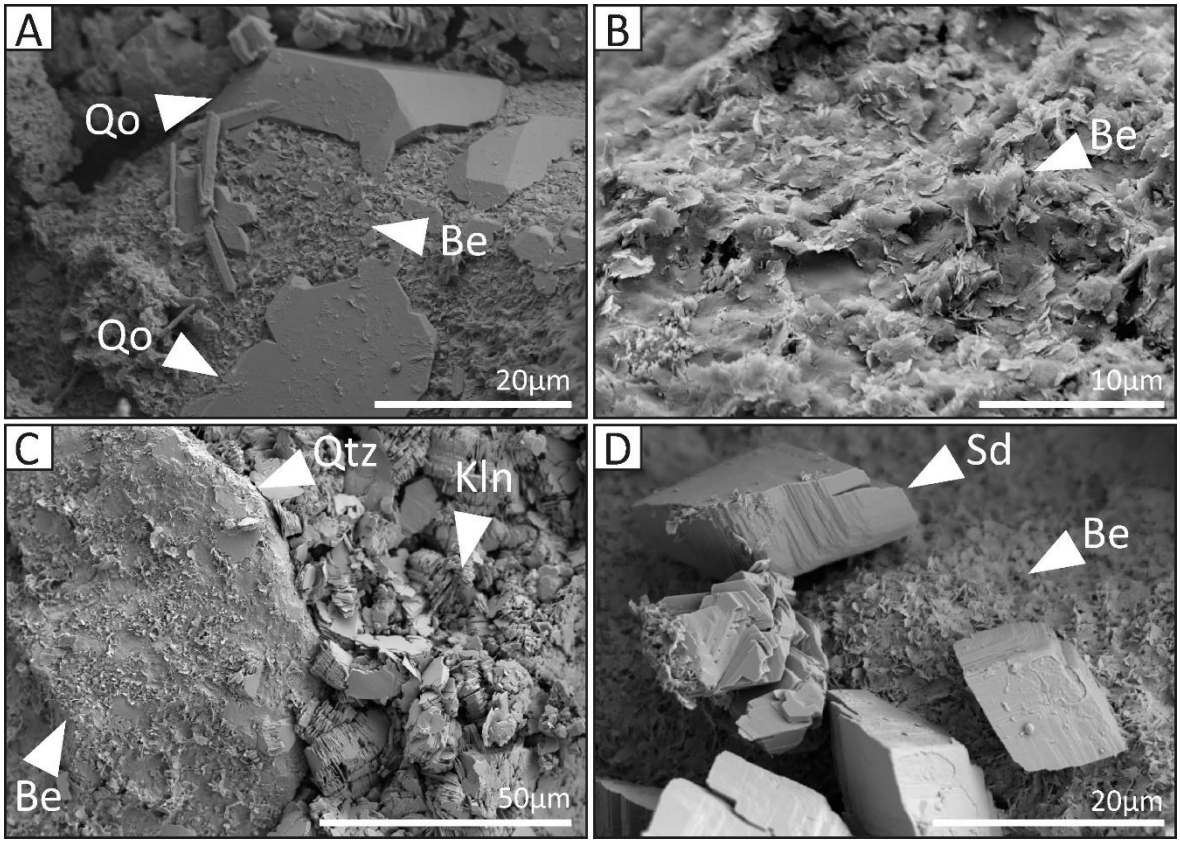

Figure 3.5: SEM images illustrating the grain-coating nature of berthierine before the hydrothermal experiments. Where Be = berthierine; Kln = kaolinite; Qo = quartz overgrowth; Qtz = quartz; Sd = Siderite. A) Quartz overgrowths interacting with grain-coating berthierine. B) Flake-shaped berthierine detrital crystals. C) Quartz grain partly covered by patchy, discontinuous berthierine coat. D) Siderite growth post-berthierine precipitation but closely associated.

The applied automated mineralogy technique allowed collection of chemical data across each sample. The EDS spectra of each analysed point were automatically compared to the newly developed mineral classification that includes the pre-defined chemical compositions of each mineral observed throughout the experimental steps. The sandstone can be classified as subarkosic, comprising, by weight, approximately 54% quartz. Orthoclase is the most common alkali feldspar (~ 11%) and albite the most common plagioclase (~ 5%). In agreement with the XRD results, kaolinite (~ 9%) and berthierine (~ 6%) are the most abundant clay minerals, while siderite (~ 8%) the most common carbonate cement. This technique also identified small amounts of chlorite (< 2%).

SEM-EDS and AQM analysis was performed on core samples, taken from locations adjacent to the ones used for the hydrothermal experiments, to evaluate the significance of the compositional variability of the pre-reaction material. The analysis was performed both perpendicular (e.g., sample 1) (Figure 3.6A) and longitudinal (e.g., sample 2) (Figure 3.6B) to the long axis of the cores and suggests a consistent elemental and mineral distribution (Tables 3.3, 3.4 and 3.5).

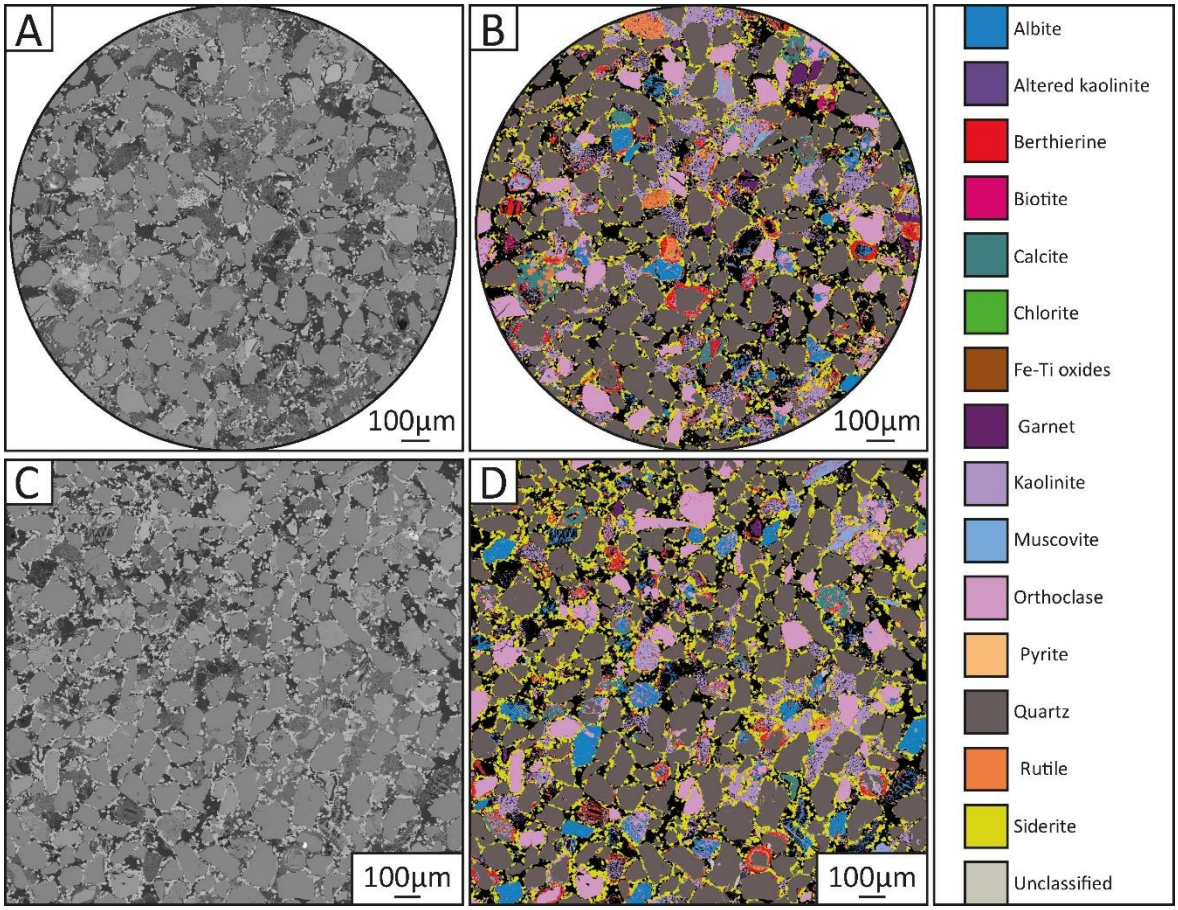

Figure 3.6: Backscattered electron images (BEIs) of the Cook Formation core material, before the hydrothermal treatment, with associated AQM analysis. A) SEM image taken from a circular surface perpendicular to the long axis of the analysed core. B) Mineral map of (A) showing the increased content of berthierine, kaolinite and siderite. C) SEM image taken from a planar surface longitudinal to the long axis of the analysed core. D) Mineral map of (C). Note the absence of chlorite.

The use of the same mineral classification library for the AQM analysis of all the experimentally treated samples, and not one tailored per experimental run, was required to capture the evolution of berthierine and chlorite content with increasing temperature. To achieve that, the developed library allowed minor quantities of extraneous elements to be present in the chemical structure of mineral phases, which are not normal constituents of the reported mineral. For example, quartz presents minor impurities (<1%) of Fe, K and Al with values of 0.15, 0.05 and 0.05 respectively, and the composition was used for all experimental runs and maintained consistency with AQM analysis.

For each mineral included in the classification list, the range of the tolerated concentrations for each element, as well as for ratios between two elements, were used to define the mineral phase. The mineral recipe used for this research, including the chemistry criteria (e.g., element concentration of each mineral), is presented in Appendix A (Table A.1).

Sample 1 (Perpendicular to the long axis)		
Mineral	**Weight %**	**Assigned Composition**
Quartz	52	O 50.75; Si 48.99; Fe 0.15; K 0.05; Al 0.05;
Kaolinite	12	O 49.22; Si 25.11; Al 24.86; Fe 0.69; K 0.1; Ca 0.02; Na 0.01; Mg 0;
Orthoclase	11	O 45.02; Si 29.03; K 14.39; Al 10.89; Fe 0.33; Na 0.27; Ba 0.07; Ca 0;
Siderite	6.8	Fe 53.2; O 44.39; Si 2.41;
Berthierine	6.4	O 39.51; Fe 21.42; Si 20; Al 16.84; K 1.2; Mg 0.88; Ca 0.15;
Albite	3.6	O 45.82; Si 32.19; Al 12.04; Na 9.69; Ca 0.24; K 0.01; Mg 0;
Rutile	2.4	Ti 50.96; O 49.04;
Chlorite	1.7	O 39.98; Si 37.7; Fe 17.01; Al 3.81; Na 0.58; Mg 0.41; Ca 0.34; K 0.17;
Biotite	1.4	O 40.76; Si 25.95; Fe 13.18; Al 11.93; K 6.97; Mg 1.21;
Muscovite	1.2	O 44.36; Si 24.82; Al 16.99; K 7.32; Fe 6.13; Mg 0.38;
Calcite	0.9	O 55.57; Ca 44.43;
Garnet	0.6	O 41.3; Fe 20.85; Si 17.05; Al 12.13; Ca 5.26; Mg 3.4;
Pyrite	0.1	Fe 51.62; S 48.38;

Table 3.3: Modal mineralogy of sample 1 shown in Figures 3.6A–B

Sample 2 (Longitudinal to the long axis)		
Mineral	**Weight %**	**Assigned Composition**
Quartz	55	O 50.14; Si 49.6; Fe 0.16; K 0.08; Al 0.03;
Kaolinite	6.7	O 49.42; Si 24.91; Al 24.9; Fe 0.67; K 0.09; Na 0; Ca 0; Mg 0;
Orthoclase	11	O 44.53; Si 29.64; K 13.87; Al 11.19; Fe 0.4; Na 0.33; Ba 0.03;
Siderite	9.6	Fe 53.04; O 45.33; Si 1.63;
Berthierine	5.0	O 39.69; Fe 21.94; Si 19.68; Al 16.32; K 1.31; Mg 0.89; Ca 0.17;
Albite	6.0	O 45.58; Si 32.34; Al 12.09; Na 9.79; Ca 0.2; K 0;
Rutile	0.5	O 50.36; Ti 49.64;
Chlorite	1.8	O 40.9; Si 36.55; Fe 16.98; Al 3.55; Na 0.94; Ca 0.46; Mg 0.46; K 0.16;
Biotite	1.3	O 41.52; Si 28.63; Al 12.28; Fe 10.42; K 6.51; Mg 0.64;
Muscovite	2.0	O 45.1; Si 24.39; Al 16.25; K 7.9; Fe 6.01; Mg 0.35;
Calcite	0.5	O 57.27; Ca 42.73;
Garnet	0.6	O 40.95; Fe 22.93; Si 17.56; Al 12.16; Ca 3.48; Mg 2.92;
Pyrite	0.1	Fe 52.39; S 47.61;

Table 3.4: Modal mineralogy of sample 2 shown in Figures 3.6C–D.

Elements	Sample 1	Sample 2
O	61.98	63.35
Si	22.47	25.76
Al	6.97	3.64
Fe	2.87	3.39
K	2.5	1.18
Ca	1.95	0.93
Mg	0.48	0.86
Na	0.41	0.56
Ti	0.15	0.11
S	0.09	0.08
Mn	0.08	0.08
Cl	0.05	0.07
Total	100	100

Table 3.5: SEM-EDS elemental analysis of the Cook Formation (Well 30/6-17R, 2434.8 m) prior to the hydrothermal treatment (samples 1 and 2). All data are reported in atomic %.

3.4.2 Post-experiment mineralogical evaluation

3.4.2.1 Berthierine-to-chlorite transformation

The focus of the AQM analysis was to identify, separate, and quantify berthierine and chlorite phases at each experimental step. Berthierine and chlorite have similar chemical compositions, hence potential minor differences in elemental concentrations are required for the successful distinction between the two. The range of the elemental concentration for the identification of berthierine was determined by collecting EDS spectra from the ooidal and grain-coating structures in the initial sample, where berthierine was present with certainty. Similarly, the chemical signature of chlorite was determined by targeting the neoformed chlorite grain coats in the samples from the higher-temperature experiments. The two chemical compositions showed a subtle difference in the aluminium concentration, which in berthierine and chlorite was ~ 17 wt.% and ~ 5 wt.%, respectively. Previous studies on berthierine formation and chlorite authigenesis also confirm that berthierine is aluminium-rich (Iijima and Matsumoto 1982; Curtis et al. 1984).

The produced mineralogy maps illustrate the high berthierine content at 100 °C (Figure 3.7A) and the elevated chlorite content at 250 °C (Figure 3.7C). There is an increasing contact association between berthierine and chlorite with increasing temperature while the initial strong association of berthierine with pore space is diminishing (Figure 3.7B). Chlorite shows significant contact with

quartz and siderite in each temperature step Figure 3.7D). The declining trend regarding quartz is credited to the increase in chlorite content, therefore associated with more and different minerals.

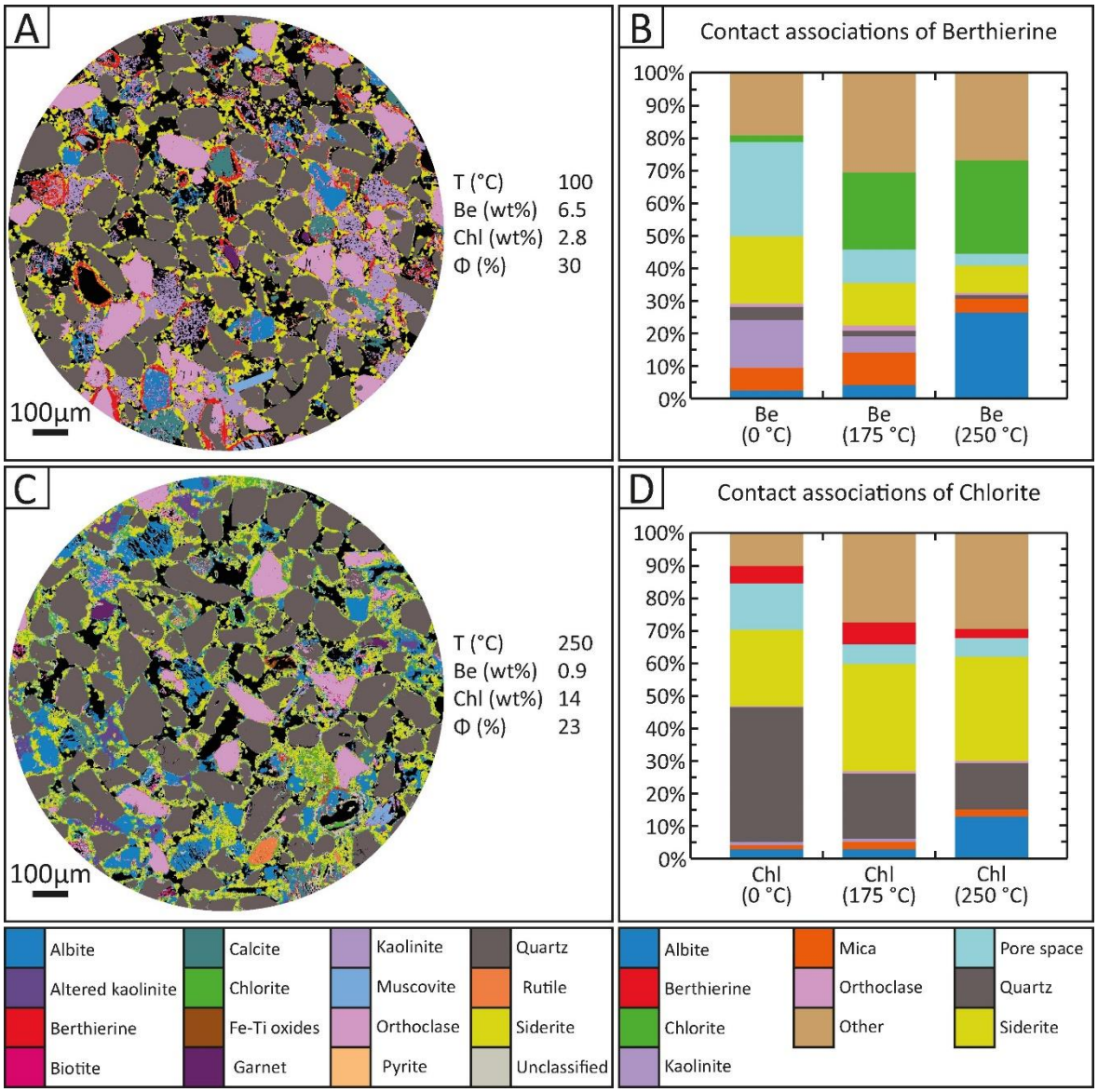

Figure 3.7: Representative automated mineralogy maps and mineral contact associations. Where Be = berthierine; Chl = chlorite; Other = altered kaolinite, calcite, Fe-Ti oxides, garnet, pyrite, rutile, and unclassified. Porosity values are determined via helium pycnometry. A) Mineral map of the sample treated at 100 °C showing that berthierine concentration is higher than that of chlorite. B) Contact association of berthierine with other minerals and pore space. Note the progressive increase in contact association with chlorite. C) Mineral map illustrating the increased chlorite content of the sample treated at 250 °C. D) Contact association of chlorite with other minerals and pore space. The weak contact with pore space and the strong contact with quartz indicate a higher textural occurrence as coats. Note the strong association with siderite, a potential source for authigenic chlorite.

3.4.2.2 Occurrence and morphology of authigenic chlorite

The following petrographic types of authigenic chlorite were observed: 1) grain coats (Figure 3.8A, B), 2) rosette-like clusters on the chloritized surfaces expanding into the pore space Figure 3.8C), and 3) cabbage-head chlorites affixing at the platelets of the grain-coating chlorites (Figure 3.8D).

The grain coats form independently of size and shape of the substrate grains. They consist of euhedral, pseudohexagonal crystals oriented perpendicular to subperpendicular to the grain surfaces with a face-to-edge and face-to-face foliaceous pattern. The less volumetrically significant chlorite rosettes are composed of euhedral platelets in a divergent arrangement. Cabbage-head chlorite aggregates are mainly observed affixing at the surface of well-developed chlorite surfaces. Small amounts are formed directly on the substrate grain surfaces.

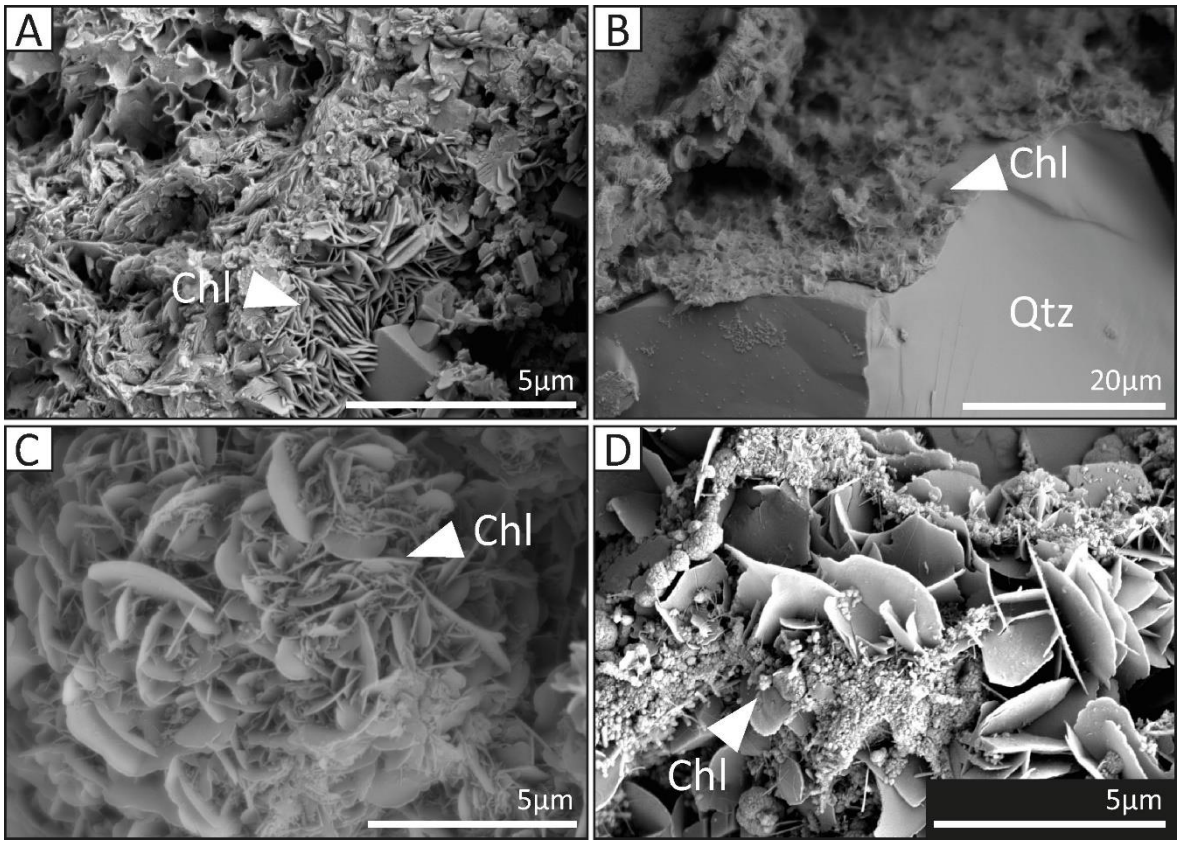

Figure 3.8: SEM photomicrographs showing chlorite precipitation and morphology after hydrothermal treatment at 250 °C. A) Partly tangentially oriented, well-developed authigenic chlorite platelets. B) Chlorite grain coat covering a quartz grain. Chlorite develops in a face-to-edge pattern. C) Rosette-like clusters of chlorite. D) Cabbage-head chlorite surrounding well-developed chlorite crystal plates.

3.4.2.3 Siderite occurrence and chlorite authigenesis

With increasing temperature, siderite crystals display zonation patterns in terms of iron, calcium, and magnesium contents (Figure 3.9A). From core to rim the calcium content is decreasing. A magnesium-enriched zone is present in the middle part of the crystals. Central dissolution voids, containing increased calcium and magnesium concentrations, were mainly observed at temperatures higher than 200 °C (Figure 3.9B). SEM imaging illustrates the partial or complete engulfment of siderite by authigenic chlorite crystals (Figure 3.9C, E) and the presence of calcite crystals beside siderite dissolution voids which most likely acted as seeds for siderite development (Figure 3.9D). Chlorite-coat precipitation was enhanced on host grain surfaces directly next to the

dissolving siderite crystals (Figure 3.9E). Therefore, the thickest authigenic chlorite coats were observed next to siderite crystals whose initial rhombic shape was progressively deformed to rounded crystal faces.

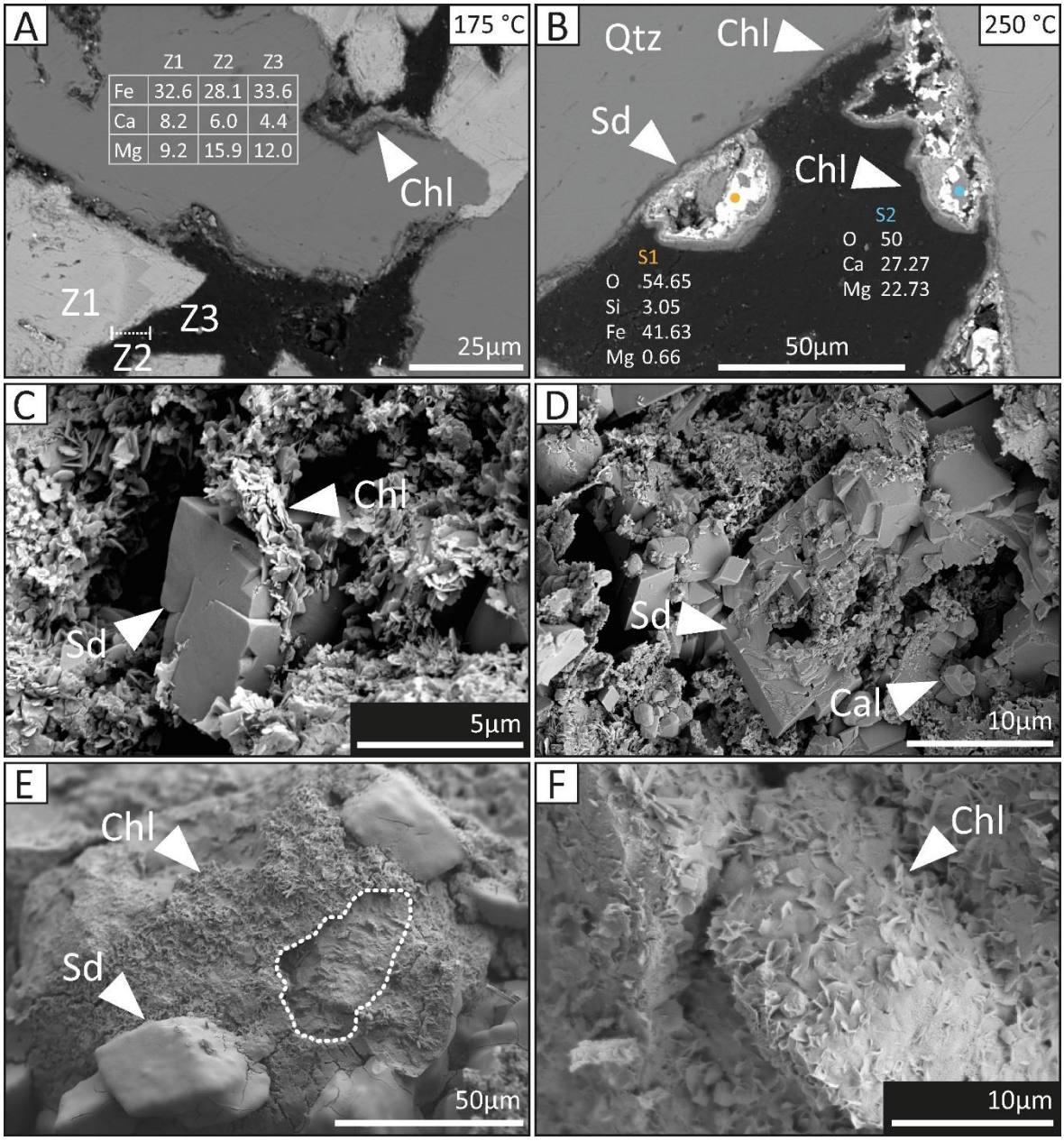

Figure 3.9: Siderite dissolution further promotes chlorite authigenesis. Where Cal = calcite; Chl = chlorite; Qtz = quartz; Sd = siderite. Data reported in atomic per cent normalized to oxygen by stoichiometry. A) As experimental temperature increases and dissolution progresses, zonation of siderite due to variations in the Ca, Mg, and Fe content becomes more evident. B) Siderite dissolution and chlorite precipitation around margins of pore space. Chlorite-coat precipitation on the rim of the dissolved crystals. Brighter colour in the dissolved crystal represents Fe-dominated areas. Note the increased calcium and magnesium content in the central parts of the crystals as determined by SEM-EDS analysis. C) Chlorite partly engulfing a siderite crystal. D) Siderite crystal undergoing dissolution, hence the hollow cores. Note the presence of calcite crystals, which possibly acted as seeds for siderite development. E) Chlorite precipitation due to siderite decomposition. Note the progressive loss of the rhombohedral morphology of the siderite crystals. The dashed frame corresponds to the outline of a dissolved siderite crystal. F) Authigenic chlorite completely covering a siderite crystal.

3.4.2.4 Quartz cement and other diagenetic alterations

The abundance of quartz in each sample, pre- and post-experiment, remained constant at ~ 50%. Replacement of kaolinite by dickite was recognized by the gradual coarsening and morphological evolution of the kaolinite crystals. Dickite presents a euhedral blocky habit as opposed to the booklet morphology of the initial pseudohexagonal kaolinite crystals. Based on SEM imaging, minor formation of zeolite minerals, such as natrolite presenting a prismatic habit and analcime showing a trapezohedron form, was observed at Experiments 5 and 6.

3.4.3 Quantification of berthierine-to-chlorite transformation, clay-coat characteristics, and porosity evolution

The AQM method displays a progressive decrease of berthierine and concurrent increase of chlorite content (Figure 3.10A). The temperature range of berthierine-to-chlorite transformation is constrained between 100 °C and 175 °C, with approximately 150 °C being the critical temperature where chlorite overcomes berthierine content. The results from Experiment 6 showed that, by weight, berthierine decreased to ~ 1% while chlorite increased to ~ 14%.

The dataset from the quantitative, Petrog-based, analysis revealed an increasing trend of the coat coverage with increasing temperature. The temperatures of 150 °C and 200 °C exhibit the main increment zone with average values of ~ 28% and ~ 47%, respectively (Figure 3.10B). No significant increase occurred beyond that point. However, surface area covered by clay coats was observed on every grain. Pre-experimental clay-free surfaces coated by siderite crystals (Figure 3.11A) present extensive coverage after the hydrothermal runs at the highest temperatures (Figure 3.11C).

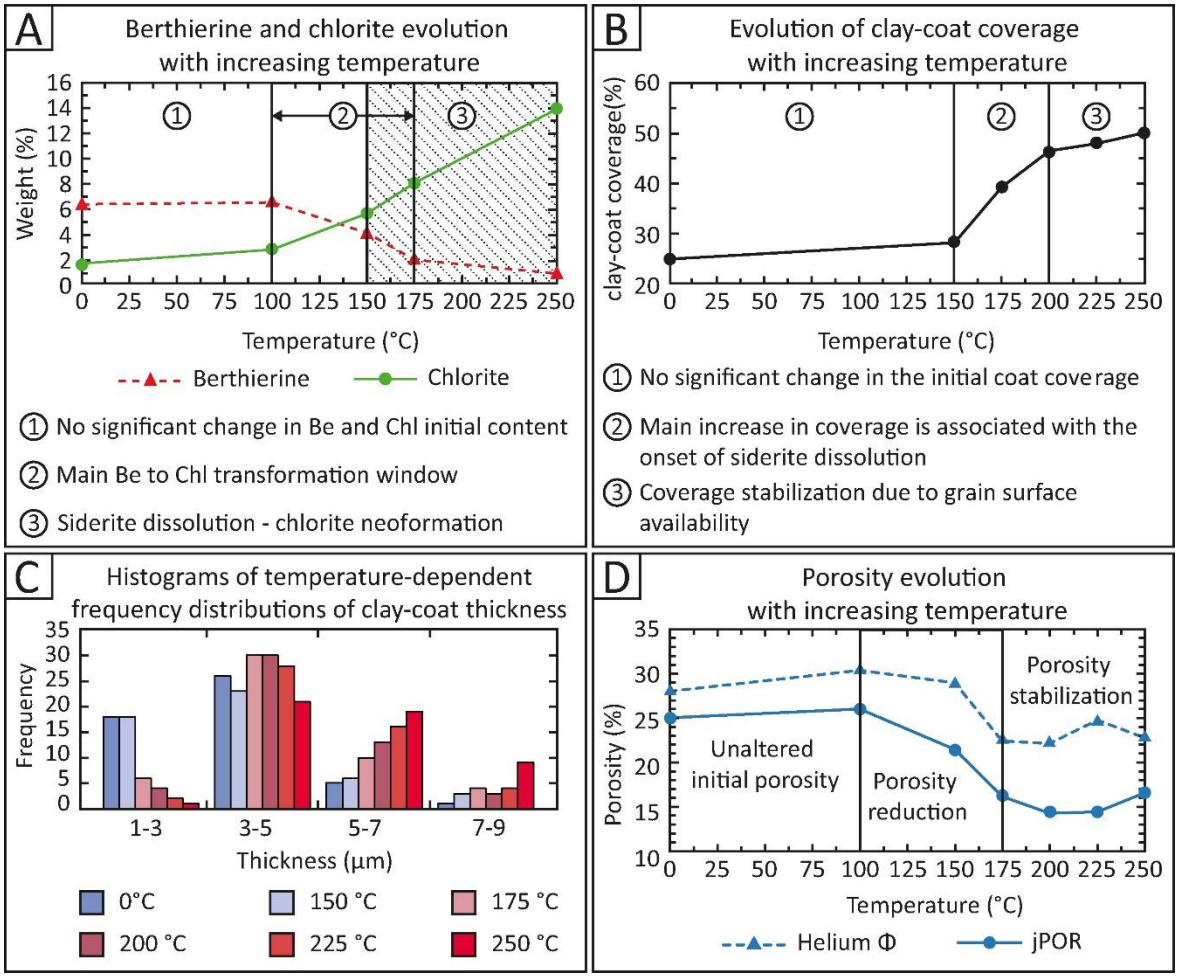

Figure 3.10: Quantification of berthierine and chlorite content, clay-coat thickness, clay-coat coverage, and porosity with increasing experimental temperature. A) Diagram showing the interdependence of berthierine, chlorite, and siderite. The temperature range for berthierine-to-chlorite transformation is based on the AQM examination and, the siderite's input on chlorite authigenesis is based on SEM imaging. B) Cross-plot of clay coverage against experimental temperatures as determined via Petrog. Highest coverage is observed at temperatures greater than 175 °C. C) Frequency-distribution histogram for all the temperature steps divided by thickness groups as determined via ImageJ. The majority of the thickest coats are observed at temperatures between 200 °C and 250 °C. C) Porosity evolution as derived by helium pycnometry and jPOR analysis. Porosity reduction is significant between 150 °C and 175 °C. Stabilization of porosity is observed at experimental temperatures greater than 175 °C.

A frequency histogram illustrating the distribution of the thickness of the clay coats, in four categories, with increasing temperature is depicted in Figure 3.10C. 74% of the measurements belonging to Class 1 derive from samples hydrothermally treated up to 150 °C. Group 2 presents a uniform distribution between each temperature step. A significant increase in the coat thickness is observed in temperatures greater than 175 °C. On average 33% of the measurements belonging to Classes 3 and 4 derive from Experiment 6.

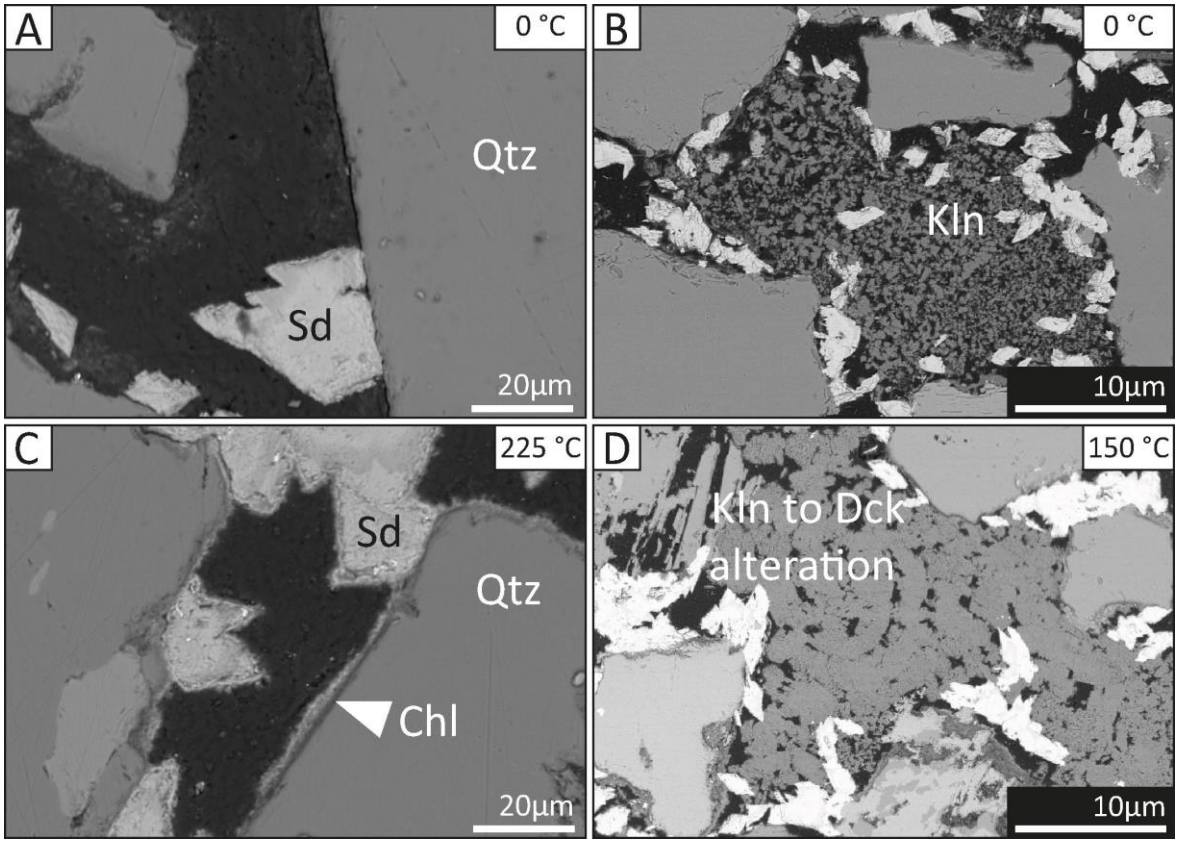

Figure 3.11: SEM images showing the increase in coat coverage and the main primary porosity reduction mechanism. Where Chl = chlorite; Dck = dickite; Kln = kaolinite; Qtz = quartz; Sd = siderite. A) Clay-free quartz surface before the experiments. B) Initial pore-filling kaolinite with visible microporosity before hydrothermal treatment. C) Chlorite neoformation, promoted by siderite dissolution, on an initial clay-free quartz surface after the hydrothermal experiment at 225 °C. D) Alteration of kaolinite to porosity-occluding dickite.

Results of helium pycnometry showed a porosity decrease from an initial value of ~ 28% to ~ 23% at 250 °C. The main porosity reduction phase takes place between the experimental temperatures of 150 °C and 175 °C followed by a maintenance phase. 2D porosity measurements reveal a similar trend; however, there is a 6.5% discrepancy between the helium and jPOR techniques (Figure 3.10D). Reduction of primary porosity is mainly ascribed to the alteration of kaolinite to dickite (Figure 3.11B, D). Visibility of microporosity in the pore filling is progressively decreasing from the experimental temperature of 175 °C onwards. Secondary porosity is generated through the dissolution of albite and siderite grains.

3.5 Discussion

The present-day depth and temperature of the Cook Formation is approximately 2400 m and 90 °C, respectively. Therefore, assuming that the borderline between the eodiagenetic and mesodiagenetic realm is at about 2000 m depth and 70–90 °C temperature (Worden and Burley 2003), the Cook Formation is an ideal candidate for developing a better understanding about mineral diagenetic alterations occurring during the transition from eodiagenesis to mesodiagenesis.

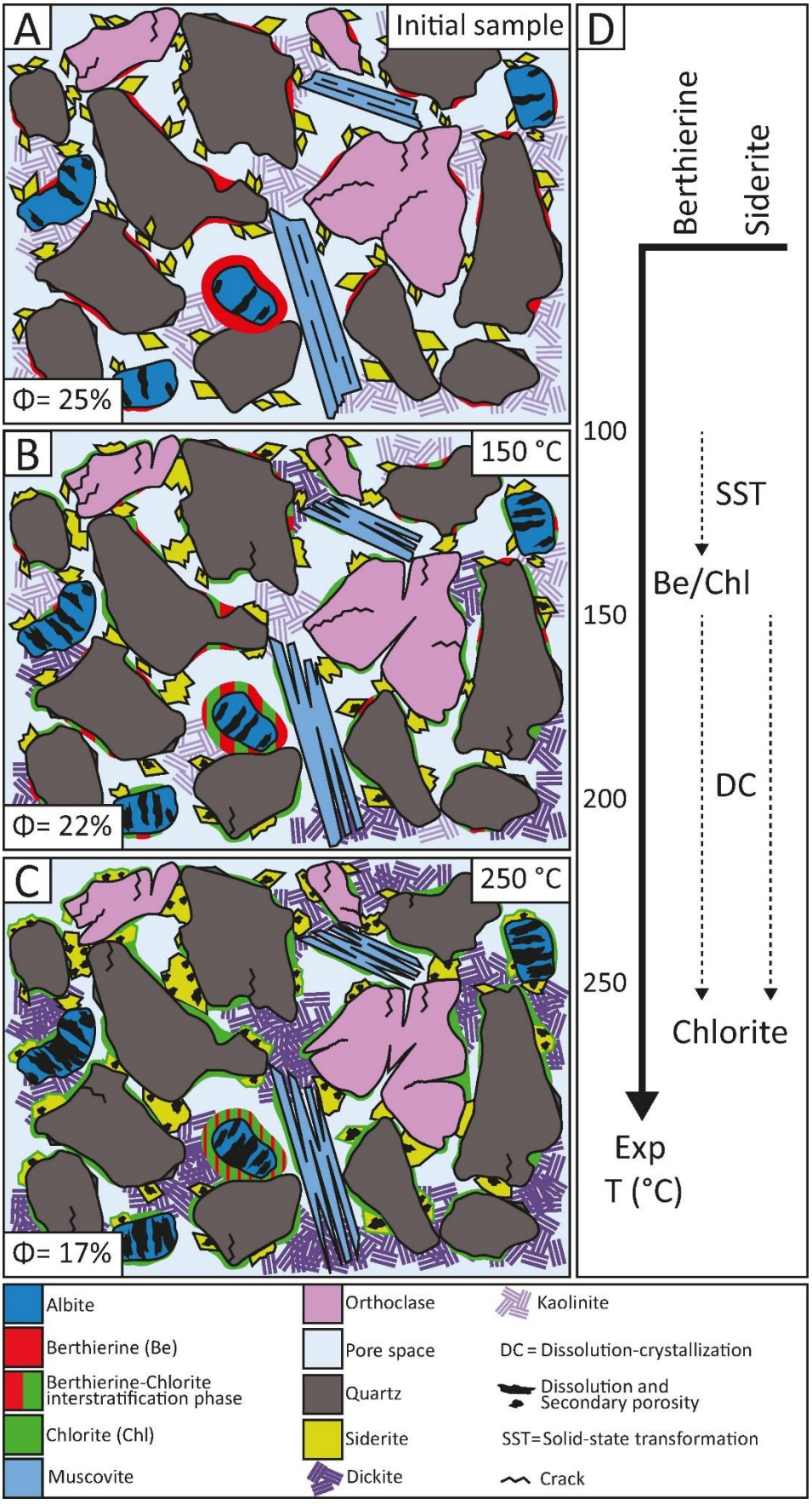

Figure 3.12: Cartoon summarizing the main diagenetic alterations and reservoir-quality evolution of the sandstone samples during the experimental procedure. A) Detrital grains coated by discontinuous berthierine coats and lozenge-

shaped siderite crystals. The primary pores are partly filled with kaolinite. B) As temperature increases, cracks in detrital grains, mainly orthoclase, develop and the intergranular pores are progressively filled with dickite, a polymorph of the kaolinite group. Authigenic chlorite starts replacing berthierine. Siderite dissolution begins with individual siderite crystals losing their initial shape and merging together. Chlorite precipitates on precursor-free grain surfaces due to siderite dissolution. C) The conversion of berthierine to chlorite is completed. Further chlorite nucleation is identified on the rims of the dissolving siderite crystals. Hollow cores are prominent, enhancing secondary porosity. Coat coverage is increased with thicker grain coats located mainly next to siderite crystals. Secondary intragranular porosity is generated by the extensive dissolution of albite, which, however, together with mica dissolution promotes further dickitization, hence reducing primary intergranular porosity. D) Chloritization mechanisms of berthierine and siderite with increasing experimental temperature.

Several, mainly isochemical, reactions have been reported as responsible for chlorite authigenesis in deeply buried sandstones (Curtis et al. 1985; Smith and Ehrenberg 1989; Worden and Morad 2003; Worden et al. 2018c). The main detrital and early diagenetic Fe-rich minerals involved in these reactions include detrital chlorite and biotite, berthierine, trioctahedral smectite, siderite, ankerite, ilmenite, and other Fe-rich heavy minerals (Worden et al. 2020). In this paper, an experimental approach has been taken to investigate berthierine to chlorite transformation and subsequent association of the generated authigenic chlorite with reservoir-quality evolution (Figure 3.12). The experimental results quantitatively identify that berthierine can be a precursor for chlorite precipitation in sandstones, and in the presence of siderite will produce robust clay coats on clean substrate surfaces or where berthierine and siderite precursors pre-exist.

3.5.1 Initial berthierine and siderite

Although various genetic pathways for the precipitation of berthierine have been proposed (Bhattacharyya 1983; Van Houten and Purucker 1984; Harder 1989; Mu et al. 2015), an abundant supply of Fe and reducing conditions are essential for its crystallization (Curtis and Spears 1968; Curtis 1985). Based on the proposed depositional environment of the sandstone used, berthierine is most likely the product of early diagenesis. The Cook sandstone was interpreted as a prograding sandflat formed in a tide-influenced marginal marine setting (Livbjerg and Mjøs 1989). Depositional settings in the vicinity of river mouths favour the development of berthierine (Ehrenberg 1993; Worden and Morad 2003; Morad et al. 2010) due to brackish pore-water compositions, which have low concentrations of dissolved sulphate ions, abundant supply of iron-bearing particles via river waters (Bailey 1988; Odin 1988; Odin 1990), and high sedimentation rates promoting anoxic conditions. The absence of pyrite in the samples suggests negligible bacterial sulphate reduction processes such that sufficient concentrations of Fe^{2+} will be present enabling berthierine precipitation.

The morphology of the siderite cement and the textural evidence of siderite postdating berthierine (Figures. 3.4C, 3.5D) indicate siderite precipitation at a later diagenetic stage. Early diagenetic siderite mostly develops in the form of nodules or more pervasive cement (Curtis et al. 1986)

whereas the lozenge-shaped crystals fringing detrital grains observed in the samples are common precipitates in early mesodiagenesis. Siderites with similar crystal habit have been found synchronous with quartz overgrowths (Karim et al. 2010).

3.5.2 Authigenic grain coating chlorite

3.5.2.1 Berthierine-to-chlorite transition

The conversion of berthierine to chlorite has been proposed to occur at temperatures greater than 60 °C (Jahren and Aagaard 1989; Aagaard et al. 2000; Worden and Morad 2003). Mineral reactions take place through different mechanisms which have different activation energies, therefore affected by different temperatures (Lasaga 1998). It will be shown that chloritization of berthierine is the product of a mixture of the solid-state transformation (SST) and dissolution-precipitation (DC) mechanisms.

Solid-state transformation (SST) can explain the chloritization of berthierine up to an experimental temperature of ~ 150 °C. SST is less energetically demanding than DC, as it requires less disruption of chemical bonds, and thus is favourable in lower-energy settings. SST has been proposed by several authors as the dominant mechanism responsible for the progressive replacement of 7Å-layered minerals by 14Å-layered minerals (Banfield and Bailey 1996; Ryan and Reynolds 1996; Xu and Veblen 1996). According to SST, phyllosilicate reactions are relatively volume conservative retaining the crystal habit and leading to similar shape and size between the parental and daughter minerals. AQM revealed an increase in chlorite and a concomitant decrease in berthierine content; however, the sum of the volume of the two minerals, up to 150 °C, remained constant. SEM examination did not show any evidence for dissolution features and no change in the average clay-coat thickness and coverage was observed.

An increase in temperature is one of the factors that has been considered to raise the possibility of DC (Altaner and Ylagan 1997). DC typically leads to large morphological changes between the initial and final clay mineral (Cuadros 2012). In natural systems, the recrystallization of low-temperature, berthierine-derived, chlorites to the higher-temperature chlorites is efficient at temperatures near 200 °C (Walker 1993). This process involves an increase in crystal size and structural changes such as polytype transformation and disappearance of the berthierine-chlorite interstratifications (Hillier 1994). The significant increase in chlorite volume (Figure 3.10A), the new rosette and cabbage head chlorite precipitates (Figure 3.8), and the increase in coat thickness (Figure 3.10C) and coverage (Figure 3.10B) at temperatures between 175 °C and 250 °C suggest a transition from the SST to the DC mechanism. DC also requires dissolution of entire mineral particles with their dissolved species passing into the bulk of the solution to provide the necessary reactive elements for chlorite

authigenesis. Al and Fe were sourced principally from albite and siderite decomposition, respectively, which occurred with increasing temperature.

Assessment of the hydrothermal reactor experiments provides valuable quantitative and qualitative data on the transformation of berthierine to chlorite as a function of temperature. The incorporation of fluid chemistry offers great potential for chlorite prediction at the field and reservoir scales.

3.5.2.2 Role of siderite and neoformation of authigenic chlorite coats

The high contact association of siderite with chlorite suggests the interdependence between the two minerals (Figure 3.7D). Chloritization of siderite proceeds solely through the DC mechanism. Siderite dissolution promotes chlorite authigenesis as evidenced by the thick chlorite coats observed adjacent to decomposing siderite crystals (Figure 3.9E) and by the complete engulfment of the dissolving crystals by authigenic chlorite (Figure 3.9F).

Iijima and Matsumato (1982) proposed the dissolution of siderite as a source of Fe for chlorite. They demonstrated the replacement of siderite by berthierine and subsequent berthierine-to-chlorite transformation in Paleogene and upper Triassic coal-measure formations in Japan. Chlorite neoformation as a direct precipitate from solution, directly on clean, mainly quartz, surfaces (Figure 3.11C), contributes to the major increase in the volume of chlorite at 250 °C. Previous hydrothermal experiments have also demonstrated that authigenic chlorites can be direct precipitates and do not necessarily require pre-existing precursors (Small et al. 1992; Haile et al. 2015).

3.5.3 Effect of grain coats on quartz cementation and porosity evolution

The present porosity (~ 28%) of the Cook Formation is solely accredited to mechanical compaction processes and is in accord with porosity values of siliciclastic reservoirs that have not yet entered the chemical compaction phase (Houseknecht 1987; Paxton et al. 2002; Taylor et al. 2010).

Minor amounts of clay, as little as 1–2% of the rock volume, have the ability to coat large surface areas of sandstone grains and affect reservoir quality positively (Bloch et al. 2002). The authigenic chlorite coats produced in our experiments increase in continuity and thickness, thus preserving porosity at an average value of ~ 23% at temperatures between 175 °C and 250 °C. Grain coverage, from both chlorite and siderite crystals, insulates the grains and decreases the surface area available for quartz precipitation. Moreover, the enrichment of the initial Si-supersaturated solution with Al and Fe compounds strengthens chlorite authigenesis at the expense of quartz cement. The ~ 5% reduction of porosity is attributed mainly to dickite authigenesis occluding

primary pores. Secondary porosity through albite and siderite dissolution contributes to the maintenance of overall porosity.

The optimum chlorite coat volume and thickness that will not result in the deterioration of the reservoir quality of a given reservoir is variable, and depends mainly on pore and pore-throat size. Pittman et al. (1992) suggested an optimum volume ranging between 5 and 13% for the Tuscaloosa Formation and between 4% and 7% for the Berea Sandstone. A coat thickness between 5 µm and 10 µm has been documented in several studies as beneficial for preservation of reservoir quality (Anjos et al. 2003; Sun et al. 2014). In agreement with these observations, the volume and thickness of the synthesized chlorite coats have not exceeded 14% and 10 µm, respectively. Quartz cementation is effectively retarded without occluding primary pores.

3.5.4 Relevance of experiments to subsurface analogues

Although the experimental conditions were modelled as closely as possible to reservoir conditions, there are some differences. The short duration of the experiments and the simplified fluid chemistry are key differences but they are partially compensated for by the elevated temperatures used for the experiments in this study. Furthermore, all the experiments started with an excess supply of silica to instigate quartz cementation. In natural settings, such conditions occur over prolonged periods of geological time, with silica and other reactants being derived from various sources.

In the Knarr (Well 34/3-1S) and Veslefrikk (Well 30/3-4) Fields, offshore Norway, the Cook Formation reservoir is located at depths of ~ 3700 m and ~ 3000 m, respectively. The corresponding temperature is ~ 135 °C, and the presence of partial or complete chlorite coats is significant, allowing the preservation of excellent reservoir quality (Hasnain and Jahren 2017; Skarpeid et al. 2017). Given the present-day depth (2400 m), temperature (90 °C), and absence of chlorites in the pre-experiment samples, one can hypothesize that the conversion of berthierine takes place between 90 °C and 135 °C. The study by Jahren and Aagaard (1989) on samples from multiple Jurassic clastic reservoirs offshore Norway suggests that continuous recrystallization of berthierine to chlorite occurs between 70 °C and 160 °C. At higher temperatures, berthierine is rendered unstable relative to chlorite (Iijima and Matsumoto 1982). The experimental results have produced observations comparable to the aforementioned natural systems showing that the main temperature window of berthierine to chlorite conversion lies between 100 °C and 175 °C with a noticeable stepwise change at ~ 150 °C, where chlorite becomes the dominant phase compared to the precursor berthierine clay. Likewise, the produced chlorite coats significantly inhibit quartz overgrowth development.

Further experiments remain to be performed using a volumetrically low fluid-to-rock ratio in a hydrothermal setup that allows fluid sampling at experimental conditions. This, to study the role of fluid chemistry, representative of the microenvironment of clay precipitation, of the core material both pre- and post-reaction, and develop a more comprehensive understanding of the chemical and reaction parameters for authigenic chlorite formation.

3.5.5 Implications for prediction of reservoir quality

The ability to predict the presence of grain-coating chlorite, and any other reservoir quality-influencing authigenic mineral, would lead to better-informed decisions during oil and gas exploration and for geothermal exploration where predictive models of reservoir properties are critical. Chlorite has been the subject of many diagenetic studies; however, no proven method of predicting chlorite coats in data-poor frontier settings exists. In more mature settings where core data are available, the probability of chlorite coats can be assessed using sedimentological and petrographic data sets (Berger et al. 2009; Sun et al. 2014; Stricker et al. 2016b; Dutton et al. 2018; Stricker and Jones 2018). Studies of the distribution of precursor clay coats and chlorite in modern sedimentary environments have revealed that it is imperative to define specific sub-environments of deposition to fully understand and predict chlorite grain coats in ancient and deeply buried sandstones (Wooldridge et al. 2017b; Griffiths et al. 2018; Griffiths et al. 2019a; Griffiths et al. 2019b; Virolle et al. 2019b; Virolle et al. 2020). Temperature plays a key role in the rate of authigenic-chlorite precipitation in sandstones. The experimental approach applied in this study has clearly recognized that with the correct geochemical components and progressive temperature increase within a sandstone body, then chlorite coats develop in preference to quartz cement. The quantitative data, assessing the thermally driven chlorite-coat authigenesis from precursor minerals, can be used to improve predictability of reservoir quality modelling in high-temperature (> 150 °C), deeply buried reservoir sandstones.

3.6 Conclusions

1. Hydrothermal experiments simulating burial diagenesis, using naturally occurring sandstone samples, selected for their initial content of berthierine and siderite, and an artificial silica-supersaturated solution, were undertaken at specific temperature steps and constant duration to assess the impact of chlorite authigenesis on reservoir quality of sandstones. Quantitative datasets regarding i) the volume of berthierine and chlorite, ii) the clay-coat thickness and coverage and, iii) porosity were produced at each temperature step.

2. The hydrothermal-reactor experiments have identified berthierine as precursor for chlorite in high-temperature environments. In addition, the experiments reveal the significant role of siderite to allow continued authigenesis of chlorite as grain coats. Chlorite is formed from berthierine transformation, replacement of siderite and neoformation on precursor-free substrate surfaces. Dissolution of albite and siderite provided the Al and Fe ions, important for chlorite authigenesis.

3. Chlorite authigenesis initiates with solid-state transformation at low experimental temperatures (100 °C) transitioning to dissolution crystallization at the higher-temperature spectrum. The threshold temperature for this transition is ~ 150 °C. Future long-duration experiments using various fluid compositions are needed to further develop and confirm these initial findings.

4. The hydrothermally synthesized chlorite coats are morphologically akin to naturally occurring chlorite coats. A significant increase in clay-coat thickness (form an average value of 3.8 µm at the experimental temperature of 150 °C to 5.4 µm at the experimental temperature of 250 °C) and clay coverage (from ~ 28% at 150 °C to ~ 50% at 250 °C) resulted in porosity preservation through offering fewer nucleation sites for quartz to precipitate. Dickitization of kaolinite is the dominant process reducing primary porosity. Secondary intracrystalline porosity contributing to the overall porosity maintenance was generated by the dissolution of albite and siderite crystals.

Chapter 4: Experimental simulation of burial diagenesis and subsequent 2D-3D characterization of sandstone reservoir quality

This chapter has been submitted for publication to a peer-reviewed journal.

Supporting data for this chapter are available online at http://doi.org/10.15128/r30v838056z, http://doi.org/10.15128/r32514nk484 , and http://doi.org/10.15128/r3bc386j205.

4.1 Summary

Good reservoir quality in deeply buried sandstones is commonly correlated with the occurrence of grain coats that inhibit quartz cementation. The development of reliable models that can predict reservoir quality relies on incorporating quantitative understanding of these diagenetic processes. Hydrothermal experiments simulating burial diagenesis, were integrated with multi-scale X-ray tomography to quantify the 3-dimensional evolution of grain coat volume and porosity with increasing temperature; while microscopic and automated quantitative mineralogy analysis was used to track the associated mineralogical alterations. To simulate reservoir evolution, sandstone samples from the Lower Jurassic Cook Formation (Oseberg Field, 30/6-17R, Norway) were exposed to a silica supersaturated Na_2CO_3 (0.1 M) solution for up to 360 hours at temperatures of 100–250 °C. The experimental results show the main porosity and permeability reduction window is associated with pore-filling kaolinite, and lies between 150 and 200 °C, above which little change occurs. Grain coat volumetric increases start to occur at ~ 150 °C through precipitation of authigenic chlorite, and continues to 250 °C, irrespective of the experimental duration. Together with pre-existing siderite coats the newly precipitated chlorite prevents the loss of reservoir quality by inhibiting quartz overgrowth development. Pore flow simulations based on the observed temperature-dependent 3-dimensional pore networks allow us to characterize pore-throat and permeability evolution, and build a conceptual model for the impact of a diagenetic overprint on the reservoir quality.

4.2 Introduction

A wide range of geoscience applications, including hydrocarbon extraction, CO_2 storage, aquifer development and geothermal exploration, rely on predictive models that describe the reservoir properties of a target formation. Realistic reservoir quality predictions require an understanding of how diagenesis, and associated factors, influence porosity and permeability.

Quartz cementation and clay authigenesis profoundly influence the quality of sandstone reservoirs by modifying the nano-to macroscale reservoir properties (Morad 1998; Worden and Morad 2000; Worden and Morad 2003; Taylor et al. 2010; Bjørlykke 2014). Quartz cementation, typically initiating at temperatures greater than ~ 80 °C, is the main cause of porosity and permeability reduction during progressive burial in sandstone reservoirs (McBride 1989; Bjørlykke and Egeberg 1993; Worden and Morad 2000), but grain coating clays can limit extensive quartz cementation by forming a barrier at the interface between detrital grains and intergranular pore space. Authigenic chlorite is reported to be the main clay coat controlling porosity preservation (Ehrenberg 1993;

Ehrenberg et al. 1998; Jahren et al. 1998; Anjos et al. 2003; Berger et al. 2009; Dutton et al. 2018; Stricker and Jones 2018), with numerous detrital and early diagenetic precursor minerals, including berthierine and siderite, allowing authigenic chlorite formation during burial. Authigenic chlorite grows perpendicular to grain surfaces and can indiscriminately coat any mineral grain at any orientation (Worden et al. 2020), and so it is the continuity of the coat that dictates the effectiveness of quartz cement inhibition (Ajdukiewicz and Lander 2010; Ajdukiewicz and Larese 2012; Dowey et al. 2012). In contrast, authigenic pore filling clays, such as kaolin minerals, have a detrimental effect on reservoir quality by blocking primary intergranular pore space (Osborne et al. 1994; Martín-Martín et al. 2007; Mahmic et al. 2018).

Experimental simulation of diagenesis can provide useful models of porosity (microscopic pore texture, referring to the shape, size and distribution of pores and throats and their interconnectivity) and permeability evolution during diagenesis; data essential for reconstructing more realistic mathematical reservoir models, and for larger-scale basin modelling (Bloch 1994). Temperature-controlled laboratory experiments have investigated clay mineral coat growth and quartz cement nucleation (Pittman et al. 1992; Hillier 1994; Aagaard et al. 2000; Lander et al. 2008; Ajdukiewicz and Larese 2012; Haile et al. 2015), but while these studies provide valuable insight into the effect of diagenesis on rock properties, quantitative understanding of diagenetic processes remains challenging.

Numerous techniques, such as imbibition, buoyancy, He pycnometry, gas adsorption, and mercury intrusion porosimetry, can be employed to directly measure porosity and examine pore-throat textures in reservoir rocks. However, these techniques can only characterize the interconnected porosity at the time of analysis (Anovitz and Cole 2015). Additionally, microscopic methodologies, such as light and scanning electron microscopy, can reflect the nature of porosity and its association with mineralogy but, since they only examine the 2D rock surface, are incapable of analysing 3D pore-throat distribution and their interconnectivity. 3D pore characterization is possible via statistical (Hazlett 1997; Liang et al. 2000; Keehm et al. 2004) and process-based modelling (Bakke and Øren 1997; Øren and Bakke 2002). However, statistical models cannot capture the complexity of the pore morphology and tortuosity in natural rock samples, and process-based models cannot adequately replicate the fabrics of heterogeneous and diagenetically complex units.

Over the last decade, the direct measurement of mineral and pore space characteristics in the 3D domain has become possible through the use of X-ray computed tomography (XCT) (Ketcham and Carlson 2001; Cnudde and Boone 2013; Wildenschild and Sheppard 2013). It has been applied to both sandstone (Lindquist et al. 2000; Golab et al. 2010; Bin et al. 2013; Schmitt et al. 2016;

Thomson et al. 2018; Zhang et al. 2019; Thomson et al. 2020) and carbonate (Youssef et al. 2007; Bultreys et al. 2015; Pak et al. 2016; Fheed et al. 2018) units to qualitatively and quantitatively characterize porosity and microscopic pore textures. XCT is a non-invasive and non-destructive technique that provides a unique opportunity to record volume and geometry alterations of mineral and pore structures during experiments. When combined with other characterization methods, it allows a high-resolution 3D representation of the pore system and mineral distribution, which can then further assist in improving our understanding of the mechanisms that govern fluid flow (Andrä et al. 2013; Markussen et al. 2019).

In this study, we extend the methods reported by Charlaftis et al. (2021) to quantify the 3D data of the hydrothermally treated samples; applying a multi-scale X-ray tomography (XCT) approach allowed the volumetric quantification of the mineralogical and pore-throat alterations, induced by the experimental process, in the 3D domain. High-resolution scanning electron microscopy (SEM) imaging and automated quantitative mineralogy (AQM) were used as complementary methods. Using naturally occurring sandstone samples from the Lower Jurassic Cook Formation, we compare simplified single-stage heating experiments with those more closely simulating burial diagenesis. The captured 3D geometry of the pore phase is used to computationally simulate fluid flow and determine permeability. This research presents a new integrated approach on experimental diagenesis that can lead to improved characterization of the mineralogical and petrophysical properties, thus enabling more accurate reservoir quality prediction of sandstone reservoirs.

4.3 Materials and Methods

The sandstone samples used in this study are obtained from core material from the Lower Jurassic Cook Formation of the Oseberg Field (Norway, Well 30/6-17R). All the samples are chosen from a depth of 7988.18 ft. (2434.8 m) based on their initial mineralogical content and to exclude heterogeneity from the experimental process. Comprehensive mineralogical evaluation of the starting material using X-ray diffraction, SEM, and AQM techniques can be found in Charlaftis et al. (2021).

The single-stage experiments entail the 3D analysis of five plugs (samples S1-S5), ~ 5 mm in diameter, each of which was subjected to hydrothermal treatment at specific temperature conditions and constant duration. The experiments were carried out in a Parker Autoclave Engineers 500ml cylindrical 316 stainless steel pressure vessel. During all experimental runs, silica gel granules and an aqueous solution of 0.1 M Na_2CO_3 (reagent grade) dissolved in high purity water (Milli-Q) were used as a source of silica and pore fluid, respectively. For detailed information on the

experimental process and justification regarding the experimental conditions chosen, see Charlaftis et al. (2021).

The multi-stage experiments use the same configuration, but a single, ~ 0.3 x 2.4 cm, plug (sample S6) was subjected to sequential hydrothermal treatment at temperatures of 70, 100, 150, 200 and 250 °C with a duration of 72 hours per temperature. Between each experimental stage, the sample was removed and air dried.

4.3.1 X-ray tomography

XCT data of samples S1 to S5 were collected using a Zeiss Xradia VersaXRM 410 microscope operated at 100 kV and 125 µA (no beam filtration), and the reconstructed datasets have a spatial resolution of 3.8 µm/voxel (3D equivalent of a pixel). All samples were imaged before and after the experiment. The XCT data of sample S6 was collected using a BP proprietary XCT system (double-helix scanning trajectory (Trond et al. 2012)), Sunbury-on-Thames (UK), operated at 80 kV and 120 µA. The sample was imaged with a spatial resolution of 5.57 µm/voxel between each experimental stage, and higher resolution (1.7 µm/voxel) images collected from a smaller region. The data were reconstructed using an algorithm that corrects for geometric motion errors via passive auto-focus (Kingston et al. 2011) and iterative reprojection alignment (Latham et al. 2018). For more information on the XCT acquisition characteristics of the raw data and the analysed subvolumes please refer to Appendix A (Table A.2). Raw XCT data are also available online at http://doi.org/10.15128/r30v838056z (S1, S2, S5), http://doi.org/10.15128/r32514nk484 (S6, 5.57 µm/voxel), and http://doi.org/10.15128/r3bc386j205 (S6, 1.7 µm/voxel).

4.3.2 Image processing

To aid the reader, XCT resolution is colour-coded in all figures as green (5.57 µm/voxel), light blue (3.8 µm/voxel), and orange (1.7 µm/voxel). The image processing workflow (Figure 4.1) was performed in Thermo Scientific Avizo® (v 2019.2). All scans for each sample were spatially registered to enable direct comparison of the microstructure before and after each temperature treatment. An anisotropic diffusion filter was employed to denoise all low and medium-resolution datasets (Weickert et al. 1998) but was not required for the highest resolution data.

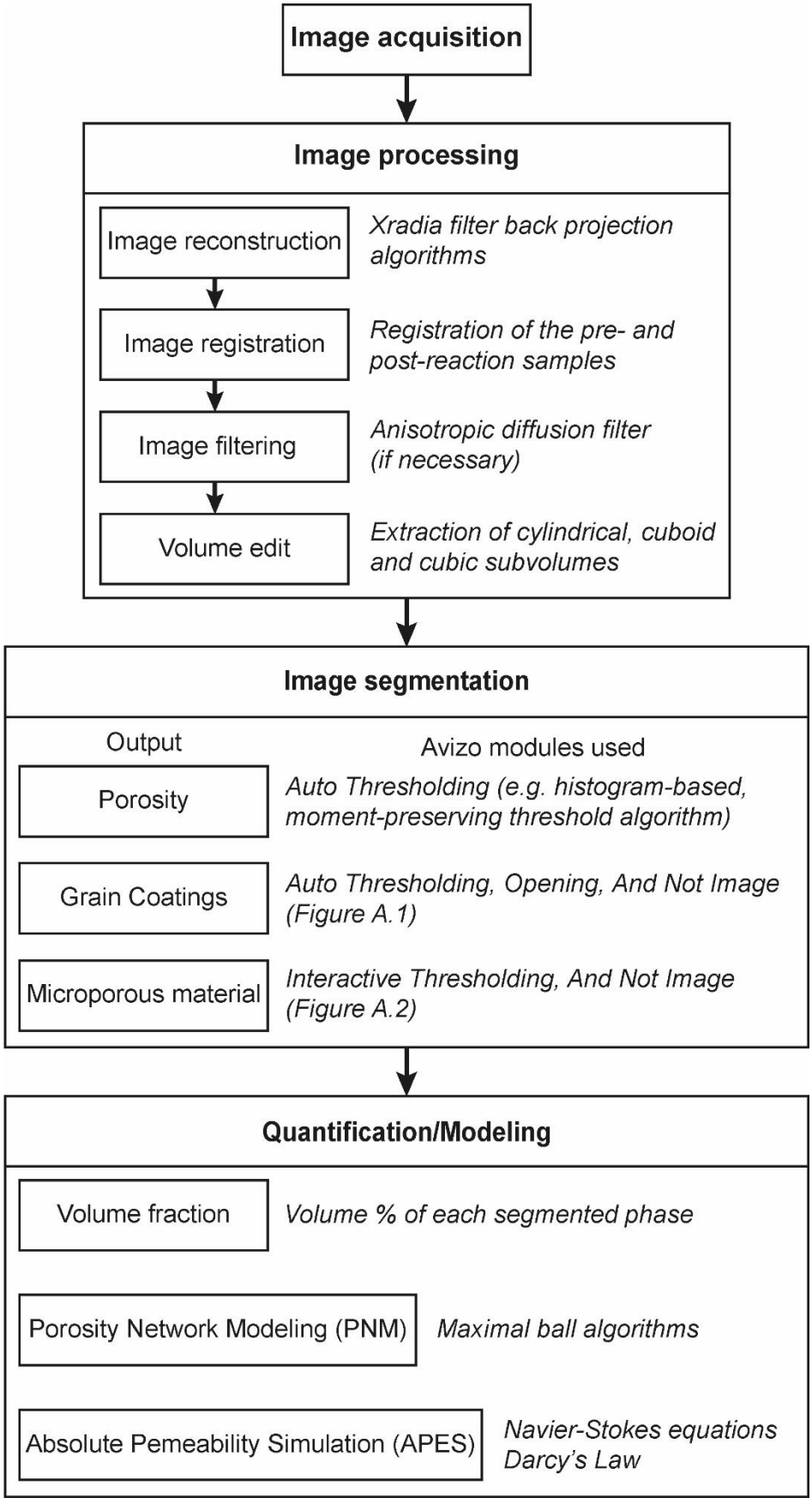

Figure 4.1: XCT processing workflow devised for pore phase, grain coat and microporous material analysis, and porosity and permeability modelling.

Representative cylindrical and cuboidal subvolumes were extracted from all samples (Figure 4.2A, B) to exclude voxels from potentially contaminated exterior surfaces. After initial testing, to ensure that the cubic subvolumes were representative of the larger sample volume, flow simulations were performed only on the cubic subvolumes to minimise computation time.

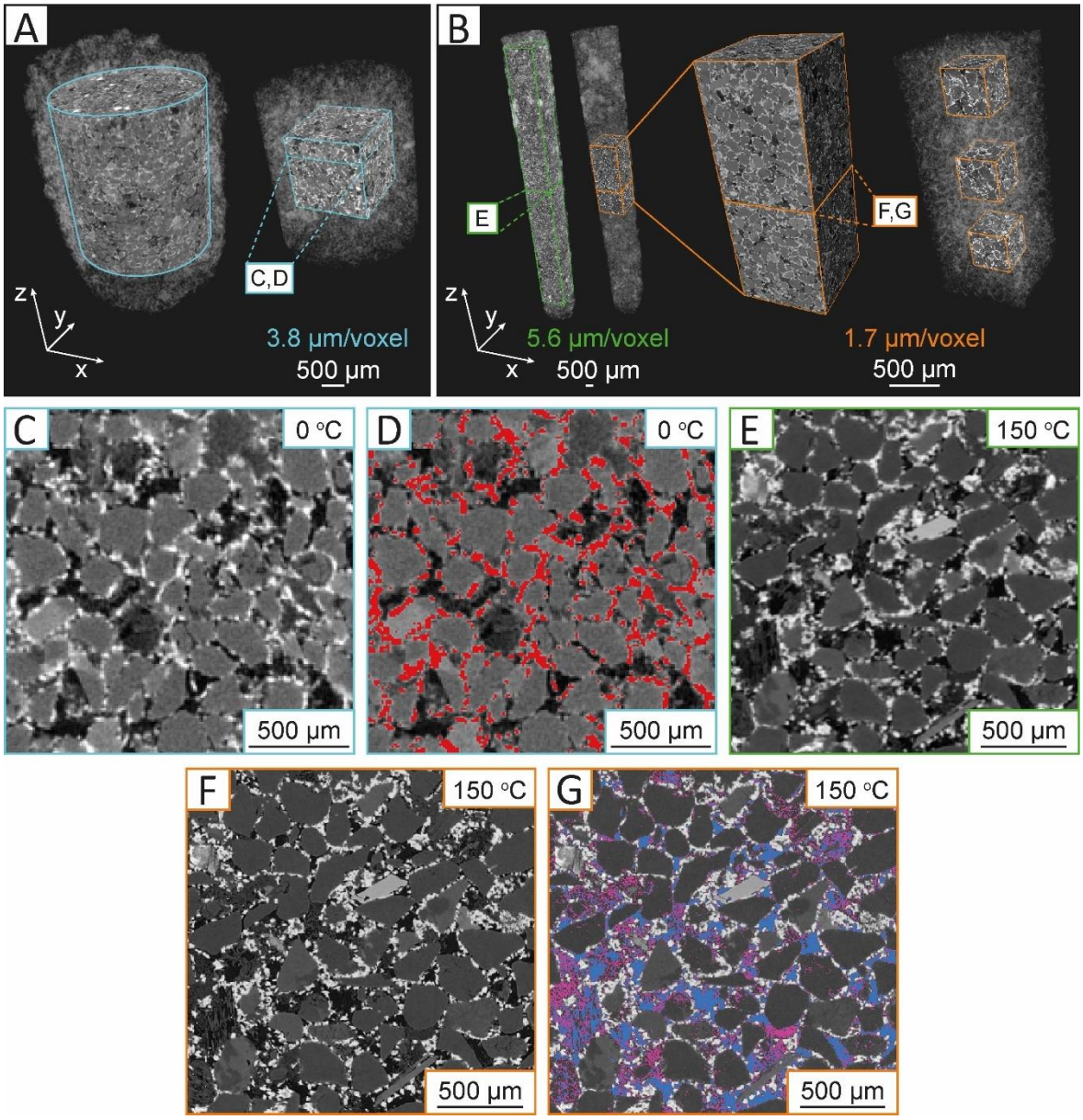

Figure 4.2: Multi-scale XCT analysis. 3D Volume rendering of the cylindrical and cubic subvolumes (A) extracted from samples S1-S5 scanned with a resolution of 3.8 µm/voxel (outlined in light blue). B) 3D volume renders of sample S6. S6A is scanned with a resolution of 5.57 µm/voxel (outlined in green), whereas the subsection S6B and subsequent cubic subvolumes S6C1 (top), S6C2 (middle) and S6C3 (bottom) are scanned with a resolution of 1.7 µm/voxel (outlined in orange). 2D slices through the tomography data showing the grey scale image (C) and with the segmented grain coating phase (D). E, F) 2D registered slices from data collected at different resolutions (Sample S6A and S6B after being hydrothermally treated up to 150 °C). G) Selection of the macropore (blue) and microporous volume (purple) phases.

4.3.3 Image analysis

Minerals have X-ray absorption characteristics dependent on their density and atomic mass; represented in the 3D images as differences in greyscale value (Figure 4.2C, E, F). These differences were exploited to perform digital segmentation using a histogram-based, moment-preserving threshold algorithm (Tsai 1985) to identify all voxels of grain coating material (Figure 4.2D) and porosity (Figure 4.2G). This algorithm preserves the mathematical moments of the original greyscale image, giving a more realistic segmentation than single value-based global methods. At higher resolutions (S6B and S6C1-C3), it was also possible to segment microporous material (mainly clay phases) using a combination of the moment preserving and a watershed threshold algorithm (Figure 4.2G). This material occupies some primary pore spaces and exerts a major influence on the reservoir properties of the experimentally treated samples, and microfractures within framework grains. For more information on the segmentation process and the associated uncertainty analysis, see Appendix A.

4.4 SEM imaging, automated mineralogy, and image integration

Sub-micron scale features that are challenging to quantify with high accuracy in the 3D image can be captured through direct correlation of the 3D data with high-resolution 2D microscopy after image registration. After the hydrothermal experiments, sample S6 was mounted in a block of resin and polished to expose a planar surface that lies within the 3D tomography volume. Backscatter SEM imaging of the carbon-coated polished block was carried out on a Hitachi SU-70 FEG SEM scanning electron microscope with an energy-dispersive detector (EDS) at an acceleration voltage of 20kV and measured beam current of 0.6 nA.

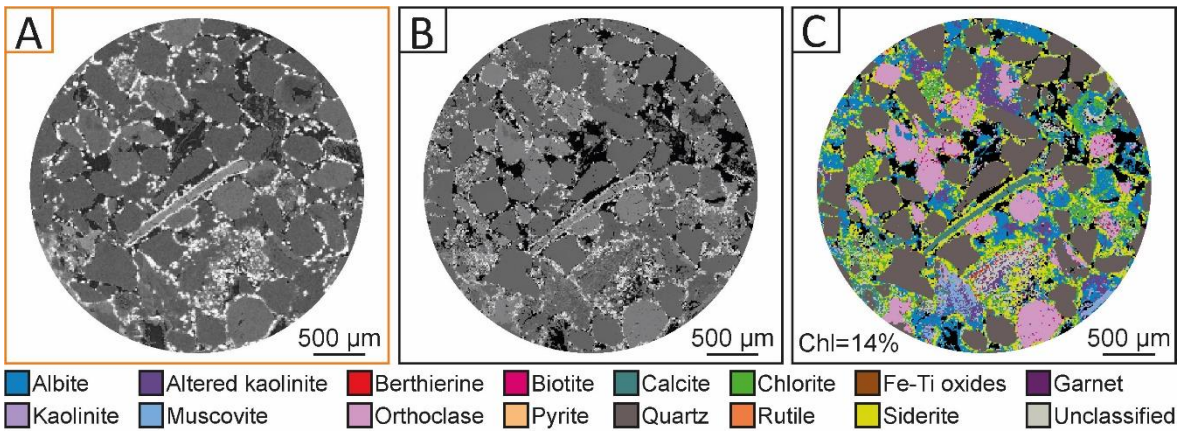

Figure 4.3: Registered XCT and SEM slice with associated AQM analysis of sample S6 after being hydrothermally treated up to 250 °C. A) 2D slice through 3D greyscale XCT data. B) Registered SEM slice. Variations in grain and pore size in the images are due to damage during the polished section preparation for SEM analysis. C) In-situ mineral map. Where Chl = chlorite

AQM was performed on a Zeiss Gemini SUPRA 40VP field emission scanning electron microscope coupled with a Bruker XFlash® 60 EDS detector. Images were collected using a high-resolution raster, with a step size of 3.5 microns at a 255x magnification and a 20 kV acceleration voltage. Dwell time was adjusted to capture approximately 20,000 counts per pixel. The 2D section image was then registered to the corresponding slice of the 3D data to support the XCT segmentation (Figure 4.3).

4.5 Porosity and permeability characterization

4.5.1 Pore network modelling

Pores disconnected from the axial through-going network were removed (as inaccessible to flow), and a conservative separation algorithm (marker extent = 7) was applied to define individual pores and pore throats (Figure A.4). Pore Network Modelling (PNM), based on the maximum ball concept (Silin et al. 2003; Silin and Patzek 2006; Dong et al. 2007), was applied to the separated pore volume to extract a topologically equivalent network of the pores and throats. The maximal ball algorithms construct the maximum spheres fitted to, and centred on, each pore. The largest spheres are defined as pore bodies, and chains of smaller spheres connecting these pore bodies are defined as throats. Pore radius represents the radius of a sphere with equivalent volume as the analysed pore. Throat radius is defined as the minimal distance between the central line and the border of the throat. Coordination number is the number of throats connected to a given pore, which reflects the spatial connectivity of the pore space.

4.5.2 Absolute permeability simulation

The Absolute Permeability Experiment Simulation (APES) built-in Avizo module was used to compute a scalar estimate of permeability at each experiment. This simulates fluid flow as a single-phase flow by implementing the finite volume method (Harlow and Welch 1965) to solve the Stokes equations for velocity and pressure fields. The APES fluid flow simulations were run with flow parallel to the long axis (e.g., z-direction) of the sample, driven by a pressure differential (ΔP = 30kPa) imposed across the analysed subvolume, and a convergence criterion set to a value of 10^{-6}. The simulation assumes no loss of fluid through the faces parallel to the flow direction and adds accommodation zones to inflow and outflow faces to ensure a quasi-static pressure field over the faces. The APES then solves for the velocity field in the interconnected pore space, and the volumetric flux (Q) across the sample end faces is computed. Permeability (k) is then obtained using Darcy's Law.

4.6 Results

The XCT-analysed grain coats are defined as all the Fe-rich minerals (e.g., siderite, berthierine, chlorite) fringing primary minerals such as quartz and K-feldspars. The separation of the Fe-rich phases is not possible as the density of the phases and close association and intergrowths prevent attenuation-based segmentation. The microporous material is mainly kaolinite pore-filling clay and, to a lesser extent, micropores within fractured grains. For both the single- and multi-step treatment, we present the volumetric changes of each phase of interest and compare the pre- and post-reaction pore network characteristics and permeability models of each sample.

To aid the reader, XCT resolution is colour-coded in the bounding boxes of the relevant figures (as per section 2, green = 5.57 µm/voxel, light blue = 3.8 µm/voxel, and orange = 1.7 µm/voxel). Where data from multiple resolutions are plotted on the same graph, the data series themselves are colour-coded.

4.6.1 Experimental suite 1: Single-stage thermal treatment.

The XCT results show that the initial porosity of the cylindrical samples was ~ 5–7%, with the cubic subvolumes showing slightly higher values (~ 10%). This difference is caused by the smaller volume of the analysis and the natural heterogeneity within the samples. Both sample sets show no change in porosity at 100°C, and only modest (<1% reduction, cubic sample only) at 150 °C. Porosity decreases at the experimental temperatures of 200, 225 and 250 °C (Figure 4.4A).

At temperatures > 200 °C the bulk porosity change hides additional complexity. The S4 (cylindrical subvolume) shows a reduction in porosity from 7.1% to 6.0%, and in S5, porosity shows a very similar decrease from 6.3 to 5.1%. The cessation of further porosity loss is associated with grain coat growth (Figure 4.4A, D, E). Local increases in porosity are caused by the development of dissolution pores (Figure 4.4B, C).

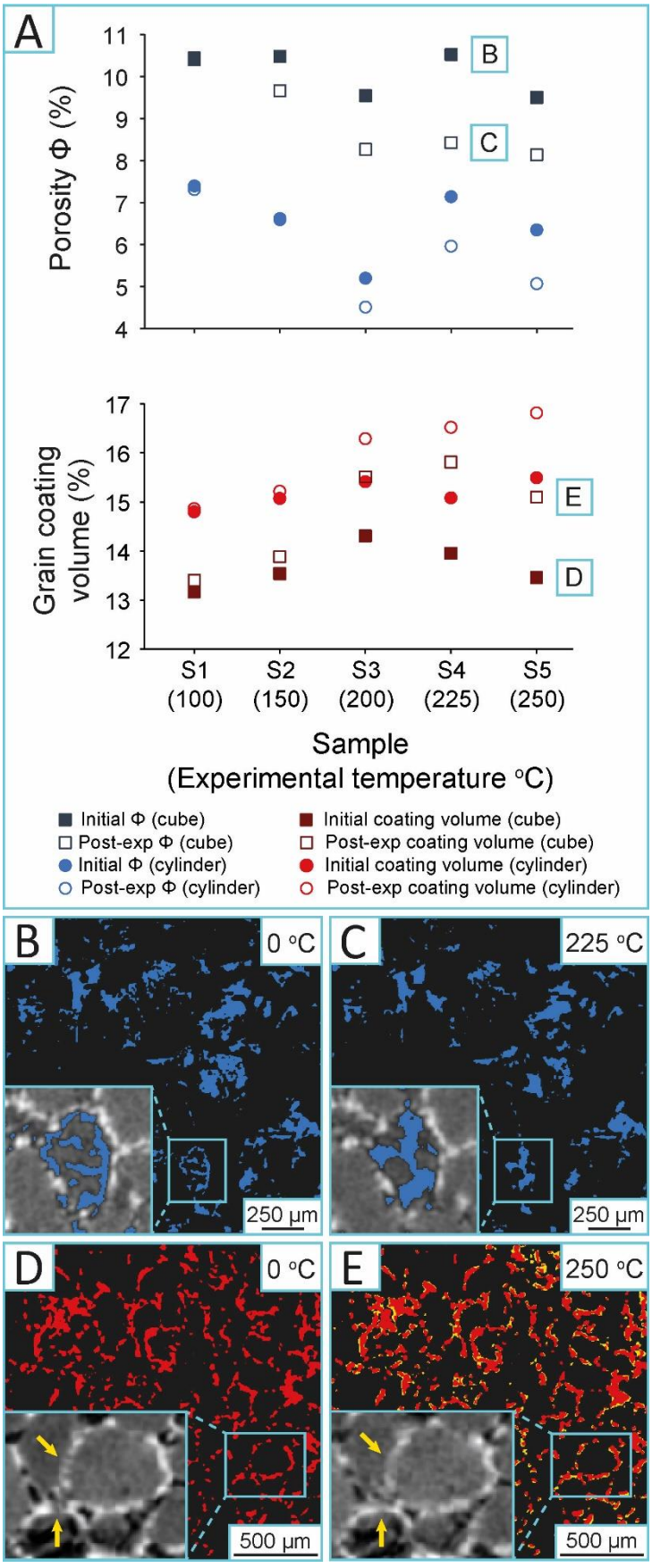

Figure 4.4: Quantification of porosity and grain coat volume, pre- and post- reaction, of samples S1-S5. The error associated with the presented XCT measurements is <0.1% (see Appendix A). A) Porosity and grain coat volumetric change

of the cylindrical and cubic (500 voxel^3) subvolumes of each sample/temperature. Significant porosity reduction and grain coat volume increase occur at the experimental temperatures of 200, 225 and 250 °C. The grain coat volumetric increase corresponds to the stabilization of porosity reduction at temperatures higher than 200 °C. B) 2D slice of the thresholded porosity phase of sample S4 before the experiment and (C) after the experiment at 225 °C showing the porosity decrease. Note the development of secondary porosity due to feldspar dissolution. Initial (D) and final grain coat volume (E) after the hydrothermal treatment at 250 °C. The newly precipitated phase (yellow) contributes to the increase of the thickness and continuity (yellow arrows) of the initial coats.

Grain coat volume increases from 15.1% to 16.5% for sample S4 and, from 15.5% to 16.8% for sample S5 (Figure 4.4A). The 3D observations indicate increase of both the coat thickness and coat continuity (Figure 4.4D, E). Previous microscopic analysis has identified this as precipitation of authigenic chlorite coats (Charlaftis et al. 2021). The porosity and grain coat volume measured on the smaller cubic subvolumes show the same trend as the larger cylindrical subvolumes, but with small differences (mean 3.6% difference in porosity, 1.5% difference in grain coat volume) because of the heterogeneity of the local microstructure.

A comparison of the pre- and post-reaction pore network and permeability models of each sample shows the effect of these alterations, in terms of pore connectivity, pore and throat size and, absolute permeability (Figure 4.5). In agreement with the total porosity, up to temperatures of 150 °C there are negligible changes in the volume of the connected pore network (Figure 4.5B), or in the mean pore diameter, although there is still some pore isolation and “snap off” in some areas of the pore network. While there is some heterogeneity in the initial permeability, controlled by the sample structure, no significant change in permeability is seen in samples subjected to temperatures up to 150 °C.

As the temperature increases, there are volume reductions of the connected porosity of up to 30% (reduction from 7.2% to 4.9% at 250 °C), accompanied by reductions in both mean pore diameter (9% reduction, from 126 µm to 115 µm at 250 °C) and throat radii (15% reduction, from 27 µm to 23 µm at 250 °C), and mean co-ordination number (from 3.3 to 2.5 at 250 °C). Consequently, the observed pore network changes start to reduce permeability (~ 2.5 mD reduction at 200 °C; ~ 4 mD reduction at 225 and 250 °C) (Figure 4.5A). Visualisation of the fluid velocity magnitude maps before and after treatment at 250 °C shows significant changes to the location of the main flow pathways (Figure 4.5B).

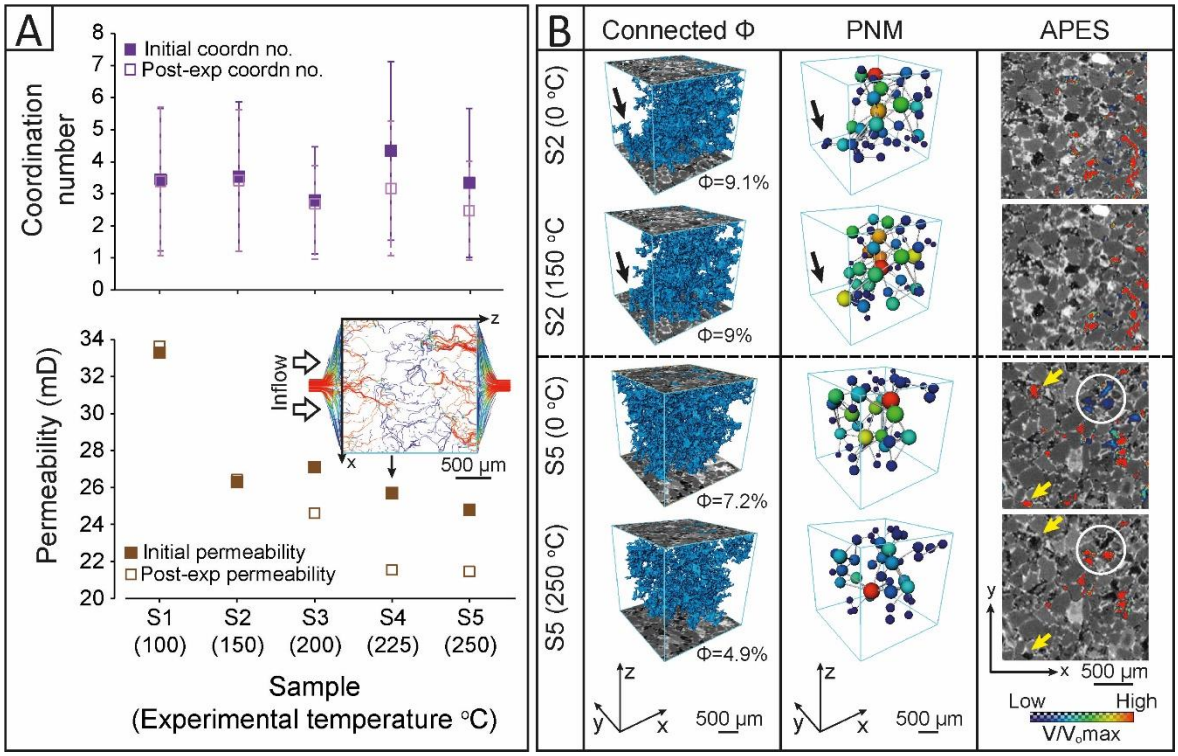

Figure 4.5: Porosity network modelling and absolute permeability simulations of the cubic subvolumes of samples S1-S5. A) Evolution of the mean coordination number (number of contacts a pore has with its neighbours) and permeability per sample/experimental temperature, derived from the pore network modelling and permeability simulations, respectively. Error bars correspond to the standard deviation. Included is a schematic diagram of the permeability simulation along the z-axis of sample S4 prior to hydrothermal treatment. The model is colour-coded, with slower streams being near the blue end of the spectrum and faster streams near the red end of the spectrum. B) 3D renders of the connected porosity (left), pore network models (middle) and fluid velocity magnitude maps (right) of samples S2 and S5 before and after the hydrothermal experiments. The pore space of the pore network models is represented as a lattice of wide pores (shown as spheres) connected by narrower throats (shown as cylinders). The size of the pore and throat indicates the inscribed radius and length, respectively. Red indicates volumetrically larger pores, and blue indicates pores with a smaller radius. The fluid velocity maps are normalized to the maximum velocity value of each sample as derived from the permeability simulation prior to the experiment. Note that slight changes between the pre- and post-reaction connected porosity network of sample S2 (black arrows) do not affect the flow pathways. Significant alterations occur at 250 °C with extinction of pre-reaction preferential pathways (yellow arrows) and flow enhancement of initially low fluid flow velocity regions (circled).

4.6.2 Experimental suite 2: Multi-stage thermal treatment.

The multi-stage thermal treatment allows the application of new understanding of temperature-dependant behaviour to a more geologically realistic scenario that simulates burial.

Figure 4.6A presents the porosity, grain coat, and microporous material evolution with increasing temperature for each of the extracted subvolumes (e.g., cuboids and 500^3 voxel cubes). As with the single-stage experiments, negligible change was observed between 0 °C and 100 °C and only temperatures ≥ 100 °C are shown here. Porosity reduction initiates at 100 °C, with the main reduction window occurring between 150 °C and 200 °C, irrespective of subvolume size and scan resolution. The porosity in sample S6A (5.57 µm resolution) reduces from 8.6% at 100 °C to 8% at 150 °C to 6.5% at 200 °C. With higher spatial resolution and a smaller scan volume (S6B, 1.7 µm

resolution), we see higher absolute values (a result of the higher resolution) and a reduction from 14.2% to 13.2% to 9.8% over the same temperatures; a 25-30 % reduction at both image resolutions. The smaller cubic subvolumes (1.7 µm resolution, S6C1-S6C3, taken from areas of low, medium and high initial porosity) show the same trend in porosity reduction but have greater variability in both the initial value and the reductions because of the greater heterogeneity preserved between these smaller volumes.

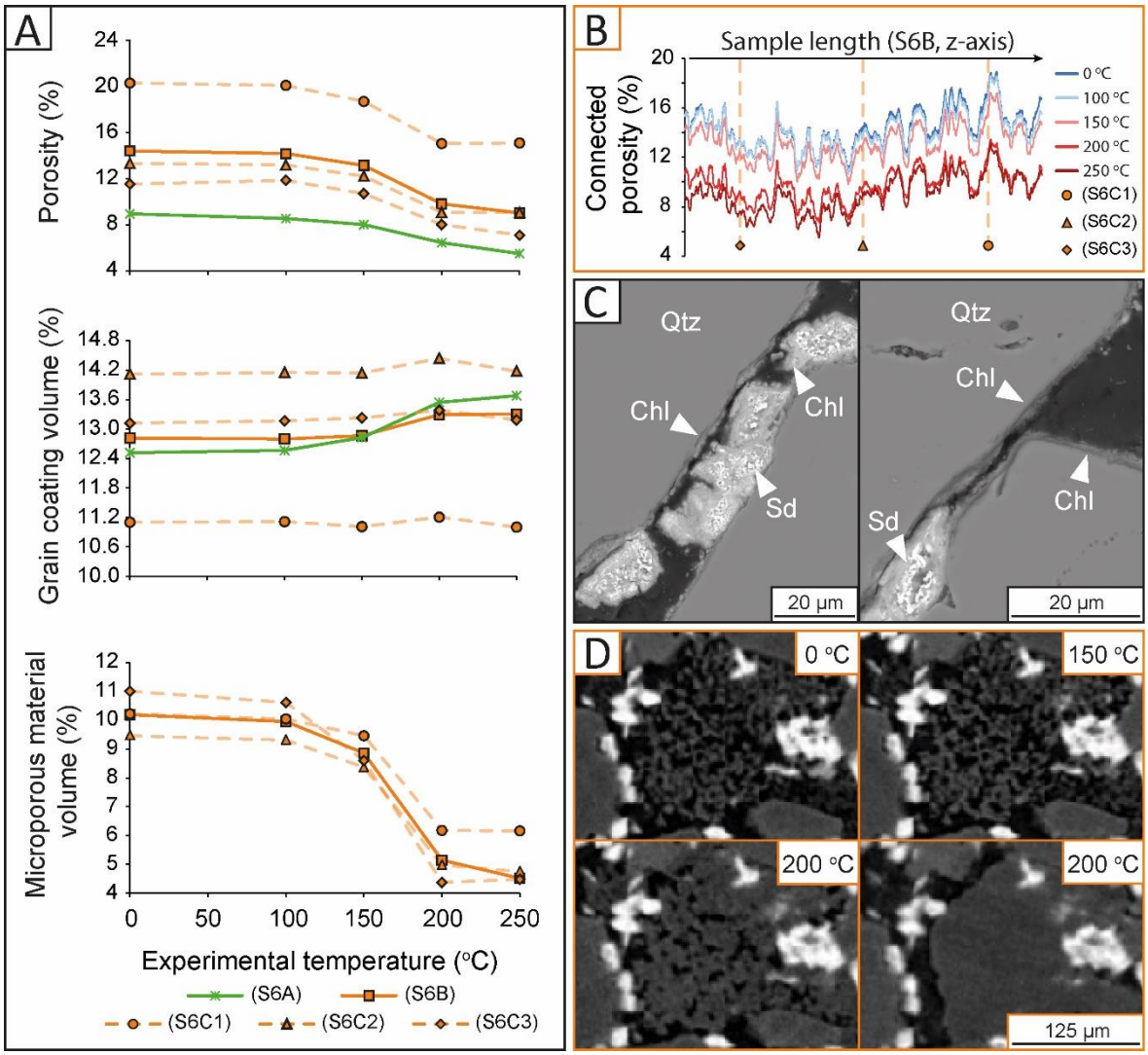

Figure 4.6: Porosity, grain coat, and microporous volume evolution of sample S6 subjected to sequential hydrothermal treatment up to 250 °C. The error associated with the presented XCT measurements is <0.1% (see Appendix A). A) Porosity, grain coat, and microporous volume plots with increasing temperature of sample S6 at different resolutions and scales. Note that porosity and microporous volume decrease occurs, primarily, between 150 and 200 °C followed by a stabilization phase. Grain coat increase is observed mainly on samples S6A and S6B at temperatures higher than 150 °C. B) Connected porosity distribution along sample length of sample S6B, colour-coded per experimental temperature, with the position of samples S6C1-SC3 indicated along that length. Porosity reduction is evident between 150 and 200 °C. C) Backscatter SEM images of the newly precipitated chlorite coats associated with siderite dissolution. Where Chl = chlorite; Qtz = quartz; Sd = siderite. D) 2D XCT images of the pore-filling kaolinite evolution destroying primary pore space.

Above 200 °C porosity reduction is retarded (as for the single-stage experiments), with reductions from 6.5% to 5.5% (5.57 µm resolution) and from 9.8% to 9% (1.7 µm resolution), and two the cubic

subvolumes (S6C1 and S6C2) show no reduction at all. This porosity-loss retardation can also be seen in the along axis evolution of the connected porosity of sample S6B (Figure 4.6B). In all cases, the reduction of the connected pore volume occurs between 150 °C and 200 °C.

Grain coat volumes show little change below 150 °C, and increases at higher temperatures are smaller than those seen in the single-stage experiments, from 12.5% to 13.7% (S6A, 5.57 µm resolution) and from 12.8% to 13.3% (S6B, 1.7 µm resolution). As in the single-stage experiments, the coat volume increase is associated with the development of authigenic chlorite coats (Figure 4.6C) and little net change in porosity. The SEM analysis revealed a progressive loss of the rhombohedral morphology of siderite crystals leading to replacement by chlorite, as well as precipitation on clean host-grain surfaces. Pre-experimental X-ray diffraction (XRD) and AQM analyses have shown an initial chlorite content of less than 2% by weight in all samples (Charlaftis et al. 2021), increasing to ~ 14% by weight chlorite after the experimental treatment (Figure 4.3C).

Microporous material is diminished by ~ 50% in all the analysed volumes. This is due to the gradual coarsening and morphological evolution of the kaolinite crystals from an initial booklet morphology with pseudohexagonal habit to a more euhedral blocky habit at 200 °C and a completely cemented phase with no visible microporosity at 250 °C (Figure 4.6D).

Based on XCT and SEM observations, albite dissolution generating secondary pore space is apparent from 150 °C onwards. Minor albitization of K-feldspar detrital grains and the formation of albite overgrowths were also observed. Albitization is generally incomplete and occurs preferentially along cleavage surfaces or microcracks presenting narrow irregular networks. Albite overgrowths form euhedral outlines on parts of the detrital feldspar grains that are not occupied by chlorite or siderite coats. Finally, authigenic quartz overgrowth precipitation was not observed in the analysed samples.

The visualizations in Figure 4.7A demonstrate a clear difference between the initial and final pore network model of the hydrothermally treated sandstone sample. The post-experiment network is less dense, owing to the porosity loss, with the number of the extracted pore bodies and throats decreasing from 1188 to 750 and from 4758 to 1822, respectively. Pore connectivity has been drastically decreased with the mean coordination number being dropped from 8 (0 °C) to 4.9 (250 °C). Equally, pore and throat radius distributions reveal a shift towards smaller pore and throat sizes, with the mean pore radius decreasing from ~ 75 to ~ 73 µm and the mean throat radius from ~ 17 to ~ 15 µm (Figure 4.7B-D).

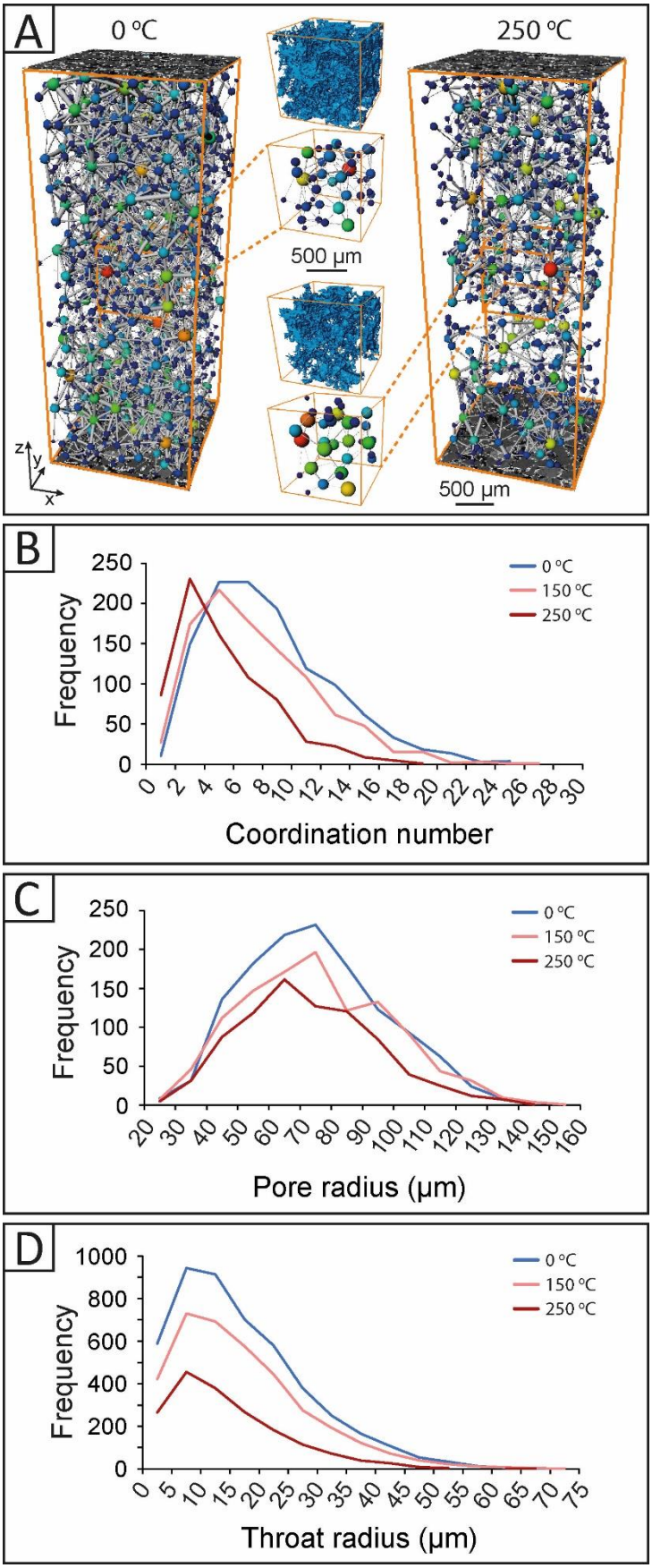

Figure 4.7: Comparison between the PNM data of the initial (0 °C), middle (150 °C) and final (250 °C) experimental stage of sample S6B. A) 3D visualization of pore network model of the whole sample and a zoomed-in cubic subset (S6C2) with

the equivalent 3D volume rendering of the connected porosity. Pore and throat size of the porosity models indicates the inscribed radius and length, respectively. Larger pores are shown in red and smaller pores are shown in blue. Frequency distribution plot of the coordination number of pores (B), pore radius (C) and, the throat radius (D) per experimental temperature. Colours indicating temperature and volume resolution are as on previous figures.

Again, similar to the single-stage experiments, the APES results show a decrease in permeability with increasing temperature (Figure 4.8A) for all samples, with the main phase of permeability reduction occurring between 150 and 200 °C. These samples show greater variability in both the initial permeability and the reduction, driven by microstructural differences between the sample locations within S6B. Above 200 °C, the APES shows only small changes (both increase and decrease) in permeability; consistent with the negligible changes in the porosity and microporous volumes at this temperature.

Figure 4.8B-C display the APES models of sample S6C2 at 0 °C and 250 °C. The results indicate a reduction from an initial value of 29 mD to 17 mD. S6C1, which is located in a highly porous region within the larger cuboid volume (S6B), has an initial permeability value of 160 mD and presents the largest permeability change. Although the preferential fluid flow pathways are preserved as in sample S6C2, permeability at the end of the experiment is reduced to 65 mD (Figure 4.8D, E).

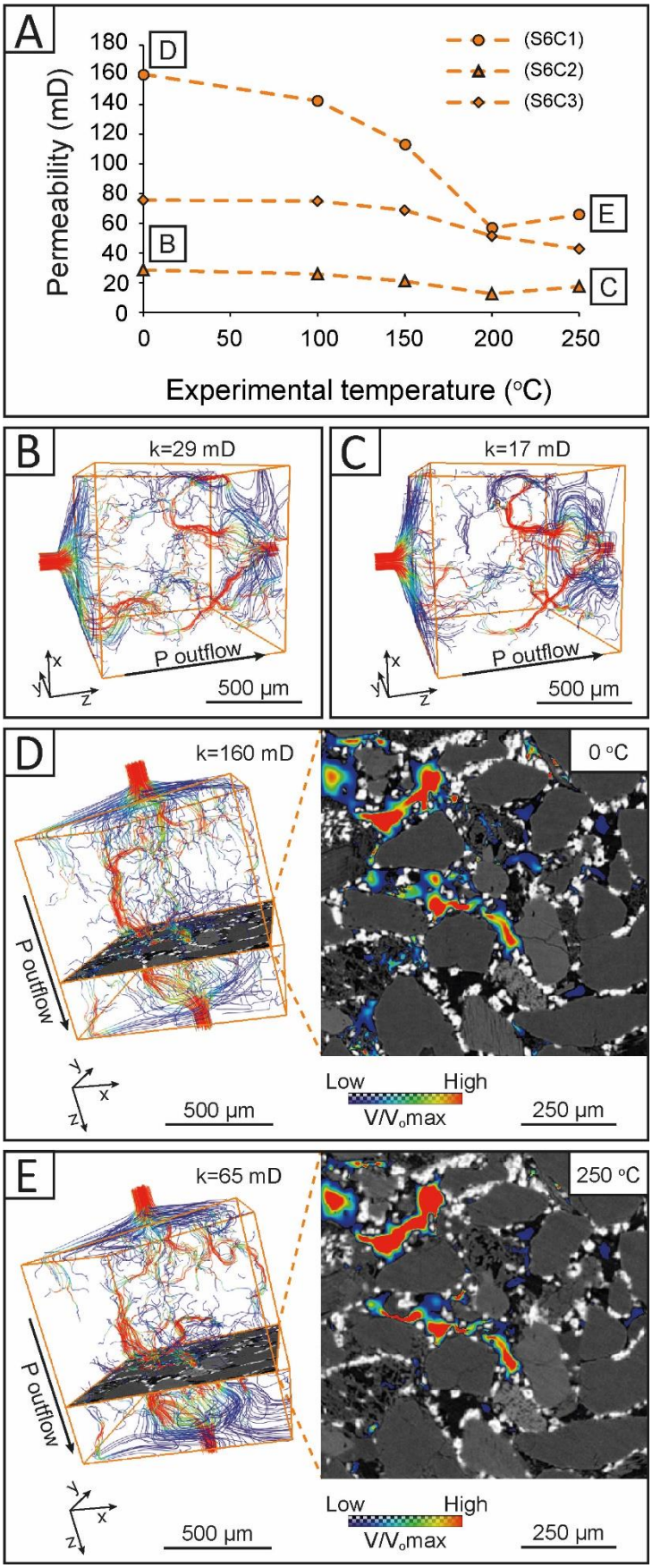

Figure 4.8: Absolute permeability simulation of 500 voxel^3 subvolumes (S6C1-C3) extracted from sample S6. The error associated with the presented XCT measurements is <0.1% (see Appendix A). A) Permeability evolution with increasing

temperature. The main reduction window lies between 150 and 200 °C. B) Permeability model of sample S6C2 prior and after (C) to hydrothermal treatment at 250 °C. Red streamlines represent preferential fluid flow pathways, while blue indicate areas of reduced velocity magnitude. Colour of streamlines shows the velocity normalized to the maximum velocity in the pre-treatment sample. D) Pre- experiment permeability model of sample S6C1 with associated 2D velocity magnitude map. E) Permeability model and 2D velocity magnitude map at 250 °C. The maps are normalized to the maximum velocity value derived from the pre-experiment permeability simulation. Permeability reduction is attributed to the extinction of low-velocity magnitude pathways, mainly associated with microporous material.

4.7 Discussion

The experimental results presented in this research have identified an association between grain coat increase (total volume) and ceasing of porosity loss in the 3D domain. Pore network and permeability models yield similar behaviour.

4.7.1 Grain coat and porosity volume versus experimental treatment and image resolution

The analysis of the single-stage samples (S1-S5, 3.8 µm/voxel) shows a grain coat volumetric increase of ~ 9% (from 16.8% to 15.5%) at 250 °C, whereas the multi-step sample (S6B, 1.7 µm/voxel) presents an increase of ~ 4%. This difference is partly attributed to the applied multi-scale analysis. To test this, we took a randomly positioned high-resolution subvolume from the pre-treatment S6 data (~ 14.1% coat) and down-sampled the data to match the voxel resolution of the S1-S5 datasets. Reapplying the segmentation workflow (Figure A.5) on the down-sampled data yields a grain coat volume of ~ 18.5%, caused purely by the difference in resolution between the two images. This is further validated by the equal drop of porosity (from ~ 13.3% to ~ 8.5%) after down-sampling. Considering this difference when calculating the grain coat volume increase from 0 °C to 250 °C we infer a calculated value of ~ 5.2% for the down-sampled data, 31% higher than the ~ 4% calculated for the high-resolution data. However, this is still lower than the ~ 9% volumetric increase recorded for the single-stage sample implying an additional influencing parameter derived from the experimental treatment each sample has experienced (discussed in section 4.3).

The accuracy of any image-based analysis of pore geometries or subsequent flow simulation is influenced by the pore segmentation (Iassonov et al. 2009; Peng et al. 2014). Higher resolution images will always allow more precision and better capture of fine porosity but will also mean a smaller area or volume being analysed. The down-sampled data of the 1.7 µm/voxel dataset yielded a porosity comparable to that of the 3.8 µm/voxel dataset (~ 8.5 %) suggesting that the 3.8 µm/voxel data are unable to resolve the 50% of the porosity that is in the smallest pores.

4.7.2 Physical- versus XCT-based porosity measurements and role of microporous clay

When compared with helium pycnometry measurements, low-resolution tomography-based porosities are significantly lower. The initial XCT-based image porosity (mean 6.6%, 3.8 µm/voxel) of the single-stage samples is lower than the helium pycnometry value (~ 28%) (Charlaftis et al. 2021) for the same sample volume (the cylindrical volume). In accordance with previous studies, significant differences between the two techniques are to be expected, given the spatial scales of the measurements (Callow et al. 2020). Here, the samples being analysed are the same, and the difference is caused by the spatial resolution of the XCT data. The missing porosity is mainly credited to the unresolved microporous regions (e.g., below the maximum voxel resolution) that contribute to the total porosity (Saxena et al. 2019), and to a lesser extent, to partial volume effects occurring between high-contrast edges (e.g., grain coats and void space).

An appraisal of those parameters was performed on sample S6B (1.7µm/voxel), which presents an initial XCT-derived porosity and microporous volume of ~ 14.5% and ~ 10%, respectively (Figure 5A). Pore space within the clay mineral fraction is dominated by disconnected intragranular micropores (Milliken and Curtis 2016). Depending on texture, approximately 61% of the bulk volume of diagenetic kaolinite is microporosity (Hurst and Nadeau 1995). Blocky compact kaolinite minerals present an average microporosity of 20% (Alansari et al. 2019). By adding the estimated microporous volume, the XCT-derived total porosity increases to ~ 20.5%, compared to a helium-derived value of ~ 28%. Although sample S6B is not volumetrically equal to samples S1-S5, the higher resolution imaging increases the pore volume quantified from the XCT data.

4.7.3 Diagenetic evolution and subsequent influence on reservoir quality

The difference in the diagenetic history between the single- and multi-stage samples is reflected in the evolution of the grain coating material.

In both scenarios, the grain coat volumetric increase is attributed to the development of chlorite coats (Figure 4.6C) which can be formed by siderite replacement and neoformation on precursor-free substrate surfaces. The progressive temperature increase adopted in the multi-stage treatment causes a gradual dissolution of the siderite crystals. In contrast, the single-stage treatment instigates an abrupt decomposition associated with dissolution voids at the central parts of the siderite crystals (Charlaftis et al. 2021). The rapid siderite decomposition promotes a higher concentration of Fe ions, thus increased chlorite precipitation rates given sufficient temperatures. Based on our observations, precipitation rates are temperature-dependent and not time-dependent. Irrespective of experimental duration, both treatments suggest a synchronous,

temperature-wise, initiation of chlorite development. This validates the widely held view that temperature is the principal control on chlorite coat authigenesis (Hillier 1994; Ajdukiewicz and Larese 2012).

The hydrothermal experiments were all performed in a silica supersaturated system, yet the main mineralogical change causing porosity reduction is the evolution of the pore-filling kaolinite (Figure 4.6D), not the development of quartz cement overgrowths. Temperature increase coupled with silica availability and the observed dissolution of feldspars assist the transformation of kaolinite to dickite. The initiation of this replacement occurs at ~ 150 °C, comparable to natural systems where it is reported to occur in the temperature range of 110–165 °C. (Ehrenberg et al. 1993; Beaufort et al. 1998).

The experimental results suggest that the authigenic chlorite coats develop in preference to quartz cement at temperatures > 150 °C. The overall grain coat volumetric increase is crucial for the effectiveness of quartz cement inhibition by offering fewer nucleation sites for quartz to precipitate. It also provides a mechanism for preserving effective storage space and connected pathways for unrestricted fluid flow at the pore scale. Figure 4.9 summarizes the main diagenetic processes observed during the hydrothermal treatment.

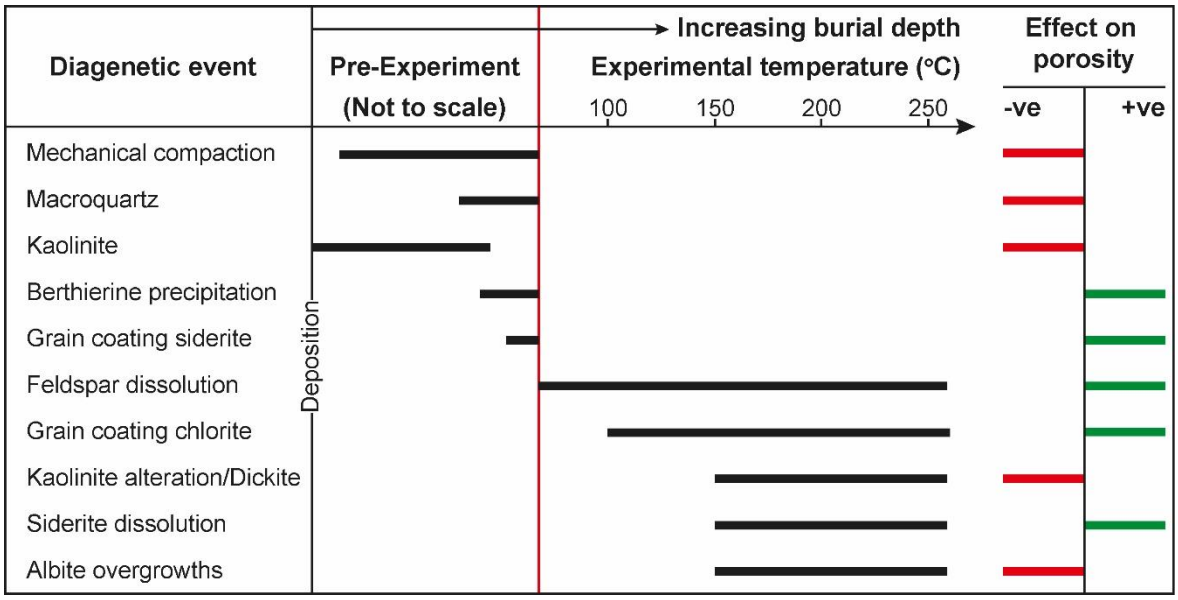

Figure 4.9: Paragenetic sequence of the main diagenetic processes occurring before and during the hydrothermal experiments with an indication regarding the effect on porosity of each. The experimental temperature range of each process is based on the 2D and 3D analysis performed by Charlaftis et. al 2021 and the present chapter. Red line separates the pre to post-reaction diagenetic events. Temperatures used replicate those commonly encountered in many deep burial diagenetic sedimentary successions. Temperatures higher than 200 °C have been included to allow reactions to take place through to completion and within a timeframe suitable for the research undertaken.

The evolution of the pore networks indicates that the magnitude of diagenesis governs the pore and throat sizes and pore connectivity. The decrease in size of pore and throat radii is attributed to the progressive kaolinite cement evolution and, to a lesser extent, to albite overgrowth development. Kaolinite progressively chokes primary pores, and many of the throats have been completely sealed resulting in fluid flow restriction. The permeability models indicate that, between 150 °C and 200 °C, initial areas of reduced velocity magnitudes are converted to preferential fluid flow pathways, whereas others cease to exist. This suggests that microporosity plays an important role not only in the ability of rocks to store fluids but also to permit fluid flow. The dissolution of unstable grains, such as feldspars, and the pore filling kaolinite cement drive increased flow to parts of the network that initially had low flow velocity magnitudes. At temperatures higher than 200 °C permeability is stabilized. Dissolution pore space becomes interconnected with intergranular pores, thereby maintaining an open pore system with improved effectiveness.

4.7.4 Future work

Natural diagenetic conditions cannot be fully reproduced in the laboratory due to the short experimental time compared to a geological timeframe and the simplification and uncertainties associated with the chosen aqueous chemistry. However, the experimental approach presented here reveals the changing pore-throat characteristics and identifies the critical threshold temperature above which the increase in grain coat volume prevents further porosity reduction. Targets for future experiments would be prolonged experimental times and an X-ray compatible hydrothermal setup to allow observation during precipitation. This would permit better constraint of the temporal changes in porosity and the associated changes in permeability. From the technical perspective, synchrotron-based imaging with monochromatic X-rays would also help to capture phase distribution (e.g., chlorite and siderite) that cannot be easily resolved by lab scanners.

4.8 Conclusions

The integration of hydrothermal experiments coupled with XCT 3D quantitative assessment and microscopic and modelling techniques provides an opportunity to probe the evolution of petrophysical and mineralogical properties of sandstone reservoirs across a continuum of temperature scales. This work presents the analysis of two sets of hydrothermal experiments on naturally occurring sandstone samples, using an artificial silica supersaturated solution, at specific temperature steps (i.e., from 0 °C up to 250 °C), in an attempt to glean more information and gain greater understanding on burial diagenesis and its implication on reservoir quality. Quantitative datasets, per experimental set, regarding; i) the volume of grain coats and microporous material,

ii) pore-throat characteristics and iii) porosity and permeability, were produced. The main findings of this study are:

1. A 3-dimensional quantitative confirmation of the effectiveness of grain coats on porosity preservation in high-temperature sandstone reservoirs. Regardless of the experimental duration, the XCT analysis identified that grain coat volumetric increase initiates at ~150 °C and becomes dominant between 200 °C and 250 °C. SEM analysis revealed the synthesis of authigenic chlorite coats that are morphologically akin to naturally occurring chlorite coats. The newly precipitated chlorite coats alongside the pre-existing siderite grain coats contribute to the inhibition of quartz cementation and the cessation of porosity loss during the same temperature interval.

2. The main porosity-reduction window lies between 150 °C and 200 °C and is mainly associated with the evolution of pore filling kaolinite blocking primary pore space and the destruction of microporosity.

3. The samples from the single-stage heating approach were scanned with a spatial resolution of 3.8µm/voxels showing a ~ 9% volumetric increase of the grain coating material at 250 °C. Porosity remained unaltered up to 150 °C and reduced by ~ 13% at 200 °C and ~ 20 % at 250 °C. Porosity models have captured the reduction in the pore-throat connectivity as well as the reduction of the pore and throat sizes with increasing temperature. The mean coordination number was reduced from 3.3 to 2.5, the pore radius from ~ 126 to ~ 115 µm and the throat radius from ~ 27 to ~ 23 µm at 250 °C. Permeability was reduced from ~ 26 mD (200 °C) to ~ 22 mD (250 °C).

4. The higher resolution scans (e.g., 1.7 µm/voxel) of the multi-stage sample showed a volumetric increase of the grain coating material of ~ 4 % from 200 °C onwards. The AQM analysis identified the presence of ~ 14%, by weight, chlorite content. Porosity was reduced by ~ 32% at 200 °C and ~ 37 % at 250 °C. The mean coordination number was decreased from an initial value of 8 to 4.9 at 250 °C, and the mean pore and throat radius was decreased by 2 µm. The microporous material was diminished by ~ 50%. Permeability evolution of three analysed cubic subvolumes decreases mainly between 150 and 200 °C.

The 3D quantitative data can be used to improve predictability of reservoir quality modelling in high-temperature (>150 °C), deeply buried reservoir sandstones.

Chapter 5: Interdependence between bacterial EPS and early grain coat development

The study presented in the current chapter used an experimental method to demonstrate proof of principle of the approach taken, showing that bacterial biofilms, with progressive temperature increase, can be associated with grain coat formation.

5.1 Summary

Bacteria are the most abundant forms of life we know on our planet, able to survive in a variety of habitats, that also play an important role in mineral formation and transformation processes. This is especially true in the case of clay minerals due to their abundance in soils and sediments. In natural environments, clay minerals have been found in extracellular polymeric substances (EPS) derived from bacterial biofilms, thus indicating that EPS facilitate their nucleation. Here, we present laboratory experiments in which unconsolidated quartz grains were seeded with *Geobacter sulfurreducens* cells and exposed to a mineral medium solution for 96 hours at temperatures of between 60 and 120 °C. The experimental data show the interdependence between EPS and the early formation of grain coating material. Initially, the occurrence of EPS promotes the development of web and bridging structures binding the sand grains and creating EPS-coated surfaces. With increasing temperature, an amorphous mineral phase grows preferentially on these surfaces suggesting that EPS can act as a template for mineral nucleation. At temperatures > 100 °C, the order of crystallinity of the amorphous phase increases, transitioning to poorly-ordered structures with rosette-like textures.

5.2 Introduction

Grain-coating clays in sandstones have long been demonstrated to act as effective barriers preventing quartz cementation through offering fewer nucleation sites for quartz to precipitate, especially during prolonged burial diagenesis (Bloch et al. 2002). Authigenic chlorite is the most reported effective grain-coating clay occurring in sandstone reservoirs (Huggett et al. 2015; Dutton et al. 2018; Stricker and Jones 2018; Worden et al. 2020) and is likely to result from the transformation of precursor clays (Charlaftis et al. 2021) formed during deposition or soon afterwards (Bloch et al., 2002). Detrital clay aggregates, potential sources for diagenetic chlorite coats, have been found on sand grains in modern estuarine environments (Dowey et al. 2017; Wooldridge et al. 2017a; Virolle et al. 2019a) where bio-sediment interaction is prominent.

Microbial activity at the sediment-water interface promotes the development of biofilm structures. Biofilm is defined as an assemblage of microbial cells of multiple species, such as bacteria, archaea, fungi, cyanobacteria, algae and other microbial eukaryotes, attached to a surface and embedded in a matrix consisting of extracellular polymeric substances (EPS). EPS consist of organic molecules such as polysaccharides (50-90%), proteins, lipids and nucleic acids (P. Stoodley et al. 2002). EPS are structurally and functionally essential for biofilm growth and stability and are believed to be involved in the initial steps of microbial adhesion to surfaces (Costa et al. 2018).

In estuary and shallow lagoonal settings, most sediment is composed of noncohesive, unconsolidated sand grains. Biofilms provide important ecosystem functions, including sediment stabilization (Vignaga et al. 2013; Paterson et al. 2018), sediment transportation and bedform stabilization (Malarkey et al. 2015; Schindler et al. 2015). For example, diatom movement in near-surface sediments is facilitated by EPS stands, which produce a sticky web bridging grain surfaces (Higgins et al. 2003). Therefore, EPS contributes to the sediment fabric by enhancing the cohesive forces between sediments and changing the micromorphology of individual grains (Van Colen et al. 2014).

Numerous studies document microbe-clay mineral interactions and their importance in geological processes (Folk and Lynch 1997; Douglas and Beveridge 1998; Konhauser and Urrutia 1999; Dong 2012; Cuadros 2017). Minerals affect the physical environment where microorganisms live and support microbial growth by providing essential nutrients, while biofilm structures support mineral genesis and or transformation by providing the chemical conditions and nucleation sites necessary. Precipitation from solution, weathering of silicate minerals, and transformation of pre-existing clay minerals are the main routes leading to clay mineral formation through microbe-clay interactions.

A two-step process proposed for the biogenic clay authigenesis includes the initial encrustation of iron surrounding cells or filaments followed by Al-Si complexion (Konhauser et al. 1993; Konhauser and Urrutia 1999). This initial cellularly-bound iron phase acts as a ligand that promotes the precipitation of an amorphous, poorly crystallized aluminosilicate phase engulfing the cell wall or EPS. Further mineralization results in more crystalline phases (Sánchez-Navas et al. 1998) tangentially oriented to the substrate surface (Konhauser and Urrutia 1999). Ueshima and Tazaki (2001) showed that EPS of biofilms could serve as a template for layer-silicate synthesis. Nontronite (e.g., iron-rich smectite) layers were found embedded in EPS from metalliferous sediments of the Iheya Basin, Japan, suggesting that EPS catalyses the precipitation of the mineral. Nontronite formation was induced by the accumulation of Si and Fe ions from the ambient sea water (Ueshima and Tazaki 2001).

Wooldridge et al. (2017a) identified a positive statistical correction between sediment biofilm abundance (chlorophyll-a) and clay-coat coverage in the intertidal siliciclastic sediments of the Ravenglass Estuary (UK). Duteil et al. (2020) performed laboratory experiments producing clay-coated quartz sands, texturally akin to those observed in modern and ancient estuarine sands, by mixing EPS, derived from intertidal diatom biofilms, with clay minerals and quartz reference materials. The produced clay coats resulted from the interaction of the EPS with the basal surface and the particle edge sites of the clay mineral platelets.

The findings of the aforementioned experiments are associated with microorganisms living in aquatic environments. However, close occurrence of biofilms and clay minerals can also be found in the soil microbiome, where bacteria are the most abundant and diverse organisms. In this study, bacterial-biofilm-rich, pure sand samples were synthesized and used in hydrothermal experiments to test the influence of biofilm communities and EPS on early mineral precipitation and identify potential alterations with progressive temperature increase simulating burial diagenesis. The specific questions being addressed are: (1) how the biofilms coat the sand grains, (2) do biofilms act as a growth surface, (3) is the stickiness of the biofilms the main reason for clays to coat the surface of quartz grains, and (4) does mineral authigenesis continue on biofilm surfaces only or expand on clean grain surfaces with increasing temperature? An artificial solution was used for the synthesis and preservation of the microbial communities and also used to promote mineral precipitation during each experimental run. Textural and mineralogical evaluation of the samples and determination of the elemental composition of the associated experimental solution was performed using scanning electron microscopy (SEM), energy-dispersive X-ray spectroscopy (SEM-EDS), X-ray diffraction (XRD), and triple quadrupole inductively coupled plasma mass spectrometry (TQ ICP-MS). The experimental results provide important insights into the role played by EPS growth and temperature on clay mineral nucleation and subsequent diagenetic evolution.

5.3 Materials and methods

The experimental process followed in this research is based on the following requirements: (1) to ensure the production of EPS that bridge and coat the pure sand grains, (2) the artificial solution is enriched with the correct geochemical components to sustain the development of biofilm communities, and, with progressive temperature increase, allow mineral nucleation, and (3) the use of quartz as a substrate acts as a silica source, important for mineral formation.

5.3.1 Sand grains and microorganism and cultivation

Unconsolidated pure quartz sand grains were used as a template for the development of biofilm communities. Biofilm growth was laboratory-synthesized using *Geobacter sulfurreducens* cultures, selected for their wide distribution in soils, freshwater and or marine environments (Coates et al. 1996; Lonergan et al. 1996; Venkateswaran et al. 1999; Lovley et al. 2004). The *Geobacter* cultures were obtained from laboratory stocks from the University of Tübingen (Germany).

The strains were cultivated in the dark under anoxic conditions (N_2:CO_2; 90:10 headspace) at 35 °C in a modified mineral medium (pH 6.8, Table 5.1 and 5.2) with the addition of 40 mM fumarate as electron acceptor, 25mM acetate as electron donor, and 2 mM cysteine. Growth and cell concentration were monitored by optical density measurements at 600 nm (OD600). Stationary

phase cultures of *G. sulfurreducens* were harvested by centrifugation at 5000 rpm at 10 °C three times for 20 minutes and washed with bicarbonate buffer (30 mM, pH 6.8) to prepare a cell suspension with a final cell density of 10^9 cells/mL.

Salts	g	mM	**Buffer**	g	mM	**Additives**	mL/L
KH_2PO_4	0.6		$NaHCO_3$	2.5	30	Trace elements	1
NH_4Cl	0.3	5.61				Vitamin solution	1
$MgSO_4$ x 7 H_2O	0.5	2				Selenite/Tungstate solution	1
$CaCl_2$ x 2 H_2O	0.1	0.68					

Table 5.1: Mineral medium content (per litre of distilled water).

Trace elements		**Vitamins**		**Selenite-Tungstate**	
Compound	mg/L	Compound	mg/L	Compound	mg/L
$FeCl_2$·4 H_2O	1500	Cyanocobalamin	10	NaOH	400
$ZnCl_2$	70	p-Aminobenzoic acid	10	Na_2SeO_3·5 H_2O (Toxic)	6
$MnCl_2$·4 H_2O	100	D(+)-Biotin	2	Na_2WO_4·2 H_2O	8
$CoCl_2$·6 H_2O	190	Nicotinic acid	20		
$CuCl_2$·2 H_2O	2	Ca-D(+)-Pantothenate	5		
$NiCl_2$·6 H_2O	24	Pyridoxamine-Dihydrochloride	50		
Na_2MoO_4·2 H_2O	36	Thiamine-Dihydrochloride	10		
H_3BO_3	6				
HCl 25 %-ig	10 ml				

Table 5.2: Additives content (per litre of distilled water). Trace element solution (Widdel et al. 1983), vitamin solution (Widdel and Pfennig 1981), Selenite-Tungstate solution (Widdel and Bak 1992).

Subsequently, 10 mL of the cell suspension was dispensed in a newly prepared mineral medium (pH 6.8). 50 g of pure sand grains were placed in 250ml serum bottles. 50 mL of the new medium was then added in the bottles under anoxic conditions and let in the dark at 35 °C for incubation. The bottles were manually rotated daily to ensure biofilm development in between the sand particles (Figure 5.1C).

5.3.2 Experimental setup

Hydrothermal reactor experiments were carried out in a Parr© Series 4560 Mini Reactor comprised of a cylindrical 316 stainless steel pressure vessel (600 ml) operating at temperatures up to 350 °C and sealed and secured by means of split rings. The vessel is heated by a quartz fabric mantle housed in an aluminium shell. The temperature during the experiment was controlled within ±0.5 °C by means of a Eurotherm© controller.

Four experiments were performed at temperatures between 60 and 120 °C under strictly closed conditions. For all the experimental runs, a Teflon vessel was used as an additional contamination-preventing measure. The bacteria growth medium was used as pore fluid. The experimental setup is depicted in Figure 5.1A-B.

In each experiment, five grams of the pure sand grains seeded with Geobacter cells were placed in the sample holder, and the sample assembly was lowered into the vessel. The vessel was gradually filled with 100 ml of the mineral medium, sealed, and heated to the experimental temperature at 2.5 °C per minute. All samples were held at the desired experimental temperature for 96 hours before the heater was switched off. Once cooled to room temperature, the vessel was removed from the reactor, and the sample was removed and air-dried.

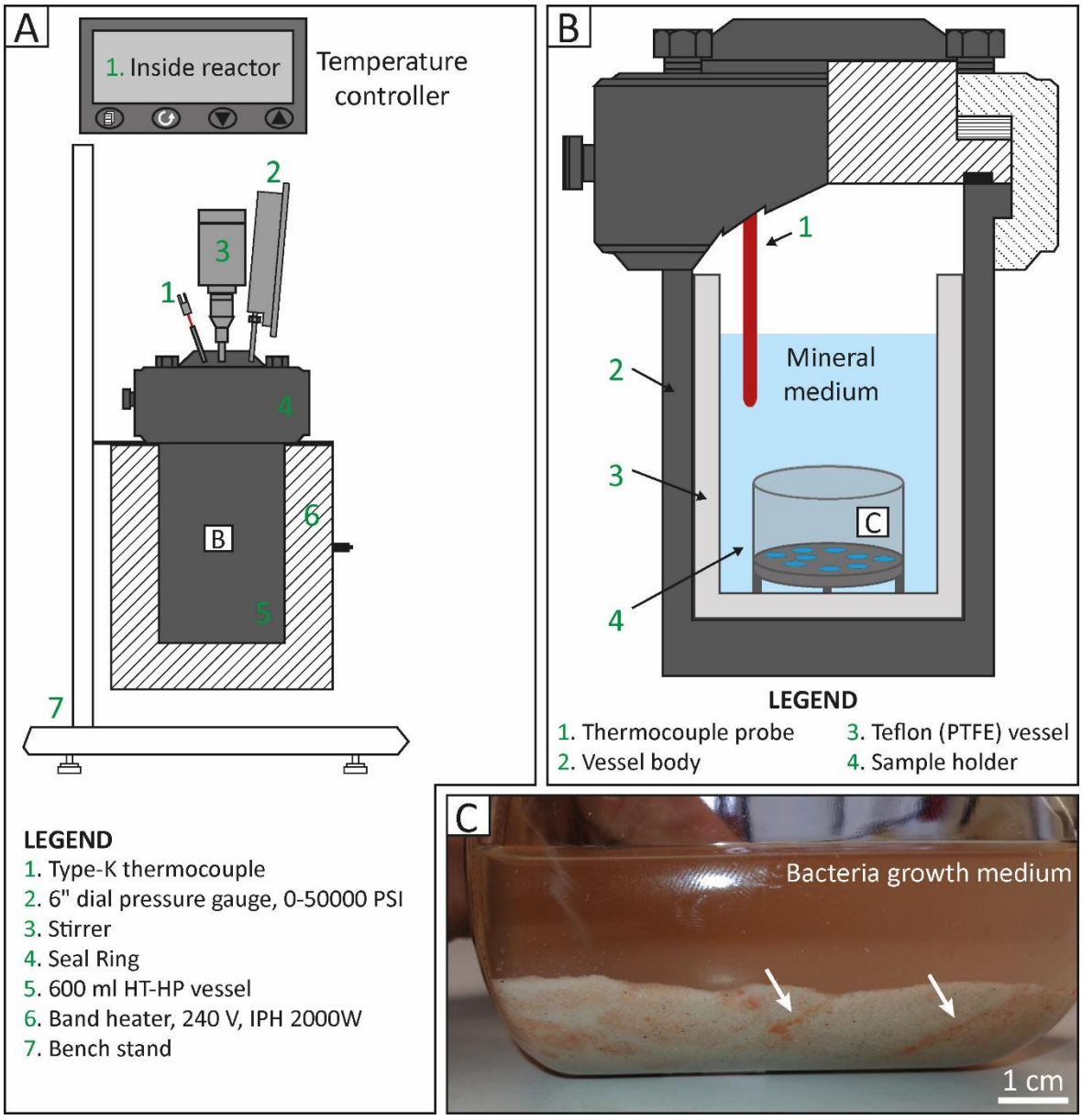

Figure 5.1: Illustration of the experimental setup. A) Schematic representation of the hydrothermal vessel and its main parts utilized for the biofilm experiments. The system comprises solely stainless-steel components and a Eurotherm temperature control. B) The interior of the hydrothermal vessel. C) Pure sand grains seeded with Geobacter cells. Note the biofilm (white arrows) development in between the sand particles.

5.3.3 Analytical techniques

5.3.3.1 Sample mineralogy

The quartz sand samples were studied electron optically using a Hitachi SU-70 field emission gun scanning electron microscope (SEM) equipped with an energy-dispersive detector (EDS). The samples were carbon-coated (20nm) to avoid charging, reduce thermal damage and improve the secondary electron signal. Secondary and backscatter electron imaging was conducted at acceleration voltages of 15 kV with a beam current of 0.6 nA. SEM-EDS was used for rapid elemental identification of the new, due to the experimental treatment, mineral precipitates.

The mineralogy of the samples was also evaluated by X-ray powder diffraction. The bulk unconsolidated sand samples were disaggregated and powdered to a mean particle diameter of between 5 and 10 μm. The sample as a slurry was dried overnight at 80 °C, re-crushed to a fine powder and back-packed into an aluminium cavity mount, producing a randomly orientated sample for presentation to the X-ray beam. Mineralogy was analysed using a PANalytical X'Pert3 Diffractometer, an MPD Goniometer with graphite monochromator (copper anode at 40 kV, 40 mA) and a 45 position automatic sample changer. The analysis was performed at 2θ angles between 4.5˚ and 75˚, with a step size of 0.013˚/s and nominal time per step of 0.2 s.

The clay fraction (<2 μm fraction) was separated from the bulk sample using ultrasound and centrifugation. A 25 ml aliquot of the clay suspension was evaporated to dryness at 80 °C, and the total weight was determined. The samples were analysed as an untreated clay, after saturation with ethylene glycol vapour overnight and heated at 380 °C for 2 hours and 550 °C for 1 hour. The samples were then analysed at 2θ= 3–35° (step size of 0.05° per second).

5.3.3.2 Evaluation of the artificial solution

Aqueous bulk solutions were analysed to establish the elemental composition before and after the experiments at 60, 80 and 100 °C. Liquid fraction could not be obtained from the hydrothermal vessel after the experiment at 120 °C as the solution was consumed by the reaction. The measurements were performed using a Thermo Elemental triple quadrupole inductively coupled plasma mass spectrometry (TQ ICP-MS) using a combination of single quad kinetic energy discrimination (KED) and triple quad (using O_2 as the reaction cell gas) modes to remove potential interferences and hence enhance accuracy. A preliminary scan of the samples was used to outline elemental abundances, and then synthetic multielement standards were created from ICP grade single element standards to cover the range of abundances anticipated for each element. The samples were diluted 20-fold prior to measurement; this has been corrected in the following data. A Rhodium (Rh) internal standard was used to correct for inter-sample signal drift.

5.4 Results

5.4.1 Sand grains pre- and post-biofilm growth

The initial unconsolidated pure sand samples were composed of quartz grains of subangular to subrounded shape. SEM imaging indicated that some grains showed smooth surfaces while others showed prominently etched and or conchoidal fracture surfaces (Figure 5.2A-D).

The associated EDS analysis (e.g., spectrum 1–8, Table 5.3) confirms that the starting material is quartz and shows the low Si content in regions of quartz surfaces covered by biological material. EPS connect to quartz grain surfaces developing webs (Figure 5.2E-F) and strands (Figure 5.2G-H) that link individual sand grains and bridge the void space between them.

Experimental Temperature	**Spectrum**	**Elements**									
		O (%)	**Si (%)**	**Na (%)**	**Mg (%)**	**Fe (%)**	**K (%)**	**Ca (%)**	**S (%)**	**Cl (%)**	**P (%)**
0 °C (Pure sand)	1, 2, 3, 4	67.7	33.3	-	-	-	-	-	-	-	-
0 °C (Biofilm-rich pure sand)	5	64.9	31.6	3.1	-	-	0.1	0.1	-	0.2	-
	6	43.5	3.9	42.2	1.5	-	1.1	0.2	2.5	3.1	2
	7	40.6	0.4	45.6	1.1	-	1.7	0.3	3	5.1	-
	8	47.5	1.6	31.3	3.4	0.4	1.6	1.6	2.5	4.1	6
60 °C	9	55.4	14	18.3	2.3	-	0.7	2.2	1	1.8	4.1
	10	43.7	0.9	36.7	3.5	-	1.2	3.1	1.4	4.7	4.9
	11	53	10.5	27.2	1.9	-	0.4	1.2	3.1	0.4	2.3
80 °C	12	61.8	23.6	9.6	1.9	-	-	1.4	-	-	2.3
	13	61.1	26	10.5	2.5	-	-	-	-	-	-
	14	63.2	24	4	1.9	-	-	5.2	-	-	1.7
100 °C	15	43.7	4.9	39.7	3.4	-	1	0.6	1.9	3.3	1.5
	16	61.1	22.2	11.1	1.9	-	-	1.4	-	-	2.3
	17	52.4	12.5	21.9	9	0.2	0.4	0.4	0.7	1.3	1.2
120 °C	18	66.4	33.1	0.5	-	-	-	-	-	-	-
	19	56.9	22.9	15.5	0.7	-	1.7	-	-	1.6	0.7
	20	40.4	2.8	44.9	0.4	-	2.7	-	1.8	4.8	2.1

Table 5.3: Quantification results of the SEM-EDS elemental analysis of spectrum 1-20 as shown in Figure 5.2–5.5. All data are reported in atomic percent normalised to oxygen by stoichiometry.

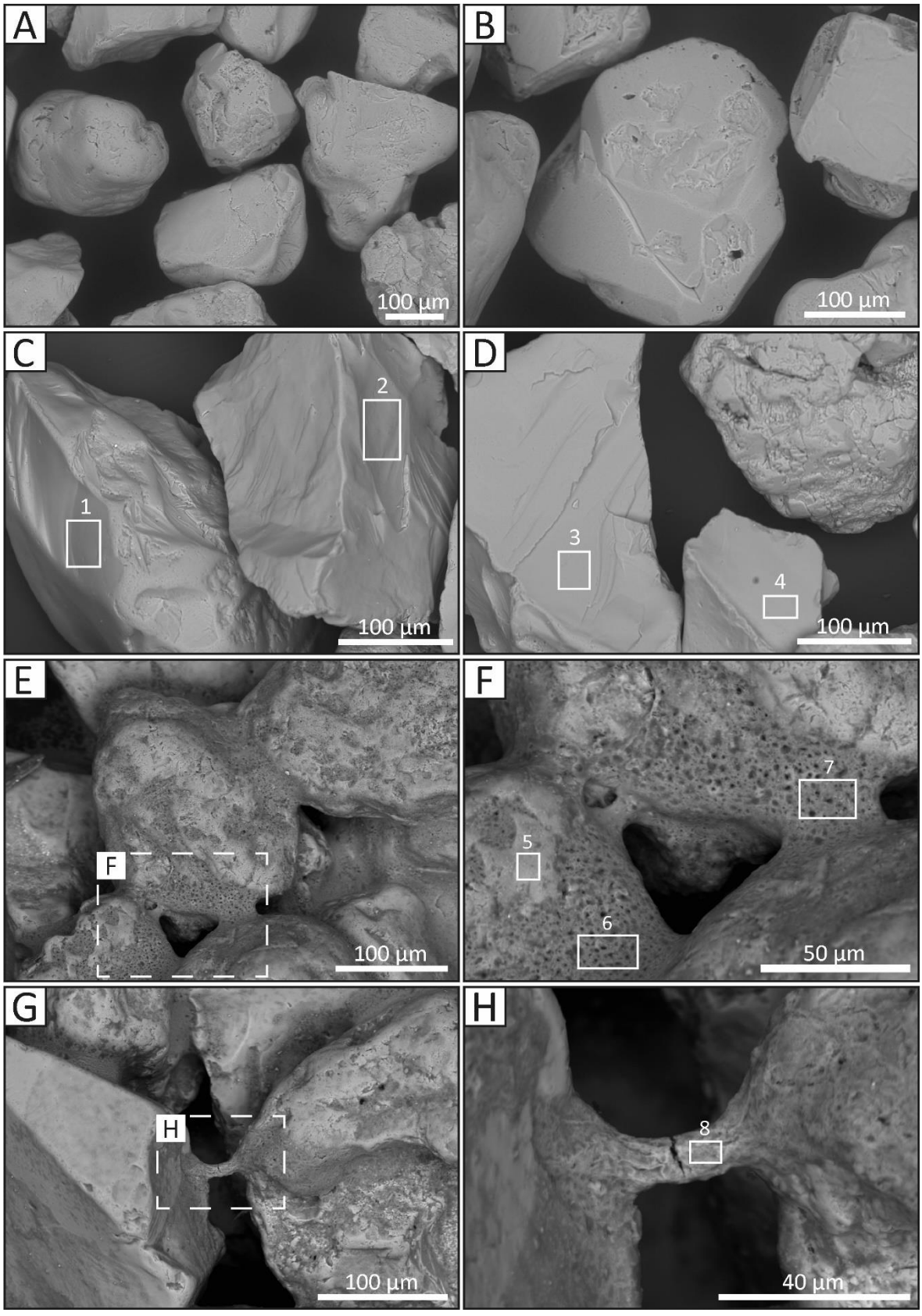

Figure 5.2: Pure sand (quartz) sample (starting material) before and after being seeded with Geobacter cell forming biofilm structures. Diverse types of quartz grains were present. For the associated EDS analysis (e.g., spectrum 1–8) refer to Table 3. A) SE image of the unconsolidated quartz grains, B) Some grains are rounded to sub rounded, C) Some grains showed conchoidal surfaces, D) Some grains showed etched surfaces. E) Binding of quartz grains by the extracellular polymeric

substances (EPS) matrix of the Geobacter biofilm structures. F) EPS web linking quartz grains. G, H) Bridging structure between two quartz grains due to EPS strands.

5.4.2 Hydrothermally treated biofilm-rich sand samples

At 60 °C, spheroidal aggregates are developed on the surface of the host grains (Figure 5.3A-D). The EDS analysis indicates the presence of Mg in regions of quartz surfaces covered by the neoformed mineral precipitates. At 80 °C, the formation of a clay-like material is linked to EPS strands and webs (Figure 5.3E-H). Mineral growth appeared to be favoured at cavities and edged surfaces of the biocoated grains (Figure 5.3E, F). The crystals are strongly curled, and individual crystals cannot be resolved. Additionally, rhombic-shaped crystals appeared mixed with the amorphous material as well as on EPS-free surfaces (Figure 5.3E, H).

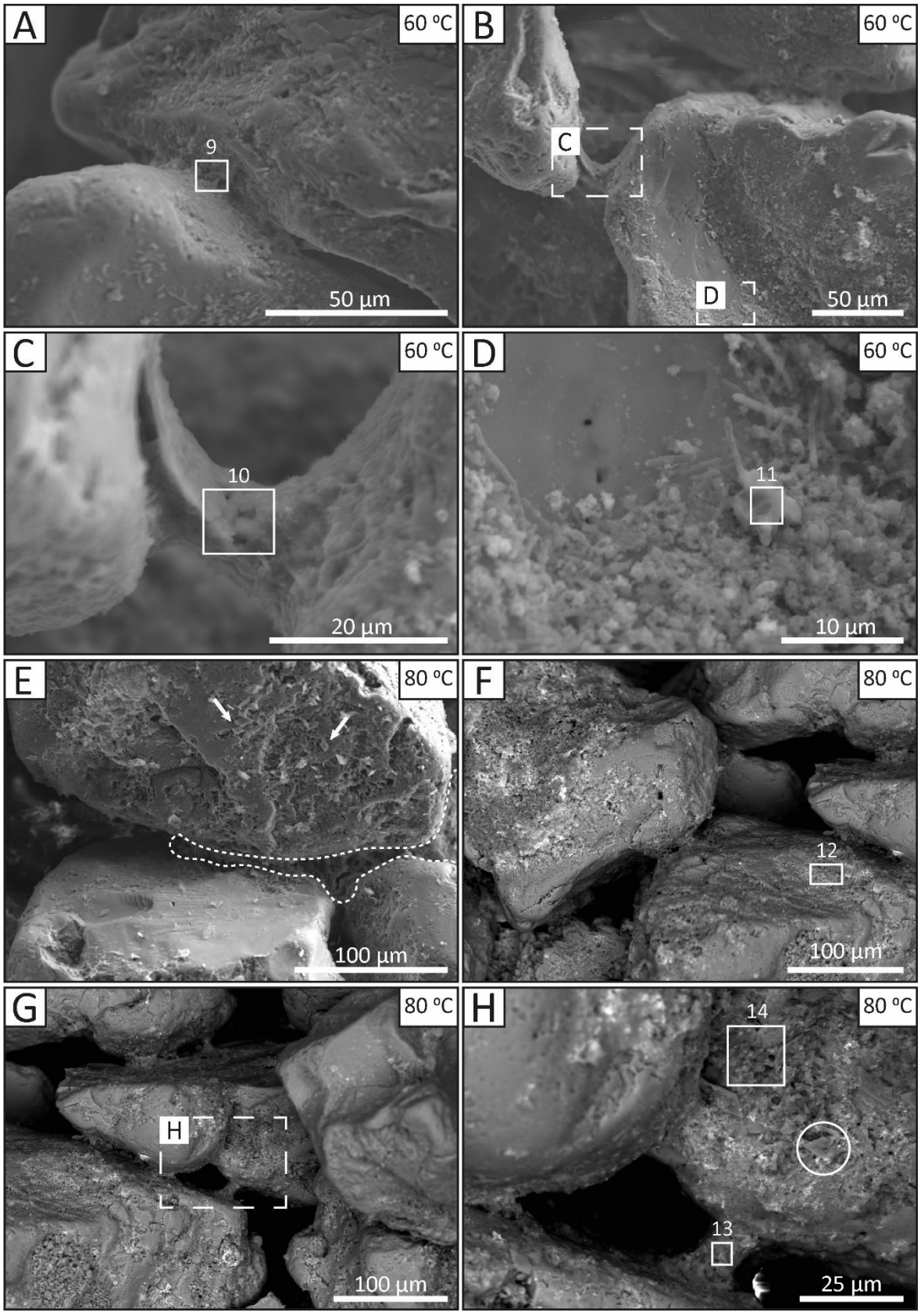

Figure 5.3: SEM photomicrographs of quartz grain samples with developed biofilm structures and neoformed mineral phases after hydrothermal treatment at 60 °C (A–D) and 80 °C (E–H). For the associated EDS analysis (e.g., spectrum 9–14) refer to Table 3. A) Binding of quartz grains due to EPS. B, C) Preserved EPS strands. D) Zoomed in area of (B) showing the spherical humps on the surface of the host grain. E) SE image showing the contact between two quartz grains. Note the change in the texture of the binding material. Rhombic-shaped crystals developed on EPS-free quartz grain surfaces

(arrows). F, G) BSE images showing new mineral precipitates partially covering quartz grain surfaces. H) BSE image showing the preservation of an EPS strand. Note the amorphous material adjacent to the contact between the quartz grains and the rhombic-shaped crystals (circle) blended in the amorphous phase after the hydrothermal treatment.

After the hydrothermal experiment at 100 °C, the loose quartz grains transformed to a more rigid framework due to a change of the EPS texture associated with mineral growth (Figure 5.4A). The EPS strands are still preserved, and a thin layer of EPS coating several grains is observed (Figure 5.4B). Mineral precipitation occurs mainly in regions surrounding grains bounded by EPS (Figure 5.4C). The new precipitates are low-ordered structures with chemical compositions differing from the detrital material (Figure 5.4D).

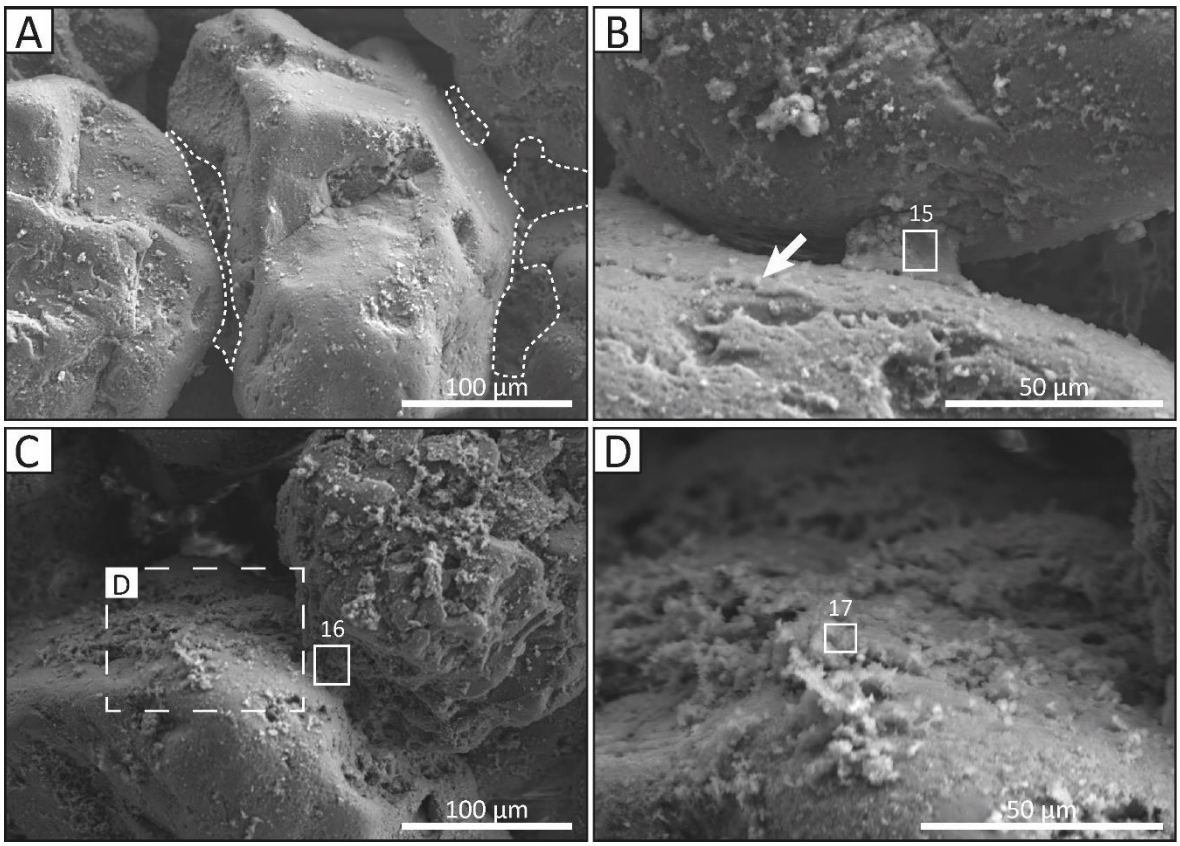

Figure 5.4: SEM photomicrographs after hydrothermal treatment at 100 °C. For the associated EDS analysis (e.g., spectrum 15–17) refer to Table 3. A) The binding of quartz grains (outlined) remains unaltered. B) Only small strands are preserved. Note the presence of a thin EPS layer covering the surface of a grain (arrow). C, D) Microcrystalline material in close proximity to EPS binding two quartz grains.

At 120 °C, quartz grains are partially coated by the neoformed mineral phase with strands and web structures, similar to those developed by the biofilm growth, being the primary targets (Figure 5.5A, F). Sharp contacts between clean quartz surfaces and the regions covered by the grain coating material are prominent. Rosette-like textures, indicative of an increase of the order of crystallinity, are also observed (Figure 5.5C).

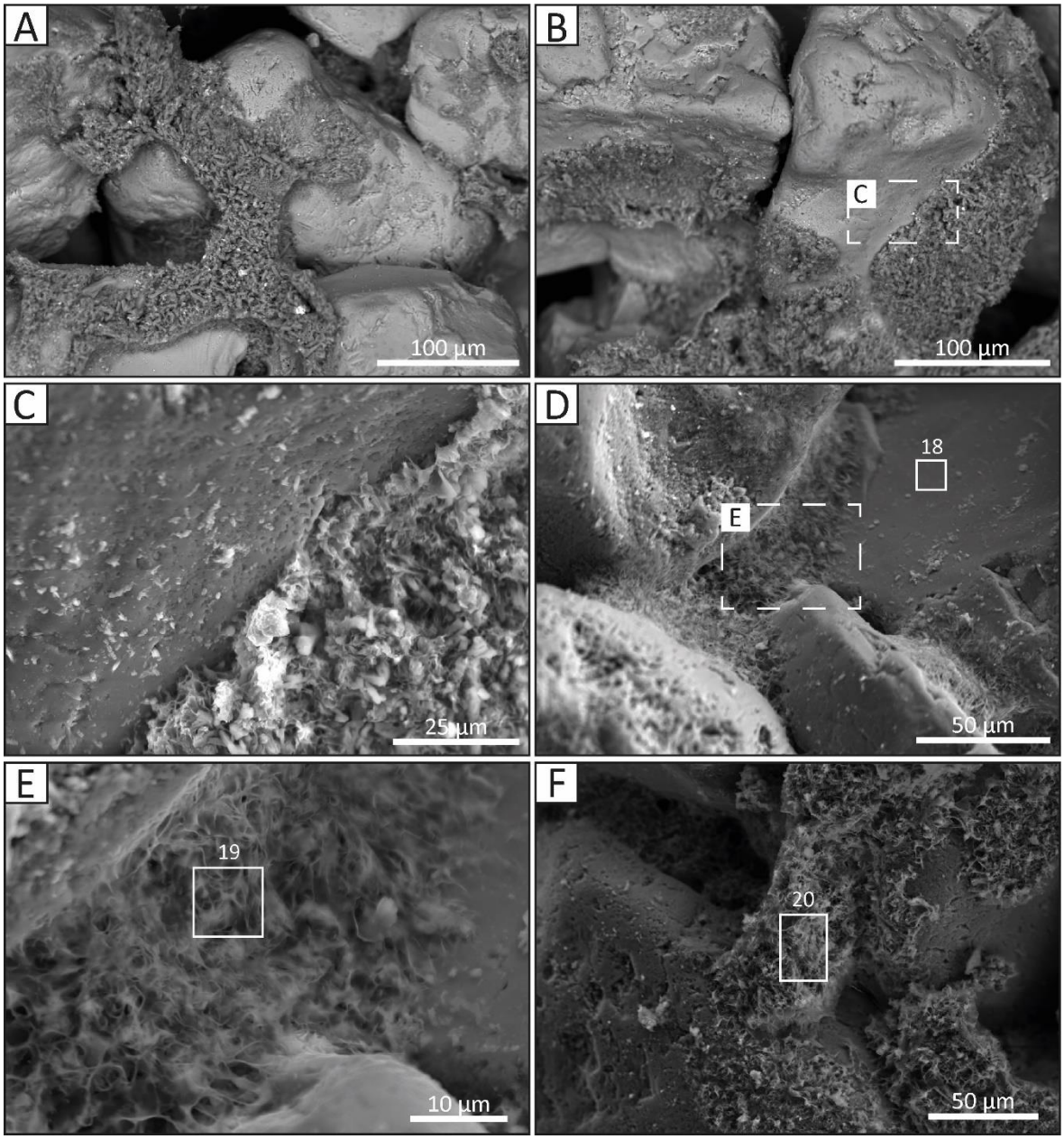

Figure 5.5: SEM photomicrographs showing the interrelation of biofilm structures and neoformed mineral phases after hydrothermal treatment at 120 °C. For the associated EDS analysis (e.g., spectrum 18–20) refer to Table 3. A) BSE image showing the precipitated mineral that forms a web linking quartz grains. The EPS web developed before the experiment possibly acted as a nucleation substrate for the precipitation of the new mineral. B, C) The mineral selectively coats specific regions of the grain, further promoting the hypothesis that mineral authigenesis begins from regions previously coated by EPS. Note the presence of rosette-like clusters. D, E) Mineral authigenesis occurred between quartz grains bounded by EPS before the experiment. F) Strand with extensive mineral growth bridging two quartz grains.

5.4.3 XRD and reacted aqueous solutions

The whole rock XRD and < 2-micron fraction analysis of the pre-experiment sample validated that the starting material is composed solely of quartz (Figure 5.6A, B). The clay-separate analysis could not identify the morphologically clay-like material observed under the SEM. This is likely due to the lack of abundance of the newly precipitated phase either because the amount precipitated is insufficient to be captured by this technique or due to the nature of the phase (e.g., grain coating)

that, even after the ultrasound and centrifugation separation treatment, remained attached to the grains and did not make it into the analysis. However, traces of dolomite were identified at temperatures > 60 °C (Figure 5.6C), suggesting that the rhombic-shaped crystals observed under the SEM are dolomite crystals.

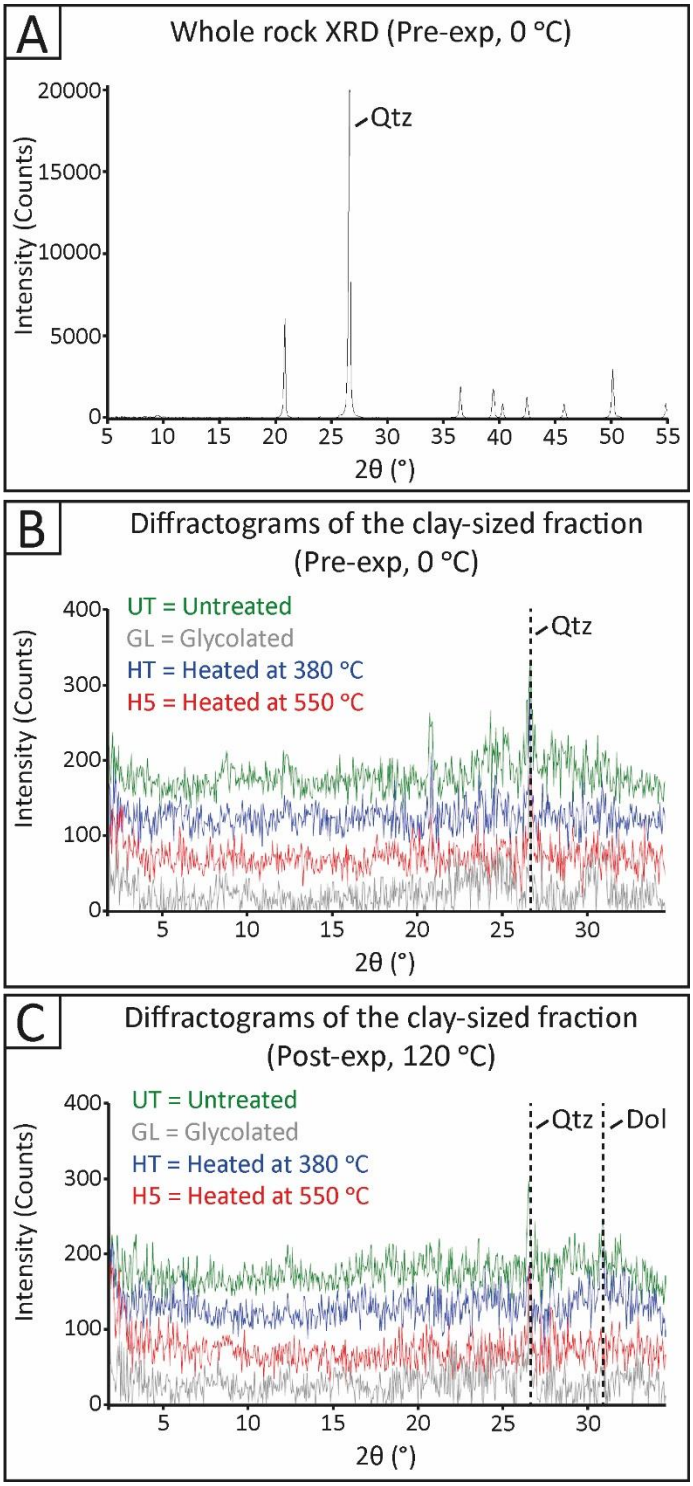

Figure 5.6: Representative XRD patterns of the sand grains used for the hydrothermal treatment. Where Qtz = quartz; Dol = dolomite. A) Whole rock XRD of the initial material. Overlaid diffractograms of the < 2 mm fraction of the pre-exp sample

(B) and the sample hydrothermally treated at 120 °C (C), after the various chemical and heat treatments. Traces of dolomite (peak at 32° 2ϑ) have been identified in samples experimentally treated at > 60 °C.

The elemental concentration of the analysed fluid samples is provided in Table 5.4. The greatest change is observed in the concentration of Mg and Ca, with values decreasing from 48493.2 ug/L to 995.9 ug/L and 2587.9 ug/L to 9.2 ug/L, respectively. A similar decreasing trend, however, volumetrically less significant, is followed by Fe, whereas Na and K remained relatively constant.

Element	Experimental temperature (°C)			
	0	60	80	100
B	105.8	136.4	139.9	137.9
Na	3015082.3	3744446.8	3564936.0	4221123.9
Mg	48493.2	51359.1	25017.3	995.9
K	174499.6	226379.6	209346.6	248416.7
Ca	2587.9	1621.1	887.1	9.2
Mn	11.0	59.2	14.9	0.6
Fe	31.3	12.4	4.3	0.2
Co	38.7	30.6	20.7	8.8
Ni	7.7	132.2	1089.3	244.8
Cu	0.8	7.6	39.8	11.3
Zn	29.6	42.7	18.2	9.3
Se	0.6	0.6	0.8	1.1
Mo	14.0	62.8	1292.4	770.2
W	0.1	1.1	18.6	16.0

Table 5.4: Elemental analysis of the mineral medium at each experimental stage between 0 and 100 °C. Highlighted in green are the elements showing the biggest change that are also commonly associated with clay mineral and carbonate cements. Elemental concentrations are reported in ug/L.

5.5 Discussion

5.5.1 Association of EPS with grain stabilization

Biological cohesion occurs where organic molecules (e.g., extracellular polymeric substances, EPS) are secreted by organisms, such as bacteria and microphytobenthos, that inhabit natural sediments forming biofilms at the sediment surface. The EPS matrix prevents sand grains from moving independently by creating bonds between them (Decho 2000). Our initial experiment of seeding pure sand grains with *Geobacter* cells demonstrates that biofilm colonization preferentially happens on quartz substratum with abraded surfaces and points of contact between sand particles. After the successful adhesion and attachment, further biofilm growth, and thus a significant increase in the EPS content, is controlled by the adsorption of dissolved constituents and sufficient nutrient provision from the aqueous environment.

At near-neutral pH, EPS have a net negative charge in their surface produced by carboxylic, hydroxyl and phosphoryl groups so that they can attract and retain cation species (Cuadros 2017). The presence of monovalent (Na^+) and divalent (Ca^{2+}, Mg^{2+}) cations in the mineral medium (pH=6.8)

used, potentially helped in bridging negatively charged groups within polymers and between the different surfaces of microbes and sand particles leading to biostabilization (de Brouwer et al. 2002; Flemming and Wingender 2010). Therefore, interactions between EPS and the surface of quartz grains could be the result of electrostatic bonds formed between charged groups of EPS and silanol groups (Tang et al. 2015). Additionally, the biocolonization of the unconsolidated sand grains occurred in conditions with low energy impact (i.e., low hydraulic conditions and low mobility of sand particles). This allowed the bacteria to produce and sustain the observed cohesive bio-coating and bridging structures.

5.5.2 Association of EPS with mineral formation

Mineralisation developing in association with bacteria is inevitably dependent upon the available counter-ions, and hence, the chemical composition of the waters in which the microorganisms are growing (Konhauser et al. 1998). Biofilms, owing to their chemical reactivity and large surface area, are considered ideal scavengers of metal cations (Geesey et al. 1988). In our experiments, Mg and Ca cations were bound by the surface of the polymers. The continued adsorption results in surface site saturation, and once critical supersaturation has been reached, critical nuclei become established. With increasing temperature and given the appropriate geochemical components provided by the mineral medium, mineral growth continues abiogenically transitioning from an initial amorphous phase to a low order crystalline material with rosette-like textures (Figure 5.5C).

Except for the morphologically clay-like mineral phase, rhombic-shaped dolomite crystals were also observed; however, their abundance is volumetrically less significant. The limited abundance of the dolomite crystals can be attributed to the fact that amorphous phases have lower interfacial free energies, and hence, a faster nucleation rate than those of more stable, crystalline phases. As a result, Mg is primarily used by the clay-like phase, thus preventing extensive calcium carbonate precipitation on the EPS-coated surfaces. This could also explain why dolomite is sporadically found on EPS-free quartz grain surfaces (Figure 5.3E).

5.5.3 Implications and future work

The work presented here is the first time that experimental work using artificially synthesized bacterial biofilm communities on pure sand particles, has attempted to test the hypothesis that the origin of early mineral grain coats is associated with EPS-coated surfaces. The experimental results suggest that mineral neoformation in the form of grain coats may have an important biotic contribution in various sedimentary environments where EPS-secreting bacteria exist. Further experiments remain to be performed to improve the applied experimental procedure and develop a more comprehensive understanding of these initial findings.

Advanced imaging techniques such as cryogenic focused ion beam scanning electron microscopy (Cryo-FIB-SEM) and cryo-transmission electron microscopy (Cryo-TEM) can be used to maintain samples in as near-to-native as state as possible. This, to decipher more finely the structure of potential mineralized bacteria as well as the first stages of biomineralization.

Before any hydrothermal treatment, a polyethylene cylinder can be used to sample the undisturbed synthesized biofilm-rich sand grains. The samples can then be dehydrated and impregnated with polyester resin under vacuum as described by (Eickhorst and Tippkötter 2008). After polymerization, the samples can be removed from the PE cylinder and visualized using X-ray computed tomography (XCT) to capture the pore space and the inorganic sediment matrix. The XCT-derived surface area of the grains can then be used to calculate the biocolonized surface area per sand grain as described by (Probandt et al. 2018). The procedure can be repeated after each hydrothermal experiment to evaluate whether the surface area covered by the neoformed grain coating mineral phases matches, in approximation, the surface area initially covered by the bacterial communities.

The overall experimental procedure can be repeated using a mixture of reference clay minerals with pure quartz grains that can then be used as a substrate for bacteria cultivation and further hydrothermal treatment. Finally, further experiments can be conducted to investigate how fluid compositions replicating fresh, brackish, and saline waters would impact bacterial cultures and early mineral precipitation.

5.6 Conclusions

1. Unconsolidated pure sand grains were used as a template for the development of bacterial biofilm communities. Biofilm growth was laboratory synthesized using *Geobacter sulfurreducens* cultures and a modified mineral medium. Subsequently, the biofilm-rich sands were hydrothermally treated at temperatures between 60 and 120 °C, simulating early diagenetic conditions. This research has experimentally demonstrated the symbiotic relationship between bacterial EPS and grain coating development.
2. The experimental results provide evidence of the ability of the synthesized bacterial EPS surfaces to serve as a template for mineral synthesis. The formation of an amorphous mineral phase, which is morphologically similar to a poorly developed clay mineral phase, and dolomite crystals was induced by the adsorption of Mg and Ca cations from the EPS surface and further interaction with silicate anions.

3. With increasing temperature, the crystallinity of the amorphous clay phase is also increasing. Rosette textures are observed at temperatures > 100 °C. Dolomite crystals also precipitate on EPS-free surfaces from solution.
4. These initial findings enhance our understanding on the formation of thinly layered grain coating material resembling precursor phases that can potentially govern later diagenetic processes.

Chapter 6: General synthesis, conclusions, and future work

This chapter summarises and discusses the results of the preceding chapters and outlines the main conclusions and opportunities for future work.

6.1 Sandstone reservoir quality and grain coats

A wide range of geoscience applications, including hydrocarbon extraction, subsurface storage, aquifer development and geothermal exploration, rely on predictive models that describe the reservoir properties of a target formation. Especially in poorly explored and constrained regions, prediction of reservoir parameters along with an assessment of the geological development is essential for reducing uncertainties. Realistic reservoir quality predictions require an understanding of how diagenesis, and associated factors, influence porosity and permeability.

Quartz cementation and clay authigenesis profoundly influence the quality of sandstone reservoirs by modifying the nano-to macroscale reservoir properties (Morad 1998; Worden and Morad 2000; Worden and Morad 2003; Taylor et al. 2010; Bjørlykke 2014). Authigenic clay mineral coats, in particular chlorite coats, are often closely associated with high porosities and the absence of quartz cement in deeply buried sandstones (Pittman et al. 1992; Ehrenberg 1993; Berger et al. 2009; Stricker and Jones 2018). Authigenic grain-coating chlorite tends to form continuous layers that line the interface between detrital grains and intergranular pore space. Authigenic chlorite can indiscriminately coat any mineral grain at any orientation (Worden et al. 2020). The completeness of coverage of chlorite grain coats is considered the principal factor dictating the effectiveness of quartz cement inhibition (Ajdukiewicz and Lander 2010; Ajdukiewicz and Larese 2012; Dowey et al. 2012).

Although chlorite has been the subject of many diagenetic studies, no proven method of predicting chlorite coats in data-poor frontier settings exists. In more mature settings where core data are available, the probability of chlorite coats can be assessed using sedimentological and petrographic data sets (Berger et al. 2009; Sun et al. 2014; Stricker et al. 2016b; Dutton et al. 2018; Stricker and Jones 2018). Studies of the distribution of precursor clay coats and chlorite in modern sedimentary environments have revealed that it is imperative to define specific sub-environments of deposition to fully understand and predict chlorite grain coats in ancient and deeply buried sandstones (Wooldridge et al. 2017b; Griffiths et al. 2018; Griffiths et al. 2019a; Griffiths et al. 2019b; Virolle et al. 2019b; Virolle et al. 2020). Additionally, the role of biofilm-EPS, abundant in modern coastal environments (Wooldridge et al. 2017a; Virolle et al. 2019a) in controlling clay coat development with increasing burial, requires further detailed investigation.

Previous temperature-controlled laboratory experiments have investigated clay mineral coat growth and quartz cement nucleation (Pittman et al. 1992; Hillier 1994; Aagaard et al. 2000; Lander et al. 2008; Ajdukiewicz and Larese 2012; Haile et al. 2015), and while these studies provide valuable insight into the effect of diagenesis on rock properties, a quantitative understanding of diagenetic

processes remains challenging. As demonstrated in this study, a multidisciplinary approach comprising hydrothermal experiments coupled with an array of 2D and 3D evaluation techniques can mark a significant step forward in our knowledge of burial diagenetic processes, such as mineral transformations and associated mechanisms, the importance of biofilms for clay authigenesis, and provide quantitative data that can be used to improve predictability of reservoir quality modelling in deeply buried reservoir sandstones.

6.2 Temperature-controlled hydrothermal experiments on naturally occurring sandstone samples

Although natural diagenetic conditions cannot be fully reproduced in the laboratory due to the short experimental time compared to a geological timeframe and the simplification and uncertainties associated with the chosen aqueous chemistry, experimental simulation of diagenesis is critical to provide accurate data of mineralogical and petrophysical properties evolution during diagenesis. In this research, naturally occurring sandstone samples from the Lower Jurassic Cook Formation (Oseberg Field, 30/6-17R, Norway) were exposed to a silica supersaturated Na_2CO_3 (0.1 M) solution for up to 360 hours at temperatures of 100–250 °C. This, to investigate the role played by precursor clays, temperature, and Fe-rich minerals, such as siderite, upon chloritization processes, decline of quartz precipitation, and subsequent preservation of reservoir quality.

The borderline between the eodiagenetic and mesodiagenetic realm is at about 2000 m depth and 70–90 °C temperature (Worden and Burley 2003). The present-day depth and temperature of the Cook Formation is approximately 2400 m and 90 °C, respectively, and therefore an ideal candidate for developing a better understanding about mineral diagenetic alterations occurring during the transition from eodiagenesis to mesodiagenesis. Previous hydrothermal experiments replicating burial diagenesis on the same Formation qualitatively showed that thin, discontinuous, poorly crystalline chlorite precursor coats will start to recrystallize to chamosite at about 70 °C (Aagaard et al. 2000).

Reduced availability of silica in solution results in restricted quartz precipitation at elevated temperatures (Walderhaug 1994; Worden and Morad 2000). In this research, all the experiments started with an excess supply of silica to instigate precipitation of quartz cement and maintain supersaturation throughout the experiments. The experimental temperatures were selected to exceed the commonly accepted threshold of 80 °C for quartz cementation (Walderhaug et al. 2000; Lander et al. 2008) and the threshold of 60 °C proposed for the transformation of Fe-rich precursor clays to chlorite (Ehrenberg 1993; Worden and Morad 2003).

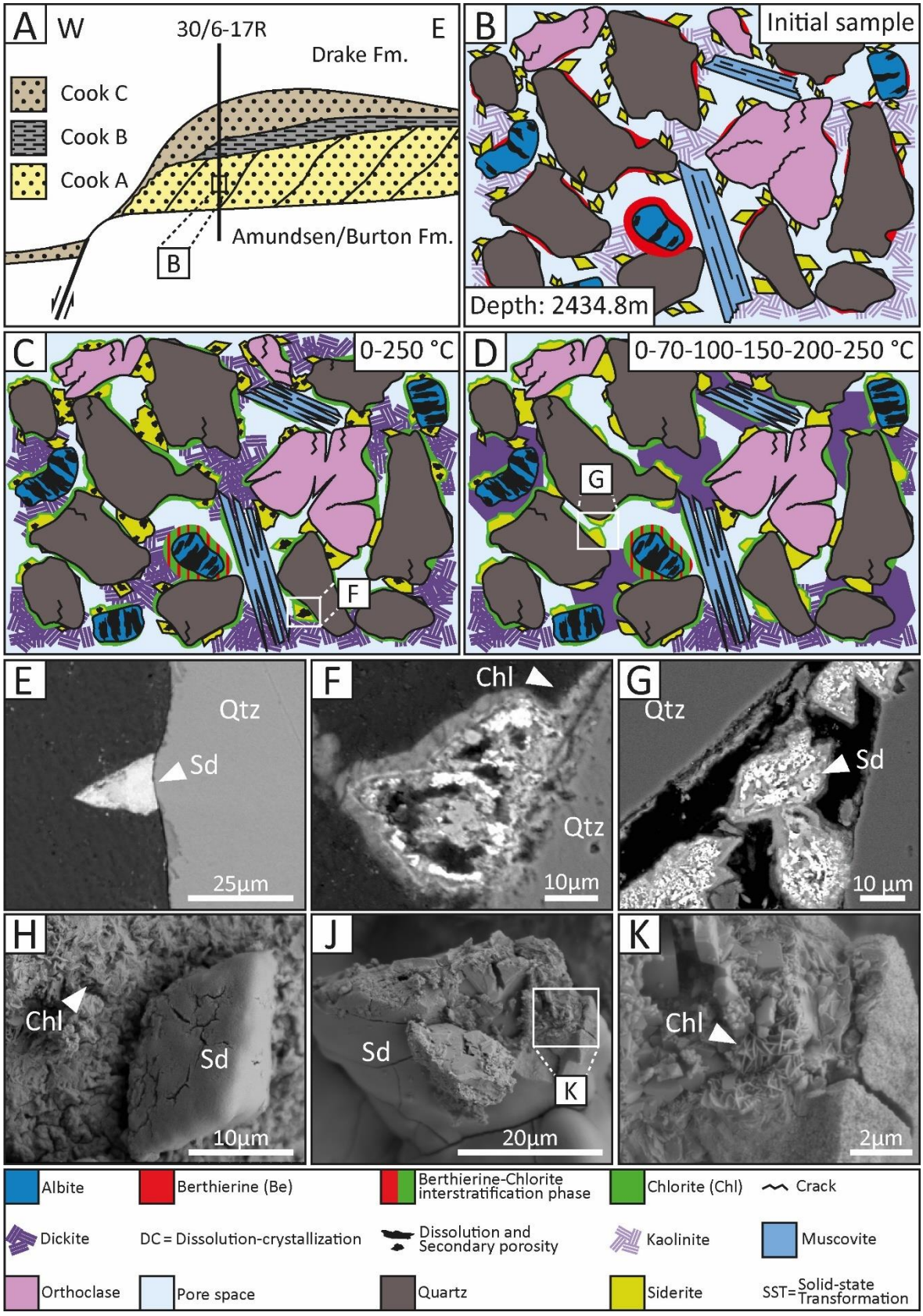

Figure 6.1: Summary illustrations and SEM images, showing siderite's dissolution pattern, of the single and multi-stage hydrothermal experiments at 250 °C. Where Chl, chlorite; Qtz, quartz; Sd, siderite. A) Depositional model for the development of the Cook Formation sand ridges. Cook A deposited by westward progradation, Cook B in response to sea level rise and Cook C due to tidal currents (After Livbjerg and Mjøs 1989). B) Schematic illustration of the pre-experiment, present day Cook Formation sandstone samples. The detrital grains are coated by discontinuous berthierine coats and

lozenge-shaped siderite crystals. Primary pores are partly filled with kaolinite. C) Summary cartoon of the main diagenetic alterations of the sandstone samples of the single-stage heating experiment. The key points are the transformation of berthierine to chlorite, the abrupt dissolution of siderite crystals and associated chlorite authigenesis, and the kaolinite to dickite transformation. D) The multi-stage heating experiments follow a similar diagenetic path. The main difference is siderite's dissolution pattern. E) Single siderite crystal before the experiments. F) Hollow core of a dissolving siderite crystal produced during the single-stage heating experiment. Note the chlorite development on the rims of the dissolving siderite crystals. G) During the multi-stage heating experiments, siderite dissolution begins with individual siderite crystals losing their initial shape and progressively merging together. Hollow cores are not common. H) Chlorite precipitates on a precursor-free grain surface located next to a dissolving siderite crystal. J) Progressive dissolution of a single siderite crystal. K) Siderite replacement by chlorite. Note the tangentially oriented authigenic chlorite platelets on the rims of the decomposing siderite crystal.

Additionally, the experiments were conducted under zero flow conditions (to mimic the closed-system where grain-coating chlorites are likely to develop during bed scale diagenesis (Worden et al. 2020)), with a solution that is non-reactive (e.g. Fe-free chemical composition) with the Fe-rich minerals, and proved to generate strong quartz-cementing conditions (Ajdukiewicz and Larese 2012).

The experiments were divided into single-stage heating experiments, where each sample was subjected to a specific temperature step, and multi-stage heating experiments more closely simulating burial diagenesis (Figure 6.1B–D).

6.3 Important chlorite precursor minerals of the Cook Formation

The main detrital and early diagenetic Fe-rich minerals involved in reactions associated with chlorite authigenesis include detrital chlorite and biotite, berthierine, trioctahedral smectite, siderite, ankerite, ilmenite, and other Fe-rich heavy minerals (Worden et al. 2020). The Cook Formation samples used in the hydrothermal experiments were selected for the high content of berthierine and siderite.

The Cook sandstone was interpreted as a prograding sandflat formed in a tide-influenced marginal marine setting (Livbjerg and Mjøs 1989) (Figure 6.1A). Depositional settings in the vicinity of river mouths favour the development of berthierine (Ehrenberg 1993; Worden and Morad 2003; Morad et al. 2010; Saïag et al. 2016). Berthierine is an aluminous, Fe^{2+}-rich, 1:1, 7 Å clay belonging to the kaolinite-serpentine series that has been proposed to transform into chlorite at temperatures > 60 °C (Jahren and Aagaard 1989; Aagaard et al. 2000). The forms of berthierine identified in the present research, based on their morphological characteristics, are: 1) thick concentrically laminated ooidal coats with a fibrous texture, 2) thin, patchy and discontinuous grain coats comprising a network of poorly developed, flake-shaped crystals lying subparallel to the surface of the host grains, and 3) pore-filling material.

The destabilization of eodiagenetic ferroan carbonates, such as siderite, can produce authigenic chlorite at temperatures > 120 °C (Curtis et al. 1985). In the Cook Formation, finely crystalline

siderite occurs on the rims of framework grains postdating berthierine precipitates. Crystals lying directly on host grain surfaces are also common (Figure 6.1E). Crystal habit includes lozenge-shaped isolated crystals, typical precipitates in early mesodiagenesis.

6.4 Laboratory-synthesized authigenic chlorite morphology and chloritization mechanisms

The synthesized authigenic chlorite is morphologically akin to naturally occurring chlorite in both the single-stage and multi-stage experiments. The main petrographic type includes grain coats consisting of euhedral, pseudohexagonal crystals oriented perpendicular to sub-perpendicular to the grain surfaces with a face-to-edge and face-to-face foliaceous pattern. Other, volumetrically less important, types include rosette-like clusters, and cabbage-head chlorites affixing at the platelets of the grain-coating chlorites.

Solid-state transformation (SST) has been proposed by several authors as the dominant mechanism responsible for the progressive replacement of 7Å-layered minerals, such as berthierine, by 14Å-layered minerals (Banfield and Bailey 1996; Ryan and Reynolds 1996; Xu and Veblen 1996). This process is relatively volume conservative retaining the crystal habit and leading to similar shape and size between the parental and daughter minerals. In contrast, dissolution-precipitation (DC), another mechanism proposed for the recrystallization of low-temperature, berthierine-derived chlorites to higher-temperature chlorites (Walker 1993; Hillier 1994), requires large morphological changes between the initial and final clay mineral (Cuadros 2012). The experimental results presented here have shown that chlorite authigenesis initiates with SST at low temperatures (100 °C), transitioning to dissolution crystallization at the higher-temperature spectrum (250 °C) with the threshold temperature for this transition being ~ 150 °C. The transition is marked by the significant increase in chlorite volume accompanied with the new rosette and cabbage head chlorite precipitates, and the increase in coat thickness and coverage, occurring at > 150 °C.

Other chloritization pathways that contribute to the major increase in the volume of chlorite at 250 °C, are: (1) chlorite neoformation as a direct precipitate from solution, directly on clean, mainly quartz, surfaces (Small et al. 1992; Haile et al. 2015), and (2) siderite replacement. Chlorite authigenesis resulted from siderite dissolution (Figure 6.1H-K) is evidenced by the thick chlorite coats observed adjacent to decomposing siderite crystals and by the complete engulfment of the dissolving crystals by authigenic chlorite. However, the two experimental scenarios (e.g., single-stage vs multi-stage heating) present a basic difference. The single-stage treatment instigates an abrupt decomposition associated with dissolution voids at the central parts of the siderite crystals (Figure 6.1F). The progressive temperature increase adopted in the multi-stage treatment causes

gradual dissolution of the siderite crystals (Figure 6.1G). Therefore, decreased chlorite precipitation rates indicate that precipitation rates are temperature-dependent and not time-dependent.

The experimental results have produced observations comparable to natural systems from multiple Jurassic clastic reservoirs offshore Norway where continuous recrystallization of berthierine to chlorite occurs between 70 °C and 160 °C (Jahren and Aagaard 1989). The Cook Formation reservoir of the Knarr (Well 34/3-1S) and Veslefrikk (Well 30/3-4) Fields, offshore Norway, with a corresponding temperature of ~ 135 °C, present partial or complete chlorite coats allowing the preservation of excellent reservoir quality (Hasnain and Jahren 2017; Skarpeid et al. 2017).

6.5 Quantification of mineralogical and petrophysical properties

The experimental results of both the single-stage and multi-stage heating experiments quantitatively identify that berthierine can be a precursor for chlorite precipitation in sandstones, and in the presence of siderite, will produce robust clay coats on clean substrate surfaces or where berthierine and siderite precursors pre-exist. The hydrothermal experiments were all performed in a silica supersaturated system. Yet, the main mineralogical change causing porosity reduction was the evolution of the pore-filling kaolinite and not quartz cementation. The continuous nature of the synthesized chlorite and siderite coats prevented quartz overgrowth development.

The berthierine content of the Cook Formation, by weight, before any hydrothermal treatment was ~ 6%. The results from the single-stage heating experiment at 250 °C showed that berthierine decreased to ~ 1% while chlorite increased from ~ 2% to ~ 14%. Similarly, at the end of the multi-stage heating experiment, chlorite content reached ~ 14%.

The 2D quantification of the single-stage heating experiments revealed a significant increase in clay-coat thickness (form an average value of 3.8 µm at 150 °C to 5.4µm at 250 °C) and clay coverage (from ~ 28% at 150 °C to ~ 50% at 250 °C) (Figure 6.2A-C). The 3D quantification showed a volumetric increase of the grain-coating material (e.g., combination of Fe-rich clay and siderite minerals) of ~ 9% (3.8 µm/voxel resolution) at 250 °C (Figure 6.2D-F) and 3D imaging observations indicate an increase of both the coat thickness and coat continuity. The 3D quantification of the multi-stage heating experiments also presents a grain coat volumetric increase; however, volumetrically less prominent (~ 4% at 1.7 µm/voxel resolution). This difference is partly attributed to the XCT spatial resolution effect but most importantly to the experimental treatment each sample has experienced (e.g., abrupt vs progressive temperature increase) as depicted in siderite's dissolution pattern.

The hydrothermal experiments revealed the transformation of kaolinite to dickite, capturing the gradual coarsening and morphological evolution of the pore-filling kaolinite crystals from an initial booklet morphology with pseudohexagonal habit to a more euhedral blocky habit. The initiation of this replacement occurs at ~ 150 °C. The transformation is further assisted by the temperature increase, silica availability, and the observed dissolution of feldspars. The XCT imaging identifies that kaolinite progressively chokes primary and micro pores. This is also validated by the pore network and permeability models showing restriction of fluid flow in regions occupied by kaolinite–dickite cement.

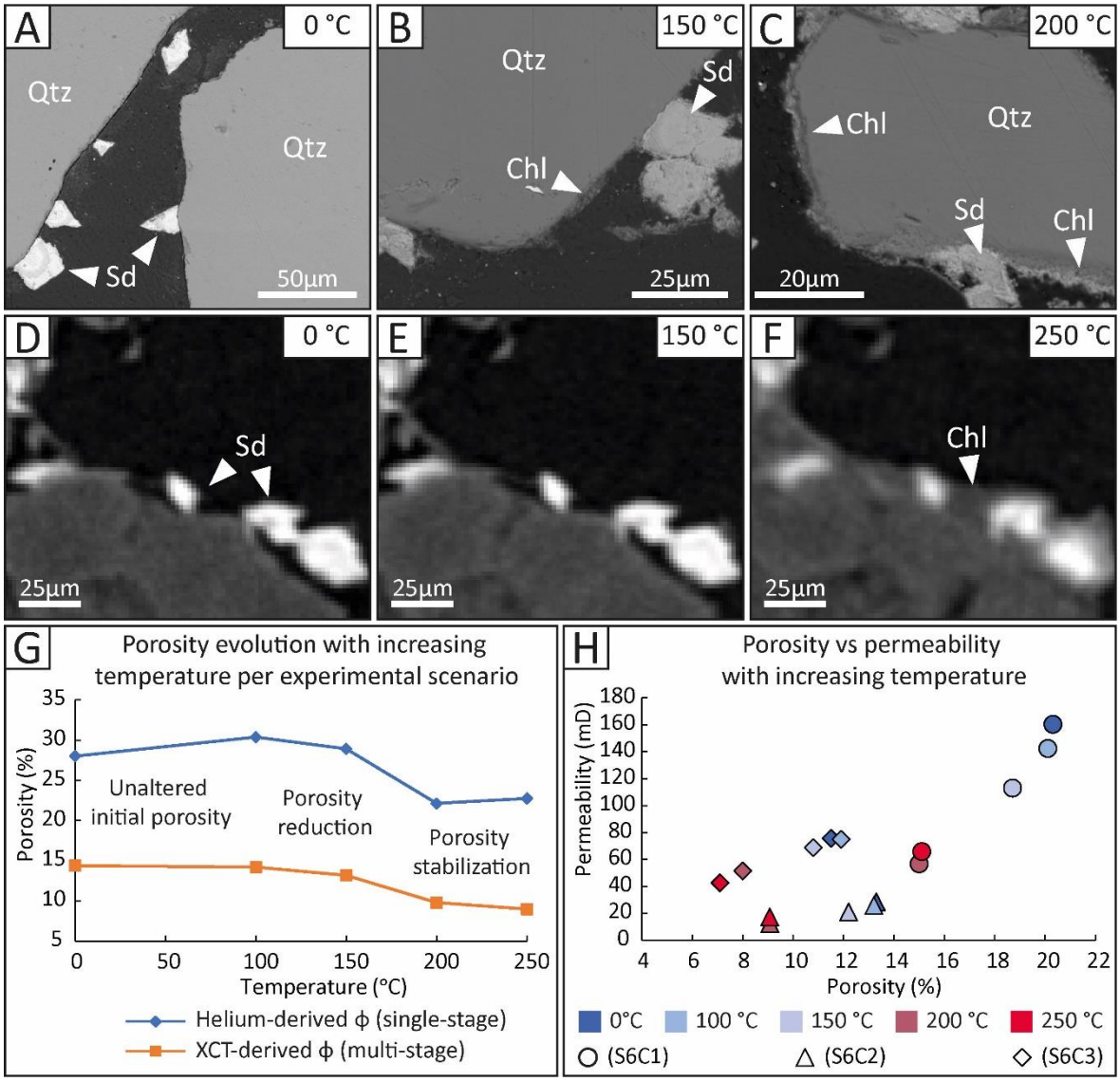

Figure 6.2: Chlorite coat development with increasing temperature and associated porosity and permeability evolution. Where Chl = chlorite; Qtz = quartz; Sd = siderite. The error associated with the presented XCT measurements is <0.1% (see Appendix A). A-C) SEM images showing the grain coat development induced by the single stage-heating experiments. D-E) 2D XCT images (1.7 µm/voxel resolution) of the grain coat evolution induced by the multi-stage heating experiments. The presence of chlorite has been confirmed by EDS analysis. G) Porosity evolution per experimental scenario. In both cases, porosity loss is ceased at temperatures > 200 °C. H) Association between porosity, permeability and temperature, derived from the multi-scale treatment, through XCT porosity quantification and permeability modelling of three cubic

subvolumes (e.g., S6C1-3, 1.7 µm/voxel resolution). Note that the main reduction window lies between 150 and 200 °C above which the reservoir quality attributes are maintained.

The experimental results demonstrate that authigenic chlorite coats develop in preference to quartz cement at temperatures > 150 °C and provide a mechanism for preserving effective storage space and connected pathways for unrestricted fluid flow at the pore scale. Ceasing of porosity loss and permeability stabilization is observed at temperatures between 200 °C and 250 °C in both experimental scenarios (Figure 6.2G, H). Pore network and permeability models have yielded similar behaviour and recorded the alterations in pore-throat connectivity, pore and throat sizes, and fluid flow with increasing temperature.

6.6 Early diagenetic grain coats mediated by bacterial activity

Microorganisms can form supracellular structures, called biofilms, consisting of surface-associated microbial cells embedded in hydrated extracellular polymeric substances (EPS) that facilitate adhesion and survival in adverse settings. Recent studies in intertidal environments have shown that adhesive biofilms and EPS have the potential to complex with quartz and clay minerals forming thin clay envelopes lining sand grains (Wooldridge et al. 2017a; Duteil et al. 2020). These clay coats are considered potential source material for diagenetic clay coats.

The biofilm-related hydrothermal experiments presented in this research is the first attempt to link early biofilm-mediated grain coat formation to later stage diagenetic coats. This, by using bacterial microorganisms and pure sand grains as a substrate for biofilm growth. The experiments have demonstrated the successful colonization of the unconsolidated sand grains by Geobacter biofilm communities and, with increasing temperature, the subsequent formation of clay-like structures adhered on EPS-coated surfaces. Future experiments are needed to further develop and confirm these initial findings.

6.7 Wider implications for reservoir quality studies

Deep saline aquifers and depleted oil and gas, and deep unmineable coal beds reservoirs are valuable targets for underground CO_2 sequestration (Bickle 2009; Ajayi et al. 2019; Kelemen et al. 2019). Once injected, CO_2 is contained underground through a combination of capillary, structural, solubility or mineral trapping (De Silva et al., 2015; Wigand et al., 2008).

CO_2 geo-mineralization, a technique converting CO_2 to solid magnesium, calcium or iron carbonate while dissolving Mg-, Ca-, Fe-rich silicates, is the most environmentally secure technology for geological storage of CO_2 (Matter and Kelemen 2009; Sanna et al. 2014). CO_2 carbonation leads to permanent fixation of CO_2 in solid phases, such as calcite, magnesite, and ankerite, thus preventing CO_2 from returning to the atmosphere.

Chlorite is a common divalent cation-bearing mineral in sedimentary rocks. The hydrothermal experiments were developed within the temperature range that is representative of CO_2 injection conditions (i.e., 50<T<150 °C) and showed that chlorite content is increasing with increasing temperature. Additionally, the high chlorite content of the Cook sandstone in other Fields, such as the Knarr and Veslefrikk Fields, makes this reservoir a potential target for CO_2 mineralization. Potential injection of CO_2, which dissolves into the native formation brine forming H_2CO_3, can decrease the pH of the brine, hence making it corrosive and reactive towards the Formation's native minerals it contacts (Xu et al. 2004). Chlorite is preferentially soluble under acidic conditions (Armitage et al. 2013). Its dissolution can release the cations necessary for the precipitation of Fe-rich carbonate minerals, amorphous carbon precipitation with Fe-oxides, and thus CO_2 mineral storage.

Geothermal operations require reservoirs with optimum combination of the highest possible temperatures and sufficient reservoir properties for exploitation. Authigenic quartz and clay cementation play a significant role in preserving or deteriorating storage capacity and flow properties. Therefore, being able to better constrain the temperature ranges under which such processes occur, and quantify the associated mineralogical alterations, will result in more reliable reservoir quality predictions. The experimental results can be incorporated into models that consider the influences of mineralogy and temperature regime on diagenesis to appraise the geothermal potential of undrilled areas or determine if there is a window of depth and temperature conditions that would be suitable for geothermal energy production from known sandstone reservoirs.

Biofilm-mediated early mineral phases can potentially represent the precursor to authigenic clays reported in many sandstone reservoirs. The wide variety of clay mineral habits and chemistries and the range of sedimentary facies in which they are found suggest that clay minerals form in various ways. The importance of EPS structures in acting as a template for mineral nucleation is crucial for understanding the relationship between the development of certain precursor phases and the sedimentary environments in which specific microbial species live. Incorporating laboratory experiments simulating burial diagenesis can expand our knowledge on the association between microbial life, precursor clay development and authigenesis, leading to better-developed reservoir quality predictive models.

6.8 Conclusions

1. Single- and multi-stage heating hydrothermal experiments simulating burial diagenesis have been undertaken to assess the impact of chlorite authigenesis on reservoir quality of

sandstones. The experiments were performed across a continuum of temperature scales (i.e., from 0 °C up to 250 °C) using naturally occurring sandstone samples from the Lower Jurassic Cook Formation and an artificial silica-supersaturated solution. The experimental results were evaluated using X-ray diffraction (XRD), scanning electron microscopy (SEM) and energy-dispersive X-ray spectroscopy (SEM-EDS), automated quantitative mineralogy (AQM), X-ray computed tomography (XCT), helium pycnometry, and pore network and permeability modelling.

2. The comparison between the single-stage and multi-stage hydrothermal treatment suggested that chlorite precipitation rates are temperature-dependent and not time-dependent. Both treatments suggest a synchronous, temperature-wise, initiation of chlorite development.
3. The hydrothermal experiments revealed that chlorite is formed from berthierine transformation, replacement of siderite and neoformation on precursor-free substrate surfaces. Chlorite authigenesis initiates with solid-state transformation at low experimental temperatures (100 °C) transitioning to dissolution crystallization from 150 °C onwards. The hydrothermally synthesized chlorite coats are morphologically akin to naturally occurring chlorite coats.
4. The increase in volume, thickness and continuity of chlorite coats resulted in the cessation of porosity loss between 200 °C and 250 °C through offering fewer nucleation sites for quartz to precipitate. Secondary porosity resulted mainly from feldspar dissolution. At lower temperatures (i.e., between 150 °C and 200 °C) porosity decreases due to evolution of pore filling kaolinite blocking primary pore space and destroying microporosity.
5. The magnitude of diagenesis governs the pore and throat sizes, pore connectivity, and fluid flow as revealed from the pore network and permeability models of the hydrothermally treated samples. With increasing temperature, pore networks become less dense due to porosity loss and fluid flow pathways enhanced or diminished based on dissolution or cementation.
6. Quartz grains exposed to biological activity can develop cohesive bio-coating and bridging structures stabilising unconsolidated sand particles. With increasing temperature, the biocoating acts as a template for the formation of early mineral phases. Mineral growth continues with increasing temperature, and the initial amorphous mineral phase transitions to poorly-ordered structures at temperatures > 100 °C.
7. Successful transition to a sustainable energy future requires accurate characterisation of both the subsurface reservoirs used as hydrocarbon and geothermal heat sources or provide storage for captured carbon and generated hydrogen. This research enhances our knowledge of the diagenetic processes, such as grain coat development, influencing reservoir quality alterations

and presents quantitative data that can be used to improve reservoir quality predictive models applied in various geoscience applications.

6.9 Suggestions for future work

There are several developments that could be implemented to expand the present research including the following:

1. Time- and pressure-dependent experiments

The optimum chlorite coat volume and thickness, which effectively inhibits quartz nucleation without diminishing reservoir quality of a given reservoir is variable. Pittman et al. (1992) suggested an optimum volume ranging between 5% and 13% for the Tuscaloosa Formation and between 4% and 7% for the Berea Sandstone. A coat thickness between 5 µm and 10 µm has been documented as beneficial for the preservation of reservoir quality (Anjos et al. 2003; Sun et al. 2014), while thicker chlorite coats (>20 µm) can reduce permeability significantly (Al-Ramadan et al. 2004). The hydrothermal configuration presented in this research can be applied to perform time-dependent, long-duration experiments, which, coupled with detailed and systematic microscopic measurements, can be used to better constrain the transition from porosity-preserving to porosity-occluding chlorite coats.

Many studies of principally siliciclastic reservoir rocks, with ages varying from early Tertiary to Jurassic, conclude that overpressure is an important contributor to porosity preservation in several hydrocarbon basins, including Central Graben, North Sea, UK (Osborne and Swarbrick 1999; Nguyen et al. 2013; Grant et al. 2014; Stricker et al. 2016a); the Gulf of Mexico, USA (Taylor et al. 2004; Ehrenberg et al. 2008; Ajdukiewicz et al. 2010; Sathar and Jones 2016); the Santos Basin, Brazil (Anjos et al. 2003) and the Indus Basin, Pakistan (Berger et al. 2009). Recent overpressure-compaction simulation experiments validate the premise that the higher the overpressure is, the more preservation effect it provides on pores (You et al. 2020). Future hydrothermal experiments using chlorite-precursor-rich reservoirs should focus on quantitatively clarifying the impact of such pressure on chlorite coat development and quartz cementation. From the analytical perspective, synchrotron-based imaging with monochromatic X-rays would help to capture phase distribution (for example, chlorite and siderite) that lab scanners cannot easily resolve.

2. *In-situ* experimental approach

The use of an experimental kit that allows the experiment to remain at constant conditions (e.g., temperature and pressure) while reaction fluid is withdrawn and XCT images captured can offer great potential for chlorite prediction at the field and reservoir scales. Incorporating in-situ fluid

sampling will permit the tracking of compositional and pH changes during the experiments to better constrain the aqueous stability of the synthesized chlorite and, therefore, develop a better understanding of the chemical and reaction parameters for the formation of chlorite at reservoir conditions. Incorporating *in-situ* XCT imaging will provide better-constrained quantitative data regarding mineral growth and dissolution rates, and associated petrophysical alterations.

3. Experimental validation of the permeability simulations

Triaxial tests can be performed on both the starting material and end-products from the hydrothermal experiments to provide a realistic simulation of the *in-situ* reservoir properties. The rock specimens can be subjected to a given fluid/gas flow rate. By measuring the pressure differential across the specimen, the pressure gradient can be determined, and the permeability coefficient calculated. The triaxial tests will help to understand how the entire rock mass responds to changes in load, stress, pore pressure, pore volume and validate the permeability values derived through the XCT-based models.

4. Experiments for Carbon Capture Utilisation and Storage (CCUS)

The Cook Formation has been identified as a potential target for carbon capture and storage. Hydrothermal experiments can be employed to investigate the potential mineralogical evolution of representative sandstone samples from the Cook Formation exposed to a brine saturated with sCO_2. The experimental results can be used to define geochemical reactions, which can then be extrapolated to longer timescales using a geochemical modelling software such as PHREEQC, and assess the potential for CO_2 storage.

Additionally, CCUS research is primarily focused on the reservoir integrity and reservoir rock characteristics, usually from seismic sections and limited core samples. Experimental modelling would allow better integration.

5. Reservoir quality modelling

The quantitative data presented in this research can be incorporated into reservoir quality simulation software, such as Touchstone or PetroMod, to better constrain our predictions of burial diagenetic processes and reservoir properties in HPHT reservoirs.

6. Biomineral experiments

The preliminary results regarding biomineral interaction presented in this research can be used to further investigate the interrelationship between microbial life and grain coating mineral development. The applied experimental configuration combined with various fluid compositions

that promote the formation of specific minerals and more precise temperature steps will help to better constrain how early grain coats develop under the influence of microbial communities.

Additionally, since subsurface storage operations can be impacted by microbial activity, the reaction of microbial communities in response to gas injection into reservoir material of such repositories can be further investigated. Given that the hydrogen economy is currently growing, the experimental setup presented in this research can be used to describe how hydrogen exposure changes microbial communities at finer scales, affecting mineral development and the overall reservoir potential of a given target formation.

Bibliography

AAGAARD, P., AND EGEBERG, P.K., 1998, Formation waters and diagenetic modifications: general trends exhibited by oil fields from the Norwegian shelf - A model for formation waters in oil prone subsiding basins, *in* Arehart, G.B., and Hulston, J.R., eds., Water-Rock Interaction: Proceedings of the 9th International Symposium, Balkema, p. 281-286.

AAGAARD, P., JAHREN, J.S., HARSTAD, A.O., NILSEN, O., AND RAMM, M., 2000, Formation of grain-coating chlorite in sandstones. Laboratory synthesized vs. natural occurrences: Clay Minerals, v. 35, p. 261-269.

AASE, N.E., BJØRKUM, P.A., AND NADEAU, P.H., 1996, The effect of grain-coating microquartz on preservation of reservoir porosity: American Association of Petroleum Geologists, Bulletin, v. 80, p. 1654-1653.

AASE, N.E., AND WALDERHAUG, O., 2005, The effect of hydrocarbons on quartz cementation: diagenesis in the Upper Jurassic sandstones of the Miller Field, North Sea, revisited: Petroleum Geoscience, v. 11, p. 215-223.

ABERCROMBIE, H.J., HUTCHEON, I.E., BLOCH, J.D., AND CARITAT, P.D., 1994, Silica activity and the smectite-illite reaction: Geology, v. 22, p. 539-542.

AHMED, W., 2008, Contrast in clay mineralogy and their effect on reservoir properties in sandstone formations: Bulletin of the Chemical Society of Ethiopia, v. 22, p. 41-65.

AJAYI, T., GOMES, J.S., AND BERA, A., 2019, A review of CO2 storage in geological formations emphasizing modeling, monitoring and capacity estimation approaches: Petroleum Science, v. 16, p. 1028-1063.

AJDUKIEWICZ, J.M., AND LANDER, R.H., 2010, Sandstone reservoir quality prediction: the state of the art: American Association of Petroleum Geologists, Bulletin, v. 94, p. 1083-1091.

AJDUKIEWICZ, J.M., AND LARESE, R.E., 2012, How clay grain coats inhibit quartz cement and preserve porosity in deeply buried sandstones: observations and experiments: American Association of Petroleum Geologists, Bulletin, v. 96, p. 2091-2119.

AJDUKIEWICZ, J.M., NICHOLSON, P.H., AND ESCH, W.L., 2010, Prediction of deep reservoir quality using early diagenetic process models in the Jurassic Norphlet Formation, Gulf of Mexico: American Association of Petroleum Geologists, Bulletin, v. 94, p. 1189-1227.

AL-RAMADAN, K.A., HUSSAIN, M., IMAM, B., AND SANER, S., 2004, Lithologic characteristics and diagenesis of the Devonian Jauf sandstone at Ghawar Field, Eastern Saudi Arabia: Marine and Petroleum Geology, v. 21, p. 1221-1234.

ALANSARI, A., SALIM, A.M.A., JANJUHAH, H.T., BIN ABD RAHMAN, A.H., AND FELLO, N.M., 2019, Quantification of clay mineral microporosity and its application to water saturation and effective porosity estimation: A case study from Upper Ordovician reservoir, Libya: Journal of Natural Gas Geoscience, v. 4, p. 139-150.

ALTANER, S.P., AND YLAGAN, R.F., 1997, Comparison of structural models of mixed-layer illite/smectite and reaction mechanisms of smectite illitization: Clays and Clay Minerals, v. 45, p. 517-533.

ANDRÄ, H., COMBARET, N., DVORKIN, J., GLATT, E., HAN, J., KABEL, M., KEEHM, Y., KRZIKALLA, F., LEE, M., MADONNA, C., MARSH, M., MUKERJI, T., SAENGER, E.H., SAIN, R., SAXENA, N., RICKER, S., WIEGMANN, A., AND ZHAN, X., 2013, Digital rock physics benchmarks—Part I: Imaging and segmentation: Computers & Geosciences, v. 50, p. 25-32.

ANJOS, S.M.C., DE ROS, L.F., AND SILVA, C.M.A., 2003, Chlorite authigenesis and porosity preservation in the Upper Cretaceous marine sandstones of the Santos Basin, offshore eastern Brazil, *in* Worden, R.H., and Morad, S., eds., Clay Mineral Cements in Sandstones: International Association of Sedimentologists, Special Publication 34, p. 291-316.

ANOVITZ, L.M., AND COLE, D.R., 2015, Characterization and analysis of porosity and pore structures: Reviews in Mineralogy and Geochemistry, v. 80, p. 61-164.

ARMITAGE, P.J., FAULKNER, D.R., AND WORDEN, R.H., 2013, Caprock corrosion: Nature Geoscience, v. 6, p. 79-80.

ARMITAGE, P.J., WORDEN, R.H., FAULKNER, D.R., APLIN, A.C., BUTCHER, A.R., AND ILIFFE, J., 2010, Diagenetic and sedimentary controls on porosity in Lower Carboniferous fine-grained lithologies, Krechba field, Algeria: A petrological study of a caprock to a carbon capture site: Marine and Petroleum Geology, v. 27, p. 1395-1410.

AUDET, D., AND MCCONNELL, J., 1992, Forward modelling of porosity and pore pressure evolution in sedimentary basins: Basin Research, v. 4, p. 147-162.

BAHLIS, A.B., AND DE ROS, L.F., 2013, Origin and impact of authigenic chlorite in the Upper Cretaceous sandstone reservoirs of the Santos Basin, eastern Brazil: Petroleum Geoscience, v. 19, p. 185-199.

BAILEY, S., 1980, Structures of layer silicates, *in* Brindley, G.W., and Brown, G., eds., Crystal Structures of Clay Minerals and Their X-Ray Identification: Mineralogical Society, Monograph 5, p. 1-123.

BAILEY, S.W., 1988, Odinite, a new dioctahedral-trioctahedral Fe^{3+}-rich 1:1 clay mineral: Clay Minerals, v. 23, p. 237-247.

BAKKE, S., AND ØREN, P.-E., 1997, 3-D pore-scale modelling of sandstones and flow simulations in the pore networks: Society of Petroleum Engineers Journal, v. 2, p. 136-149.

BANFIELD, J.F., AND BAILEY, S.W., 1996, Formation of regularly interstratified serpentine-chlorite minerals by tetrahedral inversion in long-period serpentine polytypes: American Mineralogist, v. 81, p. 79-91.

BARCLAY, S., AND WORDEN, R., 2000, Effects of reservoir wettability on quartz cementation in oil fields: International Association of Sedimentologists, Special Publication, v. 29, p. 103-118.

BARONNET, A., 1982, Ostwald ripenning in solution: the case of calcite and mica: Estudios geológicos, v. 38, p. 185-198.

BARONNET, A., 1992, Polytypism and stacking disorder: Reviews in Mineralogy and Geochemistry, v. 27, p. 231-288.

BAYLISS, P., 1975, Nomenclature of the trioctahedral chlorites: Canadian Mineralogist, v. 13, p. 178-180.

BEAUFORT, D., CASSAGNABERE, A., PETIT, S., LANSON, B., BERGER, G., LACHARPAGNE, J.C., AND JOHANSEN, H., 1998, Kaolinite-to-dickite reaction in sandstone reservoirs: Clay Minerals, v. 33, p. 297-316.

BEAUFORT, D., RIGAULT, C., BILLON, S., BILLAULT, V., INOUE, A., INOUE, S., AND PATRIER, P., 2015, Chlorite and chloritization processes through mixed-layer mineral series in low-temperature geological systems–a review: Clay Minerals, v. 50, p. 497-523.

BENGTSON, S., IVARSSON, M., ASTOLFO, A., BELIVANOVA, V., BROMAN, C., MARONE, F., AND STAMPANONI, M., 2014, Deep-biosphere consortium of fungi and prokaryotes in Eocene subseafloor basalts: Geobiology, v. 12, p. 489-496.

BERGER, A., GIER, S., AND KROIS, P., 2009, Porosity-preserving chlorite cements in shallow-marine volcaniclastic sandstones: Evidence from Cretaceous sandstones of the Sawan gas field, Pakistan: American Association of Petroleum Geologists, Bulletin, v. 93, p. 595-615.

BEVERIDGE, T.J., 1989, The structure of bacteria, *in* Poindexter, J.S., and Leadbetter, E.R., eds., Bacteria in Nature: New York, Plenum, p. 1-65.

BHATTACHARYYA, D.P., 1983, Origin of berthierine in ironstones: Clays and clay minerals, v. 31, p. 173-182.

BICKLE, M.J., 2009, Geological carbon storage: Nature Geoscience, v. 2, p. 815-818.

BILLAULT, V., BEAUFORT, D., BARONNET, A., AND LACHARPAGNE, J.C., 2003, A nanopetrographic and textural study of grain-coating chlorites in sandstone reservoirs: Clay Minerals, v. 38, p. 315-328.

BIN, B., RUKAI, Z., SONGTAO, W., WENJING, Y., JEFF, G., ALLEN, G., XIANGXIANG, Z., AND LING, S., 2013, Multi-scale method of Nano(Micro)-CT study on microscopic pore structure of tight sandstone of

Yanchang Formation, Ordos Basin: Petroleum Exploration and Development, v. 40, p. 354-358.

BIRKLE, P., VAN DIJK, C., DASGUPTA, K., MURPHY, M.J., KHARAKA, Y.K., THORDSEN, J.J., AND BISCHOFF, J.L., 2019, Controls On Illite Cementation In Unayzah Sandstones, Saudi Arabia: Mineralogy, K-Ar Dating, Numerical Modeling, and Hydrothermal Experiments: Journal of Sedimentary Research, v. 89, p. 89-109.

BJØRKUM, P.A., 1996, How important is pressure in causing dissolution of quartz in sandstones?: Journal of Sedimentary Research, v. 66, p. 147-154.

BJØRKUM, P.A., AND NADEAU, P.H., 1998, Temperature controlled porosity/permeability reduction, fluid migration, and petroleum exploration in sedimentary basins: The APPEA Journal, v. 38, p. 453-465.

BJØRKUM, P.A., OELKERS, E.H., NADEAU, P.H., WALDERHAUG, O., AND MURPHY, W.M., 1998, Porosity prediction in quartzose sandstones as a function of time, temperature, depth, stylolite frequency, and hydrocarbon saturation: American Association of Petroleum Geologists, Bulletin, v. 82, p. 637-648.

BJØRLYKKE, K., 1994, Fluid-flow processes and diagenesis in sedimentary basins: Geological Society, London, Special Publications, v. 78, p. 127-140.

BJØRLYKKE, K., 2014, Relationships between depositional environments, burial history and rock properties. Some principal aspects of diagenetic process in sedimentary basins: Sedimentary Geology, v. 301, p. 1-14.

BJØRLYKKE, K., AND AAGAARD, P., 1992, Clay minerals in North Sea sandstones Society of Sedimentary Geology (SEPM), v. 47, p. 68-80.

BJØRLYKKE, K., AND EGEBERG, P., 1993, Quartz cementation in sedimentary basins: American Association of Petroleum Geologists, Bulletin, v. 77, p. 1538-1548.

BJØRLYKKE, K., HØEG, K., AND MONDOL, N.H., 2015, Introduction to Geomechanics: Stress and Strain in Sedimentary Basins, *in* Bjørlykke, K., ed., Petroleum Geoscience: From Sedimentary Environments to Rock Physics: Berlin, Heidelberg, Springer Berlin Heidelberg, p. 301-318.

BJØRLYKKE, K., AND JAHREN, J., 2010, Sandstones and Sandstone Reservoirs, *in* Bjorlykke, K., ed., Petroleum Geoscience: From Sedimentary Environments to Rock Physics: Berlin, Heidelberg, Springer Berlin Heidelberg, p. 113-140.

BLOCH, S., 1994, Importance of Reservoir Quality Prediction in Exploration, *in* Wilson, M.D., ed., Reservoir Quality Assessment and Prediction in Clastic Rocks, SEPM Society for Sedimentary Geology, p. 0.

BLOCH, S., LANDER, H.R., AND BONNELL, L., 2002, Anomalously high porosity and permeability in deeply buried sandstone reservoirs: origin and predictability: American Association of Petroleum Geologists, Bulletin, v. 86, p. 301-328.

BONNELL, L., LARESE, R.E., AND LANDER, R., 2006a, Porosity preservation by inhibition of quartz cementation: Microquartz versus hydrocarbons: American Association of Petroleum Geologists Search and Discovery Article, v. 90061.

BONNELL, L.M., LARESE, R.E., AND LANDER, R.H., 2006b, Hydrocarbon versus microquartz inhibition of quartz cementation in North Sea sandstones: Empirical and experimental evidence: Annual AAPG Convection Abstracts, v. 15, p. 12.

BOYD, G.A., WALLACE, M.W., HOLDGATE, G.R., AND GALLAGHER, S.J., 2004, Marine clays and porosity evolution in the Nullawarre Greensand, Otway Basin, southeastern Australia: PESA Eastern Australasian Basins Symposium II, p. 22.

BRIGATTI, M.F., GALAN, E., AND THENG, B.K.G., 2006, Chapter 2 Structures and Mineralogy of Clay Minerals, *in* Bergaya, F., Theng, B.K.G., and Lagaly, G., eds., Developments in Clay Science, Elsevier, p. 19-86.

BRINDLEY, G.W., 1951, The crystal structure of some chamosite minerals Mineralogical Magazine and Journal of the Mineralogical Society, v. 29, p. 502-525.

BULTREYS, T., VAN HOOREBEKE, L., AND CNUDDE, V., 2015, Multi-scale, micro-computed tomography-based pore network models to simulate drainage in heterogeneous rocks: Advances in Water Resources, v. 78, p. 36-49.

ÇAĞATAY, M.N., SANER, S., AL-SAIYED, I., AND CARRIGAN, W.J., 1996, Diagenesis of the Safaniya Sandstone Member (mid-Cretaceous) in Saudi Arabia: Sedimentary Geology, v. 105, p. 221-239.

CALLOW, B., FALCON-SUAREZ, I., MARIN-MORENO, H., BULL, J.M., AND AHMED, S., 2020, Optimal X-ray micro-CT image based methods for porosity and permeability quantification in heterogeneous sandstones: Geophysical Journal International, v. 223, p. 1210-1229.

CAO, Z., LIU, G., MENG, W., WANG, P., AND YANG, C., 2018, Origin of different chlorite occurrences and their effects on tight clastic reservoir porosity: Journal of Petroleum Science and Engineering, v. 160, p. 384-392.

CASSAGNABERE, A., 1998, Caractérisation et interprétation de la transition kaolinite-dickite dans les réservoirs à hydrocarbures de Froy et Rind (Mer du Nord, Norvège), [13], 238 p p.

CHAFETZ, H.S., AND BUCZYNSKI, C., 1992, Bacterially induced lithification of microbial mats: Palaios, v. 7, p. 277-293.

CHARLAFTIS, D., JONES, S.J., DOBSON, K.J., CROUCH, J., AND ACIKALIN, S., 2021, Experimental study of chlorite authigenesis and influence on porosity maintenance in sandstones: Journal of Sedimentary Research, v. 91, p. 197-212.

CHEN, G.J., DU, G.C., ZHANG, G.C., WANG, Q., LV, C.F., AND CHEN, J., 2011, Chlorite cement and its effect on the reservoir quality of sandstones from the Panyu low-uplift, Pearl River Mouth Basin: Petroleum Science, v. 8, p. 143-150.

CHEN, X., AND STEWART, P.S., 2002, Role of electrostatic interactions in cohesion of bacterial biofilms: Applied Microbiology and Biotechnology, v. 59, p. 718-720.

CHO, M., AND FAWCETT, J.J., 1986, Morphologies and growth mechanisms of synthetic Mg-chlorite and cordierite: American Mineralogist, v. 71, p. 78-84.

CHUHAN, F.A., KJELDSTAD, A., BJØRLYKKE, K., AND HØEG, K., 2002, Porosity loss in sand by grain crushing - Experimental evidence and relevance to reservoir quality: Marine and Petroleum Geology, v. 19, p. 39-53.

CNUDDE, V., AND BOONE, M.N., 2013, High-resolution X-ray computed tomography in geosciences: A review of the current technology and applications: Earth-Science Reviews, v. 123, p. 1-17.

COATES, J.D., PHILLIPS, E.J., LONERGAN, D.J., JENTER, H., AND LOVLEY, D.R., 1996, Isolation of Geobacter species from diverse sedimentary environments: Applied and Environmental Microbiology, v. 62, p. 1531.

COSTA, O.Y.A., RAAIJMAKERS, J.M., AND KURAMAE, E.E., 2018, Microbial extracellular polymeric substances: Ecological function and impact on soil aggregation: Frontiers in Microbiology, v. 9, p. 1636.

COSTERTON, J.W., LEWANDOWSKI, Z., CALDWELL, D.E., KORBER, D.R., AND LAPPIN-SCOTT, H.M., 1995, Microbial biofilms: Annual review of microbiology, v. 49, p. 711-745.

CRUNDWELL, F.K., 2017, On the mechanism of the dissolution of quartz and silica in aqueous solutions: American Chemical Society Omega, v. 2, p. 1116-1127.

CUADROS, J., 2012, Clay crystal-chemical adaptability and transformation mechanisms: Clay Minerals, v. 47, p. 147-164.

CUADROS, J., 2017, Clay mineral interaction with microorganisms: a review: Clay Minerals, v. 52, p. 235-261.

CUADROS, J., AFSIN, B., JADUBANSA, P., ARDAKANI, M., ASCASO, C., WIERZCHOS, J., AND ADAMS, J., 2013, Pathways of volcanic glass alteration in laboratory experiments through inorganic and microbially-mediated processes: Clay Minerals, v. 48, p. 423-445.

CURTIS, C.D., 1985, Clay mineral precipitation and transformation during burial diagenesis: Royal Society (London), Philosophical Transactions, Series A, Mathematical and Physical Sciences, v. 315, p. 91-105.

CURTIS, C.D., AND COLEMAN, M.L., 1986, Controls on the Precipitation of Early Diagenetic Calcite, Dolomite and Siderite Concretions in Complex Depositional Sequences, *in* Gautier, D.L., ed., Roles of Organic Matter in Sediment Diagenesis, SEPM, Special Publication, p. 23-33.

CURTIS, C.D., COLEMAN, M.L., AND LOVE, L.G., 1986, Pore water evolution during sediment burial from isotopic and mineral chemistry of calcite, dolomite and siderite concretions: Geochimica et Cosmochimica Acta, v. 50, p. 2321-2334.

CURTIS, C.D., HUGHES, C.R., WHITEMAN, J.A., AND WHITTLE, C.K., 1985, Compositional variation within some sedimentary chlorites and some comments on their origin: Mineralogical Magazine, v. 49, p. 375-386.

CURTIS, C.D., IRELAND, B.J., WHITEMAN, J.A., MULVANEY, R., AND WHITTLE, C.K., 1984, Authigenic chlorites: problems with chemical analysis and structural formula calculations: Clay Minerals, v. 19, p. 471-481.

CURTIS, C.D., AND SPEARS, D.A., 1968, The formation of sedimentary iron minerals: Economic Geology, v. 63, p. 257-270.

DE BOER, R.B., NAGTEGAAL, P.J.C., AND DUYVIS, E.M., 1977, Pressure solution experiments on quartz sand: Geochim. Cosmochim. Acta, v. 41, p. 257-264.

DE BROUWER, J.F.C., RUDDY, G.K., JONES, T.E.R., AND STAL, L.J., 2002, Sorption of EPS to sediment particles and the effect on the rheology of sediment slurries: Biogeochemistry, v. 61, p. 57-71.

DE ROS, L.F., ANJOS, S.M., AND MORAD, S., 1994, Authigenesis of amphibole and its relationship to the diagenetic evolution of Lower Cretaceous sandstones of the Potiguar rift basin, northeastern Brazil: Sedimentary Geology, v. 88, p. 253-266.

DECHO, A.W., 2000, Microbial biofilms in intertidal systems: an overview: Continental Shelf Research, v. 20, p. 1257-1273.

DEER, W.A., HOWIE, R.A., AND ZUSSMAN, J., 2013, An introduction to the rock-forming minerals - 3rd ed., v. 2, The MIneralogical Society.

DEWERS, T., AND ORTOLEVA, P., 1991, Influences of clay minerals on sandstone cementation and pressure solution: Geology, v. 19, p. 1045-1048.

DIXON, S., SUMMERS, D., AND SURDAM, R., 1989, Diagenesis and preservation of porosity in Norphlet Formation (Upper Jurassic), southern Alabama: American Association of Petroleum Geologists, Bulletin, v. 73, p. 707-728.

DONG, H., 2012, Clay–Microbe Interactions and Implications for Environmental Mitigation: Elements, v. 8, p. 113-118.

DONG, H., JAISI, D.P., KIM, J., AND ZHANG, G., 2009, Microbe-clay mineral interactions: American Mineralogist, v. 94, p. 1505-1519.

DONG, H., KOSTKA, J.E., AND KIM, J., 2003, Microscopic evidence for microbial dissolution of smectite: Clays and Clay Minerals, v. 51, p. 502-512.

DONG, H., TOUATI, M., AND BLUNT, M.J., 2007, Pore Network Modeling: Analysis of Pore Size Distribution of Arabian Core Samples, SPE Middle East Oil and Gas Show and Conference: Manama, Bahrain, Society of Petroleum Engineers, p. 5.

DOUGLAS, S., AND BEVERIDGE, T.J., 1998, Mineral formation by bacteria in natural microbial communities: FEMS Microbiology Ecology, v. 26, p. 79-88.

DOWEY, P.J., HODGSON, D.M., AND WORDEN, R.H., 2012, Pre-requisites, processes, and prediction of chlorite grain coatings in petroleum reservoirs: a review of subsurface examples: Marine and Petroleum Geology, v. 32, p. 63-75.

DOWEY, P.J., WORDEN, R.H., UTLEY, J., AND HODGSON, D.M., 2017, Sedimentary controls on modern sand grain coat formation: Sedimentary Geology, v. 353, p. 46-63.

DRAKE, H., IVARSSON, M., BENGTSON, S., HEIM, C., SILJESTRÖM, S., WHITEHOUSE, M.J., BROMAN, C., BELIVANOVA, V., AND ÅSTRÖM, M.E., 2017, Anaerobic consortia of fungi and sulfate reducing bacteria in deep granite fractures: Nature Communications, v. 8, p. 55.

DRITS, V.A., IVANOVSKAYA, T.A., SAKHAROV, B.A., GOR'KOVA, N.V., KARPOVA, G.V., AND POKROVSKAYA, E.V., 2001, Pseudomorphous replacement of globular glauconite by mixed-layer chlorite-berthierine in the outer contact of dike: Evidence from the Lower Riphean Ust'-Il'ya Formation, Anabar Uplift: Lithology and Mineral Resources, v. 36, p. 337-352.

DUPRAZ, C., REID, R.P., BRAISSANT, O., DECHO, A.W., NORMAN, R.S., AND VISSCHER, P.T., 2009, Processes of carbonate precipitation in modern microbial mats: Earth-Science Reviews, v. 96, p. 141-162.

DUTEIL, T., BOURILLOT, R., GRÉGOIRE, B., VIROLLE, M., BRIGAUD, B., NOUET, J., BRAISSANT, O., PORTIER, E., FÉNIÈS, H., PATRIER, P., GONTIER, E., SVAHN, I., AND VISSCHER, P.T., 2020, Experimental formation of clay-coated sand grains using diatom biofilm exopolymers: Geology, v. 48, p. 1012-1017.

DUTTON, S.P., HUTTON, M.E., AMBROSE, W.A., CHILDERS, A.T., AND LOUCKS, R.G., 2018, Preservation of reservoir quality by chlorite coats in deep Tuscaloosa sandstones, Central Louisiana, U.S.A.: Gulf Coast Association of Geological Societies, v. 7, p. 46-58.

DUTTON, S.P., SCOTT HAMLIN, H., FOLK, R.L., CLIFT, S.J., CROSSEY, L.J., LOUCKS, R., TOTTEN, M.W., AND SCHOLLE, P.A., 1996, Early Siderite Cementation as a Control on Reservoir Quality in Submarine Fan Sandstones, Sonora Canyon Gas Play, Val Verde Basin, Texas, Siliciclastic Diagenesis and Fluid Flow: Concepts and Applications, SEPM Society for Sedimentary Geology, p. 0.

EHRENBERG, S.N., 1993, Preservation of anomalously high porosity in deeply buried sandstones by grain-coating chlorite: examples from the Norwegian continental shelf: American Association of Petroleum Geologists, Bulletin, v. 77, p. 1260-1286.

EHRENBERG, S.N., AAGAARD, P., WILSON, M.J., FRASER, A.R., AND DUTHIE, D.M.L., 1993, Depth-dependent transformation of kaolinite to dickite In sandstones of the Norwegian continental shelf: Clay Minerals, v. 28, p. 325-352.

EHRENBERG, S.N., DALLAND, A., NADEAU, P.H., MEARNS, E.W., AND AMUNDSEN, E.F., 1998, Origin of chlorite enrichment and neodymium isotopic anomalies in Haltenbanken sandstones: Marine and Petroleum Geology, v. 15, p. 403-425.

EHRENBERG, S.N., AND NADEAU, P.H., 1989, Formation of diagenetic illite in sandstones of the Garn Formation, Haltenbanken area, mid-Norwegian continental shelf: Clay Minerals, v. 24, p. 233-253.

EHRENBERG, S.N., NADEAU, P.H., AND STEEN, O., 2008, A megascale view of reservoir quality in producing sandstones from the offshore Gulf of Mexico: American Association of Petroleum Geologists, Bulletin, v. 92, p. 145-164.

EICKHORST, T., AND TIPPKÖTTER, R., 2008, Detection of microorganisms in undisturbed soil by combining fluorescence in situ hybridization (FISH) and micropedological methods: Soil Biology and Biochemistry, v. 40, p. 1284-1293.

EMERY, D., MYERS, K.J., AND YOUNG, R., 1990, Ancient subaerial exposure and freshwater leaching in sandstones: Geology, v. 18, p. 1178-1181.

ERNSTSEN, V., GATES, W.P., AND STUCKI, J.W., 1998, Microbial Reduction of Structural Iron in Clays—A Renewable Source of Reduction Capacity: Journal of Environmental Quality, v. 27, p. 761-766.

FAWAD, M., MONDOL, N.H., JAHREN, J., AND BJØRLYKKE, K., 2011, Mechanical compaction and ultrasonic velocity of sands with different texture and mineralogical composition: Geophysical Prospecting, v. 59, p. 697-720.

FERRIS, F.G., BEVERIDGE, T.J., AND FYFE, W.S., 1986, Iron-silica crystallite nucleation by bacteria in a geothermal sediment: Nature, v. 320, p. 609-611.

FERRIS, F.G., FYFE, W.S., AND BEVERIDGE, T.J., 1987, Bacteria as nucleation sites for authigenic minerals in a metal-contaminated lake sediment: Chemical Geology, v. 63, p. 225-232.

FERRIS, F.G., FYFE, W.S., AND BEVERIDGE, T.J., 1991, Bacteria as Nucleation Sites for Authigenic Minerals, *in* Berthelin, J., ed., Developments in Geochemistry, Elsevier, p. 319-325.

FHEED, A., KRZYŻAK, A., AND ŚWIERCZEWSKA, A., 2018, Exploring a carbonate reef reservoir – nuclear magnetic resonance and computed microtomography confronted with narrow channel and fracture porosity: Journal of Applied Geophysics, v. 151, p. 343-358.

FLEMMING, H.-C., AND WINGENDER, J., 2010, The biofilm matrix: Nature Reviews Microbiology, v. 8, p. 623-633.

FLORAN, R.J., AND PAPIKE, J.J., 1975, Petrology of the Low-Grade Rocks of the Gunflint Iron-Formation, Ontario-Minnesota: GSA Bulletin, v. 86, p. 1169-1190.

FOLK, R.L., AND LYNCH, F.L., 1997, The possible role of nannobacteria (dwarf bacteria) in clay-mineral diagenesis and the importance of careful sample preparation in high-magnification SEM study: Journal of Sedimentary Research, v. 67, p. 583-589.

FOLKESTAD, A., VESELOYSKY, Z., AND ROBERTS, P., 2012, Utilising borehole image logs to interpret delta to estuarine system: A case study of the subsurface Lower Jurassic Cook Formation in the Norwegian northern North Sea: Marine and Petroleum Geology, v. 29, p. 255-275.

FOMINA, M., AND GADD, G.M., 2002, Influence of clay minerals on the morphology of fungal pellets: Mycological Research, v. 106, p. 107-117.

FOMINA, M., AND GADD, G.M., 2003, Metal sorption by biomass of melanin-producing fungi grown in clay-containing medium: Journal of Chemical Technology & Biotechnology, v. 78, p. 23-34.

FORTIN, D., AND BEVERIDGE, T.J., 1997, Microbial sulfate reduction within sulfidic mine tailings: Formation of diagenetic Fe sulfides: Geomicrobiology Journal, v. 14, p. 1-21.

FORTIN, D., FERRIS, F.G., AND SCOTT, S.D., 1998, Formation of Fe-silicates and Fe-oxides on bacterial surfaces in samples collected near hydrothermal vents on the Southern Explorer Ridge in the Northeast Pacific Ocean: American Mineralogist, v. 83, p. 1399-1408.

FRANK, F.C., 1949, The influence of dislocations on crystal growth: Discussions of the Faraday Society, v. 5, p. 48-54.

FRENCH, M.W., AND WORDEN, R.H., 2013, Orientation of microcrystalline quartz in the Fontainebleau Formation, Paris Basin and why it preserves porosity: Sedimentary Geology, v. 284-285, p. 149-158.

FRENCH, M.W., WORDEN, R.H., MARIANI, E., LARESE, R.E., MUELLER, R.R., AND KLIEWER, C.E., 2012, Microcrystalline quartz generation and the preservation of porosity in sandstones: Evidence from the Upper Cretaceous of the Subhercynian Basin, Germany: Journal of Sedimentary Research, v. 82, p. 422-434.

FURUKAWA, Y., AND O'REILLY, S.E., 2007, Rapid precipitation of amorphous silica in experimental systems with nontronite (NAu-1) and Shewanella oneidensis MR-1: Geochimica et Cosmochimica Acta, v. 71, p. 363-377.

GALLOWAY, W.E., 1979, Diagenetic control of Reservoir quality in arc-derived sandstones: Implications for petroleum exploration: SEPM Special Publication, v. 26, p. 251-262.

GATES, W.P., JAUNET, A.-M., TESSIER, D., COLE, M.A., WILKINSON, H.T., AND STUCKI, J.W., 1998, Swelling and Texture of Iron-Bearing Smectites Reduced by Bacteria: Clays and Clay Minerals, v. 46, p. 487-497.

GAUPP, R., MATTER, A., PLATT, J., RAMSEYER, K., AND WALZEBUCK, J., 1993, Diagenesis and Fluid Evolution of Deeply Buried Permian (Rotliegende) Gas Reservoirs, Northwest Germany1: American Association of Petroleum Geologists, Bulletin, v. 77, p. 1111-1128.

GEESEY, G.G., JANG, L., JOLLEY, J.G., HANKINS, M.R., IWAOKA, T., AND GRIFFITHS, P.R., 1988, Binding of Metal Ions by Extracellular Polymers of Biofilm Bacteria: Water Science and Technology, v. 20, p. 161-165.

GILES, M., INDRELID, S., BEYNON, G., AMTHOR, J., WORDEN, R., AND MORAD, S., 2000, The origin of large-scale quartz cementation: Evidence from large data sets and coupled heat-fluid mass transport modeling: Special publications of the International Association of Sedimentologists, p. 21-38.

GLUYAS, J., AND CADE, C.A., 1997, Prediction of porosity in compacted sands: American Association of Petroleum Geologists, Bulletin, v. 69, p. 19-27.

GLUYAS, J.G., ROBINSON, A.G., EMERY, D., GRANT, S.M., AND OXTOBY, N.H., 1993, The link between petroleum emplacement and sandstone cementation: Geological Society, London, Petroleum Geology Conference series, v. 4, p. 1395.

GOLAB, A.N., KNACKSTEDT, M.A., AVERDUNK, H., SENDEN, T., BUTCHER, A.R., AND JAIME, P., 2010, 3D porosity and mineralogy characterization in tight gas sandstones: The Leading Edge, v. 29, p. 1476-1483.

GOLDSTEIN, R.H., AND ROSSI, C., 2002, Recrystallization in quartz overgrowths: Journal of Sedimentary Research, v. 72, p. 432-440.

GOULD, K.M., PIPER, D.J.W., AND PE-PIPER, G., 2012, Lateral variation in sandstone lithofacies from conventional core, Scotian Basin: implications for reservoir quality and connectivity 1This article is one of a series of papers published in this CJES Special Issue on the theme of Mesozoic–Cenozoic geology of the Scotian Basin. 2Geological Survey of Canada Contribution 20120021: Canadian Journal of Earth Sciences, v. 49, p. 1478-1503.

GRANT, N.T., MIDDLETON, A.J., AND ARCHER, S., 2014, Porosity trends in the Skagerrak Formation, Central Graben, United Kingdom Continental Shelf: The role of compaction and pore pressure history: American Association of Petroleum Geologists, Bulletin, v. 98, p. 1111-1143.

GRIFFITHS, J., WORDEN, R.H., WOOLDRIDGE, L.J., UTLEY, J.E.P., AND DULLER, R.A., 2018, Detrital Clay Coats, Clay Minerals, and Pyrite: A Modern Shallow-Core Analogue For Ancient and Deeply Buried Estuarine Sandstones: Journal of Sedimentary Research, v. 88, p. 1205-1237.

GRIFFITHS, J., WORDEN, R.H., WOOLDRIDGE, L.J., UTLEY, J.E.P., AND DULLER, R.A., 2019a, Compositional variation in modern estuarine sands: Predicting major controls on sandstone reservoir quality: American Association of Petroleum Geologists, Bulletin, v. 103, p. 797-833.

GRIFFITHS, J., WORDEN, R.H., WOOLDRIDGE, L.J., UTLEY, J.E.P., DULLER, R.A., AND EDGE, R.L., 2019b, Estuarine clay mineral distribution: Modern analogue for ancient sandstone reservoir quality prediction: Sedimentology, v. 66, p. 2011-2047.

GRIGSBY, J.D., 2001, Origin and growth mechanism of authigenic chlorite in sandstones of the lower Vicksburg Formation, South Texas: Journal of Sedimentary Research, v. 71, p. 27-36.

GROVE, C., AND JERRAM, D.A., 2011, jPOR: An ImageJ macro to quantify total optical porosity from blue-stained thin sections: Computers & Geosciences, v. 37, p. 1850-1859.

HADDAD, S.C., WORDEN, R.H., PRIOR, D.J., AND SMALLEY, P.C., 2006, Quartz Cement in the Fontainebleau Sandstone, Paris Basin, France: Crystallography and Implications for Mechanisms of Cement Growth: Journal of Sedimentary Research, v. 76, p. 244-256.

HAILE, B.G., HELLEVANG, H., AAGAARD, P., AND JAHREN, J., 2015, Experimental nucleation and growth of smectite and chlorite coatings on clean feldspar and quartz grain surfaces: Marine and Petroleum Geology, v. 68, p. 664-674.

HAILE, B.G., KLAUSEN, T.G., CZARNIECKA, U., XI, K., JAHREN, J., AND HELLEVANG, H., 2018, How are diagenesis and reservoir quality linked to depositional facies? A deltaic succession, Edgeøya, Svalbard: Marine and Petroleum Geology, v. 92, p. 519-546.

HAIMSON, B., AND LEE, H., 2004, Borehole breakouts and compaction bands in two high-porosity sandstones: International Journal of Rock Mechanics and Mining Sciences, v. 41, p. 287-301.

HARDER, H., 1989, Mineral genesis in ironstones: a model based upon laboratory experiments and petrographic observations, *in* Young, T.P., and Taylor, W.E.G., eds., Phanerozoic Ironstones: Geological Society of London, Special Publication 46, p. 9-18.

HARLOW, F.H., AND WELCH, J.E., 1965, Numerical Calculation of Time-Dependent Viscous Incompressible Flow of Fluid with Free Surface: The Physics of Fluids, v. 8, p. 2182-2189.

HASNAIN, S.M., AND JAHREN, J., 2017, Reservoir quality preserving processes in Lower Jurassic Cook Formation of Veslefrikk area, 79th EAGE Conference and Exhibition 2017, European Association of Geoscientists & Engineers, p. 1-3.

HASZELDINE, R.S., BRINT, J.F., FALLICK, A.E., HAMILTON, P.J., AND BROWN, S., 1992, Open and restricted hydrologies in Brent Group diagenesis: North Sea: Geological Society, London, Special Publications, v. 61, p. 401.

HATTORI, I., UMEDA, M., NAKAGAWA, T., AND YAMAMOTO, H., 1996, From chalcedonic chert to quartz chert: diagenesis of chert hosted in a Miocene volcanic-sedimentary succession, Central Japan: Journal of Sedimentary Research, v. 66.

HAZLETT, R.D., 1997, Statistical characterization and stochastic modeling of pore networks in relation to fluid flow: Mathematical Geology, v. 29, p. 801-822.

HEALD, M., AND RENTON, J., 1966, Experimental study of sandstone cementation: Journal of Sedimentary Petrology, v. 36, p. 977-991.

HEALD, M.T., AND LARESE, R.E., 1974, Influence of coatings on quartz cementation: Journal of Sedimentary Petrology, v. 44, p. 1269-1274.

HENDRY, J.P., AND TREWIN, N.H., 1995, Authigenic quartz microfabrics in Cretaceous turbidites: evidence for silica transformation processes in sandstones: Journal of Sedimentary Research, v. 65.

HIGGINS, M.J., MOLINO, P., MULVANEY, P., AND WETHERBEE, R., 2003, The structure and nanomechanical properties of the adhesive mucilage that mediates diatom-substratum adhesion and motility1: Journal of Phycology, v. 39, p. 1181-1193.

HILLIER, S., 1994, Pore-lining chlorites in siliciclastic reservoir sandstones: electron-microprobe, sem and xrd data, and implications for their origin: Clay Minerals, v. 29, p. 665-679.

HOGG, A.J.C., SELLIER, E., AND JOURDAN, A.J., 1992, Cathodoluminescence of quartz cements in Brent Group sandstones, Alwyn South, UK North Sea: Geological Society, London, Special Publications, v. 61, p. 421-440.

HORNIBROOK, E.R., AND LONGSTAFFE, F.J., 1996, Berthierine from the lower cretaceous Clearwater formation, Alberta, Canada: Clays and Clay Minerals, v. 44, p. 1-21.

HOUSEKNECHT, D.W., 1987, Assessing the relative importance of compaction processes and cementation to reduction of porosity in sandstones: American Association of Petroleum Geologists, Bulletin, v. 71, p. 633-642.

HUGGETT, J., BURLEY, S., LONGSTAFFE, F., SAHA, S., AND OATES, M., 2015, The nature and origin of authigenic chlorite and related cements in Oligo–Miocene reservoir sandstones, Tapti Gas Fields, Surat Depression, offshore western India: Journal of Petroleum Geology, v. 38, p. 383-409.

HUGGETT, J.M., GALE, A.S., AND HAZELL, C., 2018, Early diagenesis of the lower Vectis Formation, Wealden Group Lower Cretaceous, Barremian), Sandown, Isle of Wight: Proceedings of the Geologists' Association, v. 129, p. 782-789.

HUMPHREYS, B., KEMP, S., LOTT, G., DHARMAYANTI, D., AND SAMSORI, I., 1994, Origin of grain-coating chlorite by smectite transformation; an example from Miocene sandstones, North Sumatra back-arc basin, Indonesia: Clay Minerals, v. 29, p. 681-692.

HUMPHREYS, B., SMITH, S.A., AND STRONG, G.E., 1989, Authigenic chlorite in Late Triassic sandstones from the Central Graben, North Sea: Clay Minerals, v. 24, p. 427-444.

HURST, A., AND NADEAU, P.H., 1995, Clay Microporosity in Reservoir Sandstones: An Application of Quantitative Electron Microscopy in Petrophysical Evaluation1: American Association of Petroleum Geologists, Bulletin, v. 79, p. 563-573.

IASSONOV, P., GEBRENEGUS, T., AND TULLER, M., 2009, Segmentation of X-ray computed tomography images of porous materials: A crucial step for characterization and quantitative analysis of pore structures: Water Resources Research, v. 45.

IIJIMA, A., AND MATSUMOTO, R., 1982, Berthierine and chamosite in coal measures of Japan: Clays and Clay Minerals, v. 30, p. 264-274.

JAHREN, J., AND AAGAARD, P., 1989, Compositional variations in diagenetic chlorites and illites, and relationships with formation-water chemistry: Clay Minerals, v. 24, p. 157-170.

JAHREN, J., OLSEN, E., AND BJØRLYKKE, K., 1998, Chlorite coatings in deeply buried sandstones - examples from the Norwegian shelf, *in* Arehart, G.B., and Hulston, J.R., eds., Water-Rock Interaction, p. 321-324.

JAHREN, J., AND RAMM, M., 2000, The porosity-preserving effects of microcrystalline quartz coatings in arenitic sandstones: Examples from the Norwegian continental shelf, *in* Worden, R.H., and Morad, S., eds., Quartz Cementation in Sandstones, Blackwell Science Ltd, p. 271-280.

JAHREN, J.S., 1991, Evidence of Ostwald ripening related recrystallization of diagenetic chlorites from reservoir rocks offshore Norway: Clay minerals, v. 26, p. 169-178.

JAISI, D.P., DONG, H., AND LIU, C., 2007, Influence of biogenic Fe(II) on the extent of microbial reduction of Fe(III) in clay minerals nontronite, illite, and chlorite: Geochimica et Cosmochimica Acta, v. 71, p. 1145-1158.

JAMES, W.C., WILMAR, G.C., AND DAVIDSON, B.G., 1986, Role of quartz type and grain size in silica diagenesis, Nugget Sandstone, south-central Wyoming: Journal of Sedimentary Research, v. 56, p. 657-662.

JEANS, C., WRAY, D., MERRIMAN, R., AND FISHER, M., 2000, Volcanogenic clays in Jurassic and Cretaceous strata of England and the North Sea Basin: Clay Minerals, v. 35, p. 25-56.

KANTOROWICZ, J.D., 1990, The influence of variations in illite morphology on the permeability of Middle Jurassic Brent Group sandstones, Cormorant Field, UK North Sea: Marine and Petroleum Geology, v. 7, p. 66-74.

KARIM, A., PE-PIPER, G., AND PIPER, D.J.W., 2010, Controls on diagenesis of Lower Cretaceous reservoir sandstones in the western Sable Subbasin, offshore Nova Scotia: Sedimentary Geology, v. 224, p. 65-83.

KASHEFI, K., SHELOBOLINA, E.S., ELLIOTT, W.C., AND LOVLEY, D.R., 2008, Growth of Thermophilic and Hyperthermophilic Fe(III)-Reducing Microorganisms on a Ferruginous Smectite as the Sole Electron Acceptor: Applied and Environmental Microbiology, v. 74, p. 251-258.

KEEHM, Y., MUKERJI, T., AND NUR, A., 2004, Permeability prediction from thin sections: 3D reconstruction and Lattice-Boltzmann flow simulation: Geophysical Research Letters, v. 31.

KELEMEN, P., BENSON, S.M., PILORGÉ, H., PSARRAS, P., AND WILCOX, J., 2019, An Overview of the Status and Challenges of CO2 Storage in Minerals and Geological Formations: Frontiers in Climate, v. 1, p. 9.

KESSARKAR, P.M., PURNACHANDRA RAO, V., SHYNU, R., MEHRA, P., AND VIEGAS, B.E., 2010, The Nature and Distribution of Particulate Matter in the Mandovi Estuary, Central West Coast of India: Estuaries and Coasts, v. 33, p. 30-44.

KETCHAM, R.A., AND CARLSON, W.D., 2001, Acquisition, optimization and interpretation of X-ray computed tomographic imagery: applications to the geosciences: Computers & Geosciences, v. 27, p. 381-400.

KINGSTON, A., SAKELLARIOU, A., VARSLOT, T., MYERS, G., AND SHEPPARD, A., 2011, Reliable automatic alignment of tomographic projection data by passive auto-focus: Medical Physics, v. 38, p. 4934-4945.

KNAUSS, K.G., AND WOLERY, T.J., 1988, The dissolution kinetics of quartz as a function of pH and time at 70°C: Geochimica et Cosmochimica Acta, v. 52, p. 43-53.

KONHAUSER, K.O., 1998, Diversity of bacterial iron mineralization: Earth-Science Reviews, v. 43, p. 91-121.

KONHAUSER, K.O., AND FERRIS, F.G., 1996, Diversity of iron and silica precipitation by microbial mats in hydrothermal waters, Iceland: Implications for Precambrian iron formations: Geology, v. 24, p. 323-326.

KONHAUSER, K.O., FISHER, Q.J., FYFE, W.S., LONGSTAFFE, F.J., AND POWELL, M.A., 1998, Authigenic mineralization and detrital clay binding by freshwater biofilms: The Brahmani river, India: Geomicrobiology Journal, v. 15, p. 209-222.

KONHAUSER, K.O., FYFE, W.S., FERRIS, F.G., AND BEVERIDGE, T.J., 1993, Metal sorption and mineral precipitation by bacteria in two Amazonian river systems: Rio Solimões and Rio Negro, Brazil: Geology, v. 21, p. 1103-1106.

KONHAUSER, K.O., SCHULTZE-LAM, S., FERRIS, F.G., FYFE, W.S., LONGSTAFFE, F.J., AND BEVERIDGE, T.J., 1994, Mineral Precipitation by Epilithic Biofilms in the Speed River, Ontario, Canada: Applied and Environmental Microbiology, v. 60, p. 549.

KONHAUSER, K.O., AND URRUTIA, M.M., 1999, Bacterial clay authigenesis: a common biogeochemical process: Chemical Geology, v. 161, p. 399-413.

KOSTKA, J.E., DALTON, D.D., SKELTON, H., DOLLHOPF, S., AND STUCKI, J.W., 2002, Growth of Iron(III)-Reducing Bacteria on Clay Minerals as the Sole Electron Acceptor and Comparison of Growth Yields on a Variety of Oxidized Iron Forms: Applied and Environmental Microbiology, v. 68, p. 6256-6262.

KOSTKA, J.E., HAEFELE, E., VIEHWEGER, R., AND STUCKI, J.W., 1999a, Respiration and Dissolution of Iron(III)-Containing Clay Minerals by Bacteria: Environmental Science & Technology, v. 33, p. 3127-3133.

KOSTKA, J.E., WU, J., NEALSON, K.H., AND STUCKI, J.W., 1999b, The impact of structural Fe(III) reduction by bacteria on the surface chemistry of smectite clay minerals: Geochimica et Cosmochimica Acta, v. 63, p. 3705-3713.

KRISTIANSEN, K., VALTINER, M., GREENE, G.W., BOLES, J.R., AND ISRAELACHVILI, J.N., 2011, Pressure solution – The importance of the electrochemical surface potentials: Geochimica et Cosmochimica Acta, v. 75, p. 6882-6892.

LAND, L.S., 1997, Mass transfer during burial diagenesis in the Gulf of Mexico sedimentary basin: an overview.

LANDER, R.H., LARESE, R.E., AND BONNELL, L.M., 2006, Why do microquartz coatings preserve sandstone reservoir quality?: Annual AAPG Convection Abstracts, v. 15, p. 60.

LANDER, R.H., LARESE, R.E., AND BONNELL, L.M., 2008, Toward more accurate quartz cement models: The importance of euhedral versus noneuhedral growth rates: American Association of Petroleum Geologists, Bulletin, v. 92, p. 1537-1563.

LANSON, B., BEAUFORT, D., BERGER, G., BAUER, A., CASSAGNABERE, A., AND MEUNIER, A., 2002, Authigenic kaolin and illitic minerals during burial diagenesis of sandstones: a review: Clay Minerals, v. 37, p. 1-22.

LASAGA, A.C., 1998, Kinetic Theory in the Earth Sciences: Princeton, New Jersey, Princeton University Press, 811 p.

LATHAM, S.J., KINGSTON, A.M., RECUR, B., MYERS, G.R., DELGADO-FRIEDRICHS, O., AND SHEPPARD, A.P., 2018, Reprojection Alignment for Trajectory Perturbation Estimation in Microtomography: IEEE Transactions on Computational Imaging, v. 4, p. 271-283.

LEDER, F., AND PARK, W.C., 1986, Porosity reduction in sandstone by quartz overgrowth: American Association of Petroleum Geologists, Bulletin, v. 70, p. 1713-1728.

LEWANDOWSKI, Z., AND BEYENAL, H., 2013, Fundamentals of biofilm research, CRC press.

LI, S., TIAN, J., LIN, X., ZUO, Y., KANG, H., AND YANG, D., 2020, Effect of alkaline diagenesis on sandstone reservoir quality: Insights from the Lower Cretaceous Erlian Basin, China: Energy Exploration & Exploitation, v. 38, p. 434-453.

LIANG, Z., IOANNIDIS, M.A., AND CHATZIS, I., 2000, Permeability and electrical conductivity of porous media from 3D stochastic replicas of the microstructure: Chemical Engineering Science, v. 55, p. 5247-5262.

LIMA, R.D., AND DE ROS, L.F., 2002, The role of depositional setting and diagenesis on the reservoir quality of Devonian sandstones from the Solimões Basin, Brazilian Amazonia: Marine and Petroleum Geology, v. 19, p. 1047-1071.

LIN, Q., NEETHLING, S.J., DOBSON, K.J., COURTOIS, L., AND LEE, P.D., 2015, Quantifying and minimising systematic and random errors in X-ray micro-tomography based volume measurements: Computers & Geosciences, v. 77, p. 1-7.

LINDQUIST, W.B., VENKATARANGAN, A., DUNSMUIR, J., AND WONG, T.-F., 2000, Pore and throat size distributions measured from synchrotron X-ray tomographic images of Fontainebleau sandstones: Journal of Geophysical Research: Solid Earth, v. 105, p. 21509-21527.

LIPPMANN, F., 1973, Sedimentary carbonate minerals: Berlin, Springer-Verlag.

LIVBJERG, F., AND MJØS, R., 1989, The Cook Formation, an offshore sand ridge in the Oseberg area, northern North Sea, *in* Collinson, J.D., ed., Correlation in Hydrocarbon Exploration: Norwegian Petroleum Society, Graham and Trotman, p. 299-312.

LONERGAN, D.J., JENTER, H.L., COATES, J.D., PHILLIPS, E.J., SCHMIDT, T.M., AND LOVLEY, D.R., 1996, Phylogenetic analysis of dissimilatory Fe(III)-reducing bacteria: Journal of Bacteriology, v. 178, p. 2402.

LOS RÍOS, A., WIERZCHOS, J., SANCHO, L.G., AND ASCASO, C., 2003, Acid microenvironments in microbial biofilms of antarctic endolithic microecosystems: Environmental Microbiology, v. 5, p. 231-237.

LOVLEY, D.R., HOLMES, D.E., AND NEVIN, K.P., 2004, Dissimilatory Fe(III) and Mn(IV) Reduction, Advances in Microbial Physiology, Academic Press, p. 219-286.

LYNCH, F.L., 1996, Mineral/water interaction, fluid flow, and Frio sandstone diagenesis: evidence from the rocks: American Association of Petroleum Geologists, Bulletin, v. 80, p. 486-504.

MACHEMER, S.D., AND HUTCHEON, I.D., 1988, Geochemistry of early carbonate cements in the Cardium Formation, central Alberta: Journal of Sedimentary Research, v. 58, p. 136-147.

MAHMIC, O., DYPVIK, H., AND HAMMER, E., 2018, Diagenetic influence on reservoir quality evolution, examples from Triassic conglomerates/arenites in the Edvard Grieg field, Norwegian North Sea: Marine and Petroleum Geology, v. 93, p. 247-271.

MAKOWITZ, A., AND SIBLEY, D., 2001, Crystal Growth Mechanisms of Quartz Overgrowths in a Cambrian Quartz Arenite: Journal of Sedimentary Research, v. 71, p. 809-816.

MALARKEY, J., BAAS, J.H., HOPE, J.A., ASPDEN, R.J., PARSONS, D.R., PEAKALL, J., PATERSON, D.M., SCHINDLER, R.J., YE, L., LICHTMAN, I.D., BASS, S.J., DAVIES, A.G., MANNING, A.J., AND THORNE, P.D., 2015, The pervasive role of biological cohesion in bedform development: Nature Communications, v. 6, p. 6257.

MARCHAND, A.M.E., SMALLEY, P.C., HASZELDINE, R.S., AND FALLICK, A.E., 2002, Note on the Importance of Hydrocarbon Fill for Reservoir Quality Prediction in Sandstones: American Association of Petroleum Geologists, Bulletin, v. 86, p. 1561-1571.

MARJANAC, T., AND STEEL, R.J., 1997, Dunlin Group sequence stratigraphy in the northern North sea: a model for Cook Sandstone deposition: American Association of Petroleum Geologists, Bulletin, v. 81, p. 276-292.

MARKUSSEN, Ø., DYPVIK, H., HAMMER, E., LONG, H., AND HAMMER, Ø., 2019, 3D characterization of porosity and authigenic cementation in Triassic conglomerates/arenites in the Edvard Grieg field using 3D micro-CT imaging: Marine and Petroleum Geology, v. 99, p. 265-281.

MARTÍN-MARTÍN, J.D., GÓMEZ-GRAS, D., SANFELIU, T., THIRY, M., RUIZ-CRUZ, M.D., AND FRANCO, F., 2007, Extensive dickitization of the permo-triassic fluvial sandstones from the eastern Iberian Range, Spain: Clays and Clay Minerals, v. 55, p. 481-490.

MATLACK, K.S., HOUSEKNECHT, D.W., AND APPLIN, K.R., 1989, Emplacement of clay into sand by infiltration: Journal of Sedimentary Petrology, v. 59, p. 77-87.

MATTER, J.M., AND KELEMEN, P.B., 2009, Permanent storage of carbon dioxide in geological reservoirs by mineral carbonation: Nature Geoscience, v. 2, p. 837-841.

MCBRIDE, E., LAND, L., DIGGS, T., AND MACK, L., 1988, Petrography, stable isotope geochemistry and diagenesis of Miocene sandstones, Vermilion Block 31, offshore Louisiana.

MCBRIDE, E.F., 1989, Quartz cement in sandstones: a review: Earth-Science Reviews, v. 26, p. 69-112.

MCILROY, D., WORDEN, R.H., AND NEEDHAM, S.J., 2003, Faeces, clay minerals and reservoir potential: Journal of the Geological Society, v. 160, p. 489-493.

McKinley, J.M., Worden, R.H., and Ruffell, A.H., 2003, Smectite in sandstones: a review of the controls on occurrence and behavior during diagenesis, *in* Worden, R.H., and Morad, S., eds., Clay MIneral Cements in Sandstones: International Association of Sedimentologists, Special Publication 34, p. 109-128.

McMahon, P.B., Chapelle, F.H., Bradley, P.M., and Falls, W.F., 1992, Role of microbial processes in linking sandstone diagenesis with organic-rich clays: Journal of Sedimentary Research, v. 62, p. 1-10.

Melvin, J., and Knight, A.S., 1984, Lithofacies, diagenesis and porosity of the Ivishak Formation, Prudhoe Bay area, Alaska: Clastic diagenesis: AAPG Memoir, v. 37, p. 347-365.

Milliken, K., Mack, L., and Land, L., 1994, Elemental mobility in sandstones during burial: whole-rock chemical and isotopic data, Frio Formation, South Texas: Journal of Sedimentary Research, v. A64, p. 788-796.

Milliken, K.L., 1998, Carbonate Diagenesis in Non-Marine Foreland Sandstones at the Western Edge of the Alleghanian Overthrust Belt, Southern Appalachians, *in* Morad, S., ed., Carbonate Cementation in Sandstones, International Association of Sedimentologists, Special Publication, p. 87-105.

Milliken, K.L., and Curtis, M.E., 2016, Imaging pores in sedimentary rocks: Foundation of porosity prediction: Marine and Petroleum Geology, v. 73, p. 590-608.

Molenaar, N., Cyziene, J., Sliaupa, S., and Craven, J., 2008, Lack of inhibiting effect of oil emplacement on quartz cementation: Evidence from Cambrian reservoir sandstones, Paleozoic Baltic Basin: GSA Bulletin, v. 120, p. 1280-1295.

Moncure, G., Lahann, R., Siebert, R., McDonald, D., and Surdam, R., 1984, Origin of secondary porosity and cement distribution in a sandstone/shale sequence from the Frio Formation (Oligocene): Clastic diagenesis: AAPG Memoir, v. 37, p. 151-161.

Morad, S., 1998, Carbonate Cementation in Sandstones: Distribution Patterns and Geochemical Evolution: Carbonate Cementation in Sandstones, p. 1-26.

Morad, S., Al-Ramadan, K., Ketzer, J.M., and De Ros, L.F., 2010, The impact of diagenesis on the heterogeneity of sandstone reservoirs: a review of the role of depositional facies and sequence stratigraphy: American Association of Petroleum Geologists, Bulletin, v. 94, p. 1267-1309.

Morad, S., and Aldahan, A.A., 1987, Diagenetic chloritization of feldspars in sandstones: Sedimentary Geology, v. 51, p. 155-164.

Morad, S., Ismail, H.N.B., De Ros, L.F., Al-Aasm, I.S., and Serrhini, N.-E., 1994, Diagenesis and formation water chemistry of Triassic reservoir sandstones from southern Tunisia: Sedimentology, v. 41, p. 1253-1272.

Morad, S., Ketzer, J., and De Ros, L., 2012, Linking diagenesis to sequence stratigraphy: an integrated tool for understanding and predicting reservoir quality distribution: Linking Diagenesis to Sequence Stratigraphy. Special Publication of the International Association of Sedimentologists, v. 45, p. 1-36.

Moraes, M.A., and De Ros, L.F., 1992, Depositional infiltrated and authigenic clays in fluvial sandstones of the Jurassic Sergi Formation, Reconcavo Basin, northeastern Brazil, *in* Houseknecht, D.W., and Pittman, E.W., eds., Origin, Diagenesis, and Petrophysics of Clay Minerals in Sandstones: SEPM, Special Publication 47, p. 197-208.

Mortimer, R.J.G., and Coleman, M.L., 1997, Microbial influence on the oxygen isotopic composition of diagenetic siderite: Geochimica et Cosmochimica Acta, v. 61, p. 1705-1711.

Mortimer, R.J.G., Coleman, M.L., and Rae, J.E., 1997, Effect of bacteria on the elemental composition of early diagenetic siderite: implications for palaeoenvironmental interpretations: Sedimentology, v. 44, p. 759-765.

Mozley, P.S., 1989, Relation between depositional environment and the elemental composition of early diagenetic siderite: Geology, v. 17, p. 704-706.

MOZLEY, P.S., AND CAROTHERS, W.W., 1992, Elemental and isotopic composition of siderite in the Kuparuk Formation, Alaska; effect of microbial activity and water sediment interaction on early pore-water chemistry: Journal of Sedimentary Research, v. 62, p. 681-692.

MU, N., SCHULZ, H.-M., FU, Y., SCHOVSBO, N.H., WIRTH, R., RHEDE, D., AND VAN BERK, W., 2015, Berthierine formation in reservoir rocks from the Siri oilfield (Danish North Sea) as result of fluid-rock interactions: part I. Characterization: Marine and Petroleum Geology, v. 65, p. 302-316.

MURPHY, M.J., 2016, Geochemical modeling and hydrothermal experiments used to constrain the conditions of illite diagenesis in sedimentary basins, San José State University.

MURPHY, W.M., OELKERS, E.H., AND LICHTNER, P.C., 1989, Surface reaction versus diffusion control of mineral dissolution and growth rates in geochemical processes: Chemical Geology, v. 78, p. 357-380.

NEEDHAM, S.J., WORDEN, R.H., AND MCILROY, D., 2005, Experimental production of clay rims by macrobiotic sediment ingestion and excretion processes: Journal of Sedimentary Research, v. 75, p. 1028-1037.

NGUYEN, B.T.T., JONES, S.J., GOULTY, N.R., MIDDLETON, A.J., GRANT, N., FERGUSON, A., AND BOWEN, L., 2013, The role of fluid pressure and diagenetic cements for porosity preservation in Triassic fluvial reservoirs of the Central Graben, North Sea: American Association of Petroleum Geologists, Bulletin, v. 97, p. 1273-1302.

NGUYEN, D.T., HORTON, R.A., AND KAESS, A.B., 2016, Diagenesis, plagioclase dissolution and preservation of porosity in Eocene and Oligocene sandstones at the Greeley oil field, southern San Joaquin basin, California, USA: Geological Society, London, Special Publications, v. 435, p. 265-282.

NIEMEIJER, A.R., SPIERS, C.J., AND BOS, B., 2002, Compaction creep of quartz sand at 400–600°C: experimental evidence for dissolution-controlled pressure solution: Earth and Planetary Science Letters, v. 195, p. 261-275.

ODIGI, M.I., AND AMAJOR, L.C., 2010, Geochemistry of carbonate cements in Cretaceous sandstones, southeast Benue Trough, Nigeria: Implications for geochemical evolution of formation waters: Journal of African Earth Sciences, v. 57, p. 213-226.

ODIN, G.S., 1988, The verdine facies: introduction to the verdine facies, *in* Odin, G.S., ed., Green Marine Clays: Oolitic Ironstone Facies, Verdine Facies, Glaucony Facies and Celadonite-bearing Facies - A Comparative Study, Elsevier, p. 53-56.

ODIN, G.S., 1990, Clay mineral formation at the continent-ocean boundary: the verdine facies: Clay Minerals, v. 25, p. 477-483.

OELKERS, E.H., BJORKUM, P.A., AND MURPHY, W.M., 1996, A petrographic and computational investigation of quartz cementation and porosity reduction in North Sea sandstones: American Journal of Science, v. 296, p. 420-452.

OELKERS, E.H., BJØRKUM, P.A., WALDERHAUG, O., NADEAU, P.H., AND MURPHY, W.M., 2000, Making diagenesis obey thermodynamics and kinetics: the case of quartz cementation in sandstones from offshore mid-Norway: Applied Geochemistry, v. 15, p. 295-309.

ØREN, P.-E., AND BAKKE, S., 2002, Process based reconstruction of sandstones and prediction of transport properties: Transport in Porous Media, v. 46, p. 311-343.

OSBORNE, M., HASZELDINE, R.S., AND FALLICK, A.E., 1994, Variation in kaolinite morphology with growth temperature in isotopically mixed pore-fluids, Brent Group, UK North Sea: Clay Minerals, v. 29, p. 591-608.

OSBORNE, M.J., AND SWARBRICK, R.E., 1999, Diagenesis in North Sea HPHT clastic reservoirs - consequences for porosity and overpressure prediction: Marine and Petroleum Geology, v. 16, p. 337-353.

OYE, O.J., APLIN, A.C., JONES, S.J., GLUYAS, J.G., BOWEN, L., HARWOOD, J., ORLAND, I.J., AND VALLEY, J.W., 2020, Vertical effective stress and temperature as controls of quartz cementation in sandstones: Evidence from North Sea Fulmar and Gulf of Mexico Wilcox sandstones: Marine and Petroleum Geology, v. 115, p. 104289.

OYE, O.J., APLIN, A.C., JONES, S.J., GLUYAS, J.G., BOWEN, L., ORLAND, I.J., AND VALLEY, J.W., 2018, Vertical effective stress as a control on quartz cementation in sandstones: Marine and Petroleum Geology, v. 98, p. 640-652.

P. STOODLEY, K. SAUER, D. G. DAVIES, AND COSTERTON, J.W., 2002, Biofilms as Complex Differentiated Communities: Annual Review of Microbiology, v. 56, p. 187-209.

PAK, T., BUTLER, I.B., GEIGER, S., VAN DIJKE, M.I.J., JIANG, Z., AND SURMAS, R., 2016, Multiscale pore-network representation of heterogeneous carbonate rocks: Water Resources Research, v. 52, p. 5433-5441.

PATERSON, D.M., HOPE, J.A., KENWORTHY, J., BILES, C.L., AND GERBERSDORF, S.U., 2018, Form, function and physics: the ecology of biogenic stabilisation: Journal of Soils and Sediments, v. 18, p. 3044-3054.

PAXTON, S., SZABO, J., AJDUKIEWICZ, J., AND KLIMENTIDIS, R., 2002, Construction of an intergranular volume compaction curve for evaluating and predicting compaction and porosity loss in rigid-grain sandstone reservoirs: American Association of Petroleum Geologists, Bulletin, v. 86, p. 2047-2067.

PE-PIPER, G., AND PIPER, D.J.W., 2020, Significance of the chemistry and morphology of diagenetic siderite in clastic rocks of the Mesozoic Scotian Basin: Sedimentology, v. 67, p. 782-809.

PE-PIPER, G., AND WEIR-MURPHY, S., 2008, Early diagenesis of inner-shelf phosphorite and iron-silicate minerals, Lower Cretaceous of the Orpheus graben, southeastern Canada: Implications for the origin of chlorite rims: American Association of Petroleum Geologists, Bulletin, v. 92, p. 1153-1168.

PENG, J., LIU, J.K., WANG, Y., AND LIU, J.F., 2009, Origin and controlling factors of chlorite coatings-an example from the reservoir of T(3)x Group of the Baojie area, Sichuan Basin, China: Petroleum Science, v. 6, p. 376-382.

PENG, S., MARONE, F., AND DULTZ, S., 2014, Resolution effect in X-ray microcomputed tomography imaging and small pore's contribution to permeability for a Berea sandstone: Journal of Hydrology, v. 510, p. 403-411.

PICHAT, A., HOAREAU, G., CALLOT, J.P., AND RINGENBACH, J.C., 2016, Diagenesis of Oligocene continental sandstones in salt-walled mini-basins-Sivas Basin, Turkey: Sedimentary Geology, v. 339, p. 13-31.

PITTMAN, E.D., 1972, Diagenesis of quartz in sandstones as revealed by scanning electron-microscopy: Journal of Sedimentary Petrology, v. 42, p. 507-519.

PITTMAN, E.D., LARESE, R.E., AND HEALD, M.T., 1992, Clay coats: occurrence and relevance to preservation of porosity in sandstones, *in* Houseknecht, D.W., and Pittman, E.D., eds., Origin, Diagenesis and Petrophysics of Clay Minerals in Sandstones: SEPM, Special Publication 47, p. 241-255.

PITTMAN, E.D., AND LUMSDEN, D.N., 1968, Relationship between chlorite coatings on quartz grains and porosity, Spiro Sand, Oklahoma: Journal of Sedimentary Research, v. 38, p. 668-670.

PORRENGA, D.H., 1967, Glauconite and chamosite as depth indicators in the marine environment: Marine Geology, v. 5, p. 495-501.

PROBANDT, D., EICKHORST, T., ELLROTT, A., AMANN, R., AND KNITTEL, K., 2018, Microbial life on a sand grain: from bulk sediment to single grains: The ISME journal, v. 12, p. 623-633.

RAMM, M., AND BJORLYKKE, K., 1994, Porosity depth trends in reservoir sandstones - assessing the quantitative effects of varying pore-pressure, temperature history and mineralogy, Norwegian shelf data: Clay Minerals, v. 29, p. 475-490.

RAMM, M., FORSBERG, A.W., AND JAHREN, J.S., 1997, Porosity - Depth trends in deeply buried Upper Jurassic reservoirs in the Norwegian Central Graben: An example of porosity preservation beneath the normal economic basement by grain-coating microquartz, Reservoir quality prediction in sandstones and carbonates, AAPG Memoir, p. 177-199.

REMY, R.R., 1994, Porosity reduction and major controls on diagenesis of Cretaceous-Paleocene volcaniclastic and arkosic sandstone, Middle Park Basin, Colorado: Journal of Sedimentary Research, v. 64, p. 797-806.

REZAEE, M.R., AND SCHULZ-ROJAHN, J., 1998, Application of quantitative back-scattered electron image analysis in isotopic interpretation of siderite cement: Tirrawarra Sandstone, Cooper Basin (Australia), Carbonate cementation in sandstones: distribution patterns and geochemical evolution, International Association of Sedimentologists, p. 461-481.

ROHRLICH, V., PRICE, N., AND CALVERT, S., 1969, Chamosite in the recent sediments of Loch Etive, Scotland: Journal of Sedimentary Research, v. 39, p. 624-631.

ROSSI, C., MARFIL, R., RAMSEYER, K., AND PERMANYER, A., 2001, Facies-Related Diagenesis and Multiphase Siderite Cementation and Dissolution in the Reservoir Sandstones of the Khatatba Formation, Egypt's Western Desert: Journal of Sedimentary Research, v. 71, p. 459-472.

RYAN, P., AND HILLIER, S., 2002, Berthierine/chamosite, corrensite, and discrete chlorite from evolved verdine and evaporite-associated facies in the Jurassic Sundance Formation, Wyoming: American Mineralogist, v. 87, p. 1607-1615.

RYAN, P., AND REYNOLDS, R., 1996, The origin and diagenesis of grain-coating serpentine-chlorite in Tuscaloosa Formation sandstone, US Gulf Coast: American Mineralogist, v. 81, p. 213-225.

SAÏAG, J., BRIGAUD, B., PORTIER, É., DESAUBLIAUX, G., BUCHERIE, A., MISKA, S., AND PAGEL, M., 2016, Sedimentological control on the diagenesis and reservoir quality of tidal sandstones of the Upper Cape Hay Formation (Permian, Bonaparte Basin, Australia): Marine and Petroleum Geology, v. 77, p. 597-624.

SÁNCHEZ-NAVAS, A., MARTÍN ALGARRA, A., AND NIETO, F., 1998, Bacterially-mediated authigenesis of clays in phosphate stromatolites, v. 45, p. 519-533.

SANNA, A., UIBU, M., CARAMANNA, G., KUUSIK, R., AND MAROTO-VALER, M.M., 2014, A review of mineral carbonation technologies to sequester CO2: Chemical Society Reviews, v. 43, p. 8049-8080.

SATHAR, S., AND JONES, S., 2016, Fluid overpressure as a control on sandstone reservoir quality in a mechanical compaction dominated setting: Magnolia Field, Gulf of Mexico: Terra Nova, v. 28, p. 155-162.

SAXENA, N., HOWS, A., HOFMANN, R., FREEMAN, J., AND APPEL, M., 2019, Estimating Pore Volume of Rocks from Pore-Scale Imaging: Transport in Porous Media, v. 129, p. 403-412.

SCHINDLER, R.J., PARSONS, D.R., YE, L.P., HOPE, J.A., BAAS, J.H., PEAKALL, J., MANNING, A.J., ASPDEN, R.J., MALARKEY, J., SIMMONS, S., PATERSON, D.M., LICHTMAN, I.D., DAVIES, A.G., THORNE, P.D., AND BASS, S.J., 2015, Sticky stuff: Redefining bedform prediction in modern and ancient environments: Geology, v. 43, p. 399-402.

SCHMITT, M., HALISCH, M., MÜLLER, C., AND FERNANDES, C.P., 2016, Classification and quantification of pore shapes in sandstone reservoir rocks with 3-D X-ray micro-computed tomography: Solid Earth, v. 7, p. 285-300.

SHELDON, H.A., WHEELER, J., WORDEN, R.H., AND CHEADLE, M.J., 2003, An analysis of the roles of stress, temperature, and pH in chemical compaction of sandstones: Journal of Sedimentary Research, v. 73, p. 64-71.

SILIN, D., AND PATZEK, T., 2006, Pore space morphology analysis using maximal inscribed spheres: Physica A: Statistical Mechanics and its Applications, v. 371, p. 336-360.

SILIN, D.B., JIN, G., AND PATZEK, T.W., 2003, Robust determination of pore space morphology in sedimentary rocks: Annual Technical Conference and Exhibition.

SKARPEID, S.S., CHURCHILL, J.M., HILTON, J.P., IZATT, C.N., AND POOLE, M.T., 2017, The Knarr Field: a new development at the northern edge of the North Sea: Geological Society of London, Petroleum Geology Conference series, v. 8, p. 445-454.

SMALL, J.S., HAMILTON, D.L., AND HABESCH, S., 1992, Experimental simulation of clay precipitation within reservoir sandstones 1: techniques and examples: Journal of Sedimentary Petrology, v. 62, p. 508-519.

SMITH, J.T., AND EHRENBERG, S.N., 1989, Correlation of carbon dioxide abundance with temperature in clastic hydrocarbon reservoirs: relationship to inorganic chemical equilibrium: Marine and Petroleum Geology, v. 6, p. 129-135.

SOUZA, R.S., DE ROS, L.F., AND MORAD, S., 1995, Dolomite Diagenesis and Porosity Preservation in Lithic Reservoirs: Carmópolis Member, Sergipe-Alagoas Basin, Northeastern Brazil: American Association of Petroleum Geologists, v. 79, p. 725-748.

SPOTL, C., HOUSEKNECHT, D.W., AND LONGSTAFFE, F.J., 1994, Authigenic chlorites in sandstones as indicators of high-temperature diagenesis, Arkoma foreland basin, USA: Journal of Sedimentary Research, v. 64, p. 553-566.

STAL, L.J., 2003, Microphytobenthos, their Extracellular Polymeric Substances, and the Morphogenesis of Intertidal Sediments: Geomicrobiology Journal, v. 20, p. 463-478.

STAL, L.J., 2010, Microphytobenthos as a biogeomorphological force in intertidal sediment stabilization: Ecological Engineering, v. 36, p. 236-245.

STEL, H., 2009, Diagenetic crystallization and oxidation of siderite in red bed (Buntsandstein) sediments from the Central Iberian Chain, Spain: Sedimentary Geology, v. 213, p. 89-96.

STOKKENDAL, J., FRIIS, H., SVENDSEN, J.B., POULSEN, M.L.K., AND HAMBERG, L., 2009, Predictive permeability variations in a Hermod sand reservoir, Stine Segments, Siri Field, Danish North Sea: Marine and Petroleum Geology, v. 26, p. 397-415.

STORVOLL, V., BJØRLYKKE, K., KARLSEN, D., AND SAIGAL, G., 2002, Porosity preservation in reservoir sandstones due to grain-coating illite: a study of the Jurassic Garn Formation from the Kristin and Lavrans fields, offshore Mid-Norway: Marine and Petroleum Geology, v. 19, p. 767-781.

STRICKER, S., 2016, Influence of fluid pressure on the diagenesis of clastic sediments: Durham theses, Durham University.

STRICKER, S., AND JONES, S.J., 2018, Enhanced porosity preservation by pore fluid overpressure and chlorite grain coatings in the Triassic Skagerrak, Central Graben, North Sea, UK, *in* Armitage, P.J., Butcher, A., Churchill, J., Csoma, A., Hollis, C., Lander, R.H., Omma, J., and Worden, R.H., eds., Reservoir Quality of Clastic and Carbonate Rocks: Analysis, Modelling and Prediction: Geological Society of London, Special Publication 435, p. 321-341.

STRICKER, S., JONES, S.J., AND GRANT, N.T., 2016a, Importance of vertical effective stress for reservoir quality in the Skagerrak Formation, Central Graben, North Sea: Marine and Petroleum Geology, v. 78, p. 895-909.

STRICKER, S., JONES, S.J., SATHAR, S., BOWEN, L., AND OXTOBY, N., 2016b, Exceptional reservoir quality in HPHT reservoir settings: Examples from the Skagerrak Formation of the Heron Cluster, North Sea, UK: Marine and Petroleum Geology, v. 77, p. 198-215.

STUCKI, J.W., AND KOSTKA, J.E., 2006, Microbial reduction of iron in smectite: Comptes Rendus Geoscience, v. 338, p. 468-475.

SUN, Z.X., SUN, Z.L., YAO, J., WU, M.L., LIU, J.R., DOU, Z.Y., AND PEI, C.R., 2014, Porosity preservation due to authigenic chlorite coatings in deeply buried Upper Triassic Xujiahe formation sandstones, Sichuan Basin, Western China: Journal of Petroleum Geology, v. 37, p. 251-267.

SURDAM, R.C., AND BOLES, J.R., 1979, Diagenesis of volcanic sandstones, *in* Scholle, P.A., and Schluger, P.R., eds., Aspects of Diagenesis, Society of Economic Paleontologists and Mineralogists Special Publication 26, p. 227-242.

SURDAM, R.C., DUNN, T.L., HEASLER, H.P., AND MACGOWAN, D.B., 1989, Porosity evolution in sandstone/shale systems: Short Course on Burial Diagenesis, p. 61-133.

SUTHERLAND, I.W., 2001, Biofilm exopolysaccharides: a strong and sticky framework: Microbiology, v. 147, p. 3-9.

TANG, C., ZHU, J., LI, Z., ZHU, R., ZHOU, Q., WEI, J., HE, H., AND TAO, Q., 2015, Surface chemistry and reactivity of SiO2 polymorphs: A comparative study on α-quartz and α-cristobalite: Applied Surface Science, v. 355, p. 1161-1167.

TANG, L., GLUYAS, J., AND JONES, S., 2018, Porosity preservation due to grain coating illite/smectite: Evidence from Buchan Formation (Upper Devonian) of the Ardmore Field, UK North Sea: Proceedings of the Geologists' Association, v. 129, p. 202-214.

TASSE, N., AND HESSE, R., 1984, Origin and significance of complex authigenic carbonates in Cretaceous black shales of the Western Alps: Journal of Sedimentary Research, v. 54, p. 1012-1027.

TAYLOR, T., STANCLIFFE, R., MACAULAY, C., AND HATHON, L., 2004, High temperature quartz cementation and the timing of hydrocarbon accumulation in the Jurassic Norphlet sandstone, offshore Gulf of Mexico, USA: Geological Society, London, Special Publications, v. 237, p. 257-278.

TAYLOR, T.R., GILES, M.R., HATHON, L.A., DIGGS, T.N., BRAUNSDORF, N.R., BIRBIGLIA, G.V., KITTRIDGE, M.G., MACAULAY, C.I., AND ESPEJO, I.S., 2010, Sandstone diagenesis and reservoir quality prediction: models, myths, and reality: American Association of Petroleum Geologists, Bulletin, v. 94, p. 1093-1132.

TAYLOR, T.R., KITTRIDGE, M.G., WINEFIELD, P., BRYNDZIA, L.T., AND BONNELL, L.M., 2015, Reservoir quality and rock properties modeling – Triassic and Jurassic sandstones, greater Shearwater area, UK Central North Sea: Marine and Petroleum Geology, v. 65, p. 1-21.

THOMSON, A., 1979, Preservation of porosity in the deep Woodbine/Tuscaloosa trend, Louisiana: Journal of Petroleum Technology, v. 34, p. 396-403.

THOMSON, P.-R., AITUAR-ZHAKUPOVA, A., AND HIER-MAJUMDER, S., 2018, Image segmentation and analysis of pore network geometry in two natural sandstones: Frontiers in Earth Science, v. 6, p. 58.

THOMSON, P.-R., ELLIS, R., CHIARELLA, D., AND HIER-MAJUMDER, S., 2020, Microstructural analysis from x-ray ct images of the Brae Formation Sandstone, North Sea: Frontiers in Earth Science, v. 8, p. 246.

TROND, V., ANDREW, K., GLENN, M., AND ADRIAN, S., 2012, Considerations for high-magnification high-cone-angle helical micro-CT: Proc. SPIE 8506.

TSAI, W.-H., 1985, Moment-preserving thresolding: A new approach: Computer Vision, Graphics, and Image Processing, v. 29, p. 377-393.

UESHIMA, M., AND TAZAKI, K., 2001, Possible Role of Microbial Polysaccharides in Nontronite Formation: Clays and Clay Minerals, v. 49, p. 292-299.

VAGLE, G.B., HURST, A., AND DYPVIK, H., 1994, Origin of quartz cements in some sandstones from the Jurassic of the Inner Moray Firth (UK): Sedimentology, v. 41, p. 363-377.

VAN COLEN, C., UNDERWOOD, G.J.C., SERÔDIO, J., AND PATERSON, D.M., 2014, Ecology of intertidal microbial biofilms: Mechanisms, patterns and future research needs: Journal of Sea Research, v. 92, p. 2-5.

VAN HOUTEN, F.B., AND PURUCKER, M.E., 1984, Glauconitic peloids and chamositic ooids - favorable factors, constraints, and problems: Earth-Science Reviews, v. 20, p. 211-243.

VAN NOORT, R., VISSER, H.J.M., AND SPIERS, C.J., 2008, Influence of grain boundary structure on dissolution controlled pressure solution and retarding effects of grain boundary healing: Journal of Geophysical Research: Solid Earth, v. 113.

VEBLEN, D.R., 1992, Electron microscopy applied to nonstoichiometry, polysomatism, and replacement reactions in minerals: Reviews in Mineralogy and Geochemistry, v. 27, p. 181-229.

VENKATESWARAN, K., MOSER, D.P., DOLLHOPF, M.E., LIES, D.P., SAFFARINI, D.A., MACGREGOR, B.J., RINGELBERG, D.B., WHITE, D.C., NISHIJIMA, M., SANO, H., BURGHARDT, J., STACKEBRANDT, E., AND NEALSON, K.H., 1999, Polyphasic taxonomy of the genus Shewanella and description of Shewanella oneidensis sp. nov: International Journal of Systematic and Evolutionary Microbiology, v. 49, p. 705-724.

VIGNAGA, E., SLOAN, D.M., LUO, X., HAYNES, H., PHOENIX, V.R., AND SLOAN, W.T., 2013, Erosion of biofilm-bound fluvial sediments: Nature Geoscience, v. 6, p. 770-774.

VIROLLE, M., BRIGAUD, B., BEAUFORT, D., PATRIER, P., ABDELRAHMAN, E., THOMAS, H., PORTIER, E., SAMSON, Y., BOURILLOT, R., AND FÉNIÈS, H., 2021, Authigenic berthierine and incipient chloritization in shallowly buried sandstone reservoirs: Key role of the source-to-sink context: GSA Bulletin.

VIROLLE, M., BRIGAUD, B., BOURILLOT, R., FÉNIÈS, H., PORTIER, E., DUTEIL, T., NOUET, J., PATRIER, P., AND BEAUFORT, D., 2019a, Detrital clay grain coats in estuarine clastic deposits: origin and spatial distribution within a modern sedimentary system, the Gironde Estuary (south-west France): Sedimentology, v. 66, p. 859-894.

VIROLLE, M., BRIGAUD, B., LUBY, S., PORTIER, E., FÉNIÈS, H., BOURILLOT, R., PATRIER, P., AND BEAUFORT, D., 2019b, Influence of sedimentation and detrital clay grain coats on chloritized sandstone reservoir qualities: Insights from comparisons between ancient tidal heterolithic sandstones and a modern estuarine system: Marine and Petroleum Geology, v. 107, p. 163-184.

VIROLLE, M., FÉNIÈS, H., BRIGAUD, B., BOURILLOT, R., PORTIER, E., PATRIER, P., BEAUFORT, D., JALON-ROJAS, I., DERRIENNIC, H., AND MISKA, S., 2020, Facies associations, detrital clay grain coats and mineralogical characterization of the Gironde estuary tidal bars: A modern analogue for deeply buried estuarine sandstone reservoirs: Marine and Petroleum Geology, v. 114, p. 104225.

VOLLSET, J., AND DORÉ, A.G., 1984, A revised Triassic and Jurassic lithostratigraphic nomenclature for the Norwegian North Sea, Oljedirektoratet.

WALDERHAUG, O., 1990, A fluid inclusion study of quartz-cemented sandstones from offshore mid-Norway; possible evidence for continued quartz cementation during oil emplacement: Journal of Sedimentary Research, v. 60, p. 203-210.

WALDERHAUG, O., 1994, Precipitation rates for quartz cement in sandstones determined by fluid-inclusion microthermometry and temperature-history modeling: Journal of Sedimentary Research, v. 64, p. 324-333.

WALDERHAUG, O., 1996, Kinetic modeling of quartz cementation and porosity loss in deeply buried sandstone reservoirs: American Association of Petroleum Geologists, Bulletin, v. 80, p. 731-745.

WALDERHAUG, O., 2000, Modeling quartz cementation and porosity in Middle Jurassic Brent Group sandstones of the Kvitebjørn field, northern North Sea: American Association of Petroleum Geologists, Bulletin, v. 84, p. 1325-1339.

WALDERHAUG, O., LANDER, R., BJØRKUM, P., OELKERS, E., BJØRLYKKE, K., AND NADEAU, P., 2000, Modelling quartz cementation and porosity in reservoir sandstones: examples from the Norwegian continental shelf, *in* Worden, R.H., and Morad, S., eds., Quartz Cementation in Sandstones: International Association of Sedimentologists, Special Publication 29, p. 39-49.

WALGENWITZ, F., 2003, Causes for the preservation of high reservoir quality at great depth in the HP-HT reservoirs of the Elgin-Franklin fields, Central North Sea Graben, UK: 2003 AAPG International Conference & Exhibition Technical Program.

WALKER, J.R., 1993, Chlorite polytype geothermometry: Clays and Clay Minerals, v. 41, p. 260-267.

WARREN, E.A., AND PULHAM, A.J., 2001, Anomalous Porosity and Permeability Preservation in Deeply Buried Tertiary and Mesozoic Sandstones in the Cusiana Field, Llanos Foothills, Colombia: Journal of Sedimentary Research, v. 71, p. 2-14.

WAUGN, B., 1970, Formation of quartz overgrowths in the Penrith Sandstone (Lower Permian) of northwest England as revealed by scanning electron microscopy: Sedimentology, v. 14, p. 309-320.

WEIBEL, R., FRIIS, H., KAZEROUNI, A.M., SVENDSEN, J.B., STOKKENDAL, J., AND POULSEN, M.L.K., 2010, Development of early diagenetic silica and quartz morphologies - Examples from the Siri Canyon, Danish North Sea: Sedimentary Geology, v. 228, p. 151-170.

WEIBEL, R., OLIVARIUS, M., KJØLLER, C., KRISTENSEN, L., HJULER, M.L., FRIIS, H., PEDERSEN, P.K., BOYCE, A., ANDERSEN, M.S., KAMLA, E., BOLDREEL, L.O., MATHIESEN, A., AND NIELSEN, L.H., 2017, The

influence of climate on early and burial diagenesis of Triassic and Jurassic sandstones from the Norwegian–Danish Basin: The Depositional Record, v. 3, p. 60-91.

WEICKERT, J., ROMENY, B.M.T.H., AND VIERGEVER, M.A., 1998, Efficient and reliable schemes for nonlinear diffusion filtering: IEEE Transactions on Image Processing, v. 7, p. 398-410.

WHITE, J.F., TAYLOR, M.C., AND VINCENT, G.P., 1942, Chemistry of chlorites: Industrial & Engineering Chemistry, v. 34, p. 782-792.

WIDDEL, F., AND BAK, F., 1992, Gram-Negative Mesophilic Sulfate-Reducing Bacteria, *in* Balows, A., Trüper, H.G., Dworkin, M., Harder, W., and Schleifer, K.-H., eds., The Prokaryotes: A Handbook on the Biology of Bacteria: Ecophysiology, Isolation, Identification, Applications: New York, NY, Springer New York, p. 3352-3378.

WIDDEL, F., KOHRING, G.-W., AND MAYER, F., 1983, Studies on dissimilatory sulfate-reducing bacteria that decompose fatty acids: Archives of Microbiology, v. 134, p. 286-294.

WIDDEL, F., AND PFENNIG, N., 1981, Studies on dissimilatory sulfate-reducing bacteria that decompose fatty acids: Archives of Microbiology, v. 129, p. 395-400.

WIERZCHOS, J., ASCASO, C., SANCHO, L.G., AND GREEN, A., 2003, Iron-Rich Diagenetic Minerals are Biomarkers of Microbial Activity in Antarctic Rocks: Geomicrobiology Journal, v. 20, p. 15-24.

WILDENSCHILD, D., AND SHEPPARD, A.P., 2013, X-ray imaging and analysis techniques for quantifying pore-scale structure and processes in subsurface porous medium systems: Advances in Water Resources, v. 51, p. 217-246.

WILKINSON, M., AND HASZELDINE, R.S., 2011, Oil charge preserves exceptional porosity in deeply buried, overpressured, sandstones: Central North Sea, UK: Journal of the Geological Society, v. 168, p. 1285-1295.

WILKINSON, M., STUART HASZELDINE, R., ELLAM, R.M., AND FALLICK, A., 2004, Hydrocarbon filling history from diagenetic evidence: Brent Group, UK North Sea: Marine and Petroleum Geology, v. 21, p. 443-455.

WILLIAMS, L.A., PARKS, G.A., AND CRERAR, D.A., 1985, Silica diagenesis .1. Solubility controls: Journal of Sedimentary Petrology, v. 55, p. 301-311.

WILSON, M., WILSON, L., AND PATEY, I., 2014, The influence of individual clay minerals on formation damage of reservoir sandstones: a critical review with some new insights: Clay Minerals, v. 49, p. 147-164.

WILSON, M.D., 1992, Inherited grain-rimming clays in sandstones from eolian and shelf environments: their origin and control on reservoir properties, *in* Houseknecht, D.W., and Pitman, E.D., eds., Origin, Diagenesis, and Petrophysics of Clay Minerals in Sandstones, Special Publication of the Society of Economic Palaeontologists and Mineralogists 47, p. 209-225.

WILSON, M.D., AND PITTMAN, E.D., 1977, Authigenic clays in sandstones: Recognition and influence on reservoir properties and paleoenvironmental analysis: Journal of Sedimentary Petrology, v. 47, p. 3-31.

WILSON, M.D., AND STANTON, P.T., 1994, Diagenetic mechanisms of porosity and permeability reduction and enhancement, *in* Wilson, M.D., ed., Reservoir Quality Assessment and Prediction in Clastic Rocks, SEPM Short Course, p. 59-118.

WOOLDRIDGE, L.J., WORDEN, R.H., GRIFFITHS, J., THOMPSON, A., AND CHUNG, P., 2017a, Biofilm origin of clay-coated sand grains: Geology, v. 45, p. 875-878.

WOOLDRIDGE, L.J., WORDEN, R.H., GRIFFITHS, J., AND UTLEY, J.E.P., 2017b, Clay-coated sand grains in petroleum reservoirs: understanding their distribution via a modern analogue: Journal of Sedimentary Research, v. 87, p. 338-352.

WOOLDRIDGE, L.J., WORDEN, R.H., GRIFFITHS, J., AND UTLEY, J.E.P., 2019, How to quantify clay-coat grain coverage in modern and ancient sediments: Journal of Sedimentary Research, v. 89, p. 135-146.

WORDEN, R.H., ARMITAGE, P.J., BUTCHER, A.R., CHURCHILL, J.M., CSOMA, A.E., HOLLIS, C., LANDER, R.H., AND OMMA, J.E., 2018a, Petroleum reservoir quality prediction: overview and contrasting approaches from sandstone and carbonate communities, *in* Armitage, P.J., Butcher, A., Churchill, J., Csoma, A., Hollis, C., Lander, R.H., Omma, J., and Worden, R.H., eds., Reservoir Quality of Clastic and Carbonate Rocks: Analysis, Modelling and Prediction: Geological Society of London, Special Publication 435, p. 1-31.

WORDEN, R.H., BUKAR, M., AND SHELL, P., 2018b, The effect of oil emplacement on quartz cementation in a deeply buried sandstone reservoir: American Association of Petroleum Geologists, Bulletin, v. 102, p. 49-75.

WORDEN, R.H., AND BURLEY, S.D., 2003, Sandstone diagenesis: the evolution of sand to stone, *in* Burley, S.D., and Worden, R.H., eds., Sandstone Diagenesis: Recent and Ancient: International Association of Sedimentologists, Special Publication 34, p. 3-44.

WORDEN, R.H., FRENCH, M.W., AND MARIANI, E., 2012, Amorphous silica nanofilms result in growth of misoriented microcrystalline quartz cement maintaining porosity in deeply buried sandstones: Geology, v. 40, p. 179-182.

WORDEN, R.H., GRIFFITHS, J., WOOLDRIDGE, L.J., UTLEY, J.E.P., LAWAN, A.Y., MUHAMMED, D.D., SIMON, N., AND ARMITAGE, P.J., 2020, Chlorite in sandstones: Earth-Science Reviews, v. 204, p. 103105.

WORDEN, R.H., MAYALL, M., AND EVANS, I.J., 2000, The Effect of Ductile-Lithic Sand Grains and Quartz Cement on Porosity and Permeability in Oligocene and Lower Miocene Clastics, South China Sea: Prediction of Reservoir Quality: American Association of Petroleum Geologists, Bulletin, v. 84, p. 345-359.

WORDEN, R.H., AND MORAD, S., 2000, Quartz cementation in oil field sandstones: a review of the key controversies, *in* Worden, R.H., and Morad, S., eds., Quartz cementation in sandstones: International Association of Sedimentologists, Special publication 29, p. 1-20.

WORDEN, R.H., AND MORAD, S., 2003, Clay minerals in sandstones: controls on formation, distribution and evolution, *in* Worden, R.H., and Morad, S., eds., Clay Mineral Cements in Sandstones: International Association of Sedimentologists, Special Publication 34, p. 3-41.

WORDEN, R.H., NEEDHAM, S.J., AND CUADROS, J., 2006, The worm gut; a natural clay mineral factory and a possible cause of diagenetic grain coats in sandstones: Journal of Geochemical Exploration, v. 89, p. 428-431.

WORDEN, R.H., OXTOBY, N.H., AND SMALLEY, P.C., 1998, Can oil emplacement prevent quartz cementation in sandstones?: Petroleum Geoscience, v. 4, p. 129.

WORDEN, R.H., UTLEY, J.E.P., BUTCHER, A.R., GRIFFITHS, J., WOOLDRIDGE, L.J., AND LAWAN, A.Y., 2018c, Improved imaging and analysis of chlorite in reservoirs and modern day analogues: new insights for reservoir quality and provenance, *in* Dowey, P.J., Osborne, M.J., and Volk, H., eds., Application of Analytical Techniques to Petroleum Systems: Geological Society of London, Special Publication 484.

XU, H., AND VEBLEN, D.R., 1996, Interstratification and other reaction microstructures in the chlorite-berthierine series: Contributions to Mineralogy and Petrology, v. 124, p. 291-301.

XU, T., APPS, J.A., AND PRUESS, K., 2004, Numerical simulation of CO2 disposal by mineral trapping in deep aquifers: Applied Geochemistry, v. 19, p. 917-936.

YOU, L., QU, X., ZHONG, J., LI, C., WU, S., GAO, Y., AND CUI, J., 2020, Physical simulation experiments on pore evolution in high-temperature and overpressure reservoirs: Natural Gas Industry B, v. 7, p. 30-39.

YOUSSEF, S., ROSENBERG, E., GLAND, N.F., KENTER, J.A., SKALINSKI, M., AND VIZIKA, O., 2007, High resolution CT and pore-network models to assess petrophysical properties of homogeneous and heterogeneous carbonates, SPE/EAGE Reservoir Characterization and Simulation Conference: Abu Dhabi, UAE, Society of Petroleum Engineers, p. 12.

ZHANG, G., KIM, J., DONG, H., AND SOMMER, A.J., 2007, Microbial effects in promoting the smectite to illite reaction: Role of organic matter intercalated in the interlayer: American Mineralogist, v. 92, p. 1401-1410.

ZHANG, P., LEE, Y.I., AND ZHANG, J., 2019, A review of high-resolution X-ray computed tomography applied to petroleum geology and a case study: Micron, v. 124, p. 102702.

Appendix A

Supporting information related to the AQM and XCT analysis

Mineral recipe used for the AQM analysis

The mineral list for the sample analysis was created in-house based on the element wt% of the mappable phases and was used to produce a variety of visualizable informative image and data outputs. For each mineral, the range of tolerated concentrations for each element, as well as for ratios between two elements, was used to define the mineral phase (Table A.1). Minerals are placed in a list, which is checked against the chemistry of each analysed point, following a first-match principle.

Mineral	Elements	Max	Min
Quartz	O	80	20
	Fe	6	0
	Si	80	25
	K	4	0
	Al	6	0
Siderite	O	60	15
	Fe	-	35
	Si	35	-
Berthierine	O	55	23
	Mg	5	0
	Al	30	11
	Si	43	4
	K	5	0
	Fe	34.9	8
	Ca	2	-
Chlorite	O	60	5
	Si	60	13
	Fe	60	5
	Al	10.99	-
	Na	10	-
	K	1.9	-
	Ca	3	-
	Mg	6	-
Orthoclase	Ba	4.9	0
	O	55	30
	Fe	6	0
	Na	5	0
	Si	50	23
	Al	24	5
	Mg	0.001	0
	Ca	1	0
	K	35	5.01

Kaolinite	K	5	0
	Si	50	15
	Al	40	12
	O	65	15
	Na	2	-
	Ca	2	-
	Mg	2	-
	Fe	5	-
Albite	Al	14.8	5
	K	1	-
	O	60	25
	Na	12	7
	Ca	5	0
	Mg	0.1	0
	Si	50	27
Altered kaolinite	K	2	-
	Si	33	15
	Al	24	10
	O	65	15
	Na	18	2.1
	Fe	3	-
	Ca	1	0
Muscovite	Fe	12	0.1
	O	50	20
	Si	32	7
	Al	30	10
	K	14	2
	Mg	3	0
Calcite	O	65	20
	Ca	60	15
Rutile	Ti	80	30
	O	66	25
Garnet	O	55	20
	Mg	12	-
	Al	18	5
	Si	25	12
	Ca	11	1
	Fe	32	10
Fe-Ti oxides	Ti	-	80
	Fe	10	-

Biotite	Si	61	7
	Al	30	5
	Mg	22	0
	Fe	49	0
	K	12	3
	O	51	20
Pyrite	S	59	25
	Fe	80	25
	Fe:Pb	-	1
	Pb	25	0
	Cu	0.01	0
Dolomite	Al	0.001	0
	Mg	25	6
	O	65	20
	Ca	50	15
	Fe	0.99	0
	Mg	4	1
Illite	K	12	5
	Al	24	9
	Ti	2	0.01
	Si	27	15
	O	55	39
	Fe	8	2
Smectite	O	65	35
	Al	22	12
	Mg	4	0.1
	Ca	4	0.1
	Fe	8	0.1
	Si	27	13
Apatite	P	23	7
	Ca	53	33
	Cl	12	0
	O	46	28
	F	9	0.1

Table A.1: Mineral classification list, individual minerals can be defined by element concentration (e.g., min and max values) and element ratios.

XCT acquisition characteristics and XCT processing workflow

Sample	Voltage (kV)	Current (mA)	Exposure time (s)	Voxel size (µm)	Sample volume	Data size (voxel)	Data size (mm)
S1	80	125	2	3.8	full sample	1416 x 1458 x 1687	5.4 x 5.5 x 6.4
	-	-	-	3.8	cylindrical	945 x 943 x 930	3.6 x3.6 x 3.5
S2	80	125	2	3.8	full sample	1364 x 1383 x1820	5.2 x 5.3 x 6.9
	-	-	-	3.8	cylindrical	945 x 943 x 1130	3.6 x 3.6 x 4.3
S3	80	125	2	3.8	full sample	1379 x 1377 x 1757	5.2 x 5.5 x 6.7
	-			3.8	cylindrical	944 x 943 x 884	3.6 x 3.6 x 3.4
S4	80	125	2	3.8	full sample	1351x1346x1757	5.1 x 5.1 x 6.7
	-	-	-	3.8	cylindrical	942 x 939 x 1023	3.6 x 3.6 x 3.9
S5	80	125	2	3.8	full sample	1335 x 1419 x 1818	5.1 x 5.4 x 6.9
	-	-	-	3.8	cylindrical	944 x 943 x 1037	3.6 x 3.6 x 3.9
S1-S5	-	-	-	3.8	cubic	500 x 500 x 500	1.9 x1.9x 1.9
S6A	80	120	1	5.6	full sample	768 x 742 x 4000	4.3 x 4.2 x 22.4
	-	-	-	5.6	cuboid	333 x 334 x 3548	1.9 x 1.9 x 19.9
S6B	80	120	1	1.7	full sample	1880 x 1880 x 3560	3.2 x 3.2 x 6.1
	-	-	-	1.7	cuboid	1104 x 1159 x 2918	1.9 x 2 x 5
S6C1-C3	-	-	-	1.7	cubic	500 x 500 x 500	0.9 x 0.9 x 0.9

Table A.2: XCT acquisition characteristics of the raw data (full sample) and size of the analysed subvolumes.

Raw XCT data are available online at:

1. http://doi.org/10.15128/r30v838056z (Single-stage experiments, Samples S1, S2, S5)
2. http://doi.org/10.15128/r32514nk484 (Multi-stage experiments, Sample S6A)
3. http://doi.org/10.15128/r3bc386j205 (Multi-stage experiments, Sample S6B)

Grain coat segmentation process

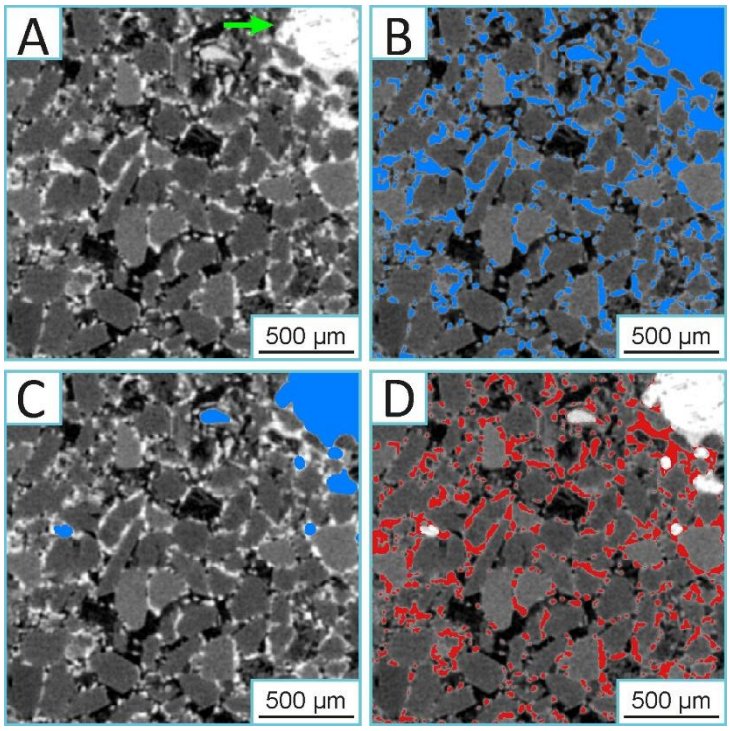

Figure A.1: Grain coat segmentation process. A) 2D tomogram of the Cook Formation (sample S5) at a resolution of 3.8 µm/voxel. B) Selection of the bright phase, including grain coating and pore filling (green arrow) phases. C) Selection of the pore filling bright phase. D) Selection of the bright phase fringing the host grains (e.g., grain coats).

The bright phase (both grain coating and pore filling) was segmented using a histogram-based, moment-preserving threshold algorithm [Tsai, 1985]. The user-defined low and high threshold greyscale values used by the algorithm to determine the placement of the phase interface are presented in Table A.3. Subsequently, the *Opening* Avizo module was applied to perform a 3D opening of the segmented binary image, using a spherical structuring element, discarding small objects and keeping the largest ones with similar shape in the original and the final image. Then a logical difference between the binary image of the overall bright phase and the pore filling bright phase was applied to acquire the grain coats.

Sample	T (°C)	Bright phase	
		Pre-exp	Post-exp
S1 (cylinder)	100	6700-11800	6900-12000
S2 (cylinder)	150	9000-15200	7500-14500
S3 (cylinder)	200	6700-14500	6500-14600
S4 (cylinder)	225	6400-14500	8900-15000
S5 (cylinder)	250	3700-8000	10800-17800
S1 (cube)	100	6600-11500	6700-11600
S2 (cube)	150	9800-13600	8300-12450
S3 (cube)	200	7600-11200	7400-11000
S4 (cube)	225	7300-11000	9800-12500
S5 (cube)	250	4000-6600	11300-16000
S6A (5.57 µm/voxel)	0	17000-24500	
S6A (5.57 µm/voxel)	100	17000-23600	
S6A (5.57 µm/voxel)	150	17000-24200	
S6A (5.57 µm/voxel)	200	16500-23000	
S6A (5.57 µm/voxel)	250	13300-17000	
S6B (1.7 µm/voxel)	0	12000-20300	
S6B (1.7 µm/voxel)	100	12000-20300	
S6B (1.7 µm/voxel)	150	12000-20300	
S6B (1.7 µm/voxel)	200	11000-15300	
S6B (1.7 µm/voxel)	250	10800-15200	

Table A.3: User-defined thresholding greyscale range employed by the moment preserving algorithm for the determination of the bright phase.

Porosity and microporous material segmentation process

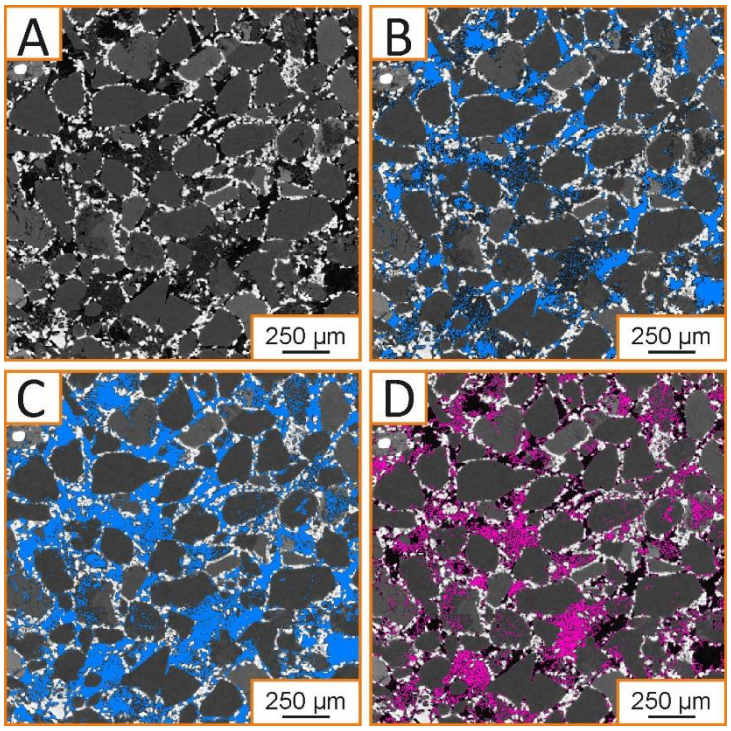

Figure A.2: Porosity and microporous material segmentation process. A) 2D tomogram of the Cook Formation (sample S6B) at a resolution of 1.7 µm/voxel. B) Selection of the imaged porosity. C) Segmentation of the pore space combined with microporous regions, such as pore filling clays and fractures within the framework grains. D) Selection of the microporous volume

The imaged pore phase was segmented using a histogram-based, moment-preserving threshold algorithm [Tsai, 1985]. The user-defined low and high threshold greyscale values used by the algorithm to determine the placement of the phase interface are presented in Table A.4. Subsequently, imaged porosity combined with microporous regions were segmented using an interactive (or watershed) threshold algorithm (Table A.5). The microporous material volume was acquired by applying a logical difference between the initial porosity binary image and the result of the last segmentation.

Sample	T (°C)	Porosity	
		Pre-exp	Post-exp
S1 (cylinder)	100	3400-6700	4300-6750
S2 (cylinder)	150	6800-9000	5300-7800
S3 (cylinder)	200	4800-6900	4800-6900
S4 (cylinder)	225	4200-6600	7000-9000
S5 (cylinder)	250	2800-3700	8000-10600
S1 (cube)	100	3400-6700	4400-6750
S2 (cube)	150	7500-9000	6100-7700
S3 (cube)	200	5000-7400	5000-7400
S4 (cube)	225	4400-6700	7000-9000
S5 (cube)	250	2650-3850	7000-10750
S6A (5.57 µm/voxel)	0	7000-15000	
S6A (5.57 µm/voxel)	100	8500-15000	
S6A (5.57 µm/voxel)	150	7000-15000	
S6A (5.57 µm/voxel)	200	7000-14800	
S6A (5.57 µm/voxel)	250	11200-12200	
S6B (1.7 µm/voxel)	0	8000-12500	
S6B (1.7 µm/voxel)	100	8000-12500	
S6B (1.7 µm/voxel)	150	8000-12500	
S6B (1.7 µm/voxel)	200	8000-11200	
S6B (1.7 µm/voxel)	250	8000-11200	

Table A.4: User defined thresholding greyscale range employed by the moment preserving algorithm for the determination of the porosity phase.

Sample	T (°C)	Porosity + microporous volume
S6B (1.7 µm/voxel)	0	9900-12300
S6B (1.7 µm/voxel)	100	9900-12300
S6B (1.7 µm/voxel)	150	9900-12300
S6B (1.7 µm/voxel)	200	9900-11050
S6B (1.7 µm/voxel)	250	9900-11050

Table A.5: User defined thresholding greyscale range employed by the moment preserving algorithm for the determination of the combination of the porosity and microporous material phases.

Uncertainty of the XCT measurements

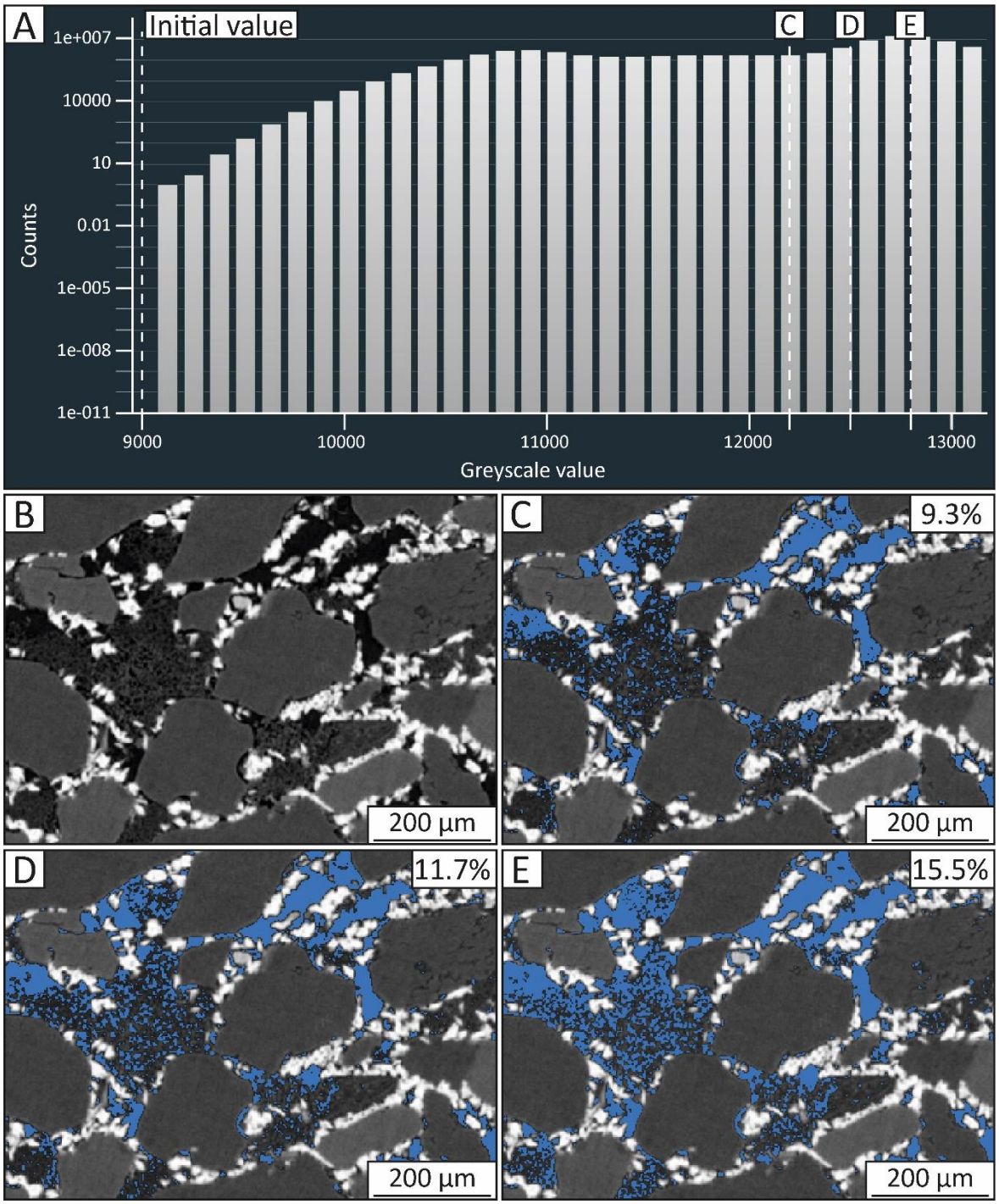

Figure A.3: Uncertainty of the porosity segmentation analysis and associated porosity values of the 2D tomograms. A) Histogram used to select the low- and high-intensity greyscale values to extract the porosity phase. B) Greyscale slice of the sample at a resolution of 1.7 µm/voxel. C) Underestimated pore phase. C) Optimum pore phase. The selection of the user-defined threshold values was made based on the geological interpretation of the data to minimise the error. D) Overestimated pore phase. Note the prominent overestimation in regions occupied by pore filling clay material.

To test the magnitude of this systematic component on the total porosity the effect of inaccurate segmentation was investigated. We take a randomly selected cubic subvolume (500x500x500) with a resolution of 1.7 µm/voxel. The imaged pore phase was segmented using the standard workflow:

using the “auto-thresholding” algorithm that is part of the standard build of the Avizo® software. This is a histogram-based, moment-preserving threshold algorithm [Tsai, 1985]. The pore phase was segmented three times using different user-defined threshold values. In this algorithm, the user defines values below which a voxel is only ever phase 1, and above which all voxels are only ever phase 2. The algorithm then applies a statistical assessment of the voxels with values between those two thresholds, assigning the voxel to phase 1 or phase 2 based on the structure of the local data. This method minimises the human interaction with the data while having the best fidelity to the geological interpretation.

In the example shown, a value of 9000 was used as a low threshold greyscale value (all voxels with a value below 9000 are defined as pore). The high threshold (above which all voxels are NOT pore) was set to 12500 based on the geological interpretation of the data as in the standard analysis procedure (Figure 1D), yielding a measured porosity of 11.7%. The upper threshold was then adjusted to 12200 (the lowest, Figure 1C) and 12800 (highest, Figure 1E), marking the extreme possible values that still gave a plausibly “adequate” (but non-optimal) segmentation based on the geological interpretation. The “just adequate” segmentations would decrease the porosity to 9.3% and increase it to 15.5%, respectively. In the workflow, we estimate that the range of values selected by different human analysts would be within 10-20 greyscale values (meaning the difference in the porosity between analysts would be <0.25%). The location of the pore/solid interface in different samples was assessed visually by the analysts to ensure consistent placement in similar pore structures and ensure the segmentation is consistent.

In any segmented dataset, there will be both the systematic and random components to the uncertainty and error in the measurement of the volume of the individual segmented objects. The systematic error in a measured volume is derived from an error in the threshold used during the segmentation process. The random error is due to the interaction of the segmentation with the partial volume effect – i.e., where the individual is located with the regular grid of the voxel matrix. Both the systematic and random components of the error are a function of the size of the measured object (i.e., volume) relative to the voxel size. Lin et al. (2015) presented a detailed assessment of both errors and demonstrated a measurement of any single individual object larger than about 260 as a combined uncertainty in the volume of less than 10%. The uncertainty reduces with increasing volume. The smallest individual pore volume identified in all the volumes analysed during this study (both pre- and post-experiment) is approximately 8000 voxels. At this volume, the uncertainty is insignificant (e.g., ~ 0.003%), and when considering the population of multiple pores of this volume this uncertainty is reduced further (Lin et al. 2015).

Marker extent parameter

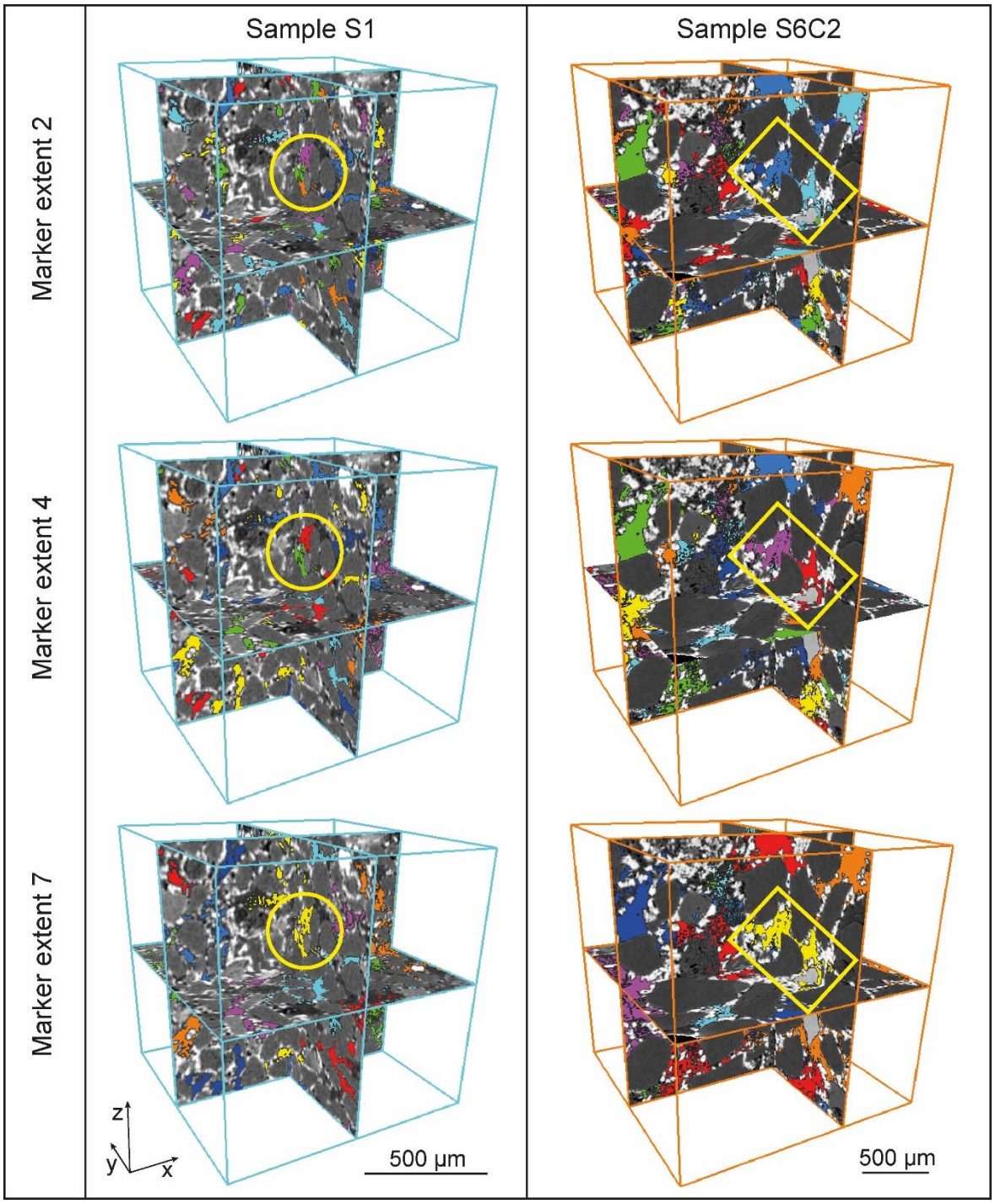

Figure A.4: 2D-3D examination of samples S1 and S6C2 to determine the marker extent parameter. Regardless of the difference in the resolution of the two samples, a marker extent value of seven is the most valid. Note the degree of separation (examples outlined in yellow) with increasing the marker extent value for each sample. The value of 2 and 4 over-separates the pore network.

The *Separate* Avizo module was used to separate the connected pore network into a set of connected and labelled pores. The degree of separation, important for the Pore Network Modelling (PNM), is dictated by the marker extent parameter. This is a contrast factor controlling the size of

seeds marking objects to be separated. The smaller this parameter is the more separated the main pore network will be, and smaller individual pores will be generated and identified. Contrarily, increasing this value can merge some markers and therefore decrease the number of separated pores. 2D-3D visualization was performed for each rock individually (pre- and post-reaction) to reliably determine the detachment of the pore structures in order to avoid under- or over-separation.

Scanning resolution effect

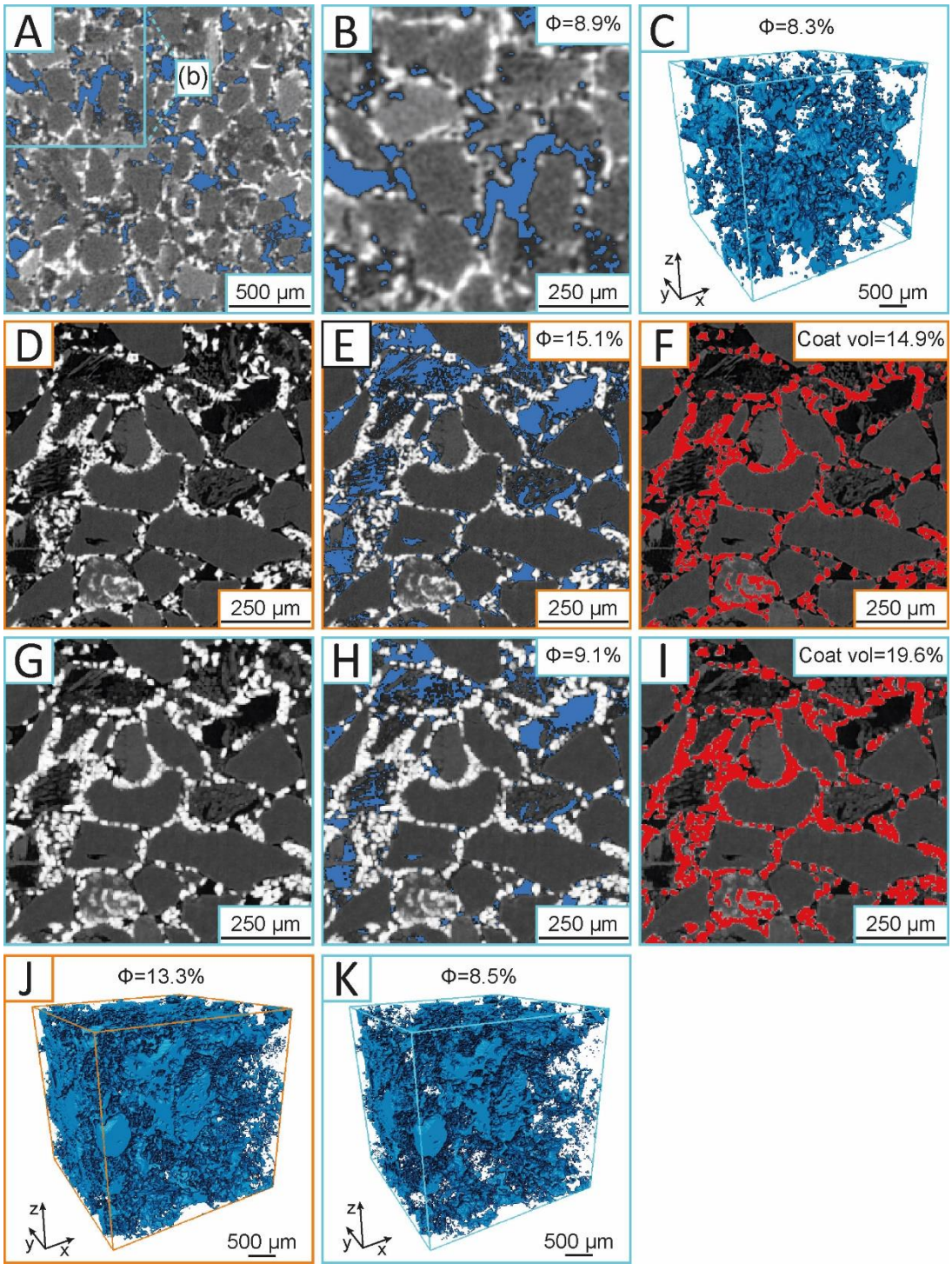

Figure A.5: Comparison between the lower resolution samples S1-S5 belonging to the first set of experiments with the higher resolution sample S6C2 of the second set of experiments. A) Greyscale slice of sample S4 with associated porosity phase. B) Cropped 2D slice matching the dimensions of sample SC62. C) 3D render of sample S4 after being cropped. D) Greyscale image of sample S6C2 and associated pore (E) and grain coats (F) phase. (G) Downsampled greyscale slice of sample S6C2 with associated porosity (H) and grain coat volume (I). 3D Porosity render before (J) and after (K) the downsampling.

The effect of the scanning resolution on the quantification of the phases of interest between the samples from both experimental suites (e.g., single- and multi-thermal) before hydrothermal

treatment was evaluated. Namely, the cubic subvolume of sample S4 was cropped to match the volume of sample S6C2. Subsequently, the *Resample* Avizo module with the maximum filter, that preserves tiny dark features on a bright background, was used to downsample (e.g., shrink the dimensions of the regular grid while recalculating the data according to it) sample S6C2 (1.7 µm/voxel) to match the resolution of sample S4 (3.8 µm/voxel). The *Volume Fraction* Avizo module was then used to quantify the pore and grain coating material phase of each sample to ascertain the resolution effect.

Appendix B

In the following paper, D.C. designed and performed the experiments and contributed to the writing of the manuscript.

- Bello A. M., D. Charlaftis, S. J. Jones, J. Gluyas, S. Acikalin and M. Cartigny, Experimental diagenesis using present-day submarine turbidite sands (submitted to a peer-reviewed journal).

In the following two papers, D.C. provided critical feedback and contributed to the writing of the manuscript.

- Aro, O. E., S. J. Jones, N. Meadows, J. Gluyas and D. Charlaftis, The importance of facies, grain size, and clay content in controlling fluvial reservoir quality – An example from the Triassic Skagerrak Formation, Central North Sea, UK (submitted to a peer-reviewed journal).
- Liu, X., S. J. Jones, D. A. T. Harper and D.Charlaftis, Impact of bioturbation on reservoir quality of potential tight gas sandstone reservoirs, Lower Carboniferous, Northumberland, UK (submitted to a peer-reviewed journal).